SEMILEPTONIC DECAYS $D^+ \rightarrow \eta^{(\prime)}\ell^+\nu$ WITH GENERIC RECONSTRUCTION OF FULLY HADRONIC D^+ AND D^0 DECAYS

A Dissertation

Presented to the Faculty of the Graduate School

of Cornell University

in Partial Fulfillment of the Requirements for the Degree of

Doctor of Philosophy

by

Richard Carl Gray

January 2009

SEMILEPTONIC DECAYS $D^+ \to \eta^{(\prime)}\ell^+\nu$ WITH GENERIC RECONSTRUCTION

OF FULLY HADRONIC D^+ AND D^0 DECAYS

Richard Carl Gray, Ph.D.

Cornell University 2009

We study the semileptonic decays $D^+ \to \eta' e^+\nu$ and $D^+ \to \eta e^+\nu$ using 818 pb^{-1} of e^+e^- collisions recorded by the CLEO-c detector located at the Cornell Electron Storage Ring. We employ a technique that uses the detector hermeticity to reconstruct the neutrino as missing energy and momentum. We improve the neutrino resolution by developing a generic algorithm to reconstruct the non-signal D, and constrain systematic uncertainties in the efficiency by using the algorithm to measure the branching fractions of D^+ and D^0 hadronic decays. We observe and measure the branching fractions of 67 hadronic decays, 32 of which are not listed in the PDG 2008. We find $\mathcal{B}(D^+ \to \eta' e^+\nu) = (2.16 \pm 0.53 \pm 0.05 \pm 0.05) \times 10^{-4}$ and $\mathcal{B}(D^+ \to \eta e^+\nu) = (11.7 \pm 0.98 \pm 0.34 \pm 0.26) \times 10^{-4}$. Among the 67 D hadronic branching fractions observed in this analysis, we discover the decay $\mathcal{B}(D^+ \to \pi^+\eta\eta) = (0.34 \pm 0.06 \pm 0.032)\%$ which is unexpectedly large considering the limited phase space available to the decay.

BIOGRAPHICAL SKETCH

Richard Carl Gray was born on May 23rd 1978 to parents Kenneth D. Gray and Linda M. Gray. Kenneth D. Gray was a school teacher and artist, the first of his family to go to college, and Linda M. Gray had a degree in education and mathematics. Richard was the eighth child in a family of 9 children. From a young age he expressed interest in math, science, and fine art. Impatient of waiting for the public school system to teach him how the world worked, Richard frequently went out of his way to learn things for himself with library books, lab kits, his brother's computer, and dissected appliances. Luckily, despite his tinkering and experiments, he avoided burning the house down. In junior high he convinced his older brother to get him a calculus text book from the University library and taught himself Calculus (just for the fun of it). Richard received an Honors at Entrance scholarship to the University of Utah, and to the dismay of his art teachers he decided to major in physics. After his first year in the physics program, he began working for the High Resolution Fly's Eye group that measured the spectrum of ultra high energy cosmic rays. He quickly became involved in the atmospheric calibration, and in addition to working on the hardware and software for the bi-static LIDAR system he also developed new analysis techniques that provided the first measurements of the aerosol distributions within the detector aperture. These measurements, (internally known as "Richard's Gray Atmosphere") helped to push the spectrum toward the expected GZK cutoff. After he finished his bachelor's degree Richard was accepted to Cornell University, where he began to work on the CLEO experiment studying semileptonic decays containing the η and η' mesons. After finishing his PhD he plans to work on the CMS experiment at Rutgers University.

I'd like to dedicate this thesis to my family and my fiance. They drive me crazy

sometimes, but I wouldn't be here without them.

ACKNOWLEDGEMENTS

TABLE OF CONTENTS

LIST OF TABLES

1.1   Motivation from $B \to \eta^{(\prime)} X$ and $B \to \eta^{(\prime)} \ell \nu$ decays

Experimental motivation for the study of heavy quark decays to η and η' mesons began over a decade ago with CLEO measurements of the $B \to \eta^{(\prime)} X$ branching fractions [1]. The size of the branching fractions were completely unexpected. The early simplistic calculations were as much as 300 times smaller than the measurements [2], and even today, modern calculations of many of these decays can be a factor of 2 or more in disagreement with data [23].

Semileptonic decays involving the η and η' are useful probes of the mechanisms that could be at work. The fact that the lepton and neutrino in the decays do not exchange gluons with the quarks in the $\eta^{(\prime)}$ enables us to cleanly isolate the $B \to \eta^{(\prime)}$ form factors. Previous CLEO measurements of $B \to \eta \ell \nu$ and $B \to \eta' \ell \nu$ gave evidence for gluonic contributions in this form factor by seeing a very large $B \to \eta' \ell \nu$ branching fraction at the 3σ level [3]. (Note that BABAR's measurement of $B \to \eta' \ell \nu$ did not see evidence for this decay [4].)

Aside from mass related effects, QCD is flavor blind, and therefore the decays $D^+ \to \eta \ell^+ \nu$ and $D^+ \to \eta' \ell^+ \nu$ provide a similar probe for enhancement of decays involving η'.

1.1.1   Unexpected $B \to \eta' X$ Decays

In 1997 CLEO published results for a study of rare B meson decays to two charmless pseudoscalar mesons [1]. The results of that study, specifically those including the η', gave theorists much to be excited about.

Prior to the CLEO measurements, much smaller branching fractions were expected for these charmless decay modes. In a theoretical paper published in 1995, [5], two

years before the publication of CLEO results, decays involving $b \to c\bar{c}s$ and $b \to u\bar{u}s$ were expected to be dominated by tree-level W-mediated decays. If contributions from gluonic penguins are ignored, one would expect huge differences between charmed and charmless branching fractions due to CKM suppression.

For example, consider the comparison of the decays $B \to \eta' + X_s$ and the decay $B \to \eta_c(1S) + X_s$, where η_c is a nearly pure $c\bar{c}$ state. The ratio of the decay rates for these two modes is

$$\frac{\Gamma(B \to \eta' + X_s)}{\Gamma(B \to \eta_c(1S) + X_s)} \sim \frac{(V_{ub})^2}{(V_{cb})^2} \frac{|<\eta'|\bar{u}\gamma_\mu\gamma_5 u|0><X_s|\bar{s}\gamma_\mu(1+\gamma_5)b|B>|^2}{|<\eta_c|\bar{c}\gamma_\mu\gamma_5 c|0><X_s|\bar{s}\gamma_\mu(1+\gamma_5)b|B>|^2} \frac{\Omega_{B \to \eta'+X}}{\Omega_{B \to \eta_c+X}},$$
(1.1)

[2], where Ω represents the available phase space for each mode given the masses of the different daughters. This equation reduces to

$$\frac{\Gamma(B \to \eta' + X_s)}{\Gamma(B \to \eta_c(1S) + X_s)} \sim \frac{1}{3} \frac{(V_{ub})^2}{(V_{cb})^2} \frac{(f_{\eta'})^2}{(f_{\eta_c})^2} \frac{(1 - m_{\eta'}^2/m_b^2)^2}{(1 - m_{\eta_c}^2/m_b^2)^2} \sim 3 \times 10^{-4},$$
(1.2)

[2].

The ratio of the measured branching fractions of the modes $B^+ \to \eta' K^+$ and $B^+ \to \eta_c K^+$ is

$$\frac{Br(B^+ \to \eta' K^+)}{Br(B^+ \to \eta_c K^+)} = \frac{(7.02) \times 10^{-5}}{(9.1) \times 10^{-4}} = 0.077,$$
(1.3)

as of 2008. Clearly, the assumptions and approximations that were made in the initial round of calculations were insufficient.

There are several ways to account for this huge disparity. First, the gluon penguin diagrams were not included, and today we know that they may not be negligible. It has also been suggested that the content of the η' may be to blame. The η' could have a significant charm component that would greatly reduce the CKM suppression. Or, the η' may have a strong coupling to gluons due to the QCD Anomaly. The QCD anomaly contributions are discussed in the subsequent sections of this paper.

1.1.2 QCD Anomaly

The concept of the QCD Anomaly is central to the discussion the η', so definition and derivation of the phenomenon is in order. The QCD Anomaly is a symmetry dependent contribution to the divergence of the axial vector current in the presence of gauge fields. These contributions are proportional to the contraction of the gauge field strength tensor and the gauge field strength tensor dual. The axial vector current, $j^{\mu 5} = \bar{\Psi}\gamma^\mu\gamma^5\Psi$, is the difference between the right handed current, $j^\mu_R = \bar{\Psi}\gamma^\mu\left(\frac{1+\gamma^5}{2}\right)\Psi$, and the left handed current, $j^\mu_L = \bar{\Psi}\gamma^\mu\left(\frac{1-\gamma^5}{2}\right)\Psi$. If the divergence of the axial vector current is non zero, it means that the left and right handed components are not conserved. Much of the discussion in this section follows chapters 3 and 19 of Peskin and Schroeder [6].

For a quantum field Ψ, we can construct two currents, $j^{\mu a}(x)$ and $j^{\mu a 5}(x)$, the vector and axial vector currents,

$$j^{\mu a} \equiv \bar{\Psi}(x)\gamma^\mu\tau^a\Psi(x), \tag{1.4}$$

$$j^{\mu a 5} \equiv \bar{\Psi}(x)\gamma^\mu\gamma^5\tau^a\Psi(x). \tag{1.5}$$

In the above equations, the matrix τ^a is a generator of whatever symmetry is intrinsic to the field Ψ.

As an example we calculate the divergence of these two currents in the case of no gauge fields and a $U(1)$ symmetry, or $\tau^a \equiv 1$. Note that if Ψ is a solution to the dirac equation, then $\partial_\mu\gamma^\mu\Psi = -im\Psi$. The divergences of the currents for this case are

$$\partial_\mu j^\mu = (\partial_\mu\bar{\Psi}\gamma^\mu)\Psi + \bar{\Psi}\gamma^\mu\partial_\mu\Psi = (im\bar{\Psi})\Psi + \bar{\Psi}(-im\Psi) = 0, \tag{1.6}$$

$$\partial_\mu j^{\mu 5} = (\partial_\mu\bar{\Psi}\gamma^\mu)\gamma^5\Psi - \bar{\Psi}\gamma^5(\partial_\mu\gamma^\mu\Psi) = im\bar{\Psi}\gamma^5\Psi + im\bar{\Psi}\gamma^5\Psi = 2im\bar{\Psi}\gamma^5\Psi. \tag{1.7}$$

The divergence of j^μ is zero, so j^μ is conserved, and implies conservation of particles, or that the number of particles that enter a surface in space is the same number that leave the surface. However, the axial current $j^{\mu 5}$ is only conserved if the mass of the particle

is zero. This indicates that the fraction of left and right handedness is not conserved if a field has mass.

We now derive the Anomalous contribution to the axial vector current for the case of a massless dirac field Ψ with a symmetry given by generators τ^a and a gauge field $A_\mu^c(x)$. Gauge invariance requires that we replace the derivative ∂_μ with the covariant derivative $D_\mu = \partial_\mu - igA_\mu^c t^c$. For QCD t^c are the color matrices.

When we take the derivative of a product of operators, such as in $j^{\mu a5}$, we must be careful to take into account how the gauge field changes as well. To calculate this we take the the symmetric limit

$$slim_{\epsilon \to 0}[\bar{\Psi}(x^\nu + \epsilon^\nu/2)\gamma^\mu\gamma^5\tau^a U(x - \epsilon/2, x + \epsilon/2)\Psi(x^\nu - \epsilon^\nu/2)], \tag{1.8}$$

where the Wilson Line

$$U(x - \epsilon/2, x + \epsilon/2) = exp(-ig \int_{x-\epsilon/2}^{x+\epsilon/2} dZ^\alpha A_\alpha^c(Z)t^c) \tag{1.9}$$

propagates the gauge from one point to another.

Given the equations of motion for a massless field,

$$\partial_\mu\gamma^\mu\Psi = -ig\gamma^\mu A_\mu^c t^c\Psi \tag{1.10}$$

and

$$\partial_\mu\bar{\Psi}\gamma^\mu = -ig\bar{\Psi}\gamma^\mu A_\mu^c t^c, \tag{1.11}$$

and noting

$$A_\mu(x + \epsilon/2) - A_\mu(x - \epsilon/2) = \epsilon^\nu\partial_\nu A_\mu(x), \tag{1.12}$$

we may solve for the divergence of the axial vector current

$$\partial_\mu j^{\mu a5} = slim_{\epsilon \to 0}\bar{\Psi}(x+\epsilon/2)igt^c[A_\mu^c(x+\epsilon/2)-A_\mu^c(x-\epsilon/2)-\epsilon^\nu\gamma^\mu\partial_\mu A_\nu^c(x)]\gamma^\mu\gamma^5\tau^a\Psi(x-\epsilon/2), \tag{1.13}$$

$$\partial_\mu j^{\mu a5} = slim_{\epsilon \to 0}\bar{\Psi}(x + \epsilon/2)[-ig\gamma^\mu\epsilon^\nu(\partial_\mu A_\nu^c - \partial_\nu A_\mu^c)t^c]\gamma^5\tau^a\Psi(x - \epsilon/2), \tag{1.14}$$

4

$$\partial_\mu j^{\mu a 5} = slim_{\epsilon \to 0} \bar{\Psi}(x + \epsilon/2)[-igt^c \gamma^\mu \gamma^5 \epsilon^\nu G^c_{\mu\nu}]\Psi(x - \epsilon/2), \qquad (1.15)$$

[6].

We solve the limit and write the divergence in terms of the field strength tensor and its dual by using the relation

$$contraction(\Psi(x + \epsilon/2), \bar{\Psi}(x - \epsilon/2)) = 2g\epsilon^{\alpha\beta\mu\gamma} G^d_{\alpha\beta}(x)t^d \frac{-i\epsilon_\gamma}{8\pi^2 \epsilon^2}, \qquad (1.16)$$

and inserting it into equation 1.15. The final expression for the anomalous contribution to the axial current divergence is

$$\partial_\mu j^{\mu a 5} = -\frac{g^2}{16\pi^2} \tilde{G}^{\mu\nu c} G^d_{\mu\nu} tr[\tau^a] tr[t^c t^d], \qquad (1.17)$$

where $G^c_{\mu\nu}$ is the gluon field strength tensor, and $\tilde{G}^{\mu\nu} \equiv \epsilon^{\alpha\beta\mu\nu} G_{\alpha\beta}$.

If the vector current $j^{\mu a 5}$ were for a singlet combination of quarks, where the matrix τ^a is replaced by a unit matrix, the trace of that matrix would be non zero and the state would have couplings to to the gauge field strength tensor (gluons for QCD). If the combination of quarks were not in a singlet state, then the trace of the τ^a matrix would be zero, and there would be no couplings to the gauge field strength tensor.

1.1.3   The Octet η^8 and Singlet η^0

We now discuss the η^8 octet and η^0 singlet that mix to form the primary components of the η and η'. The QCD Anomaly contributes to the axial vector current divergence in the singlet, η^0, but does not contribute in the octet, η^8. As an example, the quark combinations of the pion states are determined using simple symmetry arguments, then the same steps are used to infer the composition of η^8 and η^0. This discussion of the η^8 and η^0 quark content is based on the discussion in [7].

By definition the pions form an SU(2) isospin triplet where π^+, π^0, π^- correspond to $I = 1$ and $m_I = 1, 0, -1$ respectively. Let q_i be the wave function of a quark with isospin

5

$I = 1/2$, (i=1 for u or i=2 for d). Let U^i_j be a unitary $SU(2)$ triplet transformation matrix defined by

$$q'_i \equiv U^j_i q_j, \qquad (1.18)$$

where $q^1 = \bar{u}$ $q_1 = u$, $q^2 = \bar{d}$ and $q_2 = d$. The state $q'_i q'^i$ is invariant under our transformation matrix as shown by

$$q^{i'} q_i' = q^j U^i_j U^k_i q_k = q^j \delta^k_j q_k = q^i q_i, \qquad (1.19)$$

and is therefore our singlet state, $u\bar{u} + d\bar{d}$. Non-singlet states of this transformation are defined by the elements of the traceless matrix

$$T^i_j = q^i q_j - \delta^i_j \frac{1}{2}(q^k q_k), \qquad (1.20)$$

where there is an implicit sum over the k index. We find 3 linearly independant quark combinations:

$$\pi^+ = T^2_1 = \bar{d}u \qquad (1.21)$$

$$\pi^- = T^1_2 = \bar{u}d \qquad (1.22)$$

$$\pi^0 = \frac{1}{\sqrt{2}} T^1_1 = -\frac{1}{\sqrt{2}} T^2_2 = \frac{1}{\sqrt{2}}(\bar{u}u - \bar{d}d). \qquad (1.23)$$

We define the quarks u, d, and s to form an $SU(3)$ octet, and extend our definition of q^i and q_i such that $q^3 = s$ and $q_3 = \bar{s}$. Let U_3 be a unitary SU(3) transformation matrix. As in the case of SU(2) we find $q^i q_i$ to be invariant under our transformation and to therefore be the singlet of this symmetry. We define

$$\eta^0 \equiv \frac{1}{\sqrt{3}}(\bar{u}u + \bar{d}d + \bar{s}s) \qquad (1.24)$$

to be the $SU(3)$ singlet. We define the matrix

$$A^i_j = q^i q_j - \delta^i_j \frac{1}{3}(\bar{u}u + \bar{d}d + \bar{s}s) = q^i q_j - \frac{1}{\sqrt{3}}\eta^0 \qquad (1.25)$$

where the elements are members of the SU(3) octet. The off diagonal elements of this matrix give the quark content of π^+, π^-, K^+, K^-, K^0, and $\bar{K}^0$. The diagonal elements

are composed of linear combinations of, π^0 (defined in the $SU(2)$ isospin case) and A^3_3, given by $-\frac{1}{3}(\bar{u}u + \bar{d}d - 2\bar{s}s)$. We define η^8 as $-\frac{\sqrt{6}}{2}A^3_3$.

We now have a singlet u,s,d quark combination η^0 given by equation 1.24 that has a QCD anomaly contribution, and the triplet combination η^8 given by

$$\eta^8 \equiv \frac{1}{\sqrt{6}}(\bar{u}u + \bar{d}d - 2\bar{s}s) \tag{1.26}$$

that does not have a QCD anomaly contribution. Given the fact that the η is closer in mass to the off diagonal elements of the A^i_j matrix than the η', we assume that the η is mostly the octet of the SU(3) symmetry, η^8, and the η' is mostly the singlet, η^0.

1.1.4 The Mixing of η, η', and η_c

This section follows Feldman, Kroll, and Stech [10]. Neglecting charm contributions, a unitary transformation,

$$U(\alpha) \equiv \begin{pmatrix} cos(\alpha) & -sin(\alpha) \\ sin(\alpha) & cos(\alpha) \end{pmatrix}, \tag{1.27}$$

can be used to mix the η^0 and η^8 states into the physical η and η' states by

$$\begin{pmatrix} \eta \\ \eta' \end{pmatrix} = U(\theta) \begin{pmatrix} \eta^0 \\ \eta^8 \end{pmatrix}. \tag{1.28}$$

The η^0 and η^8 basis is a natural choice considering the SU(3) u,d,s symmetry. However, the SU(3) symmetry is broken by the large mass difference between the s quark and the light u and d quarks. This symmetry breaking is evidenced by the fact that in this basis 3 different mixing angles are required to describe the wave functions and decay constants of the η and η'. For example, the decay constants f^8_η, $f^8_{\eta'}$, f^0_η, $f^0_{\eta'}$, defined by

$$< 0|j^i_{\mu 5}|X > = if^i_X p_{X\mu}, \tag{1.29}$$

7

are described by 4 parameters $(f^8, f^0, \theta_8, \theta_0)$ as

$$
\begin{aligned}
f_\eta^8 &= f_8 cos(\theta), \quad f_\eta^0 = -f_0 sin(\theta) \\
f_{\eta'}^8 &= f_8 sin(\theta), \quad f_{\eta'}^0 = f_0 cos(\theta)
\end{aligned}
. \tag{1.30}
$$

In addition to the other parameters, another angle α is necessary to describe the mixing of the wave functions. The fact that a new free parameter is needed to describe every aspect of the system indicates that we are not using a fundamental basis to describe the system.

Feldman, Kroll, and Stech (FKS) proposed a different basis that separates the s quark from the light u and d quarks. The FKS basis is $\eta_q = \frac{1}{\sqrt{2}}(u\bar{u} + d\bar{d})$ and $\eta_s = s\bar{s}$. This basis requires only 1 mixing angle, ϕ, to mix the η_q and η_s into the physical η and η' via

$$
\begin{pmatrix} \eta \\ \eta' \end{pmatrix} = U(\phi) \begin{pmatrix} \eta^q \\ \eta^s \end{pmatrix}, \tag{1.31}
$$

as well as mixing the decay constants f^q and f^s into the f_η^q, $f_{\eta'}^q$, f_η^s and $f_{\eta'}^s$ via

$$
\begin{aligned}
f_\eta^q &= f_q cos(\phi), \quad f_\eta^s = -f_s sin(\phi) \\
f_{\eta'}^q &= f_q sin(\phi), \quad f_{\eta'}^s = f_s cos(\phi)
\end{aligned}
. \tag{1.32}
$$

The FKS basis decreases the number of free parameters that are needed to describe data from 5 to 3, indicating that this is a superior way to describe the η/η' system. Further, flavor symmetry allows us to relate the η^q basis state to the π^0, meaning that $f_q \sim f_\pi$.

As an example of the use of this basis in relation to the QCD Anomaly we write the mass matrix in the FKS basis and show that the off diagonal elements relate the difference in mass squared between the η' and η to the anomaly contribution. The elements of the mass matrix are defined by

$$
< 0|\partial^\mu J_{\mu 5}^i|\eta^i >= M_{\eta^i}^2 f_i \tag{1.33}
$$

and the mass matrix in the q and s basis is

$$
M_{qs}^2 = \begin{pmatrix} m_{qq}^2 + \frac{\sqrt{2}}{f_q} < 0|\frac{\alpha_s}{4\pi}G\tilde{G}|\eta^q > & \frac{1}{f_s} < 0|\frac{\alpha_s}{4\pi}G\tilde{G}|\eta^q > \\ \frac{\sqrt{2}}{f_q} < 0|\frac{\alpha_s}{4\pi}G\tilde{G}|\eta^s > & m_{ss}^2 + \frac{1}{f_s} < 0|\frac{\alpha_s}{4\pi}G\tilde{G}|\eta^s > \end{pmatrix}. \tag{1.34}
$$

In the physical η, η' basis the mass matrix is

$$M^2_{physical} = \begin{pmatrix} M^2_\eta & 0 \\ 0 & M^2_{\eta'} \end{pmatrix}. \tag{1.35}$$

We can convert the physical η and η' mass matrix to the q and s basis by the transformation

$$M^2_{qs} = U^\dagger(\phi) M^2_{physical} U(\phi), \tag{1.36}$$

that yields the result,

$$M^2_{qs} = \begin{pmatrix} M^2_\eta \cos^2(\phi) + M^2_{\eta'} \sin^2(\phi) & -\sin(\phi)\cos(\phi)(M^2_{\eta'} - M^2_\eta) \\ -\sin(\phi)\cos(\phi)(M^2_{\eta'} - M^2_\eta) & M^2_\eta \sin^2(\phi) + M^2_{\eta'} \cos^2(\phi) \end{pmatrix}. \tag{1.37}$$

The two different ways of writing the mass matrix in the q and s basis shows that the mass squared difference between the η' and η is proportional to the QCD anomaly component.

The validity of the FKS basis and the single mixing angle was tested by defining several quantities that could both be extracted from measurements and predicted by the FKS paramterization. The FKS predictions rely on the assertion that flavor symmetry requires $m^2_{qq} = M^2_\pi$ and $m^2_{ss} = 2M^2_K - M^2_\pi$. The quantities and ratios used are:

$$y = \sqrt{2} \frac{< 0|\frac{\alpha_s}{4\pi} G\tilde{G}|\eta^s >}{< 0|\frac{\alpha_s}{4\pi} G\tilde{G}|\eta^q >} = \frac{f_q}{f_s}, \tag{1.38}$$

$$a^2 = \frac{1}{\sqrt{2}f_q} < 0|\frac{\alpha_s}{4\pi} G\tilde{G}|\eta^q >, \tag{1.39}$$

$$\frac{\Gamma[J/\Psi \to \eta'\rho]}{\Gamma[J/\Psi \to \eta\rho]} = tan^2(\phi) \left(\frac{k_{\eta'}}{k_\eta}\right)^3, \tag{1.40}$$

$$\frac{\Gamma[a_2 \to \eta'\pi]}{\Gamma[a_2 \to \eta\pi]} = tan^2(\phi) \left(\frac{k_{\eta'}}{k_\eta}\right)^3, \tag{1.41}$$

$$\frac{\sigma[\pi^- P \to \eta'n]}{\sigma[\pi^- P \to \eta n]} = tan^2(\phi), \quad (s \gg M^2_P), \tag{1.42}$$

$$\frac{\Gamma[J/\Psi \to \eta'\gamma]}{\Gamma[J/\Psi \to \eta\gamma]} = tan^2(\phi) \frac{M^4_{\eta'}}{M^4_\eta} \left(\frac{k_{\eta'}}{k_\eta}\right)^3, \tag{1.43}$$

Table 1.1: Theoretical (to first order of flavor symmetry breaking) and phenomenological values of mixing parameters for η and η' in the FKS basis. This has been reproduced from reference [10].

Source	f_q/f_π	f_s/f_π	ϕ	y	$a^2 [\mathrm{GeV}^2]$
Th.	1.00	1.41	42.4°	0.78	0.281
Phen.	1.07 ± 0.02	1.34 ± 0.06	$39.3° \pm 1.0$	0.81 ± 0.03	0.265 ± 0.010

where the variable k_X is the magnitude of the 3 momentum of meson X in the restframe of the parent particle. The results of the FKS studies of these quantities are listed in Table 1.1

The large branching fractions involving η' could also be caused by a large charm component in the η' that would reduce the CKM suppression. Studies to determine the contributions of η^q, η^s, and η^c to the physical η, η', and η_c find

$$|\eta >= 0.77|\eta^q > -0.63|\eta^s > -0.006|\eta^{c0} >$$
$$|\eta' >= 0.63|\eta^q > +0.77|\eta^s > -0.016|\eta^{c0} >$$
$$|\eta_c >= 0.015|\eta^q > -0.008|\eta^s > +|\eta^{c0} > .$$

(1.44)

The charm contributions to η and η' correspond to decay constants $f^c_\eta = -(2.4 \pm 0.2)$ MeV and $f^c_{\eta'} = -(6.3 \pm 0.6)$ MeV. We estimate the ratio of the charm and q contributions to the $B \to K\eta'$ branching fraction to be approximately

$$\frac{(V_{cb})^2}{(V_{ub})^2} \frac{(f^c_{\eta'})^2}{(f^q_{\eta'})^2} \sim \frac{(0.04)^2}{(0.00317)^2} \frac{(6.3 \text{ MeV})^2}{(\sim 115 \text{ MeV})^2} = 0.48.$$

(1.45)

This means that after accounting for CKM suppression factors, the small charm component could increase the branching fraction by as much as a factor of 3. This is far from the factor of 300 required to account for the observations.

In this section we have shown that it is better to use the η^q and η^s FKS basis to describe η and η' mixing and decay constants rather than the η^0 and η^8 basis, that requires two additional mixing angles to be consistent with data. The FKS basis also allows us

to relate the decay constants and masses of the basis states to the values for the π and K. Therefore this basis is useful when trying to make predictions for how the QCD Anomaly might affect branching fractions involving η'. We have also shown that the charm component of the η' does not account for the large $B \to K\eta'$ branching fraction.

1.1.5 $B \to \eta^{(\prime)}$ Form Factor with a Singlet Contribution

The contribution to the divergence of the axial vector current from the anomaly produces a two gluon coupling to the η^0 component of the η'. In order for this two gluon coupling to contribute to the $B \to K\eta'$ there must be a mechanism where the B produces two gluons. In this section we examine two gluon production in $B \to K\eta'$ and $B \to \eta'\ell\nu$. We parametrize the anomalous two gluon contribution to these decays using the FKS basis.

There are two types of diagrams in the $B \to \eta'K$ decay that would involve the two gluon coupling of the QCD anomaly, $b \to sgg$ or $b \to sg$. The diagrams involving $b \to sgg$ are shown in Figure 1.1. The diagram involving $b \to sg$ is shown in Figure 1.2, where the spectator quark emits the second gluon in $u \to ug$, known as the spectator scattering mechanism.

Numerical estimates [13] [12] [14] for spectator and $b \to sgg$ contributions to the $B \to K\eta'$ decay rate indicate that, depending on the model, they can account for the large branching fraction of $B \to \eta'K$ to within a factor of 2 or 3. Predictions for some of the branching fractions and the experimental results are given in Table 1.2.

The semileptonic decay of $B \to \eta'\ell\nu$ or $D \to \eta'\ell\nu$ can help to clarify the mechanisms involved in the $B \to \eta'K$ decay. Unlike a fully hadronic final state, such as $B \to K\eta'$, the $B \to \eta'$ component of the semileptonic differential decay rate can be factored out from the leptonic $\ell\nu$ component. Because of this property, the semileptonic $B \to \eta'\ell\nu$ decay can measure the size of the two gluon couplings to the η'. In the case of a small

11

Figure 1.1: Feynman Diagram for the $b \rightarrow sgg$ decay. This drawing was taken from reference [12].

Figure 1.2: Feynman Diagram for the spectator scattering decay. This drawing was taken from reference [13]

Table 1.2: : A comparison of experiment with predicted branching fractions. The branching fractions from Beneke and Neubert were done including both $b \rightarrow sgg$ and spectator, with the two gluon component of the form factor, $F_{gg}(q^2 = 0)$ arbitrarily set to 0.1, [14]. The branching fractions from A. Ali were calculated using only $b \rightarrow sgg$ with the momentum fraction of the spectator quark equal to zero, [12].

Mode	Beneke, Neubert(10^{-6})	A. Ali(10^{-6})	Experiment(10^{-6})
$B^- \rightarrow K^- \eta'$	56^{+19-31}_{-14-13}	$27 - 36$	72.2 ± 5.3
$\bar{B}^0 \rightarrow \bar{K}^0 \eta'$	56^{+18+30}_{-13-13}	$30 - 37$	54.8 ± 10.1

12

lepton mass, the differential decay rate for a semileptonic decay of B to a psuedoscalar is ([15] [16])

$$\frac{d\Gamma_{B \to Pl\nu}}{dydcos(\theta_{wl})} = |V_{ub}|^2 \frac{G_F^2 k_P^3 M_B^2}{32\pi^3} sin^2(\theta_{wl})|f_1(q^2)|^2, \tag{1.46}$$

where y is the ratio q^2/M_B^2, M_B is the mass of the B meson, G_F is the fermi constant, k_P is the 3 momentum of the daughter meson, and θ_{wl} is the angle between the lepton and the W in the W rest frame. The form factor $f_1(q^2)$ embodies the sum of all diagrams contributing to the $B \to \eta'$ transition.

For the $B \to \eta'\ell\nu$ there is an enhancement channel due to the QCD anomaly through spectator gluon emission shown in Figure 1.3. Using the FKS basis, η^q and η^s, and relating the $B \to \eta^q$ form factor contribution to the $B \to \pi$ form factor, we may write the $B \to \eta'$ form factor as [17]

$$f_1(q^2) = \frac{1}{\sqrt{2}} \frac{f_{\eta'}^q}{f_\pi} F_1^{B \to \pi}(q^2) + \frac{(\sqrt{2}f_{\eta'}^q + f_{\eta'}^s)}{\sqrt{3}f_\pi} F_1^{singlet}(q^2), \tag{1.47}$$

where $f_{\eta'}^q$ and $f_{\eta'}^s$ are the FKS decay constants, $F_1^{B \to \pi}$ is the form factor from $B \to \pi\ell\nu$ decays, and $F_1^{singlet}$ describes the two gluon contribution from the spectator scattering and the QCD Anomaly. Tables 1.3 and 1.4 summarize the expected branching fractions of $B \to \eta'\ell\nu$ and $B \to \eta\ell\nu$ for different $F^{B \to \pi}$ models and values of $F^{singlet}(q^2 = 0)$. Following [17] we use the $F^{B \to \pi}$ q^2 dependance to describe $F^{singlet}$.

Using the FKS basis, we have shown that the $B \to \eta'\ell\nu$ branching fraction is particularly sensitive to the singlet contribution to the $B \to \eta'$ form factor. Measurement of the $B \to \eta'\ell\nu$ branching fraction can help determine the singlet contribution to the $B \to K\eta'$ branching fraction.

1.1.6 $B \to \eta^{(')}\ell\nu$ Measurement

The branching fractions $\mathcal{B}(B \to \eta'\ell\nu)$ and $\mathcal{B}(B \to \eta\ell\nu)$ were measured using the complete set of $\Upsilon(4S)$ data taken by the CLEO-2, CLEO-2.5, and CLEO-3 detectors, and is
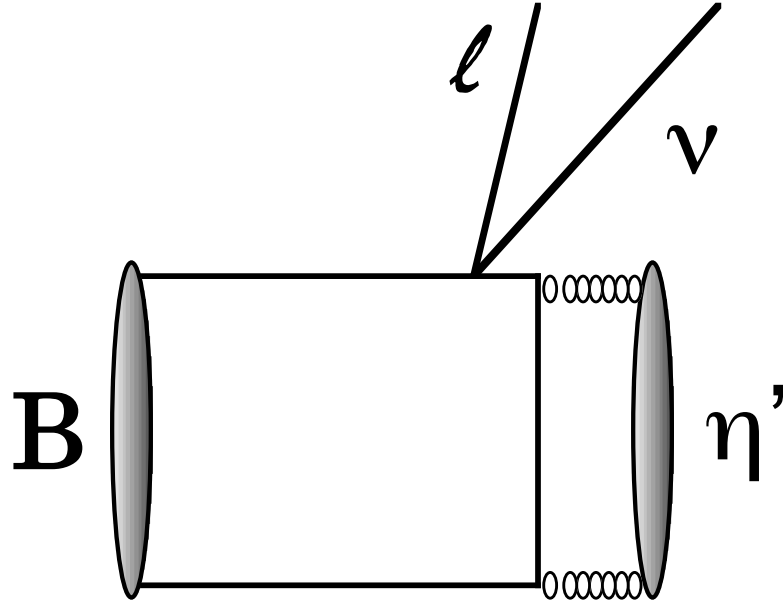
Figure 1.3: Feynman Diagram for the $b \rightarrow \ell\nu gg$ semileptonic decay. This drawing was taken from reference [17]

.

Table 1.3: The predicted branching fraction for $B \rightarrow \eta\ell\nu$ as a function of $F_+^{singlet}(0)$ for several models. The branching fractions are given in units of 10^{-5}. This table was reproduced from reference [17].

$F_+^{singlet}(0)$	0	0.2	0.4	0.6
Lattice I	$3.68^{+1.57}_{-1.29}$	$5.70^{+2.43}_{-2.00}$	$8.16^{+3.48}_{-2.86}$	$11.06^{+4.72}_{-3.88}$
Lattice II	$4.43^{+1.89}_{-1.55}$	$6.67^{+2.85}_{-2.34}$	$9.37^{+4.00}_{-3.29}$	$12.52^{+5.34}_{-4.39}$
LCSR	$4.04^{+1.72}_{-1.42}$	$6.08^{+2.59}_{-2.14}$	$8.53^{+3.64}_{-2.99}$	$11.41^{+4.86}_{-4.01}$
Average	4.00 ± 0.99	6.10 ± 1.50	8.63 ± 2.13	11.60 ± 2.86

Table 1.4: : The predicted branching fraction for $B \rightarrow \eta' l\nu$ as a function of $F_+^{singlet}(0)$ for several models. The branching fractions are given in units of 10^{-5}. This table was reproduced from reference [17].

$F_+^{singlet}(0)$	0	0.2	0.4	0.6
Lattice I	$1.80^{+0.76}_{-0.64}$	$14.57^{6.22}_{-5.11}$	$39.63^{+16.91}_{-13.91}$	$79.96^{+32.84}_{-24.02}$
Lattice II	$2.14^{+0.92}_{-0.75}$	$15.81^{+6.75}_{-5.55}$	$42.12^{+17.97}_{-14.79}$	$81.05^{34.59}_{-28.45}$
LCSR	$1.99^{+0.85}_{-0.21}$	$14.72^{+6.28}_{-5.17}$	$39.20^{+16.72}_{-13.76}$	$75.43^{+32.19}_{-26.67}$

fully described in [24]. This section outlines that analysis, the results, and the potential implications.

The $\mathcal{B}(B \rightarrow \eta' \ell \nu)$ and $\mathcal{B}(B \rightarrow \eta \ell \nu)$ were measured as part of an analysis that also studied the branching fractions and q^2 distributions of the decays $B \rightarrow \pi \ell \nu$, $B \rightarrow \pi^0 \ell \nu$, $B \rightarrow \rho \ell \nu$, $B \rightarrow \rho^0 \ell \nu$, and $B \rightarrow \omega \ell \nu$. This analysis used the method of neutrino reconstruction where the excellent detector hermiticity and the well known energy of the electron beam allow for the neutrino four-vector to be determined from energy and momentum conservation. The missing four-vector is determined by subtracting the total four-vector of all measured particles from the initial four-vector of the colliding $e^+ e^-$. If there are no other missing particles, the missing four-vector is the four-vector of the neutrino.

If the event appears to be consistent with one neutrino and no other missing particles the neutrino four-vector is combined with the lepton and meson candidates in the event that make the best $B \rightarrow X \ell \nu$ candidate. Events are deemed consistent with 1 neutrino if the missing mass is consistent with zero, the total charge is zero (no missing or extra tracks), and there is only one charged lepton in the event (number of charged leptons is generally equal to number of neutrinos).

The η is reconstructed through both the $\gamma\gamma$ and the $\pi^+ \pi^- \pi^0$ decay modes. The η' is reconstructed through $\eta' \rightarrow \pi\pi\eta(\gamma\gamma)$ and $\eta' \rightarrow \rho^0 \gamma$. We accept $\eta' \rightarrow \rho^0 \gamma$ candidates

15
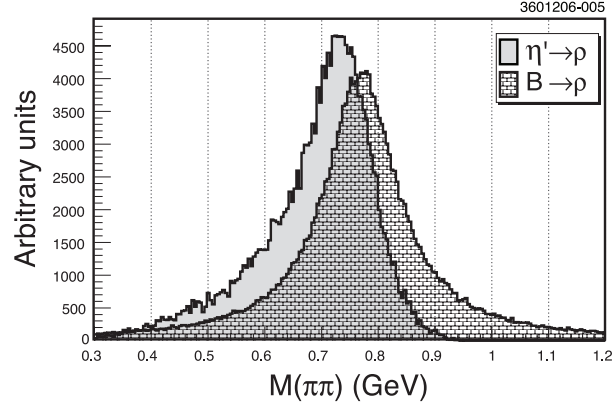
Figure 1.4: The shape of the mass of the ρ in $B \to \rho \ell \nu$ and $\eta' \to \rho \gamma$. Limited phase space in $\eta' \to \rho \gamma$ produces the asymmetry about the nominal ρ mass in this mode. Histograms are normalized to equal area.

within the ρ^0 mass range of 0.3 to 0.9 GeV/c^2, where the range is subdivided into four roughly equal mass bins. The phase space restrictions in $\eta' \to \rho^0 \gamma$ distort the ρ^0 line shape at high $\pi\pi$ mass (Figure 1.4).

In order to improve the signal to background, the $\eta' \ell \nu$ measurement was divided into two q^2 bins, $q^2 > 10$ GeV^2 and $q^2 < 10$ GeV^2. The majority of the $\eta' \ell \nu$ backgrounds occur at $q^2 > 10$ GeV^2, and the signal is mainly located in the $q^2 < 10$ GeV^2.

The data and Monte Carlo simulation are divided into bins according to recon-structed q^2, reconstructed exclusive decay mode, and reconstructed net charge (0 or ± 1). The Monte Carlo sample is also divided into bins according to true q^2 and true decay mode, that generates the efficiency and cross feed matrix between the different decays or q^2 ranges. A fit is performed using the method of Barlow and Beeston to calculate the $-2Log\mathcal{L}$.

There was not a statistically significant signal in the $B \to \eta \ell \nu$ mode and the data was converted to a 90% upper limit of $\mathcal{B}(B^+ \to \eta \ell^+ \nu) \leq 1.01 \times 10^{-4}$. For $B \to \eta' \ell \nu$ we have a statistically significant result $\mathcal{B}(B^+ \to \eta' \ell^+ \nu) = (2.66 \pm 0.80_{stat} \pm 0.57_{syst}) \times 10^{-4}$. We

also determine the lower limit for the ratio $\mathcal{B}(B^+ \to \eta'\ell^+\nu)/\mathcal{B}(B^+ \to \eta\ell^+\nu)$ to be 2.5 at the 90% confidence level.

The BABAR collaboration also measured these branching fractions in 2004 using $\mathcal{L} = 88 fb^{-1}$ [41] and again in a different analysis in 2006 using $\mathcal{L} = 316 fb^{-1}$ [42]. The results of the 2004 analysis [41] were $\mathcal{B}(B \to \eta'\ell\nu) = (2.7 \pm 1.2 \pm 0.5) \times 10^{-4}$ and $\mathcal{B}(B \to \eta\ell\nu) = (0.39 \pm 0.41 \pm 0.22) \times 10^{-4}$. Though the statistical significance of these results did not meet the standard of being considered evidence, the central values are in good agreement with the CLEO measurement. The 2006 BABAR measurement that used nearly 4× the luminosity did not find a statistically significant $B \to \eta'\ell\nu$ signal, and set a 90% upper limit $\mathcal{B}(B \to \eta'\ell\nu) < 1.3 \times 10^{-4}$. They measured $\mathcal{B}(B \to \eta\ell\nu) = (0.84 \pm 0.27 \pm 0.21) \times 10^{-4}$.

Though the CLEO and the 2006 BABAR $\mathcal{B}(B \to \eta'\ell\nu)$ measurements have very different central values, the uncertainties on both measurements are large enough such that the disagreement is only at the 2σ level. The $\mathcal{B}(B \to \eta\ell\nu)$ measurements are consistent in all cases.

1.1.7 Estimates of Two Gluon Contributions to $B \to \eta'$

In this section we use the FKS basis and phenomenology with the CLEO measurements of $\mathcal{B}(B \to \eta\ell\nu)$ and $\mathcal{B}(B \to \eta'\ell\nu)$ to determine the size of the two gluon contributions in the $B \to \eta'$ form factor. Previous theoretical studies have assumed that $F^{signlet}$ and $F^{B\to\pi}$ have the same q^2 distributions [17], but this is probably not true. This analysis expresses $\mathcal{B}(B \to \eta'\ell\nu)$ as a function of the parameter

$$\tilde{F}_s = (\int |F^{singlet}_+|^2 \Omega_{\eta'} \partial q^2)/(\int |F^{B\to\pi}_+|^2 \Omega_{\eta'} \partial q^2), \qquad (1.48)$$

where $\Omega_{\eta^{(\prime)}}$ is the available phase space in the $B \to \eta'\ell\nu$ decay. The $\tilde{F}_s$ parameter is directly related to the enhancement in the branching fraction by the two gluon coupling

regardless of the q^2 dependance of the $F^{B\to\pi}$ or $F^{singlet}$. If the $F^{singlet}$ and $F^{B\to\pi}$ have the same q^2 dependance then $\tilde{F}_s$ is equal to $|F^{singlet}(q^2 = 0)|^2/|F^{B\to\pi}(q^2 = 0)|^2$.

In terms of $\tilde{F}_s$ and $\mathcal{B}(B \to \pi^0\ell\nu)$ we may express

$$\mathcal{B}_{\eta'} = I \times \mathcal{B}_{\pi^0}\beta_{\eta'}\left((a_{\eta'}^\pi)^2 + 2\gamma_{\eta'}(a_{\eta'}^\pi)(a_{\eta'}^s)\sqrt{\tilde{F}_s} + \tilde{F}_s(a_{\eta'}^s)^2\right), \tag{1.49}$$

and

$$\mathcal{B}_\eta = I \times \mathcal{B}_{\pi^0}\beta_\eta\left((a_\eta^\pi)^2 + 2\gamma_\eta(a_\eta^\pi)(a_\eta^s)\sqrt{\tilde{F}_s\frac{\beta_{\eta'}}{\beta_\eta}}t + \tilde{F}_s\frac{\beta_{\eta'}}{\beta_\eta}t(a_\eta^s)^2\right), \tag{1.50}$$

where I is an isospin factor (2) and $\mathcal{B}_{\pi^0}$ is the $B \to \pi^0\ell\nu$ branching fraction. The $a_{\eta^{(\prime)}}^\pi$ and $a_{\eta^{(\prime)}}^s$ are functions of FKS parameters given by

$$a_{\eta^{(\prime)}}^\pi = f_{\eta^{(\prime)}}^q/f_\pi, \tag{1.51}$$

and

$$a_{\eta^{(\prime)}}^s = (\sqrt{2}f_{\eta^{(\prime)}}^q + f_{\eta^{(\prime)}}^s)/(\sqrt{3}f_\pi). \tag{1.52}$$

The other factors in the equations are given by,

$$\beta_X = (\int |F_+^{B\to\pi}|^2\Omega_X\partial q^2)/(\int |F_+^{B\to\pi}|^2\Omega_\pi\partial q^2), \tag{1.53}$$

$$\gamma_X = \frac{(\int |F_+^{B\to\pi}F_+^{singlet}|\Omega_X\partial q^2)}{\sqrt{(\int |F^{B\to\pi}|^2\Omega_X\partial q^2) \times (\int |F_+^{singlet}|^2\Omega_X\partial q^2)}}, \tag{1.54}$$

and

$$t = \left(\int |F_+^{singlet}|^2\Omega_\eta\partial q^2\right)/\left(\int |F^{singlet}|^2\Omega_{\eta'}\partial q^2\right). \tag{1.55}$$

The factors β_X, γ_X, and t contain the dependance of the branching fractions on the q^2 distributions of $F^{singlet}$ and $F^{B\to\pi}$. Only $\tilde{F}_s$ contains information about the relative size of $F^{singlet}$ compared to $F^{B\to\pi}$. For our nominal values of $\tilde{F}_s$ we assume that the q^2 distributions are the same and then vary the β_X, γ_X, and t variables to determine a theoretical systematic uncertainty on $\tilde{F}_s$ from our lack of knowledge about the q^2 distributions.

For the q^2 dependance $F^{B\to\pi}$ we use a BK paramterization,

$$f_+(q^2) = \frac{f_+(0)}{(1 - \tilde{q}^2)(1 - \alpha\tilde{q}^2)}, \tag{1.56}$$

18

with $\alpha = 0.55$, the average of a BABAR measurement [43] and a fit to lattice QCD calculations [44]. The systematic uncertainty is conservatively estimated by varying α from 0.3 to 0.7. For the $F^{singlet}$ q^2 dependance we use a BK with α nominally set to 0.55 and varied between 0 and 1.

If there were no two gluon contribution, $\tilde{F}_s = 0$, $\mathcal{B}(B \to \eta' \ell \nu)$ would be roughly half of $\mathcal{B}(B \to \eta \ell \nu)$. The fact that $\mathcal{B}(B \to \eta' \ell \nu)$ is significantly larger than $\mathcal{B}(B \to \eta \ell \nu)$ indicates that $\tilde{F}_s$ must be of order 1. The best fit of the CLEO data gives $\tilde{F}_s = 1.15 \pm 0.54 \pm 0.38 \pm 0.21$, where the errors listed are, in order, statistical, systematic, and those due to uncertainties related to this model, including the q^2 dependance of the different components. This result indicates that $F^{singlet}(q^2 = 0) \sim F^{B \to \pi}(q^2 = 0)$.

1.1.8 Application to $D^+ \to \eta^{(\prime)} \ell^+ \nu$

Another place to search for possible enhancement in branching fractions involving the η and η' system is the the $\Psi(3770)$ resonance with D meson decays. If we adopt the same model of the form factors for $D \to \eta^{(\prime)}$ as we did for $B \to \eta^{(\prime)}$ we may write

$$F_+^{D^+ \to \eta^{(\prime)}} = F_+^{D^+ \to \pi^0} \frac{f_{\eta^{(\prime)}}^q}{f_\pi} + F_+^{D \to singlet} \frac{\sqrt{2} f_{\eta^{(\prime)}}^q + f_{\eta^{(\prime)}}^s}{\sqrt{3} f_\pi}. \tag{1.57}$$

It is not clear how to relate the $F^{D \to singlet}$ form factor to the $F^{B \to singlet}$, however, we may set the value of $F^{D \to singlet}$ to zero and calculate lower limits for the branching fractions $\mathcal{B}(D^+ \to \eta' e^+ \nu)$ and $\mathcal{B}(D^+ \to \eta e^+ \nu)$ in terms of the branching fraction $\mathcal{B}(D^+ \to \pi^0 e^+ \nu)$. Branching fractions significantly larger than these lower limits may also indicate the presence of an enhancement. These branching fractions are given by

$$\mathcal{B}(D^+ \to \eta^{(\prime)} e^+ \nu) \geq \mathcal{B}(D^+ \to \pi^0 e^+ \nu) \frac{f_{\eta^{(\prime)}}^q}{f_\pi} \left(\frac{\int |F^{D \to \pi^0}|^2 \Omega_{\eta^{(\prime)}}(q^2) \partial q^2}{\int |F^{D \to \pi^0}|^2 \Omega_{\pi^0}(q^2) \partial q^2} \right) \tag{1.58}$$

.

In the above equation $\Omega_{\pi^0}(q^2)$ is the phase space factor for the $D^+ \to \pi^0 e^+ \nu$ decay for a given q^2 and $\Omega_{\eta^{(\prime)}}(q^2)$ is the phase space factor for $D^+ \to \eta e^+ \nu$ decay at a given q^2.

If we use the measured $D^+ \to \pi^0 e^+ \nu$ branching fraction of 0.373(22)(13)% and a BK form for the form factor with $\alpha = 0.37$ ([33]) we find the following lower limits for the branching fractions

$$\mathcal{B}(D^+ \to \eta' e^+ \nu) \geq 1.58 \times 10^{-4} \tag{1.59}$$

$$\mathcal{B}(D^+ \to \eta e^+ \nu) \geq 10.72 \times 10^{-4} \tag{1.60}$$

.

The above lower limits are approximately the same as results calculated by Fajfer and Kemenik [26], $\mathcal{B}(D^+ \to \eta' e^+ \nu) = 1.6 \times 10^{-4}$ and $\mathcal{B}(D^+ \to \eta e^+ \nu) = 10 \times 10^{-4}$.

Earlier analysis of $281 pb^{-1}$ of $\Psi(3770)$ CLEO data [25] measured $\mathcal{B}(D^+ \to \eta \ell^+ \nu) = 13.3 \pm 2.0 \pm 0.6$ and set a 90% upper limit $\mathcal{B}(B^+ \to \eta' \ell^+ \nu) < 3.5 \times 10^{-4}$. Based on the $\mathcal{B}(D^+ \to \eta' \ell^+ \nu)$ upper limit, the size of the $F^{D \to singlet}$ contribution could be as large as $F^{D \to singlet}/F^{D \to \pi^0} = 0.28$.

In this analysis we set out to obtain a statistically significant measurement of $D^+ \to \eta' e^+ \nu$ and to improve the measurement of $D^+ \to \eta e^+ \nu$ by using a different technique and incorporating the full data set. A $D^+ \to \eta' e^+ \nu$ branching fraction near the previous 90% upper limit would indicated a 2-gluon enhancement in the $D^+ \to \eta' e^+ \nu$ decay, and a branching fraction one or two standard deviations below the FKS minimum would constitute evidence against a two gluon contribution.

1.2 Form Factor Representation

There are sufficient events in the $D^+ \to \eta e^+ \nu$ data for a coarse measurement of the q^2 distribution, and the shape of the form factor $F_+^{D \to \eta}(q^2)$. Simple parameterizations are often used to fit form factor shapes. One such parameterization, the Becirevic-Kaidalov ("BK") form, is widely used, yet enforces scaling relations at small q^2 known to be broken by hard gluon exchange [40]. Another class of form factor parameterizations

involve series expansions around some $q^2 = t_0$ up to a fixed order with the coefficients of the expansion being the fit parameters, [40]. The difficulty that can occur with this method is poor convergence due to singularities.

For this analysis we use an improved series expansion explained in [40], that instead of expanding in $q^2 - t_0$, expands in a variable $z(q^2, t_0)$ given by

$$z(q^2, t_0) = \frac{\sqrt{t_+ - q^2} - \sqrt{t_+ - t_0}}{\sqrt{t_+ - q^2} + \sqrt{t_+ - t_0}}, \tag{1.61}$$

where $t_\pm = (m_D \pm m_\eta)$. This z maps a branch cut on the real axis onto a unit circle when the form factor is analytically continued into the complex plane. For the physical range of q^2, $|z| < 1$. The convergence of this form is much better. The form factor in this series expansion is given by:

$$F_+(q^2) = \frac{1}{P(q^2)\phi(q^2, t_0)} \sum_{k=0}^{k_{max}} a_k(t_0)[z(q^2, t_0)]^k. \tag{1.62}$$

The definitions of $P(q^2)$ and $\phi(q^2, t_0)$ are given by

$$P(q^2) \equiv z(q^2, m_{D_s^*}^2), \tag{1.63}$$

$$\phi(q^2, t_0) = \left(\frac{\pi m_c^2}{3}\right)^{1/2} \left(\frac{z(q^2, 0)}{-q^2}\right)^{1/2} \left(\frac{z(q^2, t_0)}{t_0 - q^2}\right)^{-1/2} \left(\frac{z(q^2, t_-)}{t_- - q^2}\right)^{-3/4} \frac{t_+ - q^2}{(t_+ - t_0)^{1/4}}. \tag{1.64}$$

We use this parameterization to extract form factor information from our observed $D^+ \rightarrow \eta e^+ \nu$ q^2 dependance.

CHAPTER 2

EXPERIMENTAL SETUP

The data for this analysis was provided by e^+e^- collisions generated by CESR (Cornell Electron Storage Ring) and measured by the CLEO-c detector. In the lab frame, the e^+e^- collision is precisely tuned to create two D mesons, either D^+D^- or $D^0\bar{D}^0$, nearly at rest at the center of the CLEO-c detector. This chapter describes CESR, the CLEO-c detector and the workings of the various CLEO-c detector sub components in more detail.

2.1   CESR: Cornell Electron Storage Ring

The Cornell Electron Storage Ring (CESR) was originally designed to produce e^+e^- collisions in the energy range of 9 to 16 GeV. The e^+e^- collisions for the analysis of $B \to \eta' \ell \nu$ were created by CESR with a center of mass energy of 10.58 GeV. In order to produce D^+D^- mesons for the study of $D^+ \to \eta^{(\prime)} e^+ \nu$ CESR had to go below its original design parameters down to an energy 3.77 GeV.

The electrons and positron were accelerated in three stages: a linear accelerator (linac), a synchrotron, and then the CESR storage ring itself. The configuration is shown in Figure 2.1. The linac is 30m long, and accelerates electrons emitted from a 120 kV electron gun up to 300 MeV. The positrons are produced by inserting a tungsten target into the 150 MeV point of the electron path. The electrons that collide with the target create electromagnetic showers that can produce the positrons. Since the positrons are produced roughly midway through the linac, they are not accelerated up to as high an energy at this stage, and reach roughly 160 MeV. Curved transfer lines are used like spectrum analyzers to select electrons and positrons at specific momentum and those are injected into the synchrotron. Within 1/120 s the synchrotron fully accelerates the beam and "kicker" magnets send the beam into CESR.

CESR Storage Ring

Synchrotron

e$^+$ Transfer Line

e$^-$ Transfer Line

Linac

Gun **Converter**

e$^-$

e$^+$

RF

RF

CHESS

CLEO

CHESS
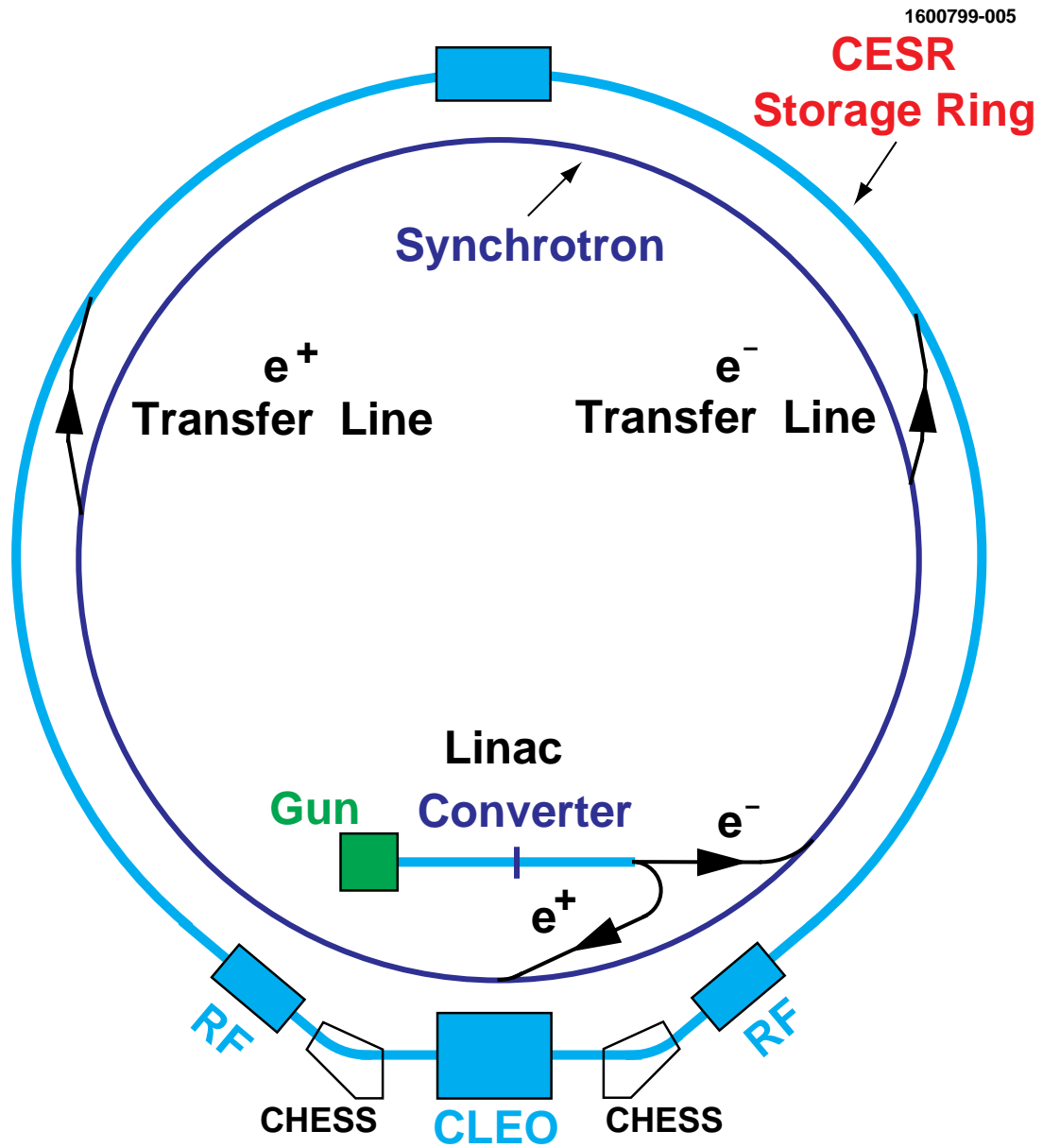
Figure 2.1: Schematic of the Cornell accelerator chain, showing the linac, synchrotron, and CESR.

CESR contains a single ring, and both electrons and positrons are stored in the same beampipe, traveling in opposite directions. We want the beams to only collide at the intended interaction point at the center of the CLEO-c detector. In order to prevent the beams from interacting at any other point in the ring, electrostatic separators provide equal and opposite kicks to the electrons and positrons. When the electrons and positrons do collide at CLEO there is a slight crossing angle (3 mrad) and hence a non zero momentum of the center of mass in the lab frame. Despite the crossing angle, the heavy mesons produced in the e^+e^- collisions are nearly at rest.

2.2 The CLEO-c Detector

The data for this analysis was provided by e^+e^- collisions generated by the CESR (Cornell Electron Storage Ring) and measured by the CLEO-c detector. The CLEO-c detector is designed to perform well for a wide variety of heavy meson physics analysis. The CLEO detector has gone through several iterations during the life of the CLEO experiment. We describe the detector in its final configuration, CLEO-c, that was used to study the D mesons. The CLEO detector is composed of several different sub-detectors, each designed with the aim of measuring the daughter particles energy, momentum, and speed of the particle. The detector is mostly cylindrical and nearly hermetic, with some sub-components having up to 93% coverage of the solid angle. Figure 2.2 shows a 3D cut away view of the detector and its sub-components.

2.2.1 Drift Chambers (DR and ZD)

Drift chamber technology is used as the primary means of detecting charged particles in CLEO-c. The drift chamber is composed of basic units called "cell"s that are composed of "sense" wires that are surrounded by "field" wires. In CLEO-c the geometry of the
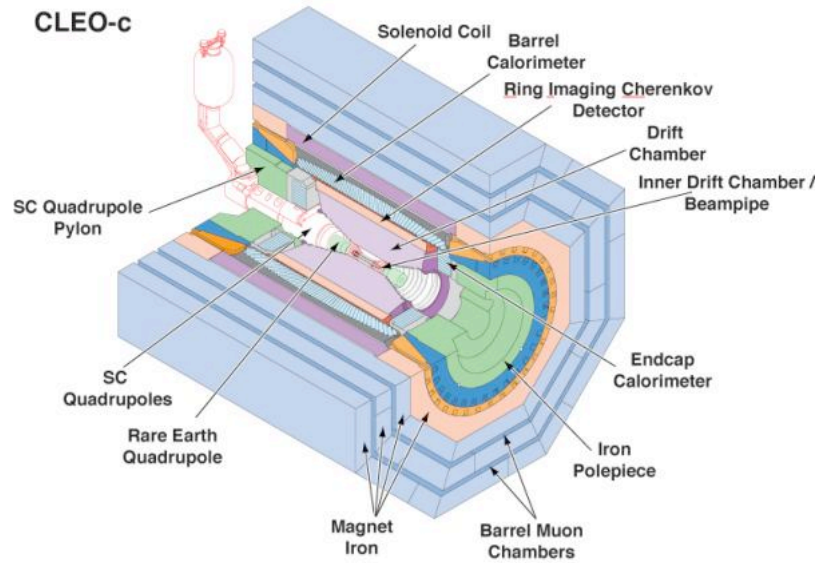
Figure 2.2: The CLEO-c detector and all of the sub-detector components.

"cell"s is approximately square with a length around 1-1.5 cm. The cell is immersed in an inert gas mixture of 60:40 helium and propane. When a charged particle passes through the cell it ionizes gas molecules along its trajectory. The trail of ionized gas is referred to as a "track". The ionized gas molecules travel through the material under the influence of the electric fields generated by the field wires toward the sense wire. The ions travel at essentially a constant speed, 28 μm/s, until it gets close enough to the wires where the electric field becomes very strong. The ion gains enough momentum to ionize other particles and begins an "avalanche" of electrons that amplifies the signal and finally hits the sense wire to create a signal pulse.

The pulse gives two pieces of information, the time that the original charged particle passed through the cell, and the total charge of the pulse tells us the energy that was lost by the original charged particle. The size of this energy loss is related to the particles velocity by the Bethe-Bloch formula, and is referred to in CLEO and this thesis as dE/dx.

The charged particles and ions are not only under the influence of the electric fields generated by the field wires, but are also within a uniform 1 Tesla magnetic field generated by a solenoid that encloses the entire drift chamber. This magnetic field points along the direction of the beam axis. The purpose of this field is to cause the paths of the charged particles to bend in a helix around the beam axis. The curvature of the path is inversely proportional to the magnitude of the momentum transverse to the direction of the magnetic field. Therefore, if we arrange the drift chamber cells such that the path that the charged particle took can be determined then we can determine the momentum of the charged particle. Information about the momentum (path) and the speed (dE/dx) can give us the particle mass and identity. Additionally, the direction that the particle curves in the helix relative to the direction of the magnetic field is related to the sign of the particles charge.

A single square cell can be used to determine the point along the face of the cell that the charged particle traveled through. Therefore, if all of the wires in the drift chamber were parallel to the beam axis then we would have no information about how the particle traversed along that direction. Therefore, we use cells with "stereo" angles to the beam axis, which means that it can have some resolution for the path along the beam axis, as well as the plane that's transverse to the beam axis.

In order to optimize our ability to determine the path of charged particle from the interaction point CLEO-c uses two concentric drift chambers, the inner chamber known as the ZD [18] and the outer drift chamber known as the DR [19]. The inner drift chamber, ZD, is designed to give good information along the beam axis, or Z axis, and so uses large stereo angles between 10.3 and 15.4 degrees from the beam pipe. The ZD contains 300 sense wires.

The main drift chamber surrounds the beam pipe and the ZD. It consists of forty-seven layers of cells. As the particle passes through the many layers of the DR its dis-

tance of closest approach in each cell that it hits gives information about its r trajectory. To contribute information about the z trajectory of the particle, thirty-one of the forty-seven DR layers are arranged in groups of four layers with alternating negative and positive stereo angles. The stereo angle is created by giving the wires in these layers a twist: unlike the wires in the axial layers, they are not strung parallel to the beam axis, but instead have different coordinates at either end. There are 9,796 sense wires in the DR drift chamber. Additional z information is provided by cathode strips surrounding the drift chamber.

All of the information from the drift chamber is used by a Kalman filter [20] to provide the best possible description of the particles path, including the effect of energy loss. The track momentum resolution at CLEO-c is $\sigma_p/p \sim 0.6\%$ at 800 MeV/c.

2.2.2   RICH

The drift chamber measured the momentum of charged particles and with measurements of dE/dx we can infer the particle speed and then with momentum and speed identify the type of particle by its mass. However, our ability to determine the speed of the particle by dE/dx measurements is not always satisfactory. We find that the separation between certain species of particles in certain momentum ranges are not very large compared to the size of the uncertainties in the dE/dx measurements. Therefore, a secondary method for determining the speed of a particle is required.

We use an instrument known as the RICH (Ring Imaging Cherenkov detector) as an additional measure of the speed of charged particles [21]. The RICH uses the properties of Cherenkov radiation to determine the speed of a particle. When particles travel faster than the speed of light in a medium they create a cone of coherent light called Cherenkov radiation. The half angle between the cone and the particles trajectory is given by

$$cos(\theta_C) = \frac{1}{n\beta} \tag{2.1}$$

where n is the refractive index of the medium and $\beta = v/c$ is the speed of the particle as a fraction of the speed of light. By measuring the angle between the particle trajectory and the Cherenkov photon we can determine the velocity of the charged particle.

The RICH is cylindrical and lies immediately outside the DR at a radius of 82 cm, and covers approximately 80% of the solid angle of the decay, or $|cos\theta| < 0.8$. The charged particles travel through a 1 cm think lithium fluoride crystal with a refractive index of 1.5 at $\approx$ 150 nm wavelength of light. If a charged particle has a speed that is higher than the speed of light in the fluoride crystal, then a photon with an opening angle dependent on the particles speed is produced. In order to minimize total internal reflections, these LiF radiators are arranged in a "sawtooth" pattern on the outer radius of the RICH barrel. The Cherenkov photons are then allowed to traverse a 16 cm long region filled with nitrogen gas where the cone of light can expand large enough to be measured. The photons pass through a calcium fluoride window into another region filled with a mixture of methane and triethylamine gas. The photons ionize the gas, and the resulting signal is amplified with a multi-wire chamber, and the charges are measured with 7.5 mm × 8 mm cathode pads. Figure 2.3 shows a schematic of the RICH.

For each track that reached the RICH a likelihood is calculated for the different mass hypothesis expected to be found in the drift chamber–namely electron, muon, pion, kaon, proton. Each mass hypothesis is expected to leave photons in different sets of cathode pads. Therefore, whichever hypothesis is most consistent with the pattern of cathode hits in data is chosen as the best match to the track.

It should be noted that the RICH has much more material in it than the drift chamber, and is estimated to be 13% of a radiation length at normal incidence. This means that a number of the photons produced in the D decays are going to decay in the RICH, and that the e^+e^- generated are going to be farther apart than when the photon decays in the calorimeter, and hence may not get reconstructed as a photon in the crystal calorimeter.
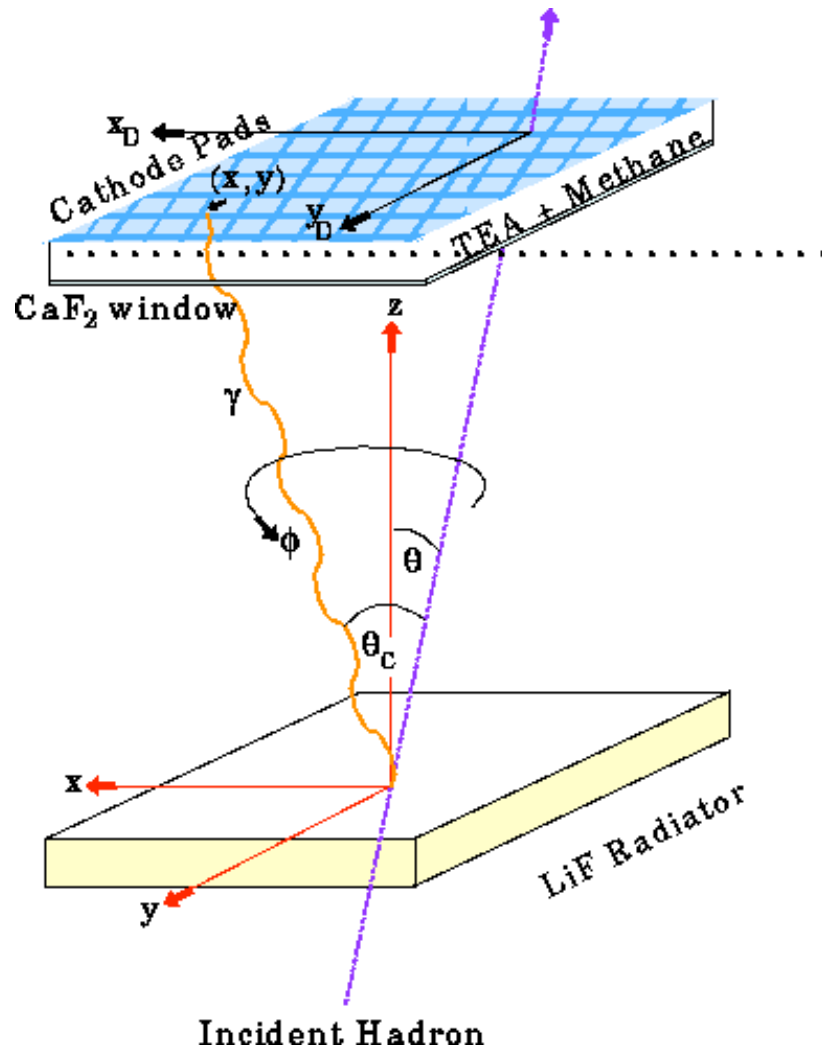
Figure 2.3: The RICH detector scheme in the CLEO-c.

The crystal calorimeter is the next detector in the path of the D's daughter particles, and is described in the following section.

2.2.3 Crystal Calorimeter

Up to this point we have only described how the CLEO-c detector collects information about charged particles. However, a large fraction of the total energy from an event

is going to be in the form of neutral particles that do not leave any tracks in the drift chambers, and no useful information in the RICH. The neutral particles that we want to be able to detect include photons, K_L, and neutral particles that can almost immediately decay to two photons such as π^0 and η.

Therefore, outside of the RICH is the CLEO Crystal Calorimeter (CC) [22] that is designed to measure the energy of electromagnetic showers. The CC (Crystal Calorimeter) is composed of 7784 cesium iodide crystals doped with thallium. Each crystal is 30cm long and 5 cm $\times$ 5 cm on the face. The long axis corresponds to over 16 radiation lengths, and the Moliére radius of the material is 3.8 cm, which is within the surface area of a single crystal. This means that almost all showers interact in the calorimeter, and transverse dimensions of an electron or photon shower can be contained in a small number of crystals.

The back end of the crystal has four photodiodes mounted on it, and the other end is mounted toward the interaction region. These crystals are arranged into 3 different sections around the other detectors: the barrel section and 2 endcap sections. The barrel section is cylindrical, and the crystals are arranged such that they nearly all look toward the interaction region, only offset with a slight angle in order to prevent photons from slipping through the cracks without leaving energy deposits. The crystals in the endcaps are aligned parallel to the beam axis, and necessarily have a hole through the middle of them for the beam pipe to enter and exit the detector. The crystal configuration has different efficiencies for detecting showers in different regions in $|cos(\theta)|$ corresponding to the holes in the endcaps and the gaps between the barrel and endcap sections. We define 4 regions of the calorimeter given in Table 2.1. Further, the structure holding the inner component of the drift chamber in place shadows the endcap region in $|cos(\theta)| >$ 0.93.

Table 2.1: Calorimeter regions. The crystal geometry is not cylindrically symmetric in the endcap, causing the overlap between the transition and good endcap regions and the approximate boundaries.

Good Barrel	$|cos\theta| < 0.82$
Transition	$0.82 < |cos\theta| < 0.86$
Good Endcap	$0.85 < |cos\theta| < 0.93$
Inner Endcap	$0.93 < |cos\theta| < 0.95$

However, not just neutral, but charged particles can also leave energy in the crystal calorimeter. These showers from charged particles can usually be distinguished from showers from photons based on where the track enters the calorimeter, or by the way that energy was deposited in the crystals. If a shower is located where the path of a track intersects the calorimeter, then it very likely has been produced by that track. However, tracks and K_L can also leave energy in the calorimeter by having a hadronic interaction with one of the atomic nuclei in the crystal. The daughters of these hadronic interactions can be long lived, and may travel some distance, even occasionally end up on the other side of the detector, before they deposit energy in the calorimeter. These showers are referred to as "splitoffs" because they are "split" "off" from the track that created them. Identifying and removing these splitoffs are going to be important later in this analysis.

We find that for showers in the good barrel or good endcap regions, the CC provides energy resolution of $\sigma_E/E \sim 5\%$ for a 100 MeV photon.

CHAPTER 3

ANALYSIS METHOD

For this analysis we set a goal to obtain a statistically significant observation of $D^+ \to \eta' e^+ \nu$ and to measure the branching fraction with an uncertainty of less than 1/3 of the central value. This level of uncertainty would give 1.5 standard deviation (σ) separation between the previous 90% upper limit and the minimum branching fraction predicted by the FKS form factor parameterization. Though greater separation is desired to confirm 2-gluon contributions to the form factor, the current goal of a 3σ branching fraction measurement pushes the limits of the CLEO-c data set, and a more ambitious goal would not be realistic. Even though we do not expect to obtain clear evidence of 2-gluon contributions, if the branching fraction has fluctuated one or two standard deviations below the FKS minimum this would be strong evidence against such a contribution.

The CLEO detector is symmetrically centered around the collision point between electrons and positrons created by CESR (Cornell Electron Storage Ring). The electrons and positrons have equal energy, and nearly opposite momentum in the lab frame with the exception of a small crossing angle of 10^{-3} radians. The beam energy and momentum is known very well compared to the energy resolution of tracks and showers. For CLEO-(2,2.5,3) the beam energy was on resonance to produce $e^+ e^- \to \Upsilon(4S)$, where $\Upsilon(4S)$ predominantly decayed to pairs of B mesons ($B^+ B^-$ and $B^0 \bar{B}^0$) that were nearly at rest. For CLEO-c the beam energy was on resonance to produce $e^+ e^- \to \Psi(3770)$, where $\Psi(3770)$ predominantly produced pairs of D mesons ($D^+ D^-$, or $D^0 \bar{D}^0$) that were nearly at rest. The fact that these mesons decay nearly at rest means that the daughter particles of each heavy meson are evenly distributed in the 4π of solid angle, and it must be determined which tracks and showers belong to which heavy meson.

The CLEO-c program has used two different types of analysis to study exclusive semileptonic decays: D-Tagging [25] and Neutrino Reconstruction [33]. The $\mathcal{B}(B^+ \to \eta^{(\prime)}\ell^+\nu)$ measurements were made using neutrino reconstruction, and the preliminary $\mathcal{B}(D^+ \to \eta^{(\prime)}e^+\nu)$ measurements were made using the D-Tagging method. Neither of these two approaches are capable of achieving the goal set for this analysis. The D-Tagging method has very small backgrounds and could claim an observation with only a few events, but given the size of the data set it is not likely to provide any information about 2-gluon couplings. The neutrino reconstruction method doubles the efficiency, but has larger backgrounds and systematic uncertainties, so would probably not achieve a statistically significant observation of this decay.

In order to accomplish the stated goal of the analysis, a new method is created that combines neutrino reconstruction with improvements inspired by D-tagging. This new method performs a generic reconstruction of the non-signal ("other side") D to improve the neutrino resolution and aid in background rejection. Furthermore, the approach can be combined with D tags to do a generic survey of the hadronic decays, and by doing so we make the first measurement of several D hadronic decays.

In the following sections there is more in-depth discussion of the D-Tagging and Neutrino Reconstruction approaches, as well as a thorough description of the new Generic Reconstruction method.

3.1 Exclusive Semileptonic Reconstruction at CLEO-c

Before delving into an in-depth discussion on the different approaches to studying exclusive semileptonic decays at CLEO-c, we describe aspects that are common to any CLEO-c analysis of this type. The special concerns involved in an exclusive semileptonic analysis are more pronounced when we first consider the study of a fully hadronic decay, $D^+ \to X^0Y^+Z^0$, where X, Y and Z represent hypothetical daughter particles that

can be observed by the CLEO-c detector. In this hypothetical analysis the mass and energy of the D mesons produced in the lab frame are well known. Therefore, the study would proceed by searching the daughter particles of the D^+D^- decays for an X^0, Y^+ and Z^0 where the sum of their four-vectors is consistent with the expected energy and mass of a D meson. There would be quality cuts on the X^0, Y^+, and Z^0 candidates to make certain that they were correctly identified, and the Monte Carlo simulation would be used to predict the efficiency for reconstructing the decay. The branching fraction for this process could be found by dividing the number of reconstructed signal events by the efficiency for detecting the process and the number of all D^+D^- events in the data set.

Now consider a study of an exclusive semileptonic decay, $D^+ \rightarrow X^0 e^+ \nu$. This does not initially appear any different from the study of $D^+ \rightarrow X^0 Y^+ Z^0$ described above. The difference is that unlike the previous example, where all of the daughters could be detected by the CLEO-c detector, under no circumstances can neutrinos be directly measured by the CLEO-c detector. Therefore, the single most important feature of these studies is that energy and momentum conservation must not only be used to identify the correct D^+ candidate, but must also be applied to the entire set of D^+D^- daughter particles to infer information about the neutrino. Due to the necessity of using energy and momentum conservation on the entire event, and not just on the D^+, the semileptonic signal can only be reconstructed when the total energy and momentum of all other daughter particles in the event can be determined. Events with multiple neutrinos, or other daughter particles with a low detection efficiency, such as K_L, do not contribute to the signal efficiency. Therefore, unlike the example $D^+ \rightarrow X^0 Y^+ Z^0$ where the efficiency was independent of how the D^- decayed, the efficiency for reconstructing an exclusive D^+ semileptonic decay is directly dependent on how well we can determine the energy and momentum of the D^- decay. Each of the analysis techniques that are described in this thesis deal with this problem differently.

As an example, consider an imaginary case where D^+ has only four possible final states: one semileptonic decay, SL, and three purely hadronic final states A, B, and C. Suppose that the efficiency for reconstructing the decay $D^+ \rightarrow SL^+$ in a $\Psi(3770) \rightarrow D^+D^-$ event is 30% for $D^- \rightarrow A^-$, 15% for $D^- \rightarrow B^-$, 7% for $D^- \rightarrow C^-$, and finally 0% for $D^- \rightarrow SL^-$. For N events of type $\Psi(3770) \rightarrow D^+D^-$, the number of $D^+ \rightarrow SL^+$ reconstructed, $N^R_{SL^+}$ is

$$N^R_{SL^+} = N_{D^+D^-} \left(\epsilon_A \mathcal{B}_A + \epsilon_B \mathcal{B}_B + \epsilon_C \mathcal{B}_C + \epsilon_{SL} \mathcal{B}_{SL} \right), \quad (3.1)$$

where ϵ_X is the efficiency given $D^- \rightarrow X$, and $\mathcal{B}_X$ is the branching fraction for $D^- \rightarrow X$. If the hadronic branching fractions, $\mathcal{B}_X$, are poorly known the value of the overall efficiency for reconstructing $D^+ \rightarrow SL^+$, or $N^R_{SL^+}/(\mathcal{B}_{SL} N_{D^+D^-})$, is also poorly known. Consider the case where the true values of the hadronic branching fractions are $\mathcal{B}_A = 15\%$, $\mathcal{B}_B = 30\%$, and $\mathcal{B}_C = 45\%$. Suppose that the branching fractions A, B, and C were unmeasured but the sum of the 3 was known. If we guessed that $\mathcal{B}_A = 20\%$, $\mathcal{B}_B = 40\%$, and $\mathcal{B}_C = 30\%$, the total efficiency for reconstructing $D^+ \rightarrow SL^+$ will be wrong by 16% of itself. The CLEO-c program aims to measure exclusive semileptonic decays to much better than a 16% systematic uncertainty. Therefore, though this is just a cartoon example of the problem, how unknown branching fractions affect the overall efficiency for measuring a specific exclusive decay mode must either be understood very well, or the branching fractions must be determined in such a way that the uncertainties cancel out.

Another issue that all exclusive semileptonic reconstruction techniques must face is the problem of extra tracks and extra showers. The algorithm used to extract tracks from drift chamber hits is not perfect. Extra (fake) tracks can be created by noise in the drift chamber or by low momentum tracks that curl several times in the drift chamber (curlers). Extra showers, or showers not associated with a neutral particle directly from the decay of the D meson, are usually generated by "splitoffs", or secondary particles

created by hadronic interactions within the calorimeter that are displaced from the parent particle. These extra tracks and showers can degrade the neutrino resolution, and can hurt the signal efficiency. One of the challenges in doing an exclusive semileptonic study is to identify and ignore these extra tracks and showers, and the Neutrino Reconstruction and D-Tagging techniuqes have very different approaches for doing this. We now discuss the D-Tagging, Neutrino Reconstruction, and Generic Reconstruction techniques in more detail.

3.2   Method of D Tagging

The D-Tagging technique was first applied by the Mark III collaboration at SPEAR [27]. It was used to search for $D^{\pm} \to \eta e^{\pm} \nu$ and $D^{\pm} \to \eta' e^{\pm} \nu$ using the first $281 pb^{-1}$ of CLEO-c data in [25]. This section gives a more in depth description of the method used in [25].

The method works by only considering events where at least one of the two D's is clearly identified as a well understood D decay with a precisely measured four-vector. This well reconstructed D is known as the D-tag. Once a D-tag is identified the signal of interest is sought out in the remaining tracks and showers in the event. The neutrino on the signal side is inferred using the four-vector of the D-tag and the four-vectors of the lepton and meson candidates for the signal D. The problem of extra tracks and extra showers is solved by simply ignoring any tracks or showers that are not part of the D-tag or the signal lepton and meson candidates. With specific decays in mind that are known to occur frequently in the data, we can confidently ignore any left over tacks and showers if we can make a convincing tag and signal.

For $D^+ D^-$ events the following six hadronic decay modes are used to create D-tags: $D^- \to K_S(\pi^+ \pi^-)\pi^-$, $D^- \to K^+ \pi^- \pi^-$, $D^- \to K^+ \pi^- \pi^- \pi^0$, $D^- \to K_S(\pi^+ \pi^-)\pi^- \pi^0$, $D^- \to K_S(\pi^+ \pi^-)\pi^- \pi^- \pi^+$, and $D^- \to K^+ K^- \pi^-$. Any of these combinations that are found must pass strict requirements and be consistent with the the expected energy and mass

of the D. In the event that there are multiple D^- candidates, the one that best matches the beam energy is chosen. In the actual analysis, the beam energy is known much better than the energy of the daughter particles in the tag. Rather than make requirements on the invariant mass of the sum of the daughter particles, consistency of the D-tag with the D meson is enforced by placing requirements on two parameters, ΔE^{tag} and M_{bc}^{tag}. The total energy of the tag must be the same as the beam energy, so we require that ΔE^{tag} is close to zero, where $\Delta E^{tag} = E_D^{tag} - E_{beam}$. Requirements are placed on the magnitude of the D-tag momentum by constructing a mass from the magnitude of the tag momentum and the beam energy, $M_{bc}^{tag} = \sqrt{E_{beam}^2 - |\vec{p}_D^{\ tag}|^2}$, known as the beam constrained mass. We require that M_{bc}^{tag} is close to the mass of the D.

The efficiency for correctly reconstructing these tags at CLEO-c can vary by more than a factor of 2 between the different decay modes. For example, the efficiency for correctly tagging a true $D^+ \rightarrow K_S(\pi\pi)\pi^+$ is 66.46% but the efficiency for correctly tagging a $D^+ \rightarrow K^-\pi^+\pi^+\pi^0$ is only 27.02% [25]. If the branching fractions of these two decays are incorrect in the Monte Carlo simulation it can cause a large uncertainty in the total number of expected tags and the total number of reconstructed signal events.

Despite the large variation in the tagging efficiencies, once the D^- tag has been found, the efficiency for reconstructing the signal semileptonic D^+, or the post-tag signal efficiency, has much less variation. Depending on which tag was found for the D^- decay, the efficiency for finding the signal can vary by as much as 5% percent of the average. For example, the post-tag efficiency for $D^+ \rightarrow \pi\pi\eta(\gamma\gamma)e^+\nu$ is on average 21.63% with a standard deviation between the different central values of 0.7% and a low of 20.44% for $D^- \rightarrow K^+\pi^-\pi^-\pi^0$ and a high of 21.89% for $D^- \rightarrow K^+K^-\pi^-$. This variation in the post-tag efficiency is from combinatoric effects. The requirements for identifying the signal lepton and $\eta^{(\prime)}$ candidate are described in [25].

As was shown in Section 3.1, the number of reconstructed exclusive semileptonic decays can depend on all of the hadronic branching fractions of the D meson. The tagged analysis takes two steps to keep this from being a problem. Firstly, the branching fractions are found by dividing by the total number of tags found without signal D restrictions rather than the total number of D^+D^- generated by CESR. By dividing by the number of tags rather than the number of D^+D^- we eliminate the need to know the fraction of the time that nature produces a decay that can be tagged. Secondly, the individual branching fractions of the tag modes are accounted for by measuring the composition of tags in data and correcting the Monte Carlo sample to match.

The advantage of this method is that you do not need to fully understand the D system in order to determine absolute branching fractions. You do not need to know the inclusive semileptonic decay rate, the rate of K_L production, or the absolute branching fractions of any decay. The only thing that has to be understood is the relative frequency for producing the different tag types and this is measured in data. The obvious drawback to this technique is that it does not make full use of the data. The inclusive branching fraction of all of the D^+ tag modes is approximately 22%, while the total $D^+ \rightarrow fully\ visible$ branching fraction is approximately 44%. Taking advantage of the additional $D \rightarrow fully\ visible$ branching fraction is problematic for the D-Tagging analysis because it is composed of a large number of rare decays. Not only would adding all of these rare decays involve a large amount of work, but attempts to count the number of rare tags without signal D restrictions can easily be overwhelmed with backgrounds.

3.3 Method of Neutrino Reconstruction

The method of Neutrino Reconstruction has been used at CLEO-2, CLEO-2.5, and CLEO-3 to study the semileptonic decays of B mesons to charmless final states and was used in CLEO's measurement of the CKM matrix element $|V_{ub}|$ [16] [24]. More

recently the method was used at CLEO-c to measure the $D \rightarrow \pi e \nu$ and $D \rightarrow K e \nu$ decays [33].

This method works by identifying events that are consistent with having one neutrino and no other unmeasured particles. The four-vector of this neutrino is inferred from energy and momentum conservation using the known four-vector of the beam subtract the total measured four-vector of the tracks and showers in the event. Once the neutrino has been identified, and event level requirements for consistency with only 1 neutrino have been met, the analysis continues very much like the $D^+ \rightarrow X^0 Y^+ Z^0$ example of the previous section. A search is performed in the tracks and showers for a suitable electron and meson candidate that can combine with the neutrino four-vector to make a good D meson candidate. A D candidate is considered good if the energy and momentum magnitude are consistent with expected values.

More specifically, the event is considered consistent with having only one neutrino if there is only one charged lepton measured in the event, and if the mass of the missing four-vector is consistent with zero. The reason for the 1 charged lepton requirement is that the number of neutrinos is typically equal to the number of charged leptons. The missing mass must be consistent with zero because the neutrino effectively has zero mass. A missing mass not consistent with zero is an indication of there being other missing particles that are not accounted for by the tracks and showers measured by the detector, such as particles that went down the beam pipe where there is no detector coverage. Once the missing mass requirement has been made, the missing energy measurement is not used again, and the magnitude of the missing momentum is inferred to be the neutrino energy.

Good D meson candidates are determined by placing requirements on two variables: $\Delta E^{sig} = E_D^{sig} - E_{beam}$ and $M_{bc}^{sig} = \sqrt{E_{beam}^2 - |\vec{p}_D^{\,sig}|^2}$. These requirements enforce energy and momentum conservation as well as the expected invariant mass of the D. Note that

this ΔE and M_{bc} are different from the quantities used in the tagged analysis. In the D-tagging analysis these two parameters were functions of only the components used in the D-tag. In Neutrino Reconstruction these quantities use the reconstructed neutrino four-vector and are functions of all tracks and showers in the event. The M_{bc} is also different because after the ΔE^{sig} is calculated, the energy/momentum of the neutrino is scaled such that ΔE^{sig} is zero in order to improve the resolution of the beam constrained mass.

This method does not fully reconstruct the contents of the event, and unlike the D-Tagging method, it does not have the luxury of being able to simply ignore extra showers and tracks based on event level information. Instead, extra showers and extra tracks must be identified on a shower by shower and track by track basis using clues offered by the distribution of those individual objects in the detector.

In order to identify and remove these extra showers we use a neural net algorithm known as "splitoff". This algorithm looks at the distance of potential splitoff showers from parent showers, as well as the shape of the energy deposition of the extra shower to see if it points back to the parent shower. This neural net is described in more detail in [29]. Showers that do not show any sign of being a splitoff are refered to as "splitoff approved". The efficiency for showers to pass the splitoff approval requirement is shown in Figure 3.1. The efficiency is near 100% for photons above 400 MeV, but drops to only 20% below 100 MeV.

Extra tracks are identified by an algorithm known as Trkman. Tracks that are considered good tracks to include in the missing energy calculation are called "Trkman approved". More detail about the trkman algorithm can be found in [30]. The efficiency for pion and kaon tracks to be trkman approved is shown in Figure 3.2. The efficiency for both pions and kaons to be trkman approved is near 100% above 250 MeV/c.

Photon SplitOff Approval Efficiency
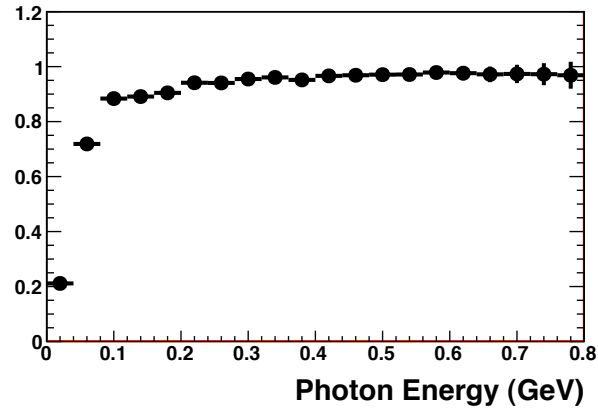
Figure 3.1: The efficiency for one shower created by a $\pi^0 \to \gamma\gamma$ to be considered splitoff approved as a function of the shower energy according to the Monte Carlo simulation.

Pion Trkman Efficiency

Kaon Trkman Efficiency
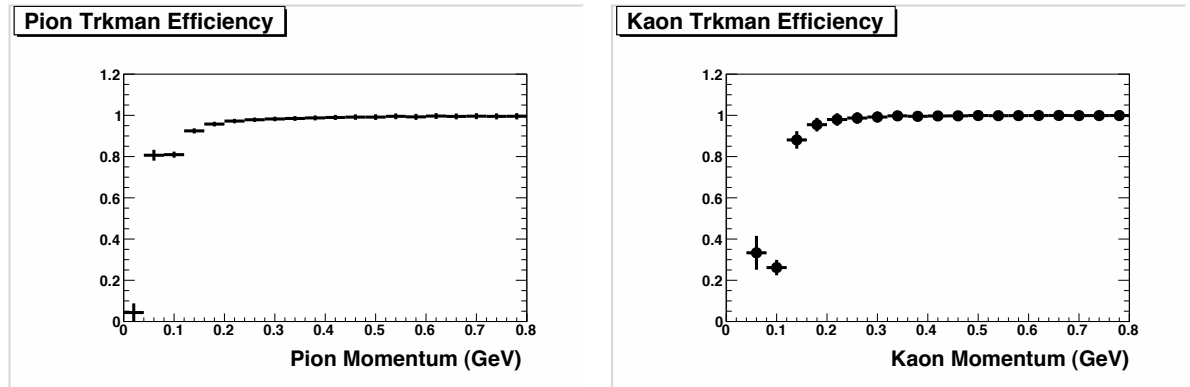
Figure 3.2: The efficiency for a pion track to be trkman approved (left) and the efficiency for a kaon track to be trkman approved (right).

This method can make significant gains in efficiency over the D-Tagging method from two sources. The first source of extra efficiency is that all hadronic D decays that produce only visible daughter particles are used to reconstruct the signal semileptonic D decays, and not just the handful of decays used to create tags. The branching fraction of the sum of the decay modes used to create tags is approximately 22%, while the branching fraction of all fully hadronic, fully visible decays (not including events that contain a $K^0 \rightarrow K_L$) is approximately 44%. Since the missing energy reconstruction method does not discriminate against specific D decays, it can potentially make use of nearly double the number of events.

The second source of extra efficiency is the fact that an event does not have to be perfectly reconstructed, as it does in the tagging method, in order to be used in the analysis. If a shower from a $\pi^0 \rightarrow \gamma\gamma$ decay were lost, or incorrectly associated with hadronic showers from a track, the D-tagging method would probably not be able to use the event. However, if the total momentum of the event excluding the neutrino was still reconstructed reasonably well, and the total energy was still close enough to the expected value to rule out missing K_L's or extra neutrinos, this event would still be perfectly good to use in Neutrino Reconstruction. Depending on the requirements on the missing mass necessary to remove the backgrounds from a particular exclusive decay, the Neutrino Reconstruction method can more than double the number of signal events seen in the D-Tagging method at CLEO-c.

This increase in efficiency comes at a cost. Limiting the restrictions on the non-signal D decay can result in much larger backgrounds than the D-Tagging method. In addition to larger backgrounds there are larger systematic uncertainties associated with the absolute branching fraction. Unlike the D-Tagging method that used the number of D-tags in the data set to determine absolute branching fractions, the neutrino reconstruction method must use the total number of D^+D^- in the data set. As in the example earlier

in this chapter, this makes the efficiency of the Neutrino Reconstruction analysis more vulnerable to systematic uncertainties related to how a generic D meson decays. The efficiency in this analysis is proportional to the fraction of the D meson decays that will allow for the neutrino to be reconstructed. Events with semileptonic decays on both sides have essentially zero efficiency, as do events with K_L's that do not leave sufficient energy in the calorimeter. Provided that these low efficiency inclusive branching fractions are well understood, the analysis method relies on the assumption that the efficiency for reconstructing the signal is independent of which non-signal $D \rightarrow fully\ visible$ decay took place. According to the splitoff approval efficiency, Figure 3.1, and the trkman efficiencies, Figure 3.2, this is probably a sufficient assumption provided that the majority of the non-signal D is in the form of tracks and showers that have momentum above 300 MeV/c. Also shower losses do not pose a significant problem as long as those showers contain a small fraction of the neutrino energy.

3.3.1 Using Separate Bins to Increase Significance

Another method that improves statistical significance of measurements made using neutrino reconstruction is to divide the data set into separate bins in such a way as to take advantage of regions of parameter space that have very good signal to background without having to sacrifice signal in regions that have only marginal, but still useful, signal to background. Note that this is not typically useful in a D-Tagging analysis because the backgrounds are already so small.

As an illustration, suppose that you have a measurement of 28 events where 14 of them are expected to be signal, and 14 of them are expected to be from backgrounds. The statistical uncertainty in the measurement is related to the figure of merit, defined as $S^2/(S + B)$ where S is the number of signal events and B is the number of background events. For this toy experiment, $S^2/(S + B) = 7$. This measurement would not be

43

considered an observation of the phenomenon, and the best estimate of the rate for the phenomenon would be $Rate = R_o \pm 0.38R_o$.

Suppose that there existed a "magic cut" that would remove all of the background at the cost of also removing half of the signal. After using this requirement there would be 7 events that were all expected to be signal. The $S^2/(S + B)$ would still be 7, just as it was before removing the background, and our knowledge of the actual rate of the phenomenon is the same as before. However, if it were an absolute certainty that there were no backgrounds then the measurement would now classify as an observation because 0 background events cannot fluctuate up to 7.

If the magic cut were used to divide the data into separate bins, rather than throw away the other 7 signal events over 14 background events, there would still be an observation of the phenomenon because one bin would have 7 signal events with 0 background. However, by including the 7 signal events over 14 background events in a separate bin the total figure of merit is now $7^2/(0 + 7) + 7^2/(7 + 14) = 9.33$ and the uncertainty in the rate of the measurement has improved. This would correspond to a rate measurement of $Rate = R_o \pm 0.33R_o$. Therefore, dividing the data into appropriate bins results in an improved measurement of the rate and an improved significance.

In the CLEO-3 analysis that studied the exclusive $b \rightarrow u\ell\nu$ decays, dividing data into bins was used to increase the statistical significance of the result. The analysis used the net charge bins $Q = 0$ and $Q = \pm 1$. As was mentioned earlier, if the total charge of all tracks does not equal zero it is an indication that an odd number of tracks are either missing or fake. Requiring that the net charge of the event is zero improves the signal to background. However, at the energy of the $\Upsilon(4S)$ the neutrino could still be reconstructed reasonably well if a low momentum track were either missing or fake. Because of this, for most of the $b \rightarrow u\ell\nu$ branching fractions measured at the $\Upsilon(4S)$ resonance,

events with net charge of ±1 still had useful signal even though the backgrounds were significantly larger than in the case of net charge 0.

3.4   Method of Generic Event Reconstruction

We have set a goal to measure the $D^{\pm} \rightarrow \eta' e^{\pm} \nu$ branching fraction with an uncertainty of no more than 1/3 of the central value. Even with all of CLEO-c data, the method of D-Tagging is not expected to have enough events to do this. However, the method of Neutrino Reconstruction is not expected to have a clean enough signal to background to do this either. We combine the best of both of these two methods in order to have a chance at achieving the stated goal. We create an analysis method that maintains the high efficiency of neutrino reconstruction by using all $D \rightarrow fully\ visible$ decays, make use of poorly reconstructed events while taking full advantage of the clean events, yet have the background rejection, resolution, and systematic uncertainty of the D-tagging method.

In addition to the other requirements we must fully understand how this new procedure is affected by the way the non-signal D decays. This procedure is based on the Neutrino Reconstruction technology and is sensitive to the inclusive semileptonic branching fraction and the rate of K_L production of the non-signal D. However, we also choose to not rely on the assumption that the efficiency for reconstructing the signal is independent of how the non-signal $D \rightarrow fully\ visible$ decays. Given the efficiency for a photon to be splitoff approved, Figure 3.1, and the efficiency for a track to be trkman approved, Figure 3.2, this may not be a good assumption to make after transitioning from the $\Upsilon(4S)$ to the $\Psi(3770)$.

At the $\Upsilon(4S)$ most tracks and showers carry a large enough momentum to have high splitoff and trkman efficiency. The low momentum and lower efficiency tracks and showers that were present typically carried a small amount of energy compared to the

energy of the missing neutrino, and so the neutrino reconstruction at this resonance was not very sensitive to loosing tracks and showers, and hence not very sensitive to the final state of the non-signal B. The $\Psi(3770)$ is a different environment than the $\Upsilon(4S)$. The total energy is smaller, the energy of the neutrino is less, there are fewer tracks and showers, with lower energy, that are more likely to have low efficiency for splitoff and trkman. This means that we are more likely to loose tracks and showers, and those lost tracks and showers are more likely to degrade the reconstruction efficiency.

For example, consider a neutrino reconstruction analysis when the non-signal D decays to one of the two hadronic decays $D^- \to K^+\pi^-\pi^-$ or $D^- \to K^+\pi^-\pi^-\pi^0$. For the decay $D^- \to K^+\pi^-\pi^-\pi^0$ the two showers in the π^0 are often below 200 MeV, where the efficiency for a shower to be splitoff approved begins to drop. In fact, the probability that both showers are splitoff approved is only about 65%. Therefore, depending on how important those two showers are, the efficiency for an event containing $D^- \to K^+\pi^-\pi^-\pi^0$ may be as low as 65% of the efficiency for an event containing $D^- \to K^+\pi^-\pi^-$. We find that if we perform a neutrino reconstruction analysis on $D^+ \to K_S(\pi^+\pi^-)e^+\nu_e$ with requirements similar to those used in [33] the efficiency given a non-signal D^- decay of $D^- \to K^+\pi^-\pi^-$ is 32%. For a non-signal D^- decay of $D^- \to K^+\pi^-\pi^-\pi^0$ the efficiency is 22%, and for a non-signal D^- decay of $D^- \to K^+\pi^-\pi^-\pi^0\pi^0$ the efficiency is 13%. This shows that even when using neutrino reconstruction at the $\Psi(3770)$ there can still be fairly large variations in reconstruction efficiency depending on how the non-signal D decays. Therefore, we must be mindful of this potential problem and find a way to understand how it impacts this analysis.

3.4.1 Splitoff Escapes and Backgrounds from $D \to K^\star e\nu$

The method of Generic D Reconstruction was originally developed to help remove backgrounds in $D^\pm \to \eta'(\rho^0\gamma)e^\pm\nu$ caused by $D \to K^{\star 0}e\nu$. This section gives a description

of how the $D \rightarrow K^\star e\nu$ was faking the $D^\pm \rightarrow \eta' e^\pm \nu$ and identify the key issue that Generic Reconstruction was developed to solve, identifying extra showers not flagged as splitoffs.

The masses of the η' and the K^{*0} are fairly close, 0.958 GeV/c^2 and 0.892 GeV/c^2 respectively. The width of the K^{*0} (0.050 GeV/c^2) is wide enough to reach the mass of the η'. This means that both a K^{*0} meson candidate and a η' meson candidate can potentially make an equally good D^- candidate when combined with the electron and neutrino within the resolution of the Neutrino Reconstruction technique ($\sim$ 0.10 GeV).

It was found through Monte Carlo studies that in Neutrino Reconstruction $D^- \rightarrow K^{\star 0} e^- \bar{\nu}_e$; $K^{\star 0} \rightarrow K^+ \pi^-$ and $D^+ \rightarrow K^- \pi^+ \pi^+$ was a primary component of the $D^\pm \rightarrow \eta'(\rho^0 \gamma) e^\pm \nu$ background. This background source is completely composed of tracks, and if splitoff showers are removed there should be no shower in the event to create a $\rho^0 \gamma$ candidate. The fake photon can come from two different sources for this type of decay. First, the $\Psi(3770)$ resonance is at a significantly lower energy than the $\Upsilon(4S)$, and unlike the data taken at the $\Upsilon(4S)$, many kaons have a low enough momentum to decay in flight within the drift chamber. Roughly 5% of all kaons decay via $K \rightarrow X\pi^0$ somewhere between the event vertex and the end of the drift chamber. If the decay occurs close to the vertex then the missing energy should still be accurately measured within the resolution of the decay products. However, decays that occur after the kaon has already generated a measurable track cause some of the kaons energy to be double counted via the extra showers produced by the π^0. Another, more frequent source of extra showers that double count energy are hadronic splitoff showers that are far enough away from the parent track to avoid being removed by the splitoff alogorithm. These extra showers are referred to as "splitoff escapes". According to the Monte Carlo simulation, approximately 15% of charged kaons and 5% of charged Pions produce a splitoff escape. The splitoff escapes
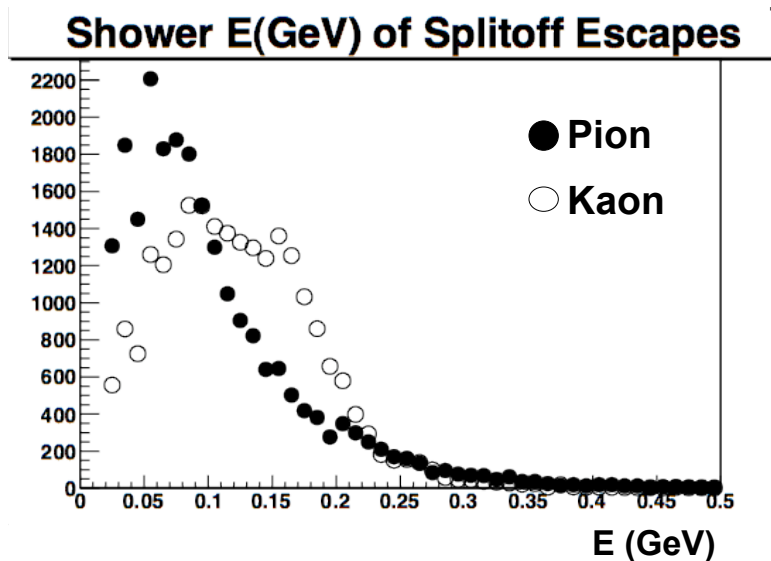
Figure 3.3: The spectrum of splitoff escape showers from pions (black) and kaons
(clear) according to the Monte Carlo simulation.

are typically in the energy range of 0.0 GeV to 0.30 GeV. Figure 3.3 shows the spectrum
of splitoff escape showers from pions and kaons, each normalized to the same area.

Not only do these extra showers from in flight decays and splitoff escapes provide a
shower to create a $\eta' \to \rho^0 \gamma$ candidate, the showers are in general degrading the neutrino
resolution and should be removed for all decay modes. Therefore, the initial purpose of
Generic Event Reconstruction was to help remove these extra showers. The method
of Generic Event Reconstruction and how it is used to remove these extra showers is
described in the following section.

3.4.2 Generic Reconstruction By Golden Composite Particles

It has been shown in the previous section that there are extra showers in the data con-
tributing to backgrounds and degrading the neutrino resolution. These extra showers
are not identified by the Splitoff algorithm, and there are not sufficient clues from the
shower shape or location to identify them as extra showers and remove them. We note

that predominantly the photons generated in a D meson decay are from either a $\pi^0 \to \gamma\gamma$ or an $\eta \to \gamma\gamma$. Therefore, in order to remove these extra showers we take a hint from the D-Tagging method and fully reconstruct the neutral component of the non-signal D as $\pi^0 \to \gamma\gamma$ or $\eta \to \gamma\gamma$ candidates and remove showers that do not appear to belong to one of these neutral particles. In D-Tagging this is done with a specific decay in mind but in the case of Generic Reconstruction we need a way to do this for a generic decay without any prior assumptions about how many π^0's or $\eta \to \gamma\gamma$'s to look for.

This is not the first attempt in a Neutrino Reconstruction analysis to fully reconstruct the neutral energy in order to remove extra showers. Early studies on using neutrino reconstruction for the CLEO-c data set at the $\Psi(3770)$ considered using "golden" π^0's to measure the neutral component of the total visible energy instead of splitoff approved showers [31]. The golden π^0's are a list of the $\pi^0 \to \gamma\gamma$ candidates that give the best description of the neutral energy in an event. Each shower in the golden π^0 list can only be used once, and showers that do not fall into a high quality π^0 candidate are removed from the total energy calculation.

We quantify the quality of candidate particles by use of the mass pull (χ_m) defined by $\chi_m = (M_U - M_N)/\sigma_M$ where M_U is the measured invariant mass of the candidate particle, M_N is the nominal mass of the particle, and σ_M is the uncertainty in the measurement. The smaller the absolute value of the mass pull ($|\chi_m|$) the better the candidate.

The original golden π^0's were selected from a list of candidates composed of showers that were not matched to any track (splitoff approval was not required). For each possible π^0 candidate we define the mass pull, $\chi_m(\pi^0) = (M_{\gamma\gamma} - M_{\pi^0})/\sigma_M$, where M_{π^0} is the known mass of the π^0, $M_{\gamma\gamma}$ is the invariant mass of the two showers in the candidate, and σ_M is the uncertainty in $M_{\gamma\gamma}$. The golden π^0 list was generated by selecting the $\pi^0 \to \gamma\gamma$ candidate with the smallest $|\chi_m(\pi^0)|$, removing any other candidates using those showers from consideration, and then repeating until all possible candidates have either been

selected or discarded. Then, only the golden π^0's with $\chi_m(\pi^0)$ between -3 and 3 were used to compute the neutral energy component of the total visible energy. Showers that were not part of one of these golden π^0's were ignored.

The preliminary studies found that the above method did not work as well as using the sum of the splitoff approved showers, and it was abandoned [31]. However, with several modifications this procedure can successfully be applied to this analysis to help remove splitoff escapes. The modifications include considering $\eta \rightarrow \gamma\gamma$ in addition to $\pi^0 \rightarrow \gamma\gamma$, loosening the $\chi_m(\pi^0)$ and $\chi_m(\eta)$ requirements used in the previous attempt, and only considering π^0 candidates composed of splitoff approved showers that have not already been used by the tracks and showers in the signal D.

Unlike neutrino reconstruction that finds the neutrino first, we begin this new procedure by selecting a signal electron and $\eta^{(\prime)}$ candidate. Then, rather than considering all showers in the event when generating our list of golden $X \rightarrow \gamma\gamma$'s, we only consider splitoff approved showers that have not already been used by the signal D. Proceeding in this way prevents us from mistakenly using a golden $X \rightarrow \gamma\gamma$ candidate where one shower is actually part of the signal side and the other is actually part of the non-signal side.

We widen the range of accepted χ_m values. Since a significant part of the extra efficiency gained by the neutrino technique over the tagged technique is the ability to make use of poorly reconstructed events, we wish to be very certain that a shower is a splitoff escape before removing it. We find that true π^0's and true $\eta \rightarrow \gamma\gamma$'s usually have a mass pull in the range of -5 to 3. However there are small tails in the distribution that can extend far out from this range, so we open up the requirements to include -25 to 15, see Figure 3.4. Since we have already required that the showers are splitoff approved, we can afford to be conservative and accept candidates out to this large mass pull range. Due to the fact that $\pi^0 \rightarrow \gamma\gamma$ is much more common than $\eta \rightarrow \gamma\gamma$, preference is given to
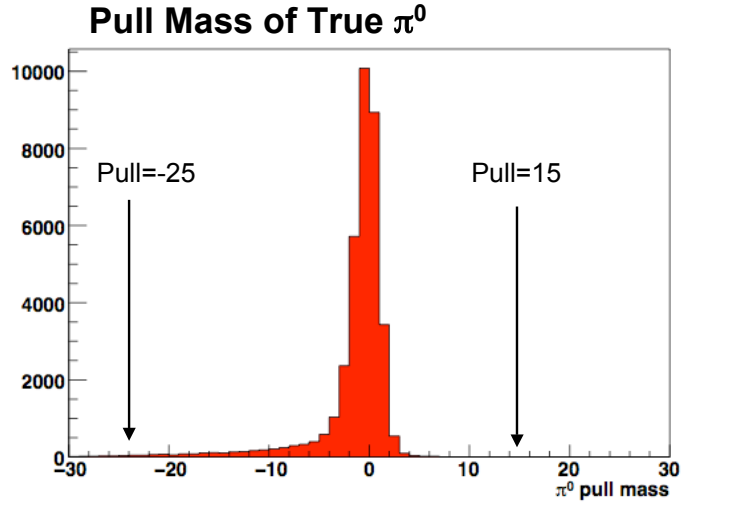
Figure 3.4: The mass pull of true π^0's according to the Monte Carlo simulation. The range of -25 to 15 easily encloses the full range of true π^0's.

π^0 candidates in the range of -5 to 3 even if there is an η candidate with a better (closer to zero) mass pull that uses one of the same showers. After this initial selection process is finished all remaining showers are divided among both π^0 and η candidates with mass pull between -25 and 15. Rather than the unconstrained sum of the shower four-vectors, the four-vectors from the mass constrained fits of the π^0 and η candidates are used in the missing energy calculation. This alone is an improvement to the missing energy calculation if there are true π^0 or η candidates with large mass pulls.

All showers remaining after the golden $X \rightarrow \gamma\gamma$ have been assigned are considered for removal. Showers that do not fit into any reasonable $X \rightarrow \gamma\gamma$ candidate could be splitoff escapes that need to be removed, but they could also be important contributions to the other side D decay, such as showers from a K_L interacting in the calorimeter, or showers from a genuine $X \rightarrow \gamma\gamma$ decay where the second photon was somehow lost. Therefore, there are instances where we obtain a more accurate measure of the neutrino energy and momentum by keeping these showers rather than throwing them

away. Showers that are splitoff escapes tend to be less than 0.25 GeV in energy. Since splitoff escapes are more common from charged kaons than they are from charged pions, and tend to have higher energy from kaons, we consider the identities of the tracks in the event when we decide which showers to remove. For events that have charged kaons we remove extra showers less than 0.25 GeV in energy. For events that do not have any charged kaons, we remove extra showers with less than 0.10 GeV in energy.

Not only is it advantageous to generically reconstruct the neutral energy, but it can also be helpful for background rejection to identify the $K_S \rightarrow \pi^+\pi^-$ in the event. The K_S has a $c\tau = 2.68$ cm, therefore, while all other tracks should coincide with the interaction point, tracks created by the decay of a K_S can be displaced several centimeters from the center of the detector. Therefore, all tracks that are not from a K_S should pass strict requirements concerning the reconstructed distance of closest approach to the interaction point. If a $\pi^\pm$ is found that does not coincide with the interaction point, and if it does not appear to belong to a $K_S \rightarrow \pi^+\pi^-$, then we know that the event has not been reconstructed properly. Therefore, the pion tracks in the non-signal D are assigned to golden $K_S \rightarrow \pi^+\pi^-$ candidates with an invariant mass within 0.012 GeV/c^2 of the known K_S mass. No charged pion is used more than once, and preference is given to candidates with invariant mass closest to the K_S mass. The K_S four-vectors of the mass constrained fit of the two pion tracks are used in the missing energy calculation.

The generic reconstruction procedure is repeated for each electron and $\eta^{(\prime)}$ candidate in the event. This means that photons considered extra showers by one candidate may not be by another candidate, and that picking the correct signal candidates provides a better description of the neutrino than picking a false candidate.

Figure 3.5 shows the difference in the reconstructed non-signal D energy and the true non-signal D energy with this new reconstruction method (histogram) and original neutrino reconstruction (black circles). The area of the two distributions are the same.

52
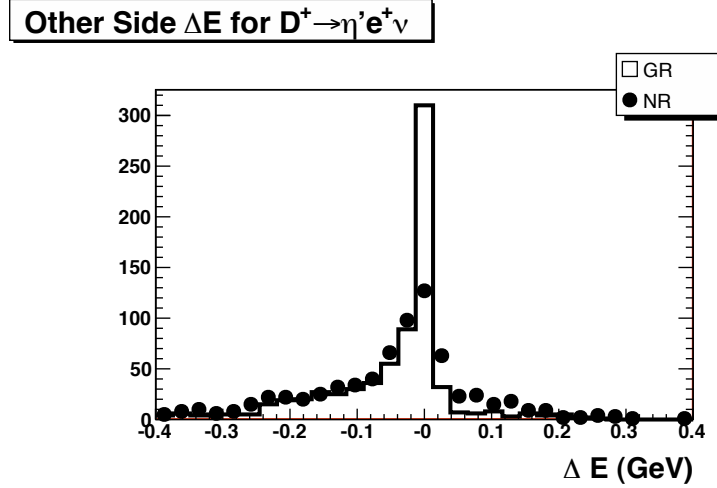
Figure 3.5: The difference between the reconstructed and the true Other Side D energy before the improvements (black circles) and after (histogram).

Many events where the energy was previously reconstructed as too high have had the energy determination greatly improved by removing the extra showers. There is also a smaller number of events that were reconstructed as too low and were improved by using the kinematically fit π^0 and η candidates instead of the sum of the four-vectors of the two showers.

At this point it is important to have an aside and briefly address the case of $K_S \rightarrow \pi^0\pi^0$. Because we only measure shower energies in the calorimeter, we convert the shower energy to photon momentum by assuming that the photon originated from the center of the detector and traveled in a straight line to reach the calorimeter and excite the crystals. In the case of $K_S \rightarrow \pi^0\pi^0$ the four photons created do not originate from the center of the detector. The question is, are these showers reconstructed as two π^0's in the generic reconstruction or are they going to be rejected by the generic reconstruction because they do not originate from the interaction point? The answer is that the displacement of the K_S decay shifts the reconstructed masses of the two π^0's downward, but not catastrophically, and not outside the -5 to 3 mass pull window. The

53

distance the K_S travels before decaying is (2.68 cm)$\beta\gamma$, where $\beta\gamma$ are the usual definitions from special relativity, $\beta = v/c$, $\gamma = 1/\sqrt{1 - \beta^2}$. The maximum displacement occurs with the maximum momentum. The maximum momentum of the K_S's at CLEO-c is approximately 1 GeV/c and corresponds to $\beta\gamma \sim 2$, and a maximum displacement from the interaction point of 5.4 cm. The radial distance from the center of the detector to the barrel of the crystal calorimeter is 1 m. The mass of the two showers is $M_{\gamma\gamma} = \sqrt{2E_1 E_2 (1 - cos(\theta_{12}))}$. At worst, the angle between the two photons is distorted by a factor of (1 m − 5.4 cm)/1 m. This pushes the reconstructed mass down by approximately 7%, or from 135 MeV/c^2 to 125 MeV/c^2. This shift is on the order of 1 σ downward. Note that the distortion in the π^0 momenta from the K_S displacement should be corrected for by using the kinematic fit of the two showers rather than the unconstrained sum of the shower four-vectors.

3.4.3   Hadronic D Mass Pull in Background Suppression

The Generic Reconstruction method makes an impressive improvement in our ability to determine the energy of the other side D meson. According to Figure 3.5 the number of signal events that reconstructed within ±20 MeV of the true energy more than doubled. However, this big improvement in the reconstruction of the other side D does not directly translate into improved signal efficiency. The improvement in the signal D energy determination is not as dramatic, see Figure 3.6. The efficiency and optimization of the neutrino reconstruction requirements are not significantly altered by the improvements. The true advantage that the generic reconstruction has given us is the power of background rejection.

Even though Generic Reconstruction does not make dramatic improvements to the signal D energy, the improvement to the other side D allows us to ask the following question: for a given lepton candidate and signal meson candidate how good is the
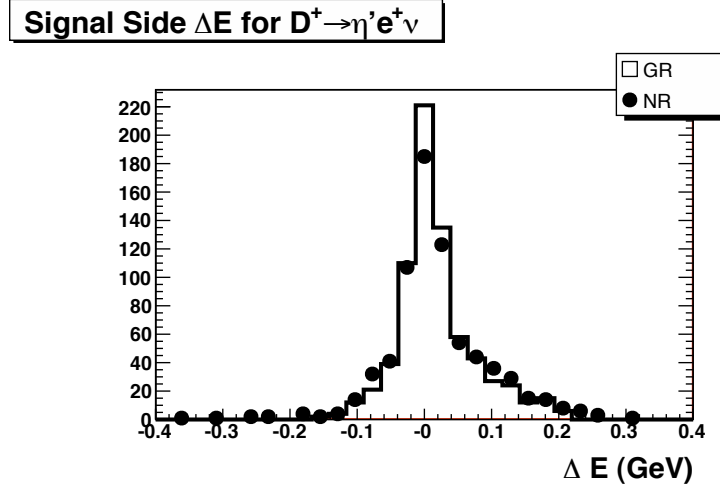
Figure 3.6: The difference between the reconstructed and true signal $D^+ \to \eta'(\pi\pi\eta(\gamma\gamma))e^+\nu_e$ energy before the improvements (black circles) and after (histogram).

hadronically decaying D candidate? To answer this question we sum up the error matrices of all of the particles in the hadronically decaying D (K, π, π^0, η, K_S) and calculate the uncertainty of the D mass calculated from the sum of those four-vectors. With this uncertainty we can calculate the D mass pull, $\chi_m(D) = (M_{measured} - M_D)/\sigma_M$. Events where everything is correctly identified should have a $\chi_m(D)$ between -3 and 3. Figure 3.7 shows the $\chi_m(D)$ distribution when the signal and other side are correctly identified (histogram), when the signal D is incorrectly identified (crosses), and when generic $D\bar{D}$ is mistaken for signal (diamonds).

How should we make use of the other side $\chi_m(D)$? If we required $\chi_m(D)$ to be within ±3 it would remove approximately 50% of our background. However, as is seen in Figure 3.6, the signal D can be reasonably well reconstructed even if the other side D is not. If we required that $\chi_m(D)$ be within ±3 it would remove 40% of our signal. To remove backgrounds without adversely affecting the efficiency we fully reconstruct the semileptonic decays likely to be backgrounds ($\pi e\nu$, $\pi^0 e\nu$, $K e\nu$, $K^* e\nu$, $K^{*0} e\nu$,

Other Side D Pull

Good Signal

Bad Signal

Generic

D Pull Mass
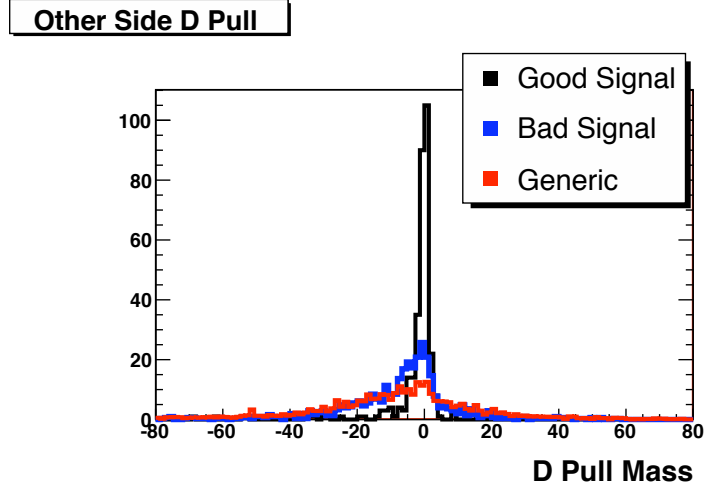
Figure 3.7: The $\chi_m(D)$ of the other side D meson. The histogram shows the distribution when the signal and the other side D are correctly identified, blue shows true $\eta'e\nu$ when either of the D's are incorrectly identified, and the red shows the distribution for generic $D\bar{D}$ misidentified as a semileptonic decay. Each distribution is normalized to have the same area.

$K^0(\pi^+\pi^-)e\nu$, $\rho e\nu$, $\rho^0 e\nu$, $\eta e\nu$, $\eta' enu$), then require that the $D^\pm \rightarrow \eta' e^\pm \nu$ other side D mass pull, $\chi_m(D^\pm \rightarrow \eta' e^\pm \nu)$, is either better than or consistent with the best $\chi_m(\text{Best})$ of all semileptonic candidates. We do this by requiring $\chi^2_m(D^\pm \rightarrow \eta^{(\prime)}e^\pm \nu) - \chi^2_m(\text{Best}) < 9$, where $\chi_m(\text{Best})$ is the D mass pull closest to zero among all of the reconstructed semileptonic decays. By making this requirement, rather than requiring the $\chi_m(D^\pm \rightarrow \eta^{(\prime)}e^\pm \nu)$ to be within ±3, we loose only 10% of our signal rather than 40%, and still remove almost 50% of the backgrounds.

For reference, we show below how the D mass pull, $\chi_m(D)$ is calculated. Each track, K_S, η and π^0 have a 7×7 error matrix where the first 3 indices refer to the momentum vector elements p_x, p_y, and p_z, the fourth is for the particle energy, and the last 3 indices refer to position x,y,z. The error matrices of each daughter particle are added together for the error matrix of the parent D. The uncertainty in the unconstrained mass of the D

is given by

$$\sigma_M^2 = \sum_i \sum_j \frac{\partial M}{\partial X_i} \frac{\partial M}{\partial X_j} E_{i,j}, \tag{3.2}$$

where $E_{i,j}$ is the sum of the 7×7 error matrices of the daughter particles, M is the mass of the collection of particles, and $X = [p_x, p_y, p_z, E, x, y, z]$. The value of the derivatives of M are given by

$$\frac{\partial M}{\partial X_i} = \left[\frac{-p_x}{M}, \frac{-p_y}{M}, \frac{-p_z}{M}, \frac{E}{M}, 0, 0, 0 \right]. \tag{3.3}$$

3.4.4   Quality Binning

The increase in efficiency of the Neutrino Reconstruction method versus the D-Tagging method is partly due to the fact that poorly reconstructed events can still be used. As was shown earlier, if we only used events where the other side D was reconstructed very well, $|\chi_m(D)| < 3$, we would loose 40% of our signal. In order to take full advantage of the improved other side D reconstruction without sacrificing the extra efficiency from poorly reconstructed events, we divide the data into two bins based on the quality of the other side D reconstruction.

Dividing the data into bins such that a portion of the signal is essentially background free increases the overall statistical significance of the measurement. A bin with essentially zero background and a large fraction of the signal can give a statistically significant observation of the decay with only a few events. Or, if there is no sign of a signal, the zero background bin can set a more restrictive 90% upper limit than a bin with backgrounds.

We separate the events into "High Quality" and "Low Quality" bins. The high quality bin contains events where there are no signs of poor reconstruction, and the "Low Quality" bin contains everything else. For example, extra showers that have not been vetoed indicate that there may be missing energy from a K_L or from a lost photon in an $X \to \gamma\gamma$. If any of the π^0 or $\eta \to \gamma\gamma$ candidates do not have a good mass pull that would

indicate that the neutral energy was poorly reconstructed. The $|\chi_m(D)|^2$ is essentially a χ^2 for the hypothesis that the collection of tracks and showers designated as an other side D is actually a D meson. Events where the $|\chi_m(D)|$ is large indicate that there is a problem with the other side D reconstruction. We define the following criteria for high quality events:

1. All showers on the other side D are either in an $X \to \gamma\gamma$ or are vetoed.

2. All $\pi^0 \to \gamma\gamma$ and $\eta \to \gamma\gamma$ must have a mass pull between -5 and 3.

3. The hadronically decaying $D^\pm$ meson must have a beam constrained mass between 1.8629 GeV/c^2 and 1.8729 GeV/c^2. Figure 3.8 shows the other side M_{BC} distribution when both the signal and the other side D are correctly identified. The beam constrained mass requirements were developed for the tagged $D^\pm \to \eta e^\pm \nu$ analysis [32], and we have simply adopted them here. (If this method is applied to decays of neutral D mesons, which have a lower mass than charged D, we instead use the requirements 1.8581 GeV/c^2 and 1.8741 GeV/c^2).

4. We require $|\chi_m(D)| < 3.0$. Figure 3.9 shows the $\chi_m(D)$ distribution when both the signal and other side D are correctly identified.

Events in the high quality bin are essentially D tags that have not been as thoroughly optimized as the specific tags used in a CLEO-c D tagging analysis. In the tagged $D^\pm \to \eta e^\pm \nu$ analysis, [32] each tag had the ΔE requirements individually optimized for both reconstruction resolution and background rejection. The high quality bin of the generic reconstruction method has replaced the specialized ΔE requirements with the generic $|\chi_m(D)| < 3$ requirement. The $|\chi_m(D)| < 3$ is automatically optimized for the expected resolution of the decay, but not necessarily for background rejection. Though the high quality bin is not as well optimized for the specific decays used in the D tagging analysis, it instead has some efficiency for reconstructing nearly all fully visible hadronic
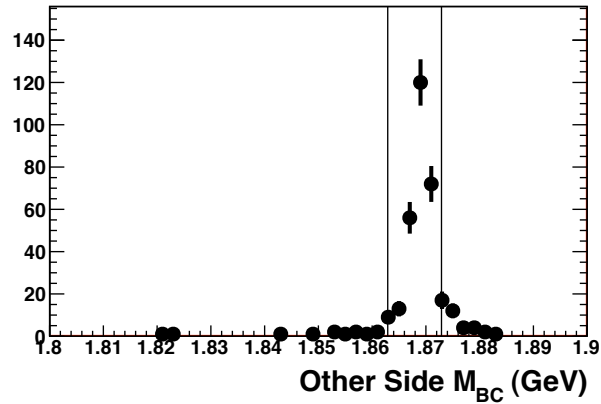
Figure 3.8: The other side beam constrained mass (M_{BC}) when the contents of both signal and other side D are correctly identified. The vertical lines show the region of M_{BC} required for the high quality bin.
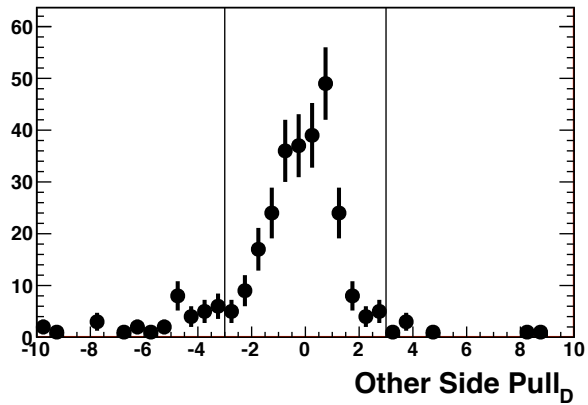
Figure 3.9: The $\chi_m(D)$ of the other side D meson when the contents of both the signal and other side D are correctly identified. The vertical lines show the region of $\chi_m(D)$ required for the high quality bin.

D decays. We therefore use the high quality bin not only to maximize the statistical significance of our semileptonic measurements but also to attempt to measure all of the hadronic D decays.

3.5   Measurement of the Hadronic D Branching Fractions

The efficiency of any CLEO-c analysis that places requirements on the entire event depends on how the non-signal D decays. A simple example of this is if we require that there is only 1 electron in the entire event. The efficiency of such a requirement is proportional to the inclusive branching fraction of D decays with no electrons.

In an analysis of exclusive semileptonic decays we require that the energy and momentum of everything except the neutrino is reconstructed. Different types of decays have different efficiencies for sufficiently reconstructing the entire energy and momentum of the non-signal D. For example, in the D-Tagging analysis the efficiency for reconstructing a semileptonic event when the non-signal D decays to $K^+\pi^-\pi^-\pi^0$ is only 50% of the efficiency when the non-signal D decays to $K^+\pi^-\pi^-$, [32]. Similarly, if we reproduce a Neutrino Reconstruction analysis similar to [33] we find that the efficiency for reconstructing $D^+ \rightarrow K_S(\pi^+\pi^-)e^+\nu$ when the non signal D is $D^- \rightarrow K^+\pi^-\pi^-\pi^0$ is approximately 70% of the efficiency when the non signal D is $D^- \rightarrow K^+\pi^-\pi^-$. Additionally, the non-signal decay $D^- \rightarrow K^+\pi^-\pi^-\pi^0\pi^0$ is only 40% as efficient as the non-signal decay $D^- \rightarrow K^+\pi^-\pi^-$. Clearly, the efficiency for reconstructing the signal depends on how the non signal D decays. The Monte Carlo simulation may therefore incorrectly predict the efficiency if the hadronic branching fractions are not correct.

In this analysis the systematic uncertainties associated with how the non-signal D decays are controlled by measuring all of the individual $D \rightarrow fully\ visible$ branching fractions with an automated procedure. As is shown in the following section, the generic reconstruction algorithm makes this task possible. This approach not only provides this

analysis with useful reweights, but also maximize the physics output of the endeavor and may impact many other analysis by potentially measuring other branching fractions that have been previously unknown. There is also the potential to see completely unexpected hadronic D decays that may not otherwise have been discovered.

3.5.1 Hadronic Branching Fraction Measurements

The systematic uncertainties associated with the hadronic branching fractions are controlled by measuring all of the hadronic branching fractions. Under other circumstances this would have been a tremendous undertaking for an analysis geared toward measuring semileptonic decays. However, the Generic Reconstruction algorithm that was developed to improve neutrino resolution and combat backgrounds in $D^{\pm} \rightarrow \eta'(\rho^0\gamma)e^{\pm}\nu$ is also an ideal tool to perform this study.

In order for the generic reconstruction algorithm to function, it requires that the contents of one of the D mesons is already identified before it can generically reconstruct the other D in terms of $\pi^{\pm}$, $K^{\pm}$, $K_S \rightarrow \pi\pi$, π^0 and $\eta \rightarrow \gamma\gamma$. Therefore, to study the hadronic decays, we simply replace the semileptonic candidate with a well understood D-tag. Rather than require that the event is consistent with one neutrino, we require that the event is consistent with no neutrinos. We require that the event has no electrons and that it is consistent with no missing energy. The generic reconstruction algorithm determines the number of each type of daughter that it can find in the remaining tracks and showers in the event, and most of the backgrounds are removed by using the high quality criteria.

The next step is to understand both the efficiency to reconstruct each decay mode correctly and the expected backgrounds for each decay. The efficiency is determined by the Monte Carlo simulaiton and is simply the number of correctly reconstructed decays of type i in a Monte Carlo sample divided by the number of decays of type i that were

generated. However, the backgrounds in each decay mode are directly related to the branching fractions that we are trying to measure. For example a K^0 can be reconstructed as $K_S \rightarrow \pi^+\pi^-$, $\pi^+\pi^-$, or $\pi^0\pi^0$ depending on the K^0 decay mode and the distance it traveled before decaying. Therefore, the decays $D^+ \rightarrow \pi^+\pi^+\pi^-$ and $D^+ \rightarrow \pi^+\pi^0\pi^0$ both have background contributions from $D^+ \rightarrow \pi^+ K^0$. If the $D^+ \rightarrow \pi^+ K^0$ branching fraction is unknown then we cannot know the amount of background in $D^+ \rightarrow \pi^+\pi^+\pi^-$ or $D^+ \rightarrow \pi^+\pi^0\pi^0$.

In order to properly account for backgrounds in all decay modes we simultaneously solve for all of the hadronic branching fractions. We do this by constructing a cross feed matrix, A_{ij}, from our Monte Carlo sample. The elements of the matrix A_{ij} are given by:

$$A_{ij} = N_{TAG}(MC)\mathcal{B}_{MC}(i)\mathcal{E}_j(i), \tag{3.4}$$

where $N_{TAG}(MC)$ is the number of signal side tags found in the Monte Carlo simulation, $\mathcal{B}_{MC}(i)$ is the branching fraction for decay i programmed into the Monte Carlo simulation, and $\mathcal{E}_j(i)$ is the efficiency for reconstructing generated decay mode i as the final state j. For example, the background in $D^+ \rightarrow \pi^+\pi^+\pi^-$ is related to $\mathcal{E}_{\pi^+\pi^+\pi^-}(\pi^+ K^0)$. The A_{ij} matrix is related to the branching fractions by the equation

$$\frac{N_{TAG}(DATA)}{N_{TAG}(MC)}\begin{pmatrix} A_{1,1} & A_{1,2} & \cdots & A_{1,N} \\ A_{2,1} & A_{2,2} & \cdots & A_{2,N} \\ \cdots & \cdots & \cdots & \cdots \\ A_{N,1} & A_{N,2} & \cdots & A_{N,N} \end{pmatrix}\begin{pmatrix} W_1 \\ W_2 \\ \cdots \\ W_N \end{pmatrix} = \begin{pmatrix} D_1 \\ D_2 \\ \cdots \\ D_N \end{pmatrix} - \begin{pmatrix} C_1 \\ C_2 \\ \cdots \\ C_N \end{pmatrix} - \begin{pmatrix} BT_1 \\ BT_2 \\ \cdots \\ BT_N \end{pmatrix},$$

$$\tag{3.5}$$

where $W_i = \mathcal{B}_{DATA}(D \rightarrow X_i)/\mathcal{B}_{MC}(D \rightarrow X_i)$, D_i is the number of data events reconstructed as decay i, C_i is the continuum background (typically very small), and BT_i is the background from bad initial tags (also typically very small). The weight W_i is the weight that needs to be applied to every $D \rightarrow X_i$ decay in the Monte Carlo sample to match the number produced in data.

The vector of weights, W_i, is solved for by multiplying the vector of background subtracted data by the inverse of the cross feed matrix. There is no need to fit a distribution to obtain a constraint on the expected backgrounds, because each A_{ii} element helps to constrain the background from decay mode i in all the other decay modes.

The statistical uncertainty in the weight is found by

$$\sigma_{W_i} = \frac{W_i}{\sqrt{\sum_j S_{ij}^2/(D_j)}}, \tag{3.6}$$

where W_i is the weight to be applied to the Monte Carlo branching fraction, $S_{ij} = \frac{N_{TAG}(DATA)}{N_{TAG}(MC)} W_i A_{ij}$, and D_j is the number of events measured in reconstructed mode j. The branching fraction of decay mode j is simply W_j multiplied by the branching fraction of mode j in the Monte Carlo simulation.

The absolute branching fractions of all decays determined by this method are proportional to $\frac{N_{TAG}(DATA)}{N_{TAG}(MC)}$. The main goal of this study is to measure branching fractions that have not been measured before or are not well known. Therefore, in order to reduce systematic uncertainties in this measurement the value of $\frac{N_{TAG}(DATA)}{N_{TAG}(MC)}$ is calibrated using previous measurements of $\mathcal{B}(D^+ \rightarrow K^-\pi^+\pi^+)$ for charged D decays, and $\mathcal{B}(D^0 \rightarrow K^-\pi^+)$ for neutral D decays. For this paper we use the most recent CLEO-c measurements of $\mathcal{B}(D^+ \rightarrow K^-\pi^+\pi^+) = 9.14\% \pm 0.20\%$ and $\mathcal{B}(D^0 \rightarrow K^-\pi^+) = 3.891\% \pm 0.070\%$.

3.6 Absolute Scale Calibration using $D^+ \rightarrow K^-\pi^+\pi^+$

The ultimate goal of this analysis is to convert the signal yields of $D^+ \rightarrow \eta^{(\prime)}e^+\nu$ to absolute branching fractions. If we define our signal efficiency (ϵ) as the number of signal events reconstructed ($N_{D^+\rightarrow SIG}$) divided by the total number in the data set, then we determine our absolute branching fractions by $\mathcal{B} = N_{D^+\rightarrow SIG}/(\epsilon N_{D^+D^-})$, where $N_{D^+D^-}$ is the number of D^+D^- in the data set. Historically Neutrino Reconstruction follows this method using the most accurate measurement of $N_{D^+D^-}$ available. However, using

the most accurate determination of $N_{D^+D^-}$ is not necessarily the best way to determine the absolute branching fractions. We can reduce the size of the systematic uncertainties in the absolute branching fractions if we measure $N_{D^+D^-}$ such that the systematic uncertainties are correlated with and the same size as the systematic uncertainties in the efficiency corrected signal yields. This is implicitly what the D-tagging analysis does by using the number of single tags instead of $N_{D^+D^-}$.

It is important to understand how $N_{D^+D^-}$ was measured for the previous CLEO-c Neutrino Reconstruction [33] and other CLEO-c "Untagged" analyses. The following discussion is based on the method used in [39] to determine $N_{D^+D^-}$. First, it should be clear that only a D-tagging analysis can determine an absolute branching fraction without relying on previous branching fraction measurements. Any measurement of $N_{D^+D^-}$ is anti-correlated with at least one absolute branching fraction. For example the value of $N_{D^+D^-}$ used in [33] was 60% anti-correlated with $\mathcal{B}(D^+ \rightarrow K^-\pi^+\pi^+)$, 48% anti-correlated with $\mathcal{B}(D^+ \rightarrow K_S\pi^+)$, and anti-correlated with several other hadronic branching fractions. Either an absolute branching fraction must already be known very well, or the branching fractions and $N_{D^+D^-}$ must be determined simultaneously. In [39] $N_{D^+D^-}$ was determined by performing a simultaneous fit for $N_{D^+D^-}$ and 6 hadronic branching fractions. This was done by using both "single tagged" and "double tagged" events. Single tagged events have one D-tag and no requirements on the other D decay in the event, which makes the efficiency for reconstructing a single tag independent of how the generic D decays . Double tagged events have both D^+ and D^- described by a tag. The double tag events are subsets of the single tagged events. Let y_i be the raw number of single tag events with decay i and let ϵ_i be the efficiency for single tagging decay i. Let y_{ij} be the raw number of double tagged events where one D is decay i and the other D is decay j and let ϵ_{ij} be the efficiency for reconstructing both tags at the same time. We

may write the following relations:

$$y_i = N_{D^+D^-} \epsilon_i \mathcal{B}_i, \tag{3.7}$$

$$y_{ij} = N_{D^+D^-} \epsilon_{ij} \mathcal{B}_i \mathcal{B}_j, \tag{3.8}$$

$$N_{D^+D^-} = \frac{y_i y_j \epsilon_{ij}}{y_{ij} \epsilon_i \epsilon_j}, \tag{3.9}$$

$$B_i = \frac{y_{ij} \epsilon_j}{y_j \epsilon_{ij}}, \tag{3.10}$$

$$N_{D^+D^-} = \frac{y_i}{\epsilon_i \mathcal{B}_i}. \tag{3.11}$$

The efficiencies are determined from the Monte Carlo simulation and we measure y_i for several types of i and y_{ij} for all combinations of the i decays. The branching fractions $\mathcal{B}_i$ and $N_{D^+D^-}$ are parameters in a simultaneous fit to the measured values of y_i and y_{ij}. All of the branching fractions are correlated with one another and anti-correlated to $N_{D^+D^-}$. If $N_{D^+D^-}$ decreases the absolute branching fractions increase to compensate.

This method gives an accurate determination of $N_{D^+D^-}$. However, as mentioned previously we don't want an accurate determination of $N_{D^+D^-}$, we want one that has the same systematic uncertainties as the signal yields. We see from Equation 3.11 that $N_{D^+D^-}$ can be obtained from one single tag yield if the branching fraction for that decay is very well known. Therefore, to obtain our systematically correlated $N_{D^+D^-}$ we reconstruct a single tag for D^+ and use Generic Reconstruction on the rest of the event. In order to make certain that the tag yield systematic uncertainties are the same as the $D^+ \rightarrow \eta' e^+ \nu$ systematic uncertainties we require that the missing energy is consistent with zero and that the number of electrons is zero.

Ideally we would measure several D^+ tag yields using Generic Reconstruction and then use independent previously measured branching fractions of those D^+ tags to determine the best value for $N_{D^+D^-}$. However, most of the branching fraction measurements for D^+ are correlated with $D^+ \rightarrow K^- \pi^+ \pi^+$ which diminishes the benefit of using multiple decays to calibrate $D^\pm \rightarrow \eta' e^\pm \nu$. So, for this statistically limited analysis

where our main goal is to remove systematic uncertainties from poorly known decays, it is sufficient to just use the $D^+ \to K^-\pi^+\pi^+$ Generic Reconstruction yields and use the absolute branching fraction for this decay determined in the double tag fit. By doing this our measurement of $\mathcal{B}(D^+ \to \eta'e^+\nu)$ is really a measurement of the ratio $\mathcal{B}(D^+ \to \eta'e^+\nu)/\mathcal{B}(D^+ \to K^-\pi^+\pi^+)$, and can potentially improve as the measurement of $\mathcal{B}(D^+ \to K^-\pi^+\pi^+)$ improves.

It should be noted that our dependence on $\mathcal{B}(D^+ \to K^-\pi^+\pi^+)$ is not unique to this calibration method or to Generic Reconstruction. It has unfortunately been neglected in the literature that all untagged CLEO-c studies that have used $N_{D^+D^-}$ are also highly correlated with the value of $\mathcal{B}(D^+ \to K^-\pi^+\pi^+)$, and this fact should be taken into account when CLEO-c values are averaged with other experiments in the PDG.

EVENT SELECTION

This chapter provides the event selection criteria used to reconstruct the hadronic decays and the different decay modes of $\eta e^{\pm}\nu$ and $\eta' e^{\pm}\nu$. We describe the electron identification, the generic requirements applied to all hadronic decays, the generic requirements applied to all semileptonic decays, and the requirements specific to each decay mode.

4.1 Electron Identification

The curvature of a track in the drift chamber gives us the track momentum and the RICH and dE/dx (ionization) information can help us to determine the mass of the particle that created the track. In addition to these clues that are available to identify all of the charged particles we can also take advantage of the fact that the electron deposits nearly all of its energy in the electromagnetic calorimeter (CC) and use $E_{CC}/|\vec{p}c| \sim 1$. In this analysis all of these pieces of information are used by the Rochester Electron Identification Package (REId) [45] to identify tracks as electrons. This package combines information about the track and the showers matched to the track in order to form an electron likelihood, F. The likelihood F ranges between 0 and 1, where 0 indicates a track least likely to be an electron, and 1 indicates a track most likely to be an electron. Tracks passing the above quality criteria and having $F > 0.8$ are considered electrons. The identification efficiency (measured in data) above $p_e = 300$ MeV/c is greater than 90% and above $p_e = 500$ MeV/c is greater than 96%. The probability that a hadron is misidentified as an electron is less than 0.8%.

In addition to the REId likelihood requirements we also require that the candidate electron track also pass the following set of track quality criteria:

1. electron track is Trkman approved.

2. electron track was fit to an electron hypothesis and the fit did not abort.

3. electron track momentum > 0.200 GeV/c.

4. electron track $|cos(\theta_z)| < 0.9$.

Electron identification occurs differently for data than for the Monte Carlo sample. The same track quality criteria listed above is also applied to the Monte Carlo tracks. However, rather than using the REId package on the Monte Carlo tracks we identify electrons based on truth table information, and then throw random numbers such that the efficiency for identifying the electron is the same as the REId efficiency in data. In the analysis we require that there is only one electron in the event in order for it to be used. This means that the rate that we loose events by having a fake lepton and a true lepton at the same time is not accounted for by only using true electrons. To fix this, we calculate the probability of having one of the non-electron tracks falsely identified as an electron, and cut out the appropriate number of events that we would expect to have more than one track identified as an electron.

4.2 Generic D Reconstruction

This section describes the generic reconstruction procedure used in both semileptonic and fully hadronic events. Keep in mind that as far as the generic reconstruction is concerned the procedure for events used to measure all of the hadronic branching fractions is the same as the procedure to reconstruct the $D^+ \rightarrow K^-\pi^+\pi^+$ yield that is used to convert the $D^\pm \rightarrow \eta' e^\pm \nu$ yield to a branching fraction. Once the event has been reconstructed the fully hadronic events used to determine the hadronic branching fractions have additional quality requirements described in following sections. However, in this stage of the analysis all of the fully hadronic events are handled in the same way.

The first step of the Generic Reconstruction is to designate which tracks and showers belong to the signal D and which should be considered part of the other side D. Identifying a suitable signal D first helps to increases the probability that the π^0's, $\eta \to \gamma\gamma$'s, and $K_S \to \pi^+\pi^-$'s made out of whatever tracks and showers remain correspond to real particles. When using generic reconstruction on semileptonic events the tracks and showers that belong to the signal D are the electron candidate and the tracks and showers in the $\eta^{(\prime)}$ candidate. When reconstructing a fully hadronic event the signal tracks and showers are taken from a D-tag. From the remaining tracks and showers the generic reconstruction algorithm generates the best list of π^0's, $\eta \to \gamma\gamma$, and $K_S \to \pi\pi$ to describe the other side D. Extra showers that were not assigned to a π^0 or an $\eta \to \gamma\gamma$ are considered for removal.

The remaining trkman-approved tracks that are not part of other side K_S's are identified as either a pion or a kaon by calculating the probability for the track to be either type of particle from the RICH and dE/dx (ionization) information. The particle identification also takes into consideration the multiplicity of kaons and pions as a function of momentum as predicted by the Monte Carlo simulation. For example, if according to dE/dx and RICH information a particle is barely more likely to be a kaon rather than a pion, it is labeled a pion because they occur more often than a kaon.

We attempt to assign all splitoff-approved showers not used by the signal side to a $\pi^0 \to \gamma\gamma$ or $\eta \to \gamma\gamma$ candidate. The π^0 candidates are generated out of pairs of showers where the minimum shower energy is greater than 30 MeV and the mass pull is between -25 and 15. The $\eta \to \gamma\gamma$ candidates are generated out of pairs of showers where the minimum shower energy is greater than of 50 MeV and mass pull between -15 and 15. There is a tighter range in $\eta \to \gamma\gamma$ candidates than in π^0 candidates because there is an enormous combinatorics rate, with very few true η, that significantly slows the data processing.

Any showers that have not been assigned to a π^0 or an η candidate are potentially splitoff escapes and are considered for removal from the list of other side D daughters. Whether or not an extra shower is removed depends on the shower energy and the identity of tracks in the event. If there is a kaon in the event, either on the signal side or the other side, we veto any extra showers with energy below 250 MeV. If there are no kaons in the event we veto any extra showers below 100 MeV. The reason for this is that events with charged kaons are more likely to have splitoff escapes and tend to create higher energy splitoff-escapes than events without kaons.

The four-vectors of the mass constrained kinematically fit π^0, η, and K_S candidates are used in the total missing energy calculation rather than the four-vectors of the individual showers and tracks. The error matrices of the other side K_S's, π^0's, η's, K's, and π's are summed and used to calculate the mass pull for the other side D.

4.3 Generic Semileptonic Requirements

This section describes the set of requirements made of all semileptonic event candidates.

1. There is only one track in the event identified as an electron. Events that have more than one lepton are likely to have more than one neutrino, so we veto events with multiple electrons.

2. The total charge from all of the trkman approved tracks in the event is equal to zero. The D^+D^- has zero net charge, so if the charge is not zero then we either have extra or missing tracks in the event.

3. The beam constrained mass of both the signal and other side D's is greater than 1.79 GeV/c^2. This exact number is somewhat arbitrary. We determine the signal yields by performing a fit on the histogram of M_{BC}^{sig} and the end of the histogram must extend low enough to offer a good "lever arm" or constraint for determin-
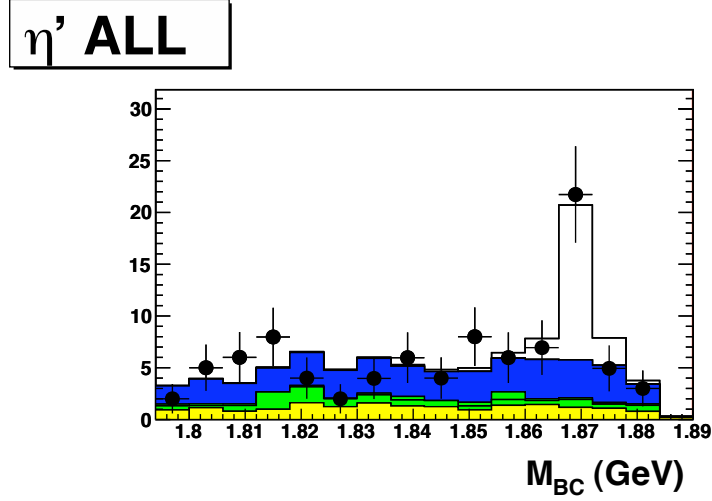
Figure 4.1: The beam constrained mass of $D^+ \rightarrow \eta' e^+ \nu$. The lower limit of 1.79 GeV/c^2 is sufficient to provide a signal free region to normalize the backgrounds.

ing the background levels. Figure 4.1 shows one of the beam constrained mass distributions and demonstrates that the 1.79 GeV/c^2 requirement is sufficient to determine the background levels.

4. The missing energy (E_{miss}) must be greater than 50 MeV. Events that appear to have more energy than the available beam energy ($E_{\mathrm{miss}} < 0$) could still pass a $M_{miss}^2 = E_{\mathrm{miss}}^2 - P_{\mathrm{miss}}^2$ requirement since the sign of the energy does not affect the calculation.

5. The sum of the energy of all splitoff-approved showers vetoed by the Generic Reconstruction must be less than 300 MeV. More vetoed shower energy than this could indicate that the generically reconstructed missing energy may not have correctly identified the true π^0's and η's. Consider the situation of a bad candidate having a smaller $|\chi_m|$ than a true candidate. In this situation all of the $X \rightarrow \gamma\gamma$ could be incorrectly identified, and leave true showers unassigned to a π^0 or η. The signature of this would be a large amount of energy from vetoed showers.

6. The angle between the neutrino and the beam axis must satisfy $|cos(\theta_\nu)| < 0.9$. This requirement ensures that the neutrino candidate is not actually another type of particle that went outside the detector fiducial range and was not detected.

7. Events are vetoed if there is evidence of a photon conversion $\gamma \rightarrow e^+e^-$, or of a $\pi^0 \rightarrow e^+e^-\gamma$ decay in the event. We have already required that the number of electrons in the event is 1, but electrons are only identified with confidence if their momentum is greater than 200 MeV/c. The primary source of continuum backgrounds are fake semileptonic events where the signal lepton is from one of these two sources, and the second electron is below the 200 MeV/c momentum cutoff and so not identified as an electron. We search for tracks that have a dE/dx consistent with an electron, opposite charge of our signal electron, and momentum less than 200 MeV/c. We do not require the track to be trkman approved. We also look for combinations of this track with the signal lepton and all splitoff approved showers in the event. If either the mass of the signal electron and a track is less than 100 MeV/c^2, or if the mass of the electron, track, and a shower is within 50 MeV/c^2 of the π^0 mass, we veto the event.

8. We veto candidates that appear to have a "wrong sign K". We require that if there is only one kaon on the other side, no $K_S \rightarrow \pi^+\pi^-$ candidates, and at least one other side pion, then that kaon must have the same charge as the signal side e. This should be true in almost all cases, whether we have a semileptonic decay from a D^+ or a D^0. Only rare doubly cabbibo suppressed decays do not follow this pattern. Further, in events where there are two kaons, 1 pion, and no K_S, we require that the pion has a charge opposite that of the signal side electron.

9. We require that the other side D found with this semileptonic candidate is consistent with the best other side D for all reasonably well-reconstructed semileptonic candidates. We explicitly reconstruct the semileptonic decays $\rho e\nu$, $\rho^0 e\nu$,

πev, $\pi^0 ev$, $K ev$, $K_S(\pi^+\pi^-)ev$, ηev, $\eta' ev$, $K^* ev$, $K^{*0} ev$. We find the candidate with $|\chi_m(D)|$ closest to zero out of all of these different semileptonic decays that have a signal side δE within ± 0.15 GeV of zero, and a $M^2_{miss}/(E_{miss} + P_{miss})$ within ± 0.15 GeV of zero. We require that the other side D mass pull of our $\eta^{(')} ev$ signal candidate (C) be within 3σ of the best other side D mass pull of all candidates by imposing $\chi^2_m(C) - \chi^2_m(\text{Best}) < 3^2$.

10. We require that all other side tracks that are not part of a K_S candidate pass a stricter set of track quality requirements than trkman approval:

    (a) We require strict d^0 and z^0 requirements, where d^0 is the distance of closest approach of the track fit to the center of the detector in the x-y plane, while z^0 is the distance along the z axis from the center of the detector. We require that $|d^0|$ be less than 0.5 cm, and that z^0 be less than 5 cm.

    (b) We require that at least 50% of the drift chamber layers traversed by the track have hits associated with that track.

    (c) We require that the track momentum is greater than 50 MeV/c and less than 2 GeV/c.

    (d) We require that the cosine the track momentum makes with the z axis be less than 0.93. This requirement ensures that the track went through enough of the drift chamber to be properly reconstructed.

11. The pion tracks on the signal side D must satisfy the "signal pion" criteria adopted from [33]. The "signal pion" criteria uses dE/dx and RICH information to select tracks that are consistent with being a pion. The dE/dx must be within 3 standard deviations of the expected value for a pion. For pion candidates in the momentum range 650 MeV/c to 750 MeV/c the dE/dx must be more consistent with a pion than a kaon. For tracks greater than 750 MeV/c, if RICH information is available,

and the number of RICH photons are greater than 3, we require that the RICH data is at least one standard deviation closer to a pion than a kaon. Finally, the track must not be part of a $K_S \rightarrow \pi^+ \pi^-$.

4.4 Generic Hadronic Event Requirements

This section describes the requirements that are applied to all events that are reconstructed as being purely hadronic. Many of these requirements are similar to the requirements in the semileptonic candidates and are made for the same reasons. This not only includes tags used to determine the hadronic branching fractions, but also the $K\pi\pi$ signal that is used to normalize the semileptonic measurements.

1. We require that there are no tracks in the event identified as an electron.

2. The total charge of trkman-approved tracks is required to be zero.

3. We require that the absolute value of the missing energy is less than 100 MeV/c to reduce backgrounds from decays with neutrinos or missing daughter particles.

4. The total energy of vetoed splitoff-approved showers is required to be less than 300 MeV/c.

5. For $D^{\pm}$ candidates with one kaon, no $K_S \rightarrow \pi^+ \pi^-$, and one or more charged pions, we require that the charge of the kaon is opposite the charge of its parent D. This is true for all charged D except for the rare doubly cabibbo-suppressed modes. And for decays with two charged K, no K_S, and one π the charge of the π must be equal to the charge of the D. For D^0 candidates, we only used D^0 tags with one kaon, then events with an other side that contains one kaon, one or more pions, and no K_S we require the charge of the other side kaon to be opposite the charge of the kaon in the tag.

6. We require that all other side tracks that are not part of a $K_S \rightarrow \pi^+\pi^-$ candidate pass the same requirements as in the semileptonic candidates.

The following additional requirements are made to events that are used to determine the branching fractions of the generically reconstructed hadronic modes.

1. We require that other side tracks have a dE/dx within 3 standard deviations of the particle identification assigned to it.

2. We require all splitoff-approved showers from the other side D are either vetoed or assigned to an η or π^0.

3. We require the other side D mass pull is within ±3.

4. All π^0 and $\eta \rightarrow \gamma\gamma$ candidates are required to have a mass pull within ±3.

5. $|\Delta E| < 100$ MeV.

6. To remove backgrounds from $K_S \rightarrow \pi^0\pi^0$ from decays with multiple π^0 we reject events containing pairs of other side π^0's with an invariant mass within 30 MeV/c^2 of the K_S.

7. For neutral D decays we require the beam constrained mass of both the tag D and the generically reconstructed D to be between 1.8581 GeV/c^2 and 1.8741 GeV/c^2. For charged D we require that the beam constrained mass is between 1.8629 GeV/c^2 and 1.8789 GeV/c^2. These are the same beam constrained mass requirements used on D tags in the D-Tagged $D^\pm \rightarrow \eta e^\pm \nu$ analysis.

8. The D tag is required to have a mass pull within ±3.

4.5 Missing Mass Requirements

For the purpose of this study the mass of the neutrino is zero. Therefore, if the missing four-vector is from a neutrino, the missing mass squared ($M^2_{\text{miss}} = E^2_{\text{miss}} - P^2_{\text{miss}}$)

should be consistent with zero. Rather than directly place requirements on M^2_{miss} we instead impose restrictions on the parameter $V = M^2_{\mathrm{miss}}/(E_{\mathrm{miss}} + P_{\mathrm{miss}})$. The V parameter is theoretically motivated by the uncertainty in the square of the missing mass. If the missing four-vector is from a single neutrino then the uncertainty in M^2_{miss} reduces to $\delta M^2_{miss} = 2E_{miss}\sqrt{(\delta E_{miss})^2 + (\delta P_{miss})^2}$. The uncertainty in the missing energy and momentum is difficult to calculate because it depends on how well you have identified discrete quantities like the mass of the tracks and the number of daughter particles. The number of standard deviations that M^2_{miss} is away from zero is proportional to $M^2_{\mathrm{miss}}/(2E_\nu)$. The missing energy and momentum have nearly the same resolution (Figure 4.2) and the best estimate of the true neutrino energy is the average of the missing energy and the missing momentum magnitude ($(E_{\mathrm{miss}} + P_{\mathrm{miss}})/2$). This gives us the V parameter.

4.6 $D^{\pm}\eta e^{\pm}\nu$ Requirements

This section describes the requirements that are placed on the different decay modes of the η in the $D^{\pm} \rightarrow \eta e^{\pm}\nu$ analysis. Three of the η decay modes are reconstructed: $\eta \rightarrow \gamma\gamma$, $\eta \rightarrow \pi^+\pi^-\pi^0$, $\eta \rightarrow \pi^0\pi^0\pi^0$. Each requirement listed below has been tuned to maximize the $S^2/(S + B)$ assuming $\mathcal{B}(D \rightarrow \eta e\nu) = 3.0 \times 10^{-4}$, the value found by the previous D-Tagging analysis. Each decay mode has requirements on the invariant mass of the η candidate ($M(\eta)$), the mass pull of the η candidate ($\chi_m(\eta)$), the V-cut, the signal side ΔE^{sig}, and the other side ΔE^{OS} are summarized in Table 4.1. Each decay mode also has requirements that are unique to its topology.

For $\eta \rightarrow \gamma\gamma$ we make additional requirements of the two showers. π^0 are much more common than η and we reject the $\eta \rightarrow \gamma\gamma$ if either of the showers could instead be described as part of a π^0. We require that neither of the two showers can be included in
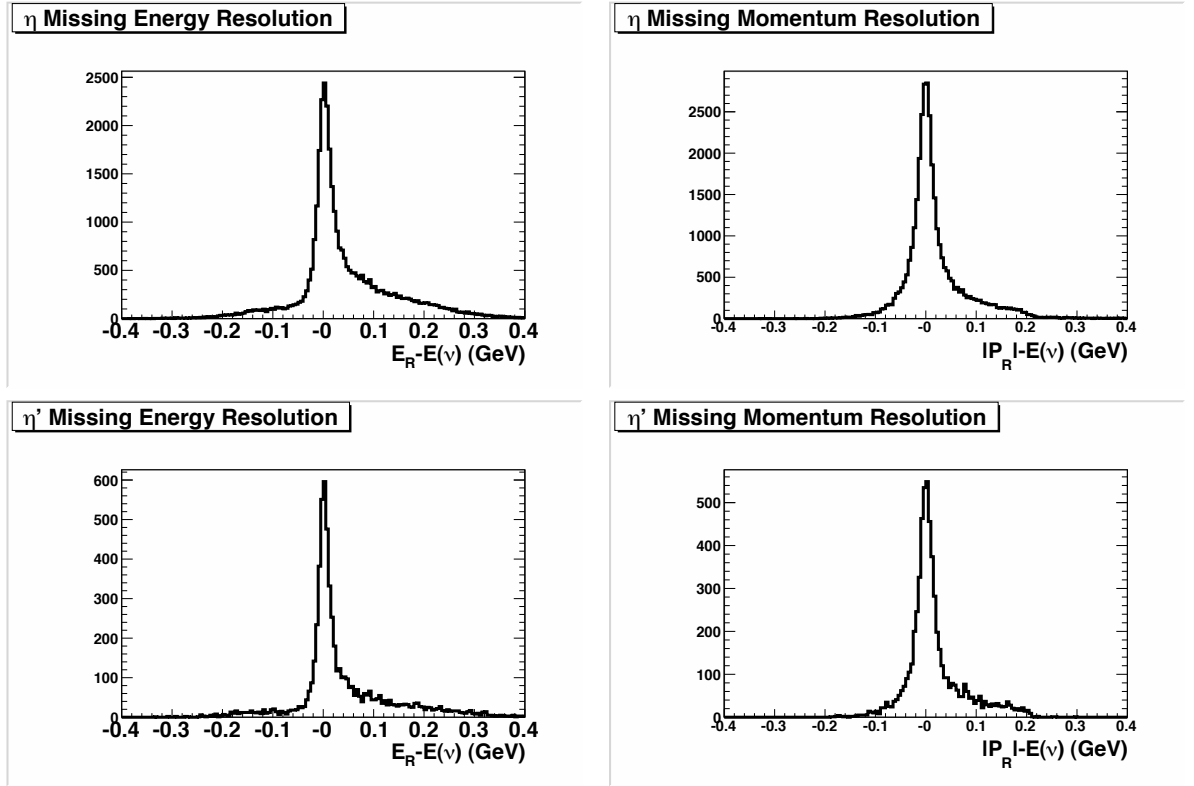
Figure 4.2: The missing energy and missing momentum distributions for $\eta e\nu$ and $\eta' e\nu$.

Table 4.1: The common requirements for the different η decay modes used in the $D^\pm \rightarrow \eta e^\pm \nu$ analysis .

Variable	$\eta \rightarrow \gamma\gamma$	$\eta \rightarrow \pi^+\pi^-\pi^0$	$\eta \rightarrow \pi^0\pi^0\pi^0$
$M(\eta)$	(495 to 580) MeV/c^2	(535 to 560) MeV/c^2	(535 to 560) MeV/c^2
$\chi_m(\eta)$	-4 to 3	-3 to 3	-3.5 to 3
V-cut	(-140 to 140) MeV	(-140 to 140) MeV	(-140 to 140) MeV
Signal ΔE	(-80 to 130) MeV	(-100 to 100) MeV	(-110 to 100) MeV
non-Signal ΔE	(-320 to 350) MeV	(-300 to 350) MeV	(-350 to 300) MeV

77

a π^0 candidate with $|\chi_m(\pi^0)| < 5$. The efficiencies for the $D \to \eta(\gamma\gamma)e\nu$ decay mode are listed in Table 4.2.

For the $\eta \to \pi^+\pi^-\pi^0$ we require that the unconstrained mass of the $\pi^0 \to \gamma\gamma$ candidate is between 100 MeV/c^2 and 150 MeV/c^2, and that it is within 3 standard deviations of the nominal π^0 mass . The efficiencies for $D^\pm \to \eta(\pi^+\pi^-\pi^0)e^\pm\nu$ are given in Table 4.3.

For the decay mode $\eta \to \pi^0\pi^0\pi^0$ we require that the unconstrained mass of each $\pi^0 \to \gamma\gamma$ candidate is between 100 MeV/c^2 and 150 MeV/c^2, and is between -3.5 and 2.5 standard deviations of the nominal π^0 mass . The efficiencies for $D^\pm \to \eta(\pi^0\pi^0\pi^0)e^\pm\nu$ are given in table 4.4.

4.7 $D^\pm \to \eta'e^\pm\nu$ Requirements

This section outlines requirements applied to the different decay modes that are used in the $D^\pm \to \eta'e^\pm\nu$ reconstruction. We reconstruct the η' candidates using the decay modes $\eta' \to \gamma\gamma$, $\eta' \to \pi^+\pi^-\eta(\gamma\gamma)$, $\eta' \to \pi^+\pi^-\eta(\pi^+\pi^-\pi^0)$, $\eta' \to \pi^+\pi^-\eta(\pi^0\pi^0\pi^0)$, $\eta' \to \pi^0\pi^0\eta(\gamma\gamma)$, and $\eta' \to \rho^0(\pi^+\pi^-)\gamma$. The $\eta' \to \rho^0\gamma$ decay mode is divided into 4 separate $\rho^0 \to \pi^+\pi^-$ mass bins : (1) 300 MeV/c^2 to 540 MeV/c^2, (2) 540 MeV/c^2 to 660 MeV/c^2, (3) 660 MeV/c^2 to 780 MeV/c^2, and (4) 780 MeV/c^2 to 900 MeV/c^2. All of the decay modes make requirements on the unconstrained mass of the η' ($M(\eta')$), the mass pull of the η' ($\chi_m\eta'$)), V-cut, signal ΔE, and non-signal ΔE. The η' decays that include η candidates also have in common requirements on the η unconstrained mass (M_η) and mass pull. The requirements for the $\pi\pi\eta$ and the $\pi^0\pi^0\eta$ decays are given in Table 4.5. The requirements for $\rho^0\gamma$ and $\eta' \to \gamma\gamma$ are given in Table 4.6.

For $\eta' \to \gamma\gamma$ we additionally require that neither of the two showers could instead be included in a π^0 candidate with $|\chi_m(\pi^0)| < 5$. The efficiency for this decay mode is given in Table 4.7.

Table 4.2: Efficiency for the $D^\pm \to \eta(\gamma\gamma)e^\pm\nu$ for each q^2 and quality bin. The efficiency $\mathcal{E}_{tot}$ is the efficiency contribution for the total $D^\pm \to \eta e^\pm\nu$. The efficiency $\mathcal{E}_{q^2}/\mathcal{B}(\eta \to \gamma\gamma)$ is the efficiency of reconstructing this decay mode and q^2 range.

Decay Mode	q^2 Bin	Quality Bin	$\mathcal{E}_{tot}$	$\mathcal{E}_{q^2}/\mathcal{B}(\eta \to \gamma\gamma)$
$\eta \to \gamma\gamma$	All	All	2.04%	5.18%
$\eta \to \gamma\gamma$	All	Low	0.69%	1.77%
$\eta \to \gamma\gamma$	All	High	1.34%	3.4%
$\eta \to \gamma\gamma$	$q^2 < 0.5 GeV^2$	All	1.09%	5.35%
$\eta \to \gamma\gamma$	$q^2 < 0.5 GeV^2$	Low	0.4%	1.96%
$\eta \to \gamma\gamma$	$q^2 < 0.5 GeV^2$	High	0.69%	3.39%
$\eta \to \gamma\gamma$	$0.5 GeV^2 < q^2 < 1.0 GeV^2$	All	0.65%	4.88%
$\eta \to \gamma\gamma$	$0.5 GeV^2 < q^2 < 1.0 GeV^2$	Low	0.21%	1.59%
$\eta \to \gamma\gamma$	$0.5 GeV^2 < q^2 < 1.0 GeV^2$	High	0.44%	3.28%
$\eta \to \gamma\gamma$	$q^2 > 1.0 GeV^2$	All	0.29%	5.29%
$\eta \to \gamma\gamma$	$q^2 > 1.0 GeV^2$	Low	0.08%	1.54%
$\eta \to \gamma\gamma$	$q^2 > 1.0 GeV^2$	High	0.2%	3.75%

The $\eta' \to \rho^0\gamma$ mode has several unique requirements that are given in the list below. The efficiencies for the $D^\pm \to \eta'(\rho^0\gamma)e^\pm\nu$ are given in Table 4.8.

1. The shower must not be included in any π^0 candidate (both showers splitoff approved) with a mass pull of magnitude less than 3.

2. We impose requirements on the angle between the photon and either of the two charged π from the ρ^0 decay in the rest frame of the ρ^0 ($\theta_{\gamma\pi}$). The η' has spin zero, and the ρ^0 has spin 1. This means that the photon must be traveling along the direction of the ρ^0 angular momentum and the decay must follow a $sin^2(\theta_{\gamma\pi})$

79

Table 4.3: Efficiency for the $D^{\pm} \rightarrow \eta(\pi^{+}\pi^{-}\pi^{0})e^{\pm}\nu$ for each q^2, and quality bin. The efficiency $\mathcal{E}_{\text{tot}}$ is the efficiency contribution to the total $D^{\pm} \rightarrow \eta e^{\pm}\nu$. The efficiency $\mathcal{E}_{q^2}/\mathcal{B}(\eta \rightarrow \pi^{+}\pi^{-}\pi^{0})$ is the efficiency of reconstructing this decay mode and q^2 range.

Decay Mode	q^2 Bin	Quality Bin	$\mathcal{E}_{\text{tot}}$	$\mathcal{E}_{q^2}/\mathcal{B}(\eta \rightarrow \pi^{+}\pi^{-}\pi^{0})$
$\eta \rightarrow \pi^{+}\pi^{-}\pi^{0}$	All	All	0.91%	3.99%
$\eta \rightarrow \pi^{+}\pi^{-}\pi^{0}$	All	Low	0.37%	1.64%
$\eta \rightarrow \pi^{+}\pi^{-}\pi^{0}$	All	High	0.54%	2.34%
$\eta \rightarrow \pi^{+}\pi^{-}\pi^{0}$	$q^2 < 0.5 GeV^2$	All	0.5%	4.23%
$\eta \rightarrow \pi^{+}\pi^{-}\pi^{0}$	$q^2 < 0.5 GeV^2$	Low	0.2%	1.74%
$\eta \rightarrow \pi^{+}\pi^{-}\pi^{0}$	$q^2 < 0.5 GeV^2$	High	0.29%	2.49%
$\eta \rightarrow \pi^{+}\pi^{-}\pi^{0}$	$0.5 GeV^2 < q^2 < 1.0 GeV^2$	All	0.28%	3.63%
$\eta \rightarrow \pi^{+}\pi^{-}\pi^{0}$	$0.5 GeV^2 < q^2 < 1.0 GeV^2$	Low	0.11%	1.48%
$\eta \rightarrow \pi^{+}\pi^{-}\pi^{0}$	$0.5 GeV^2 < q^2 < 1.0 GeV^2$	High	0.16%	2.15%
$\eta \rightarrow \pi^{+}\pi^{-}\pi^{0}$	$q^2 > 1.0 GeV^2$	All	0.12%	3.98%
$\eta \rightarrow \pi^{+}\pi^{-}\pi^{0}$	$q^2 > 1.0 GeV^2$	Low	0.05%	1.68%
$\eta \rightarrow \pi^{+}\pi^{-}\pi^{0}$	$q^2 > 1.0 GeV^2$	High	0.07%	2.3%

distribution. Backgrounds, however, tend to have a flat distribution in $cos(\theta_{\gamma\pi})$. Therefore, we require that the $|cos(\theta_{\gamma\pi})| < 0.85$. See Figure 4.3.

3. The photon candidate must have energy greater than 250 MeV if a kaon is present in the event, which helps to exclude candidates that are actually made with splitoff escape showers.

The π^0 candidate in the $\eta' \rightarrow \pi\pi\eta(\pi\pi\pi^0)$ is required to have a mass pull between ± 3. The 3 π^0 candidates in the $\eta' \rightarrow \pi\pi\eta(\pi^0\pi^0\pi^0)$ are required to each have a mass pull between -5.0 and 3.0. The 2 π^0 candidates in the $\eta' \rightarrow \pi^0\pi^0\eta(\gamma\gamma)$ are each required to

Table 4.4: Efficiency for $D^{\pm} \rightarrow \eta(\pi^0\pi^0\pi^0)e^{\pm}\nu$ for each q^2, and quality bins. The efficiency $\mathcal{E}_{tot}$ is the efficiency contribution to the total $D^{\pm} \rightarrow \eta e^{\pm}\nu$. The efficiency $\mathcal{E}_{tot}/\mathcal{B}(\eta \rightarrow \pi^0\pi^0\pi^0)$ is the efficiency of reconstructing this decay mode and q^2 range.

Decay Mode	q^2 Bin	Quality Bin	$\mathcal{E}_{tot}$	$\mathcal{E}/\mathcal{B}(\eta \rightarrow \pi^0\pi^0\pi^0)$
$\eta \rightarrow \pi^0\pi^0\pi^0$	All	All	0.73%	2.26%
$\eta \rightarrow \pi^0\pi^0\pi^0$	All	Low	0.35%	1.09%
$\eta \rightarrow \pi^0\pi^0\pi^0$	All	High	0.37%	1.16%
$\eta \rightarrow \pi^0\pi^0\pi^0$	$q^2 < 0.5 GeV^2$	All	0.35%	2.1%
$\eta \rightarrow \pi^0\pi^0\pi^0$	$q^2 < 0.5 GeV^2$	Low	0.16%	0.96%
$\eta \rightarrow \pi^0\pi^0\pi^0$	$q^2 < 0.5 GeV^2$	High	0.19%	1.14%
$\eta \rightarrow \pi^0\pi^0\pi^0$	$0.5 GeV^2 < q^2 < 1.0 GeV^2$	All	0.23%	2.15%
$\eta \rightarrow \pi^0\pi^0\pi^0$	$0.5 GeV^2 < q^2 < 1.0 GeV^2$	Low	0.11%	1.04%
$\eta \rightarrow \pi^0\pi^0\pi^0$	$0.5 GeV^2 < q^2 < 1.0 GeV^2$	High	0.12%	1.1%
$\eta \rightarrow \pi^0\pi^0\pi^0$	$q^2 > 1.0 GeV^2$	All	0.14%	3.13%
$\eta \rightarrow \pi^0\pi^0\pi^0$	$q^2 > 1.0 GeV^2$	Low	0.07%	1.74%
$\eta \rightarrow \pi^0\pi^0\pi^0$	$q^2 > 1.0 GeV^2$	High	0.06%	1.39%

have a mass pull between -3.0 and 3.0. The $\eta' \rightarrow \pi^0\pi^0\eta(\gamma\gamma)$ decay has an additional constraint on the $\eta \rightarrow \gamma\gamma$, which is that neither of the showers are part of a π^0 candidate with $|\chi_m(\pi^0)| < 3$. The efficiencies for these decays are given in Table 4.9 and Table 4.10.

Table 4.5: The requirements on common variables for the different η' decay modes involving $\eta' \to \pi\pi\eta$ and $\eta' \to \pi^0\pi^0\eta$ analysis .

Variable	$\pi\pi\eta(\gamma\gamma)$	$\pi\pi\eta(\pi^+\pi^-\pi^0)$	$\pi\pi\eta(\pi^0\pi^0\pi^0)$	$\pi^0\pi^0\eta(\gamma\gamma)$
$M(\eta')$ (MeV/c^2)	945 to 970	948 to 970	940 to 980	945 to 968
$\chi_m(\eta')$	-3 to 3	-3 to 3	-3 to 3	-3.3 to 2.5
$M(\eta)$ (MeV/c^2)	495 to 580	536 to 560	480 to 570	505 to 573
$\chi_m(\eta)$	-3 to 3	-3 to 3	-3 to 3	-3 to 3
V-cut (MeV)	-200 to 200	-140 to 140	-140 to 140	-120 to 120
Signal ΔE (MeV)	-70 to 100	-110 to 100	-110 to 100	-100 to 100
non-Signal ΔE (MeV)	-320 to 220	-350 to 300	-350 to 300	-400 to 350

Table 4.6: The requirements on common variables for $\eta' \to \rho^0\gamma$ and $\eta' \to \gamma\gamma$. Note that the V-cut and signal side ΔE vary depending on the ρ^0 mass bin.

Variable	$\rho^0\gamma$ bins(2,4)	$\rho^0\gamma$ bin(1)	$\rho^0\gamma$ bin(3)	$\gamma\gamma$
$M(\eta')$ (MeV/c^2)	936 to 980	936 to 980	936 to 980	890 to 1000
$\chi_m(\eta')$	-3.0 to 2.25	-3.0 to 2.25	-3.0 to 2.25	-3.0 to 2.15
V-cut (MeV)	-200 to 120	-200 to 50	-200 to 120	-100 to 100
Signal ΔE (MeV)	-70 to 100	-70 to 50	-200 to 50	-100 to 50
non-Signal ΔE (MeV)	-300 to 200	-300 to 200	-300 to 200	-200 to 200

Table 4.7: Efficiency for the $D^\pm \to \eta'(\gamma\gamma)e^\pm\nu$ for each quality bin. The efficiency $\mathcal{E}_{\text{tot}}$ is the efficiency contribution for the total $D^\pm \to \eta'e^\pm\nu$. The efficiency $\mathcal{E}_{\text{tot}}/\mathcal{B}(\eta' \to \gamma\gamma)$ is the efficiency of reconstructing this decay mode.

Decay Mode	Quality Bin	$\mathcal{E}_{\text{tot}}$	$\mathcal{E}_{\text{tot}}/\mathcal{B}$
$\eta' \to \gamma\gamma$	All	0.1%	4.94%
$\eta' \to \gamma\gamma$	Low	0.04%	1.99%
$\eta' \to \gamma\gamma$	High	0.06%	2.94%

Table 4.8: Efficiency for $D^\pm \to \eta'(\rho^0\gamma)e^\pm\nu$ decay mode for mass and quality bins. The efficiency $\mathcal{E}_{\text{tot}}$ is the efficiency contribution to the total $D^\pm \to \eta'e^\pm\nu$. The efficiency $\mathcal{E}_{M(\pi\pi)}/\mathcal{B}$ is the efficiency for reconstructing the $\pi\pi$ mass bin.

Decay Mode	Quality Bin	$\mathcal{E}_{\text{tot}}$	$\mathcal{E}_{M(\pi\pi)}/\mathcal{B}$
$\eta' \to \rho^0\gamma \; : \; M_{\pi\pi}(1)$	All	0.07%	5.25%
$\eta' \to \rho^0\gamma \; : \; M_{\pi\pi}(1)$	Low	0.02%	2%
$\eta' \to \rho^0\gamma \; : \; M_{\pi\pi}(1)$	High	0.04%	3.25%
$\eta' \to \rho^0\gamma \; : \; M_{\pi\pi}(2)$	All	0.16%	3.79%
$\eta' \to \rho^0\gamma \; : \; M_{\pi\pi}(2)$	Low	0.04%	0.94%
$\eta' \to \rho^0\gamma \; : \; M_{\pi\pi}(2)$	High	0.12%	2.84%
$\eta' \to \rho^0\gamma \; : \; M_{\pi\pi}(3)$	All	0.65%	4.24%
$\eta' \to \rho^0\gamma \; : \; M_{\pi\pi}(3)$	Low	0.21%	1.38%
$\eta' \to \rho^0\gamma \; : \; M_{\pi\pi}(3)$	High	0.44%	2.86%
$\eta' \to \rho^0\gamma \; : \; M_{\pi\pi}(4)$	All	0.34%	4.35%
$\eta' \to \rho^0\gamma \; : \; M_{\pi\pi}(4)$	Low	0.1%	1.32%
$\eta' \to \rho^0\gamma \; : \; M_{\pi\pi}(4)$	High	0.24%	3.03%
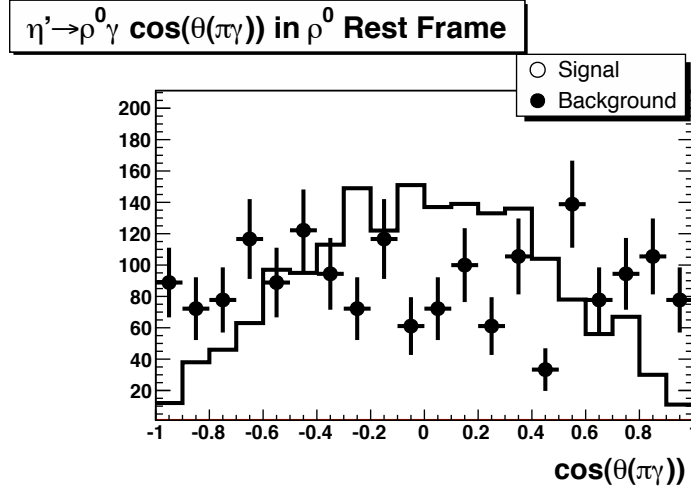
Figure 4.3: In $\eta' \to \rho^0(\pi^+\pi^-)\gamma$ decay, the cosine of the angle between one of the pions from the ρ^0 and the photon in the rest frame of the ρ^0. The histogram is signal, the black dots are background.

Table 4.9: The efficiencies of all of the $\eta' \to \pi\pi\eta$ decay modes into the q^2 bins, decay mode, and quality bins. The efficiency $\mathcal{E}$ is the efficiency contribution for the total $\eta'ev$ from this decay mode and bin. The efficiency $\mathcal{E}/\mathcal{B}$ is the efficiency of reconstructing that particular mode and bin.

Decay Mode	Quality Bin	$\mathcal{E}$	$\mathcal{E}/\mathcal{B}$
$\eta' \to \pi\pi\eta(\gamma\gamma)$	All	0.61%	3.54%
$\eta' \to \pi\pi\eta(\gamma\gamma)$	Low	0.23%	1.33%
$\eta' \to \pi\pi\eta(\gamma\gamma)$	High	0.38%	2.21%
$\eta' \to \pi\pi\eta(\pi\pi\pi^0)$	All	0.16%	1.57%
$\eta' \to \pi\pi\eta(\pi\pi\pi^0)$	Low	0.06%	0.66%
$\eta' \to \pi\pi\eta(\pi\pi\pi^0)$	High	0.09%	0.9%
$\eta' \to \pi\pi\eta(\pi^0\pi^0\pi^0)$	All	0.26%	1.82%
$\eta' \to \pi\pi\eta(\pi^0\pi^0\pi^0)$	Low	0.13%	0.97%
$\eta' \to \pi\pi\eta(\pi^0\pi^0\pi^0)$	High	0.12%	0.84%

Table 4.10: The efficiencies of all of the $\eta'ev$ decay modes into the q^2 bins, and quality bins. The efficiency $\mathcal{E}$ is the efficiency contribution for the total $\eta'ev$ from this decay mode and bin. The efficiency $\mathcal{E}/\mathcal{B}$ is the efficiency of reconstructing that particular mode and bin.

Decay Mode	Quality Bin	$\mathcal{E}$	$\mathcal{E}/\mathcal{B}$
$\eta' \to \pi^0\pi^0\eta(\gamma\gamma)$	All	0.07%	0.9%
$\eta' \to \pi^0\pi^0\eta(\gamma\gamma)$	Low	0.03%	0.39%
$\eta' \to \pi^0\pi^0\eta(\gamma\gamma)$	High	0.04%	0.5%

4.8 Hadronic D-Tag Requirements

There is a set of common D-Tag requirements applied to the daughter particles for the decay modes: $D^+ \to K^-\pi^+\pi^+$, $D^+ \to K^-\pi^+\pi^+\pi^0$, $D^+ \to K_S\pi^+\pi^0$, $D^+ \to K_S\pi^+$, $D^0 \to K^-\pi^+$, and $D^0 \to K^-\pi^+\pi^0$. For the measurement of the hadronic decays of the D^+ and the D^0 we allow tags from both charge conjugate modes, for example both $D^+ \to K^-\pi^+\pi^+$ and $D^- \to K^+\pi^-\pi^-$. However in the $D^+ \to K^-\pi^+\pi^+$ yield used to normalize the semileptonic measurements we only use positively charged D so that the systematic uncertainties associated with the generic reconstruction are the same as $\eta^{(\prime)}e^\pm v$. If we use both charges for $K^+\pi^-\pi^-$ as tag modes, and select only one tag per event, the relative other side D $K^-\pi^+\pi^+$ contribution is half what it is in the semileptonic decays. The only way around this is to either double count $D^+ \to K^-\pi^+\pi^+$ $D^- \to K^+\pi^-\pi^-$ events or to choose only one charge for the D-tag.

1. We require the hadronic D-tag candidate to have a mass pull between ±3.

2. All π^0's are required to have a mass pull between ±3.

3. All charged π are required to have a dE/dx within 3 standard deviations of the expected value for a π.

4. All charged K are required to have a dE/dx within 3 standard deviations of the expected value for a K.

5. All $K_S \to \pi^+\pi^-$ are required to be within ± 12 MeV/c^2 of the known K_S mass.

6. On the tag side $|\Delta E| < 100$ MeV.

7. On the other side $|\Delta E| < 100$ MeV.

CHAPTER 5

CORRECTIONS TO THE MONTE CARLO SIMULATION

Though great lengths have been taken to make the CLEO-c Monte Carlo simulation match the data as well as possible, we do not expect perfect agreement. Certain aspects of the Monte Carlo simulation, such as hadronic branching fractions, have not been measured before, and other processes, such as the creation of hadronic splitoff-escape showers, are difficult to simulate. This section describes a series of studies to determine how well the Monte Carlo simulation reproduces key processes and efficiencies in the data, as well as the corrections needed to make the simulation match the data.

5.1 Procedures for Determining Corrections

We compare many different aspects of the Monte Carlo simulation to the data. This section briefly describes procedures that are repeatedly used in these studies. We describe these general procedures in terms of hypothetical daughter particles such as X and Y so that they can be readily applied to any situation.

The efficiency for reconstructing a daughter particle X is studied by using the conservation of energy and momentum. We construct a "missing" four-vector from the beam energy and the total energy and momentum of everything in the event excluding X mesons. We look for events where the missing four-vector has a mass consistent with an X meson. Of those events where the "missing" four-vector is consistent with an X meson we ask how many of those events actually contained a reconstructed X meson. The reconstruction efficiency for X is the number of events with a reconstructed X meson divided by the total number of events consistent with an X.

Suppose that D decays to X through the process $D \rightarrow XYY$. We first find a well understood D tag, such as $D^+ \rightarrow K^-\pi^+\pi^+$ that passes very strict requirements such that there is very little background. We then search for 2 "Y"'s. We do not, at this point,

ask the question whether or not we measured an X in an event, and if there is an X in the event we ignore it. We simply want to know if we think there should be an X in the event. We can determine whether or not there is an X in the event by using the fact that the four-vector of the two D mesons is equal to the four-vector of the colliding beams (P_{total}). We construct a "missing" four-vector for everything else in the event besides the D-tag and the 2 "Y"'s given by

$$P_{\text{miss}} = P_{\text{total}} - (P_{\text{tag}} + P_{2Y}). \tag{5.1}$$

If this event actually contained a XYY decay then the missing mass should be consistent with the mass of the X. We fit the missing mass distribution to determine how many of these events contained an X. Now that we know how many events contained X, we ask how often we actually found an X that passed all of our requirements and had a momentum and energy consistent with the missing four-vector. The efficiency for reconstructing X is the ratio between the number of X's found and the total number of events that contained an X. The momentum dependence of the efficiency can be found by dividing the data and Monte Carlo events into bins based on $|\vec{P}_{\text{miss}}|$.

In addition to studying the efficiency of different types of real daughter particles we also need to study how often there are fake tracks and showers. In order to determine the rate that fake or extra particles get reconstructed we use events that are "double tagged". Events that are double tagged simultaneously have both D^+ and D^- described by D-tags without using any track or shower more than once. If both the D^+ and D^- tags satisfy strict requirements then any tracks or showers in the event that are not included by the tags must be a fake. If the fraction of double tagged events with fake tracks or showers is not the same in data as it is in the Monte Carlo simulation then we can modify the Monte Carlo simulation to match.

5.2 Hadronic Branching Fraction Correction

Generic Reconstruction requires that the four momentum and charge of the non-signal D is accurately determined. The efficiency for doing this depends on the number, type, and momentum of the non-signal D daughter particles. Therefore the absolute branching fractions for the different non-signal D final states help determine the $D^+ \rightarrow \eta^{(\prime)} e^+ \nu$ reconstruction efficiency.

Table 5.1 lists the efficiencies for reconstructing $D^+ \rightarrow \eta' e^+ \nu$, $D^+ \rightarrow \eta e^+ \nu$, and $D^+ \rightarrow K^- \pi^+ \pi^+$ for many of the other side D decay modes. To show the importance of each decay and to allow direct comparison between the different signal modes we also list the percent contribution that the other side decay is expected to make to the total signal efficiency given our current knowledge of that branching fraction. For example, if the contribution from $K\pi\pi^0$ is 10%, this means that 10% of all of the signal measured has a $K\pi\pi^0$ on the other side. Systematic uncertainties associated with the hadronic branching fractions are only removed from our semileptonic branching fractions if the percent contribution of each decay mode is the same in $D^+ \rightarrow K^- \pi^+ \pi^+$ as it is in $D^+ \rightarrow \eta^{(\prime)} e^+ \nu$.

As Table 5.1 shows, there is significant variation in the signal efficiency with the other side D decays mode, and this variation can lead to the total signal efficiency in data being incorrectly calculated if the hadronic branching fractions are unknown. Therefore, we use the generic reconstruction algorithm to measure the branching fractions of all of the visible D-hadronic decay modes. As discussed in Section 3.5.1 we measure these branching fractions in terms of the number of the different daughter particles (π, K, K^0, π^0, $\eta \rightarrow \gamma\gamma$) found in the final state. Once these branching fractions are measured the events in the Monte Carlo sample are reweighted to have the same composition of final states that is seen in data.

An additional complication arises concerning whether or not all of the previously known and recently measured branching fractions add to 1. For example, suppose that there are 3 branching fractions, $\mathcal{B}_A$, $\mathcal{B}_B$, and $\mathcal{B}_C$. Each of the branching fractions have independent absolute measurements: $\mathcal{B}_A = a + \sigma_a$, $\mathcal{B}_B = b + \sigma_b$, $\mathcal{B}_C = c + \sigma_c$. Since each of these measurements are independent, we cannot expect the central values to give $a + b + c = 1$ precisely, only that this sum should be within a few $\sigma = \sqrt{\sigma_a^2 + \sigma_b^2 + \sigma_c^2}$ of 1.

It is unphysical for the sum of all branching fractions to not be equal to one, and this unity must be enforced when applying corrections to the Monte Carlo sample. Therefore, unless $a + b + c$ is significantly less than 1, indicating that other unmeasured decay modes exist, we must assign values to $\mathcal{B}_A$, $\mathcal{B}_B$, and $\mathcal{B}_C$ that precisely add to 1. We determine the values of $\mathcal{B}_A$, $\mathcal{B}_B$, and $\mathcal{B}_C$, given the physical constraint that $a + b + c = 1$, by performing an $N - 1$ parameter fit to the N measurements. The Nth parameter is defined to be equal to $1 - \sum_j^{N-1} \mathcal{B}_j$ so that the physical constraint is satisfied.

Let $\mathcal{B}_j$ be the measured value of the decay j branching fraction, and $\mathcal{B}_j^{fit}$ be the value for decay j obtained in the fit. The χ^2 for this model is given by

$$\chi^2 = \left[\sum_i^{N-1} \frac{(\mathcal{B}_i - \mathcal{B}_i^{fit})^2}{\sigma_i^2} \right] + \left[\frac{(\mathcal{B}_N - (1 - \sum_j^{N-1} \mathcal{B}_j^{fit}))^2}{\sigma_N^2} \right]. \tag{5.2}$$

We minimize the χ^2 by requiring for all $i = 0...N - 1$

$$\frac{\partial \chi^2}{\partial \mathcal{B}_i^{fit}} = \frac{-2(\mathcal{B}_i - \mathcal{B}_i^{fit})}{\sigma_i^2} + \frac{2(\mathcal{B}_N - (1 - \sum_j^{N-1} \mathcal{B}_j^{fit}))}{\sigma_N^2} = 0. \tag{5.3}$$

This minimization requirement can be written as the matrix equation,

$$\begin{pmatrix} \frac{1}{\sigma_1^2} + \frac{1}{\sigma_N^2} & \frac{1}{\sigma_N^2} & \cdots & \frac{1}{\sigma_N^2} \\ \frac{1}{\sigma_N^2} & \frac{1}{\sigma_2^2} + \frac{1}{\sigma_N^2} & \cdots & \frac{1}{\sigma_N^2} \\ \cdots & \cdots & \cdots & \cdots \\ \frac{1}{\sigma_N^2} & \frac{1}{\sigma_N^2} & \cdots & \frac{1}{\sigma_{N-1}^2} + \frac{1}{\sigma_N^2} \end{pmatrix} \begin{pmatrix} \mathcal{B}_1^{fit} \\ \mathcal{B}_2^{fit} \\ \cdots \\ \mathcal{B}_{N-1}^{fit} \end{pmatrix} - \begin{pmatrix} \frac{\mathcal{B}_1}{\sigma_1^2} + \frac{1-\mathcal{B}_N}{\sigma_N^2} \\ \frac{\mathcal{B}_2}{\sigma_2^2} + \frac{1-\mathcal{B}_N}{\sigma_N^2} \\ \cdots \\ \frac{\mathcal{B}_{N-1}}{\sigma_{N-1}^2} + \frac{1-\mathcal{B}_N}{\sigma_N^2} \end{pmatrix} = 0. \tag{5.4}$$

Solving for the fit parameters $i = 1 \cdots N - 1$ yields,

$$
\begin{pmatrix}
\mathcal{B}_1^{fit} \\
\mathcal{B}_2^{fit} \\
\cdots \\
\mathcal{B}_{N-1}^{fit}
\end{pmatrix}
=
\begin{pmatrix}
\frac{1}{\sigma_1^2} + \frac{1}{\sigma_N^2} & \frac{1}{\sigma_N^2} & \cdots & \frac{1}{\sigma_N^2} \\
\frac{1}{\sigma_N^2} & \frac{1}{\sigma_2^2} + \frac{1}{\sigma_N^2} & \cdots & \frac{1}{\sigma_N^2} \\
\cdots & \cdots & \cdots & \cdots \\
\frac{1}{\sigma_N^2} & \frac{1}{\sigma_N^2} & \cdots & \frac{1}{\sigma_{N-1}^2} + \frac{1}{\sigma_N^2}
\end{pmatrix}^{-1}
\begin{pmatrix}
\frac{\mathcal{B}_1}{\sigma_1^2} + \frac{1-\mathcal{B}_N}{\sigma_N^2} \\
\frac{\mathcal{B}_2}{\sigma_2^2} + \frac{1-\mathcal{B}_N}{\sigma_N^2} \\
\cdots \\
\frac{\mathcal{B}_{N-1}}{\sigma_{N-1}^2} + \frac{1-\mathcal{B}_N}{\sigma_N^2}
\end{pmatrix}
\tag{5.5}
$$

Solving Equation 5.5 for $\mathcal{B}_i^{fit}$ we find

$$
\mathcal{B}_i^{fit} = \mathcal{B}_i + (1 - \sum_j^N \mathcal{B}_j) \frac{\sigma_i^2}{\sum_k^N \sigma_k^2}.
\tag{5.6}
$$

Any difference between 1 and the sum of all branching fraction measurements is divided up among the different fit values such that the fraction that each decay mode gains or looses is proportional to the square of the uncertainty in that decay mode. Therefore, poorly known branching fractions are changed more by the fit than ones that are known very well.

A second complication concerns whether or not we have actually measured all of the relevant D decays. Within the uncertainty of the sum of all known branching fractions there may exist a subset of decays that cannot be directly measured. This subset of unmeasured decays could either contain final states with very low efficiency, or it could be distributed over a large number of very small branching fractions that do not have a statistically significant signal in the data. Let $\mathcal{B}_U$ be the inclusive branching fraction of this potential subset of unknown decays. The size of $\mathcal{B}_U$ and whether or not the decays are efficient is a source of systematic uncertainty in the efficiency-corrected yields.

To determine the sum of all branching fractions and the uncertainty in that sum, we include unmeasured decays that are in the Monte Carlo simulation and assign to each unmeasured decay an uncertainty equal to the expected central value. We find that for $D^\pm$ the sum of the inclusive semileptonic branching fraction ($32\% \pm 0.6\%$ based on PDG 2008), the hadronic branching fractions measured in this analysis ($62.3\% \pm 1.6\%$), and

the unmeasured branching fractions that are included in the Monte Carlo simulation $(2.9\% \pm 0.9\%)$ to be $97.2\% \pm 2.0\%$. This result is 1.4σ below 100%. Though this is still perfectly consistent with this sum including all of the D^+ branching fractions, there is still room for unmeasured decays. Based on the available data there is no way of knowing if $\mathcal{B}_U$ is significant in size or efficiency. We include $\mathcal{B}_U$ when considering systematic uncertainties, but for the purposes of reweighting the Monte Carlo sample we assume that all of the different decays have already been accounted for.

5.3   Hadronic Daughter Momentum Spectrum Corrections

Tracks with higher momentum tend to have higher reconstruction efficiency than tracks with lower momentum. Also, showers and $X \to \gamma\gamma$ candidates also tend to have momentum dependent efficiencies. Furthermore the energy deposited in the calorimeter by K_L and by tracks also have some dependence on the momentum of these particles. Therefore, the momentum spectra of the different types of daughter particles in the hadronic decays affect our overall reconstruction efficiency. How well we know these distributions is a source of systematic uncertainty for the hadronic branching fraction measurements and the semileptonic branching fraction measurements.

The momenta of particles from decays that contain only two daughters, such as $D^0 \to K^-\pi^+$, are completely determined by energy and momentum conservation. However the spectra for decays with 3 or more particles are dependent on the composition of resonances that make up the branching fraction for that final state. For example, the decay $D^+ \to K^-\pi^+\pi^+$ has contributions from non-resonant $K^-\pi^+\pi^+$ as well as resonances $\bar{K}^*(892)^0\pi^+$, $\bar{K}^*(1430)^0\pi^+$, and $\bar{K}^*(1680)^0\pi^+$, where the excited K^* resonances decay to $K^-\pi^+$. Each different resonance create kaons and pions with different momentum spectra, and the exact composition of these resonances in the full $K^-\pi^+\pi^+$ final state affect the spectra of these particles in $D^+ \to K^-\pi^+\pi^+$.

Table 5.1: The efficiencies ($\mathcal{E}$) for reconstructing signal side $D^+ \rightarrow \eta' e^+ \nu$, $D^+ \rightarrow \eta e^+ \nu$ and $D^+ \rightarrow K^- \pi^+ \pi^+$ given different other side D decays. We also list the fraction of the total efficiency from this non-signal decay ($\mathcal{F}$). The decays listed below make up approximately 90% of the total efficiency. The 10% not listed is composed of more than 20 different final states.

non-signal D	$\mathcal{E}(\eta' ev)$	$\mathcal{F}(\eta' ev)$	$\mathcal{E}(\eta ev)$	$\mathcal{F}(\eta ev)$	$\mathcal{E}(K\pi\pi)$	$\mathcal{F}(K\pi\pi)$
$3 \times \pi$	11.92%	1.82%	18.31%	2%	19.43%	1.71%
$1 \times \pi \, 2 \times \pi^0$	5.86%	1.23%	8.44%	1.27%	9.85%	1.19%
$3 \times \pi \, 1 \times \pi^0$	5.89%	3.46%	7.65%	3.22%	10.09%	3.43%
$5 \times \pi$	5.33%	0.38%	6.72%	0.35%	10.92%	0.46%
$1 \times \pi \, 3 \times \pi^0$	3.31%	0.64%	4.49%	0.62%	5.79%	0.65%
$3 \times \pi \, 2 \times \pi^0$	3.12%	1.28%	3.64%	1.07%	5.42%	1.28%
$2 \times \pi \, 1 \times K$	7.55%	33.6%	10.33%	32.9%	12.15%	31.24%
$2 \times \pi \, 1 \times \pi^0 \, 1 \times K$	3.56%	10.04%	5.14%	10.38%	6.66%	10.85%
$2 \times \pi \, 2 \times \pi^0 \, 1 \times K$	1.73%	0.5%	1.83%	0.38%	3.1%	0.52%
$1 \times \pi \, 2 \times K$	3.33%	1.53%	6.47%	2.13%	8.21%	2.18%
$4 \times \pi \, 1 \times K$	3.69%	1.03%	5.31%	1.06%	6.05%	0.97%
$1 \times \pi \, 1 \times K^0$	4.23%	6.1%	5.92%	6.11%	6.77%	5.64%
$1 \times \pi \, 1 \times \pi^0 1 \times K^0$	2.46%	17.21%	3.29%	16.52%	4.11%	16.62%
$1 \times K \, 1 \times K^0$	3.4%	1.06%	4.56%	1.01%	5.64%	1.01%
$1 \times \pi \, 2 \times \pi^0 \, 1 \times K^0$	1.31%	3.6%	1.93%	3.8%	2.54%	4.03%
$3 \times \pi \, 1 \times K^0$	2.42%	7%	3.68%	7.63%	4.67%	7.81%
$3 \times \pi \, 1 \times \pi^0 \, 1 \times K^0$	1.3%	1.82%	1.84%	1.85%	2.53%	2.05%
$1 \times \pi \, 1 \times K^0 \, 1 \times \eta(\gamma\gamma)$	2.23%	1.06%	2.81%	0.96%	3.98%	1.1%
$1 \times \pi \, 1 \times \pi^0 \, 2 \times K^0$	1.81%	0.29%	3.51%	0.41%	3.46%	0.32%

It is beyond the scope of this work to attempt to disentangle the resonance composition of all of the hadronic final states. Instead we compare the spectra in data to the spectra in the Monte Carlo simulation and develop reweights to give us the correct momenta spectra and efficiencies for the hadronic decay modes.

The spectra of one type of daughter particle is correlated with the spectra of the other types of daughter particles in the decay. For example, the decay $D^+ \to K^- \pi^+ \pi^+$ has contributions from different K^{*0} resonances via $D^+ \to K^{*0} \pi^+$ with $K^{*0} \to K^- \pi^+$. Since the kaon and one of the pions have the invariant mass of the K^{*0} it is not possible to change the spectrum of the kaons and maintain the invariant mass without also changing the spectrum of the pions. To account for this correlation we determine reweights for one type of daughter particle at a time, beginning with the heaviest daughter particle, and apply the reweight for that type of particle before calculating a reweight for the next type of particle.

The reweight for a spectrum of a daughter particle in a particular decay is determined by dividing the background subtracted data spectrum by the reconstructed Monte Carlo spectrum. The reweight is normalized such that the total number of generated events remains constant. This iterative procedure is not perfect but it is easy to automate and apply to all of the decay modes without evaluating all of the resonances that might contribute to the final state.

We do not reweight spectra that do not have a statistically significant disagreement with data. In order for a spectrum to be reweighted the χ^2 per degree of freedom must be greater than 4, which prevents the spectra of rare decay modes from being corrected.

5.4 Splitoff Escape Correction

One of the major improvements made in this analysis came with identifying splitoff-escapes and excluding them from the event reconstruction. Most of the splitoff-escapes

are the result of hadronic interactions in the calorimeter. We do not expect that the hadronic interactions in the calorimeter are accurately modeled in the Monte Carlo simulation and so do not expect that the splitoff-escapes are accurately modeled. We need to measure the rate that pions and kaons create splitoff-escape showers in data and compare that to the rate in the Monte Carlo simulation.

The Monte Carlo simulation suggests that pions and kaons produce extra showers at significantly different rates. On average, pions create splitoff escapes at a rate of 4-5% per track in the momentum range of 0.2 GeV/c to 1.0 GeV/c. Kaons create extra showers by two mechanisms: in-flight decays and splitoff-escapes. An in-flight decay is when a kaon decays while traversing the drift chamber. Daughter particles from the in-flght decay can create extra showers. Both of these mechanisms for kaons to produce extra showers are dependent on the kaon momentum. The Monte Carlo simulation predicts that the total probability that a kaon creates extra showers varies from roughly 50% to 10% depending on the track momentum. On average kaon tracks produce extra showers via in-flight decays at a rate of approximately 3% per track, and generate splitoff escapes at approximately 15% per track. Figures 5.1, 5.2, and 5.3 show the probability for a track to create extra showers from pion splitoff escapes, kaon splitoff escapes, and kaon in-flight decays respectively.

We need to compare the rate of splitoff escape creation and the momentum dependance of that rate in the data to the rate in the Monte Carlo sample. First, we identify a tag, either from charged D decays ($K\pi\pi$, $K_S\pi\pi^0$, $K\pi\pi^0$, $K_S\pi$) or neutral D decays ($K\pi\pi^0$, $K_S\pi^0$, $K\pi$). The tag must have $|\Delta E| < 0.02$ GeV, and must have a beam constrained mass within 0.005 GeV/c^2 of the expected D mass. We perform the generic reconstruction of the other side and reject events that have $\eta \rightarrow \gamma\gamma$ or $\pi^0 \rightarrow \gamma\gamma$ candidates with $|(M_{true} - M_{\gamma\gamma})/\sigma_M| > 3$. We reject events with non-zero net charge. All tracks not associated with a $K_S \rightarrow \pi^+\pi^-$ must pass additional track quality requirements. We
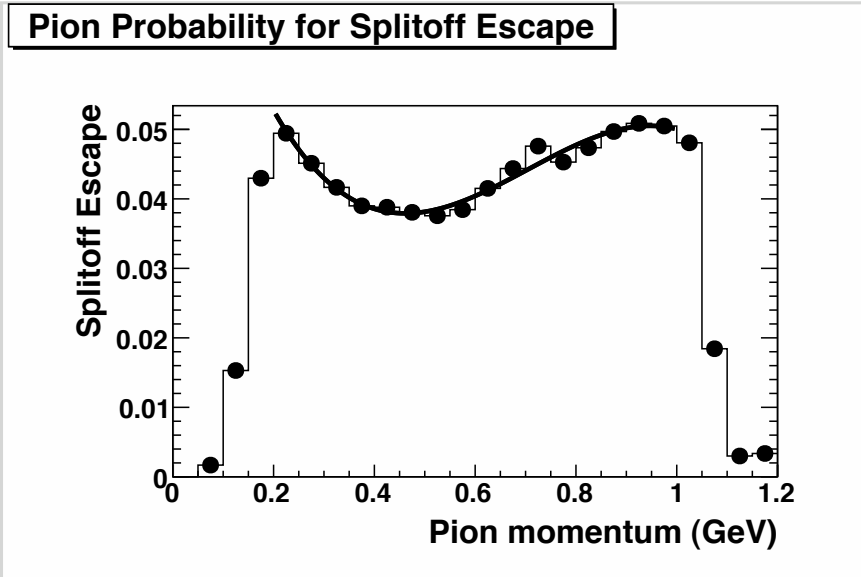
Figure 5.1: The Monte Carlo probability for a $\pi^{\pm}$ track to generate a splitoff escape extra shower as a function of the pion momentum.

.
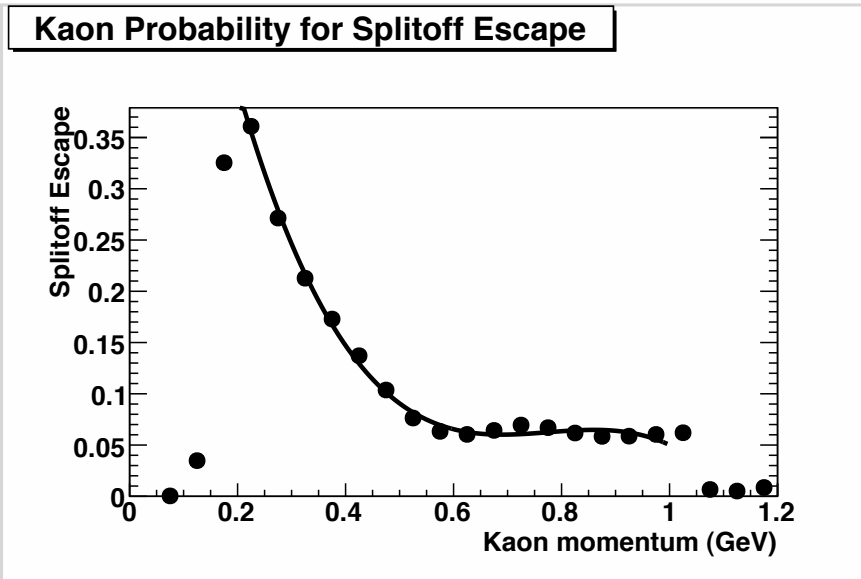
Figure 5.2: The Monte Carlo probability for a $K^{\pm}$ track to generate a splitoff escape extra shower as a function of the Kaon momentum.

.

96
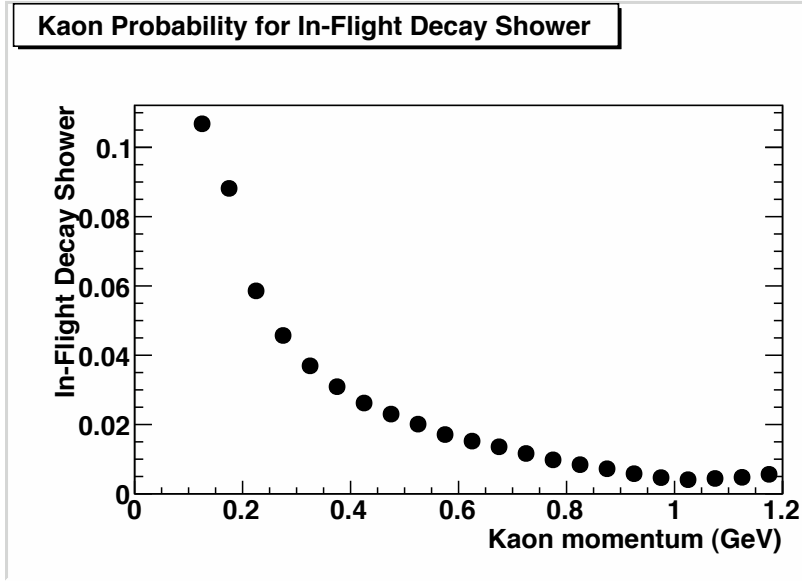
Figure 5.3: The Monte Carlo probability for a $K^{\pm}$ track to generate an extra shower from an in-flight decay as a function of the pion momentum.

.

then reconstruct the other side D using everything except showers that are not matched to a π^0 or η. For this study, all splitoff approved showers not matched to a π^0 or η are considered extra showers regardless of the shower energy or the types of tracks in the event. If the beam constrained mass of the other side is within 0.005 GeV/c^2 of the known D mass and $|\Delta E| < 0.025$ GeV then we accept the event.

We first study the splitoff escapes from pion tracks because they are backgrounds to our kaon study. We isolate splitoff escapes from pions by only considering events without kaons. In order to determine differences in the momentum dependence between data and the Monte Carlo simulation, we attribute the extra shower to the track that intersects the calorimeter closest to where the shower was found. This method can fail in two different ways. First, splitoff escape showers can be far from where the track collided with the calorimeter, and so the closest track to the shower is not necessarily the track that created it. Second, a splitoff escape could potentially be included in π^0 or η candidate while a true shower was labeled as a splitoff escape if doing so does not significantly

97

change the mass pull of the candidate or the ΔE or M_{bc} of the D candidate. Therefore, we should expect the measured momentum dependence to be distorted. However, we cannot proceed unless we assume something, so we assume that the track closest to the shower is the one that created it.

Let $\alpha_\pi(p)$ be the momentum dependent probability for a pion with momentum p to create an extra shower. For an event with N pion tracks, the probability that there are zero extra showers ($\mathcal{P}(n_\gamma = 0)$) is

$$\mathcal{P}(n_\gamma = 0) = \Pi_{i=1}^{N}(1 - \alpha_\pi(p_i)). \qquad (5.7)$$

The probability that there is only 1 extra shower created by a pion with momentum p_k is

$$\mathcal{P}(n_\gamma = 1, p_k) = \alpha_\pi(p_k)\Pi_{i \neq k}^{N}(1 - \alpha_\pi(p_i)). \qquad (5.8)$$

Therefore, the ratio ($R(p_k)$) of the number of events where exactly 1 extra shower was generated by a track with momentum p_k, and the number of events where 0 extra showers were created, but still contained a track with momentum p_k is:

$$R(p_k) = N_{n_\gamma=1,p_k}/N_{n_\gamma=0,p_k} = \frac{\alpha_\pi(p_k)}{1 - \alpha_\pi(p_k)}, \qquad (5.9)$$

$$\alpha_\pi(p_k) = \frac{R(p_k)}{1 + R(p_k)}. \qquad (5.10)$$

To determine the above ratio ($R(p_k)$), we divide the momentum distribution of tracks closest to the extra shower when there is only 1 extra shower, by the momentum distribution of all tracks in the event when there are no extra showers. For each bin of this distribution we solve for the $\alpha_\pi(p)$. Figure 5.4 shows the measured $\alpha_\pi(p)$. Note that the reconstructed shape in Figure 5.4 is not the same as the generator level shape in Figure 5.1. This is because the track closest to the splitoff escape is not necessarily the track that created it. We can infer from this plot that a splitoff escape created by a low energy pion is more likely to be far away from it than an extra shower created by a high energy pion.
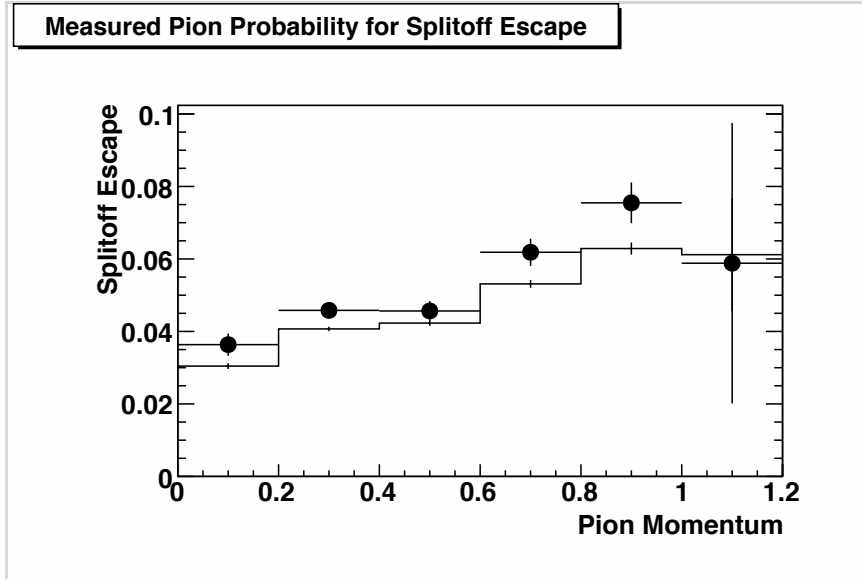
Figure 5.4: The measured probability for a π^+ to create a splitoff escape versus π momentum (GeV/c). The black dots are data and the histogram is the same measurement performed on the Monte Carlo sample.

.

In order to compare the data and the Monte Carlo sample we take the ratio of their $\alpha_\pi(p)$ distributions found for each (Figure 5.5). Within the uncertainties, the momentum dependance of α_π seems to be the same in both data and Monte Carlo samples. The total rate in data appears to be a factor of 1.139 ± 0.033 larger than the rate in the Monte Carlo simulation.

Next, we need to compare the probability for a kaon track to create extra showers in data and the Monte Carlo simulation. We do this by selecting events that have only one kaon in them. Unlike the pions, if there is an extra shower from a kaon we know which kaon it came from. However, there is a large background from events where the extra shower came from a pion. We use the results of the study of the pions and the backgrounds expected from the Monte Carlo simulation to subtract events with showers from pions from the total number of events with an extra shower. We normalize the Monte Carlo pion backgrounds using the sum of the number of events with 0 and 1

Pion Splitoff Escape Probability Reweight
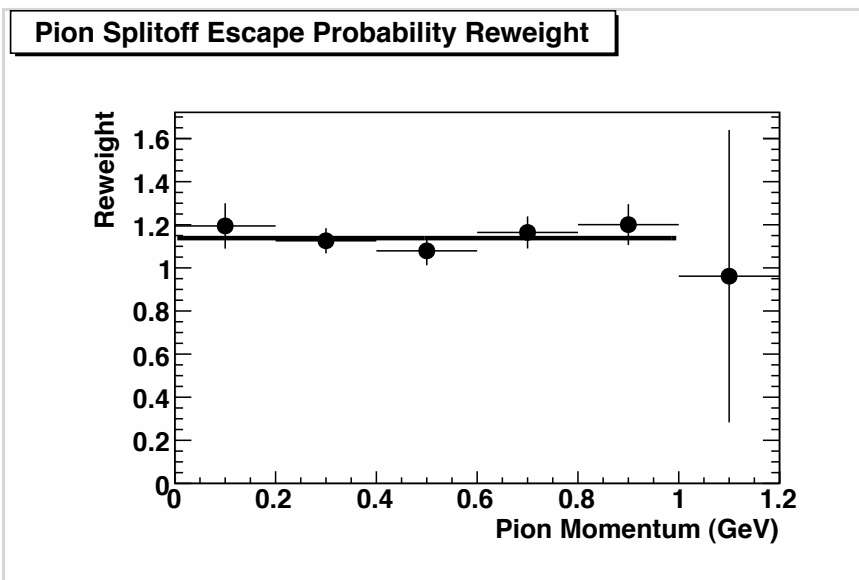
Figure 5.5: The data to Monte Carlo ratio between the probability for a π^+ to create a splitoff escape as a function of the π momentum (GeV/c). This ratio is consistent with being flat, meaning that only the total probability, rather than the momentum dependence, differs between data and Monte Carlo samples. The average ratio is 1.139 ± 0.033.

.

extra showers and also make sure via reweighting that the relative composition of events with 1 kaon and N pions is the same in data and Monte Carlo samples.

Figure 5.6 shows the momentum distribution of kaons in events that have one extra shower and only one kaon in the event as well as the expected background from events where the extra shower was created by a pion.

To determine the probability of a kaon creating an extra shower we divide the background subtracted kaon spectrum for $N_{show} = 1$ by the spectrum for $N_{show} = 0$. From this ratio and Equation 5.10 we calculate the probability for a kaon track to produce an extra shower in the event (Figure 5.7).

We find significant differences in the measured probability for both high and low momentum kaons. The process where kaons generate extra showers via in-flight decays is assumed to be well modeled by the Monte Carlo simulation since it is governed by
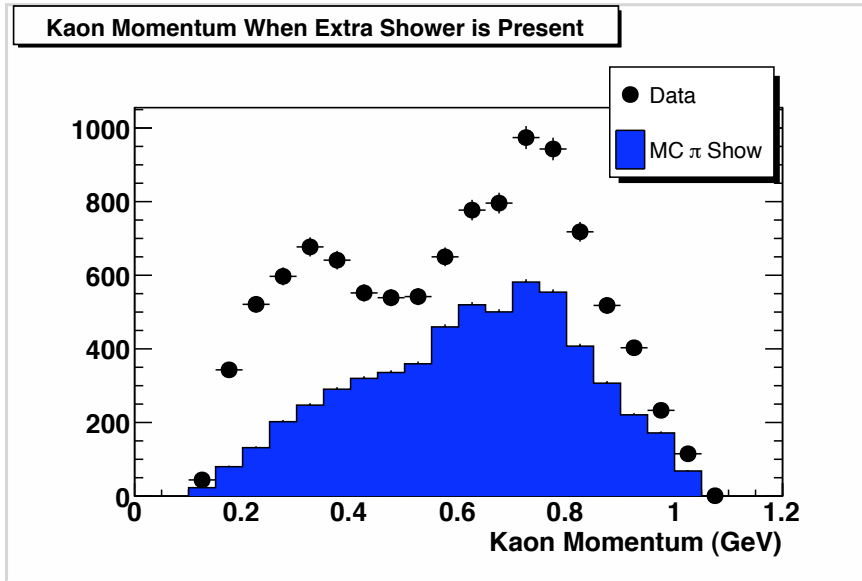
Figure 5.6: The momentum distribution of Kaons in events with only 1 kaon when there is also 1 extra shower in the event. The black dots are data. The blue histogram is the component of the data that is expected from events when the extra shower was generated by one of the pions rather than the kaon.

.
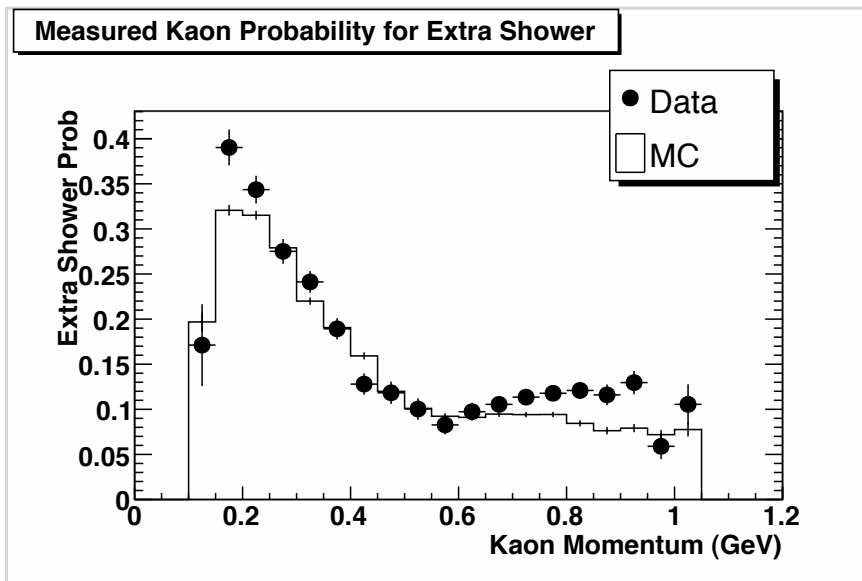
Figure 5.7: The probability of the kaon track creating an extra shower as a function of the kaon momentum. The black dots are the probability extracted from data, and the histogram is the Monte Carlo prediction.

Kaon Splitoff Escape Re-weight
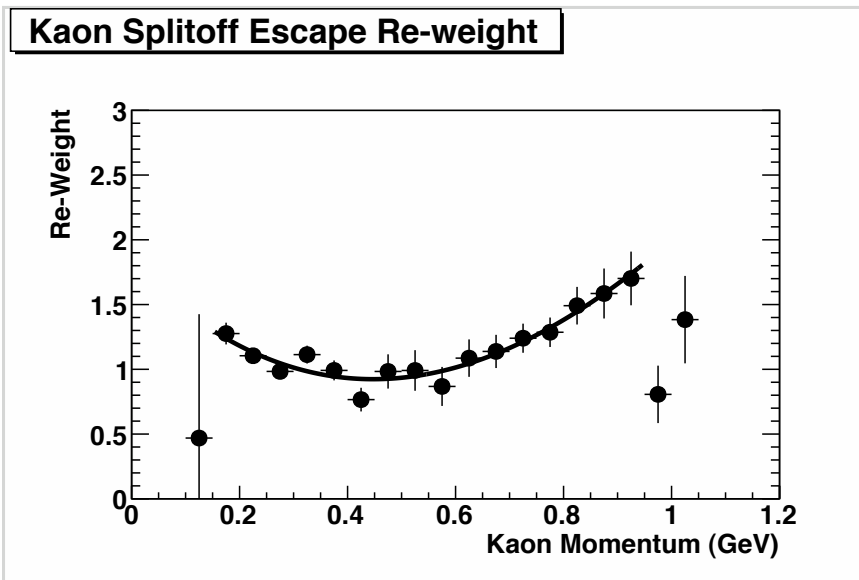
Figure 5.8: The measured splitoff escape probability divided by the Monte Carlo splitoff escape probability as a function of kaon momentum.

.

time dilation. So the differences between the data and the simulation are attributed to the simulation of hadronic interactions in the calorimeter. The reweight values to correct the kaon splitoff escape probability in the simulation is shown in Figure 5.8.

We have investigated whether or not positively and negatively charged kaons require different corrections since interactions between nuclei for K^+ and K^- are known to differ significantly. Figure 5.9 shows $\alpha(p_K)$ and the corrections for both positive and negative kaons.

To adjust the Monte Carlo sample to match the data, we first fit the Monte Carlo probabilities, α, and the reweighting factors, β, to polynomials to obtain smooth functions of momentum. Each track is given a weight of either β if it has an extra shower, or a weight of $(1 - \beta\alpha)/(1 - \alpha)$ if it does not have an extra shower. The weight of the event is the product of the track weights.

We also correct the energy distribution of these extra showers. The energy of an extra shower affects whether or not they may be included in a false π^0 or $\eta \to \gamma\gamma$ candidate.

102
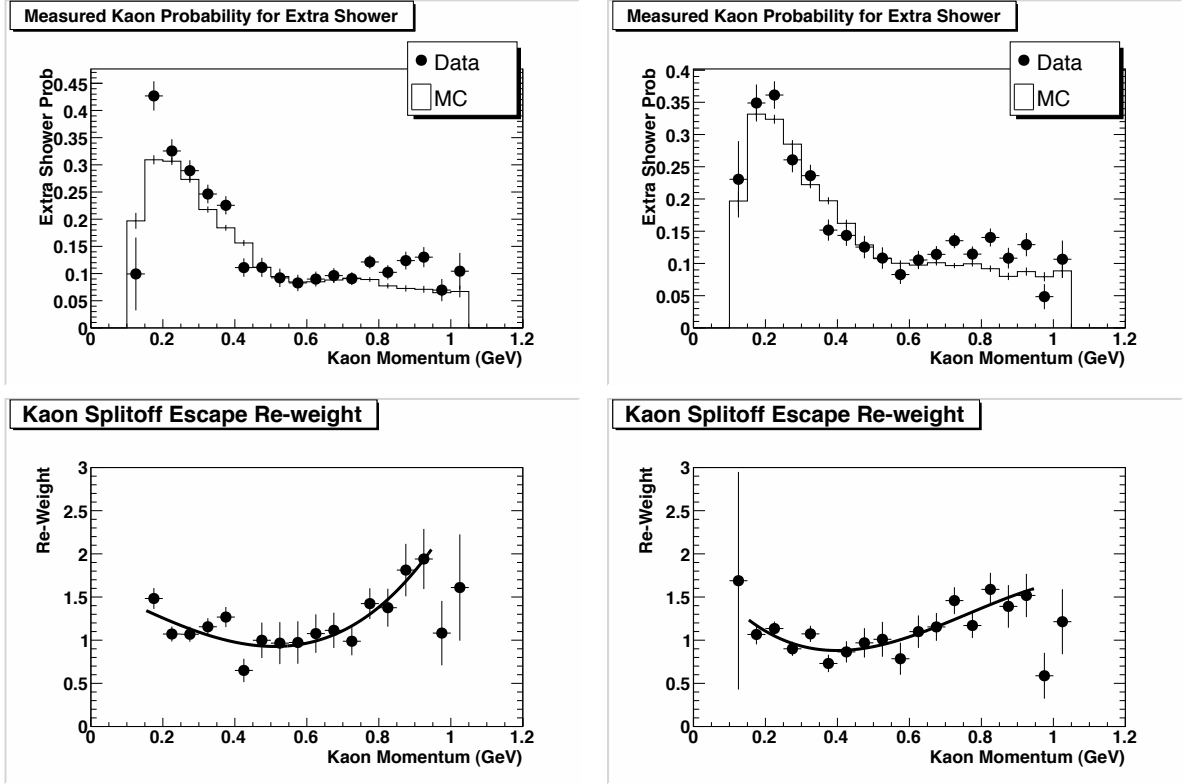
Figure 5.9: The difference in the splitoff escape probabilities, and reweights for positive K (left) and negative K (right).

This is important because if an extra shower creates a fake π^0 or η we won't be able to remove the shower from the event.

We determine corrections for the extra shower energy by using the ratio of the energy distribution in data to the Monte Carlo energy distribution. For events with kaons we subtract the expected contributions from pion showers. The reweights that are applied to the Monte Carlo sample in order to match the data are given in Tables 5.2 and 5.3.

5.5 $\eta \to \gamma\gamma$ Efficiency Correction

The $\eta \to \gamma\gamma$ efficiency correction is determined using the missing mass technique described earlier in this chapter. We obtain preliminary branching fractions for hadronic

Table 5.2: The energy distribution reweights applied to extra showers created by a pion.

Shower Energy Range (GeV)	reweight
$0.0 \ < \ E_\gamma \ < 0.05$ GeV	0.748 ± 0.055
0.05 GeV $\ \leq \ E_\gamma \ < 0.10$ GeV	1.25 ± 0.058
0.10 GeV $\ \leq \ E_\gamma \ < 0.15$ GeV	1.20 ± 0.08
0.15 GeV $\ \leq \ E_\gamma \ < 0.20$ GeV	1.01 ± 0.10
0.20 GeV $\ \leq \ E_\gamma \ < 0.25$ GeV	1.11 ± 0.14
0.25 GeV $\ \leq \ E_\gamma$	0.58 ± 0.09

Table 5.3: The energy distribution reweights applied to extra showers created by a Kaon.

Shower Energy Range (GeV)	reweight
$0.0 \ < \ E_\gamma \ < 0.05$ GeV	1.07 ± 0.06
0.05 GeV $\ \leq \ E_\gamma \ < 0.10$ GeV	1.09 ± 0.05
0.10 GeV $\ \leq \ E_\gamma \ < 0.15$ GeV	0.94 ± 0.05
0.15 GeV $\ \leq \ E_\gamma \ < 0.20$ GeV	0.72 ± 0.05
0.20 GeV $\ \leq \ E_\gamma \ < 0.25$ GeV	0.82 ± 0.08
0.25 GeV $\ \leq \ E_\gamma$	1.39 ± 0.09
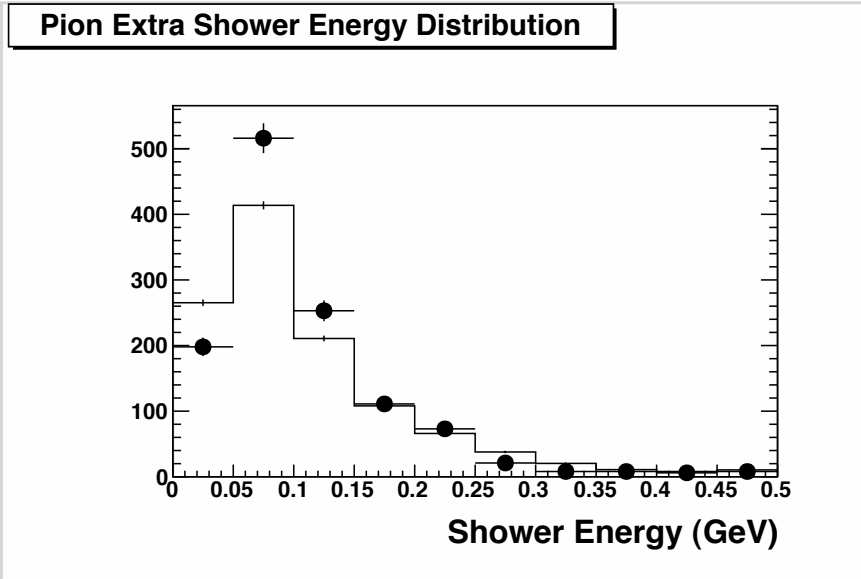
Figure 5.10: The energy distribution for extra showers created by pions in the
calorimeter. The black dots are data and the histogram is from sim-
ulation. The distributions are normalized by the number of events
with either 0 or 1 extra showers.

.
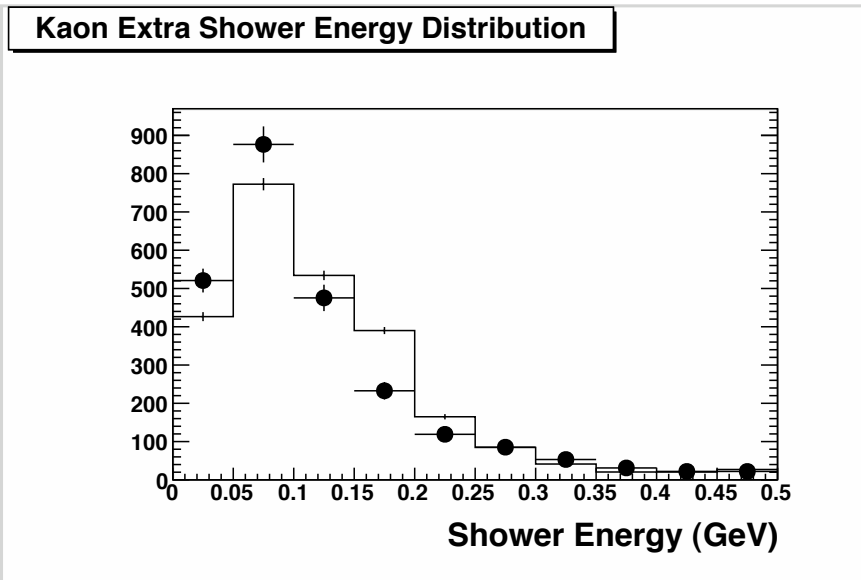
Figure 5.11: The energy distribution for extra showers created by kaons in the
calorimeter. The black dots are data and the histogram is from sim-
ulation. The distributions are normalized by the number of events
with either 0 or 1 extra showers.

.

decays that include $\eta \rightarrow \gamma\gamma$, and select events where the other side D is consistent with one of these decays. A "missing" mass is calculated using everything in the event except for possible η candidates and extra showers. Events where the missing mass is consistent with an η are selected, and the $\eta \rightarrow \gamma\gamma$ efficiency is determined by how often one of these events actually had an η candidate that passed all of our requirements.

For most of the $X+\eta$ decays that are found in the data there is a corresponding $X+K^0$ decay. Within our missing mass resolution the masses K^0 and η are close and $X + K_L$ decays can fake $X + \eta$ decays. We select $X + \eta$ decays where the corresponding $X + K_L$ decays do not overwhelm our study with background. Table 5.4 gives the preliminary branching fractions of interest. We select against decays with poor resolution and decays where the $X + K_L$ branching fraction is much larger than the $X + \eta$ branching fraction. We exclude the following decays from our study: $D^+ \rightarrow \pi^+\pi^0\pi^0\eta$, $D^+ \rightarrow \pi^+\eta$, $D^+ \rightarrow \pi^+\pi^+\pi^-\eta$, and $D^0 \rightarrow \pi^+\pi^-\pi^0\eta$.

Table 5.4: The preliminary $X + \eta$ and $X + K_L$ branching fractions that were used to decide which decays to use for the η systematic study, and which ones to select against.

X	$X + \eta$ Branching Fraction	$X + K_L$ Branching Fraction
π	0.118%	1.47%
3π	0.14%	2.8%
πK_S	0.44%	0.35%
K_S	0.16 %	too small
πk	0.75%	0.4%
$2\pi K_s$	0.27%	0.046%
$2\pi\pi^0$	0.19%	5.10%
$\pi^0 K_S$	0.37%	0.27%

MC Number Eta to GG Fit
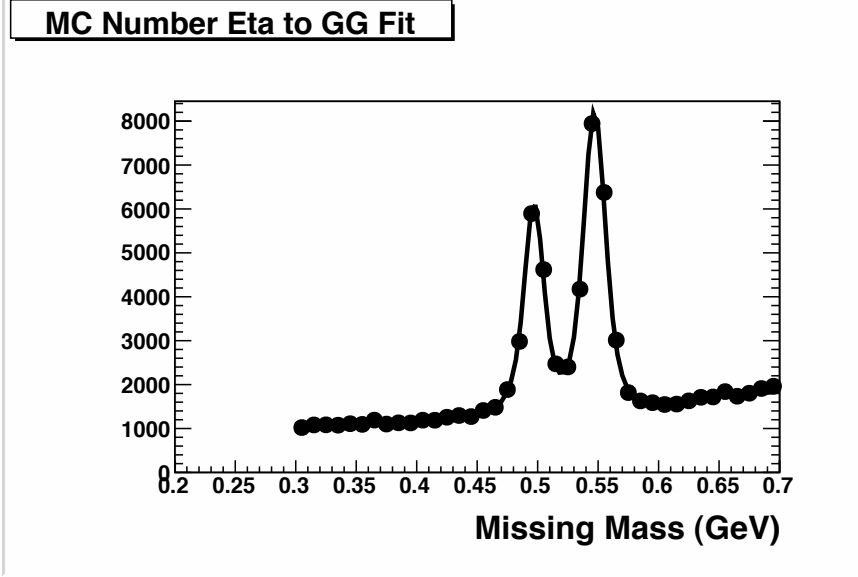
Figure 5.12: The missing mass distribution for $X\eta$ candidates with no require-
ments on η candidates or showers that could potentially be part of an
η candidate. We see two peaks. One peak is from η and the other
peak is from K_L.

The remaining $X + \eta$ decays have corresponding $X + K_L$ decays with comparable
branching fractions. The missing mass distribution for $X + \eta$ candidates clearly shows
both an η and a K_L mass peak (Figure 5.12). The two peaks overlap at approximately
the 2σ level. The K_L peak compromises our ability to accurately count the number of η
that should be used in the denominator of our efficiency calculation.

To minimize the K_L peak we impose minimal requirements on the event that have
little effect on the number of η candidates, but remove most of the K_L candidates. The
probability that an $\eta \rightarrow \gamma\gamma$ looses both showers is very low, so we require that there is
at least one shower in the event that could have come from an η. If there is only one
shower we make additional requirements. Unlike an η, showers from a K_L should be in
the direct path of the K_L. So if the extra shower energy is less than $1/2$ the η energy, the
cosine of the shower with the missing momentum must be less than 0.90. Further, if the
shower is really from an $\eta \rightarrow \gamma\gamma$, then energy conservation requires $E_\gamma + |\vec{P}_\eta - \vec{P}_\gamma| = E_\eta$.

107

We require that the E_η predicted by the shower and the missing momentum is within 0.2 GeV of the missing energy. These additional requirements diminish the relative size of the K_L peak (Figure 5.13).

To determine the η efficiency as a function of momentum we require the missing mass to be between 0.52 and 0.58 GeV/c^2. The size of the backgrounds relative to the η are determined by fitting the missing mass distribution with a linear model to describe the combinatoric backgrounds and double gaussians to describe the K_L and η contributions. Monte Carlo backgrounds to the missing momentum spectrum are scaled by the missing mass fit values to match the levels seen in data and subtracted from the data spectrum. The efficiency as a function of η momentum is the ratio of the missing momentum spectrum with requiring a reconstructed η that passes all requirements and the spectrum without requiring that an η was found. The ratio between the efficiency found in data and the efficiency found in Monte Carlo samples gives the systematic correction to the efficiency.

This analysis employs four different sets of requirements for $\eta \to \gamma\gamma$ candidates. The generically reconstructed D has low quality η ($-25 < \chi_m(\eta) < 15$) and high quality η ($-5 < \chi_m(\eta) < 3$). On the signal side, there are $\eta \to \gamma\gamma$ requirements for $D^+ \to \eta(\gamma\gamma)e^+\nu$ and separate requirements for $\eta \to \gamma\gamma$ from $\eta' \to \pi\pi\eta(\gamma\gamma)$ decay. We determine a correction for each set of requirements.

In the momentum range 0..2 GeV/c to 0.8 GeV/c the reweights are consistent with a constant correction, independent of momentum. Depending on the set of requirements the efficiency correction ranges between 0.97 and 1.006 with uncertainties of approximately 3.3% (Table 5.5).
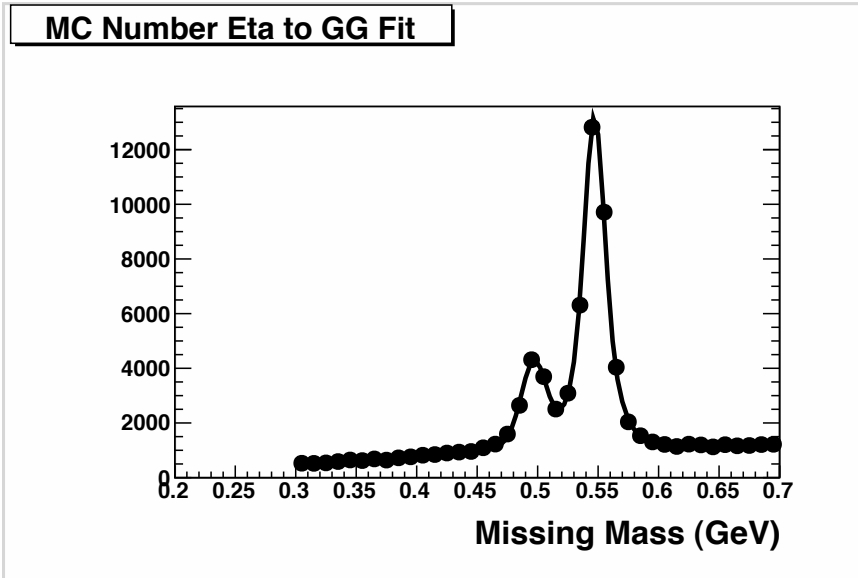
Figure 5.13: The missing mass distribution for $X + \eta$ candidates for the Monte Carlo sample. We have imposed minimal requirements to remove K_L events. Note that after adding requirements we have a much smaller K_L peak relative to the η peak than Figure 5.12.

Table 5.5: The efficiency correction and uncertainty in the correction for $\eta \rightarrow \gamma\gamma$ for the 4 different sets of η requirements used in the analysis.

Cut Set	reweight and uncertainty
Other Side Low	1.006 ± 0.033
Other Side High	0.984 ± 0.033
$D \rightarrow \eta e \nu$	0.975 ± 0.033
$D \rightarrow \eta' e \nu$	0.970 ± 0.033

Data Missing Mass Distribution of Candidate $X\pi^0$ Decays

Missing Pi0 Mass For Systematic Study
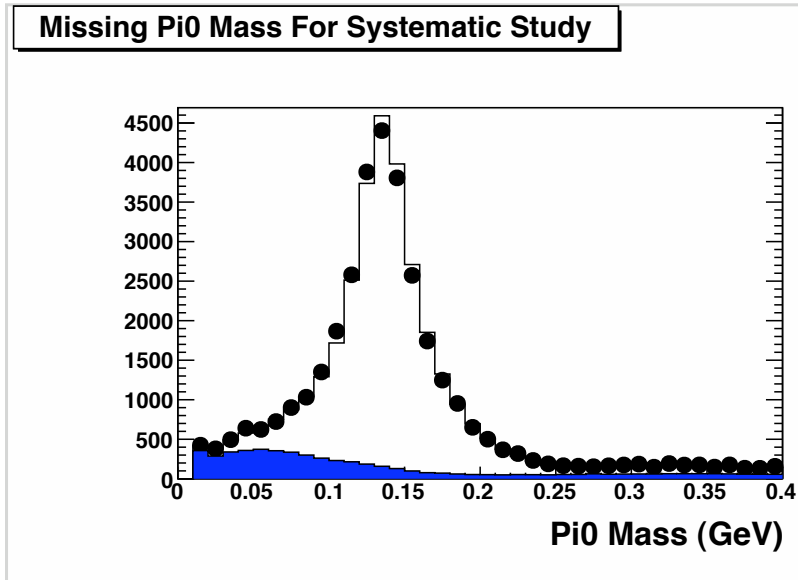
Figure 5.14: The missing mass distribution for $X + \pi^0$ candidates. Data is represented by black dots, expected signal with a clear histogram and expected backgrounds with a blue histogram .

5.6 $\pi^0 \rightarrow \gamma\gamma$ Efficiency Correction

We use the missing mass technique to determine the $\pi^0 \rightarrow \gamma\gamma$ efficiency corrections. As the mass distribution in Figure 5.14 show the backgrounds are relatively small and there is no need to impose minimal requirements as was done in $\eta \rightarrow \gamma\gamma$.

To determine the π^0 efficiency as a function of momentum we require the missing mass to be between 0.10 GeV/c^2 and 0.20 GeV/c^2 then divide the resulting background subtracted momentum distribution of events with good π^0 candidates by the distribution from all events to determine the efficiency. The ratio between the data efficiency and the Monte Carlo efficiency gives us the reweight correction that needs to be applied to the Monte Carlo sample. This analysis employs four different sets of requirements for $\pi^0 \rightarrow \gamma\gamma$ candidates. The generically reconstructed D has low quality π^0 ($-25 < \chi_m(\pi^0) < 15$) and high quality π^0 ($-5 < \chi_m(\pi^0) < 3$) criteria. For the signal side D there are two

Pi0 Efficiency With Pull -3 to 3
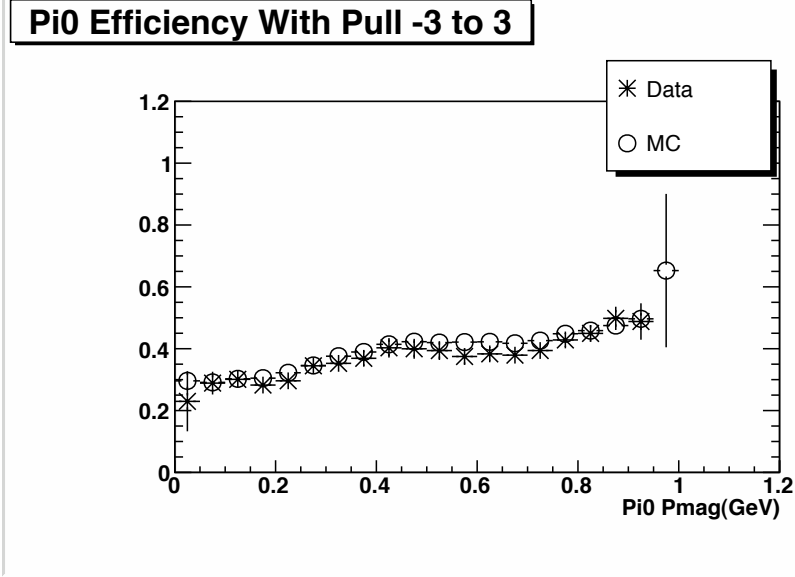
Figure 5.15: The efficiency of π^0 as a function of momentum for both data and Monte Carlo samples.

different sets of mass pull requirements ($|\chi_m(\pi^0)| < 3$ and $-3.5 < \chi_m(\pi^0) < 2.5$) used to reconstruct the various $D^+ \rightarrow \eta^{(\prime)}$ decay modes. Figure 5.15 shows the efficiency of π^0 with $|\chi_m(\pi^0)| < 3$ and Figure 5.16 shows the corresponding correction. The efficiency corrections for the different π^0 requirements are given in Table 5.6.

Table 5.6: The efficiency correction and uncertainty in the correction for $\pi^0 \rightarrow \gamma\gamma$ for the 4 different π^0 requirements used in the analysis.

Mass Pull	reweight and uncertainty
-25 to 15	0.991 ± 0.012
-5.0 to 3.0	0.964 ± 0.013
-3.0 to 3.0	0.954 ± 0.013
-3.5 to 2.5	0.958 ± 0.013

111

Pi0 Re-weight With Pull -3 to 3

Pi0 Pmag(GeV)
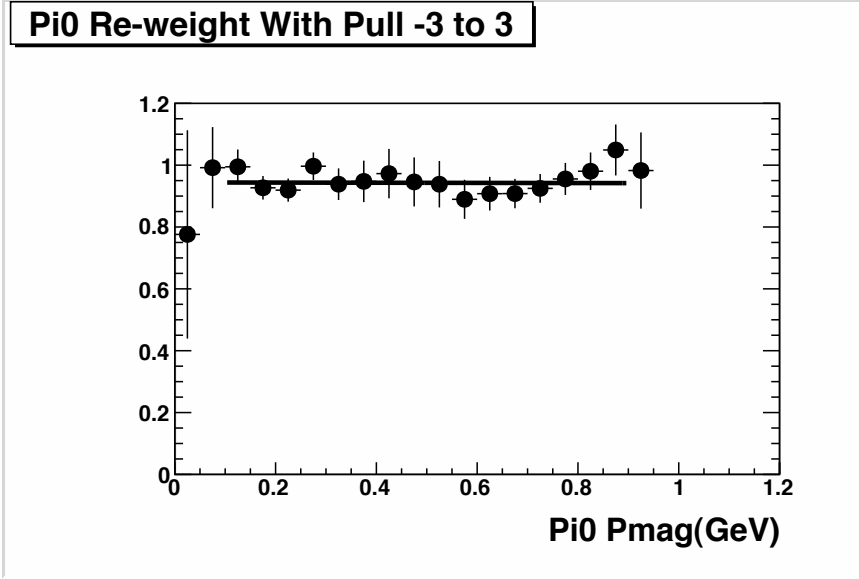
Figure 5.16: The Monte Carlo efficiency reweight for reconstructed $\pi^0 \to \gamma\gamma$ with $|\chi_m(\pi^0)| < 3$ as a function of momentum.

5.7 K_L Energy Deposition Correction

An important class of low quality events are events that contain a K_L that deposits a large fraction of its energy in the calorimeter. These events reconstruct the neutrino fairly well, but have one or more showers in the event that came from the K_L rather than a π^0 or an $\eta \to \gamma\gamma$. The details of hadronic interactions in the calorimeter are difficult to simulate so we explicitly study the K_L energy deposition to understand how often the neutrino can be reconstructed in events with a K_L.

The energy deposition of K_L in the CLEO crystal calorimeter has been previously studied for CLEO-2 [35] and CLEO-c [34]. It is necessary to repeat these studies for this analysis because previous studies did not use splitoff-approved showers and only considered the total energy deposited in the calorimeter and not the number of showers produced.

To determine the K_L corrections in this analysis we use the missing energy method outlined in Section 5.1. As was done in [34] we study the K_L by using the two D^0 decays $D^0 \rightarrow K_L \pi^+ \pi^-$ and $D^0 \rightarrow K_L \pi^+ \pi^- \pi^0$. We begin by finding a "signal side" D-tag of type $K^- \pi^+$, $K^- \pi^+ \pi^0$, or $K_S(\pi^+ \pi^-)\pi^0$. The generic reconstruction is performed on the "other side" D, and we select events where the "other side" consist of two oppositely charge pions, no kaons, no $\eta \rightarrow \gamma\gamma$, and at most one π^0 (required to have $|\chi_m(\pi^0)| < 3$). The missing four-vector is required to have a mass consistent with a K_L, and we say the K_L deposited energy if there are showers with energy greater than 0.030 GeV/c^2 within a cone of $cos(\theta) > 0.98$ around the direction of the missing momentum.

We consider events with a missing mass between 0.46 GeV/c^2 and 0.52 GeV/c^2. We subtract backgrounds predicted by the Monte Carlo simulation from both data and Monte Carlo samples. For the backgrounds subtracted from the data we normalize Monte Carlo backgrounds using the sideband region 0.36 GeV/c^2 to 0.42 GeV/c^2.

Without the splitoff requirement we find that K_L deposit showers $49.9\pm0.6\%$ for data and $44.2 \pm 0.2\%$ for the Monte Carlo simulation, which is consistent with the previous CLEO-c study [34]. With the splitoff requirement we find that data has a total rate of $39.2 \pm 0.6\%$ and the Monte Carlo sample has a total rate of $32.3 \pm 0.1\%$. We determine the K_L showering rate as a function of K_L momentum (Figure 5.17) and find that the discrepancy in the total rate is primarily due to the region $P(K_L) < 300$ MeV/c. The drop in the Monte Carlo rate below 300 MeV/c is present with or without requiring splitoff-approval, and is an artifact of the FLUKA algorithm used to simulate K_L interactions. The FLUKA code stops propogating hadronic interactions once the kinetic energy of a particle drops below 50 MeV, which corresponds to a K_L momentum of approximately 0.23 GeV/c.

To correct for the rate problem we reweight the events with and without K_L showering. In the region of K_L momentum greater than 0.30 GeV/c we give the constant
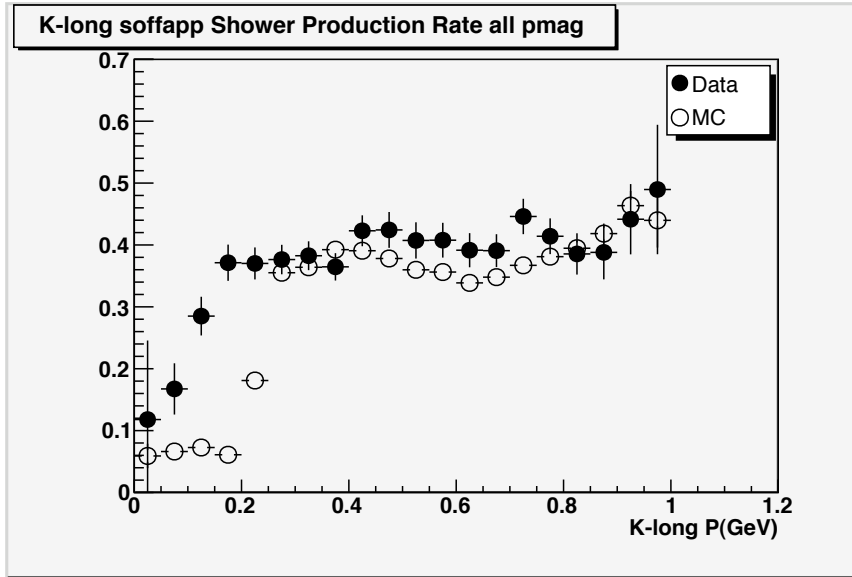
Figure 5.17: The rate that K_L produce splitoff approved showers as a function of K_L momentum. The black dots are data and the clear circles are from the Monte Carlo sample.

reweight of 1.07 ± 0.02 for K_L that create a splitoff approved shower and 0.953 ± 0.013 for K_L that do not create splitoff approved showers (uncertainties of these two weights are ant-correlated with one another). The corrections to the K_L showering rates as a function of momentum is given in Table 5.7.

Because we reconstruct π^0 and $\eta \to \gamma\gamma$ to calculate the neutral energy and remove extra showers, it is important to not only know the total energy deposited by the K_L but also the number of splitoff approved showers that are created. The number of showers produced in both data and Monte Carlo samples for the full range of K_L momentum is shown in Figure 5.18, normalized to the number of showering K_L.

To test the number of showers as a function of K_L momentum, we divide the momentum range into bins: $(0.00 - 0.25 \text{ GeV/c})$, $(0.25 - 0.50 \text{ GeV/c})$, $(0.50 - 0.75 \text{ GeV/c})$, and $(0.75 - 1.00 \text{ GeV/c})$, normalized by the number of showering K_L in each bin. The

Table 5.7: The momentum dependent reweights to the K_L showering rate. The "showering weight" is applied to K_L that did not create splitoff approved showers, and the "no showering weight" is for events that did.

K_L Momentum Range (GeV/c)	Showering Weight	No Showering Weight
0.00 - 0.05	1.99 ± 2.26	0.94 ± 0.14
0.05 - 0.10	2.53 ± 0.68	0.89 ± 0.04
0.10 - 0.15	3.92 ± 0.49	0.77 ± 0.03
0.15 - 0.20	6.09 ± 0.57	0.67 ± 0.03
0.20 - 0.25	2.04 ± 0.15	0.77 ± 0.03
> 0.25	1.07 ± 0.02	0.95 ± 0.01

reweights for events with 1 and events with 2 showers are given in table 5.8. The reweights are consistent with 1.00 for all momentum bins.

Table 5.8: K_L reweights for the number of showers produced for different regions of K_L momentum.

K_L Momentum Range (GeV/c)	1 Shower	2 Showers
0.00 - 0.25	1.02 ± 0.05	0.85 ± 0.12
0.25 - 0.50	1.03 ± 0.03	0.89 ± 0.06
0.50 - 0.75	1.01 ± 0.03	1.00 ± 0.06
0.75 - 1.00	1.01 ± 0.04	1.00 ± 0.09
All	1.02 ± 0.02	0.93 ± 0.04

Finally, we consider the fraction of the K_L energy in each of the showers produced. We consider the distribution of E_{show}/E_{K_L} for interactions with one splitoff-approved shower (Figure 5.19) and interactions with two. In the case of two splitoff-approved
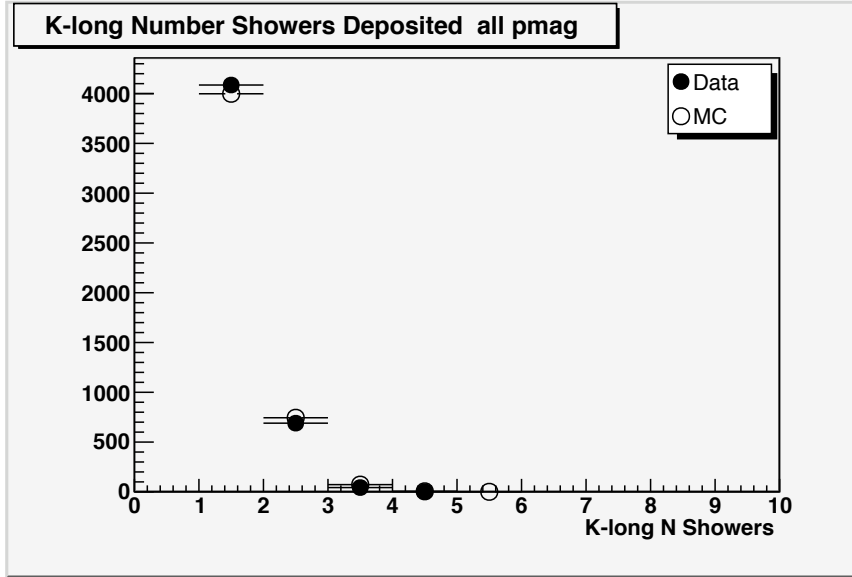
Figure 5.18: The number of splitoff approved showers created by the showering K_L in both data and Monte Carlo simulation. The Monte Carlo sample has been normalized so that the total number of showering K_L is the same as in data.

showers, we separately look at the distributions for the shower with the maximum energy (Figure 5.20) and the minimum energy (Figure 5.21).

The figures 5.19 through 5.21 show that the fraction of the K_L energy deposited in the shower is different in data than in Monte Carlo samples. For the case of K_L depositing one shower in the calorimeter we show E_{show}/E_{K_L} for the full range of K_L momentum (Figure 5.19), and divided into the different K_L momentum ranges (Figure 5.22).

The ratio between the E_{show}/E_{K_L} distribution (one shower) for data and for the Monte Carlo sample for the full momentum range is given in Figure 5.23. To get a smooth function to use as a reweight, we fit this distribution with a gaussian plus a polynomial

$$c_0 + c_1 x + c_2 x^2 + c_3 e^{(-c_4(x-c_5)^2)}, \tag{5.11}$$

where $x = E_{\text{show}}/E_{K_L}$ with 6 free parameters c_i. The fit parameters for the different momentum intervals are given in Table 5.9.
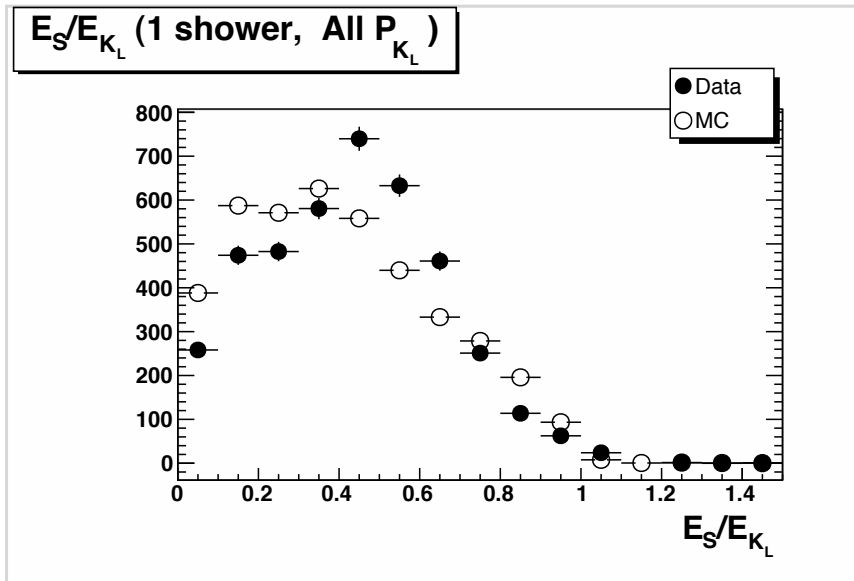
Figure 5.19: The ratio between the shower energy and the parent K_L energy in the situation where the K_L deposits only one splitoff-approved shower in the calorimeter.
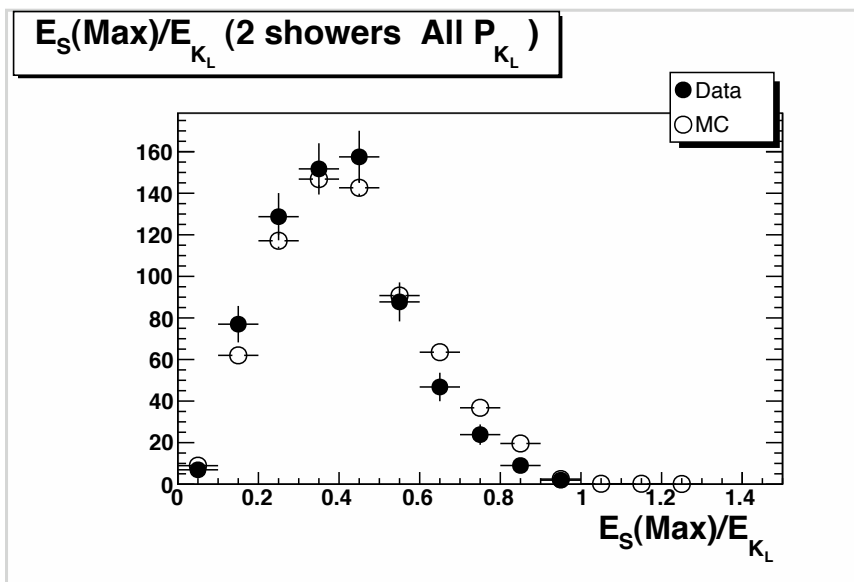
Figure 5.20: The ratio between the larger shower energy and the parent K_L energy in the situation where the K_L deposits 2 splitoff approved showers.
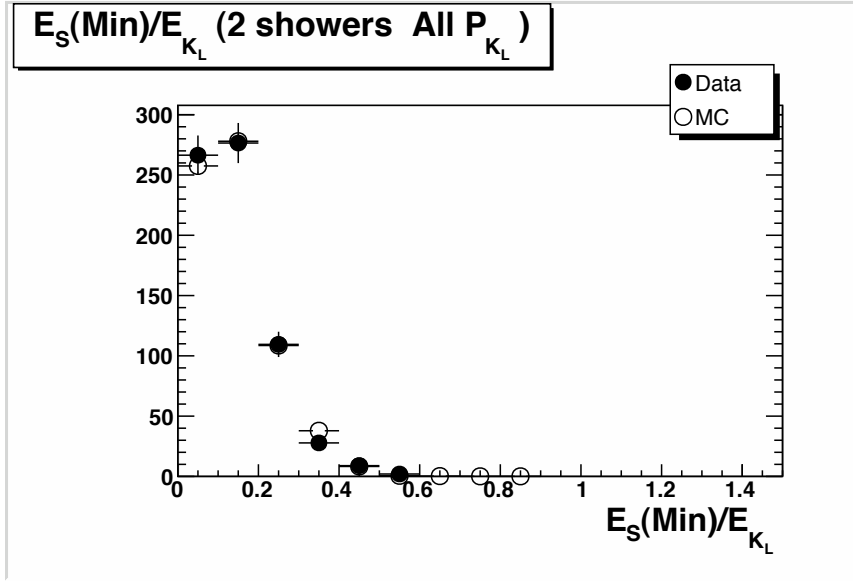
Figure 5.21: The ratio between the smaller shower energy and the parent K_L energy in the situation where the K_L deposits two splitoff approved showers.

In the case that the K_L deposits more than one shower, the ratio between the highest energy shower E_{show}/E_{K_L} distribution for data and Monte Carlo samples is fit to a line (Figure 5.25) with results given in Table 5.10. The energy distribution of the low momentum shower in the N=2 case is consistent with data and is not corrected.

To correct the Monte Carlo simulation we reweight the generator level K_L based on whether or not they produce splitoff approved showers in the calorimeter according to Table 5.7. The number of showers produced is consistent with data, so we do not reweight for the number of splitoff approved showers produced. Events with a showering K_L are given additional reweights as a funciton of K_L momentum and the E_{show}/E_{K_L} for the highest energy shower. The $N = 1$ reweights are given in Table 5.9, and the $N > 1$ reweights are given in Table 5.10.

Table 5.9: Parameters describing the E_S/E_{K_L} reweights for Number of Showers equal to one. The reweights are fit to the function: $c_0 + c_1 x + c_2 x^2 + c_3 exp(-c_4(x - c_5)^2)$, where x = E_S/E_{K_L}. The average correction for the full momentum range is given in Figure 5.23, and the corrections divided into momentum bins are shown in Figure 5.24.

K_L Momentum Range (GeV/c)	c_0	c_1	c_2	c_3	c_4	c_5
All	0.656	0.921	-1.113	0.693	38.036	0.565
0.00 - 0.25	0.483	1.174	-0.959	1.00	36.563	0.641
0.25 - 0.50	0.700	0.255	-0.207	0.537	27.943	0.533
0.50 - 0.75	0.749	0.868	-1.343	0.769	46.448	0.574
0.75 - 1.00	0.705	-0.253	-0.458	1.337	18.919	0.577

Table 5.10: Parameters describing the $E_S(\text{Max})/E_{K_L}$ reweights for K_L that produce two splitoff approved showers. The reweights are fit to the function: $b + m(x - 0.5)$, where $x = E_S(\text{Max})/E_{K_L}$. The average correction for the full momentum range is given in Figure 5.25 and the correction for the different momentum bins is shown in Figure 5.26.

K_L Momentum Range (GeV/c)	b	m
All	0.92	-0.875
0.00 - 0.25	0.78	-1.11
0.25 - 0.50	0.93	-0.93
0.50 - 0.75	0.92	-0.83
0.75 - 1.00	0.90	-0.30
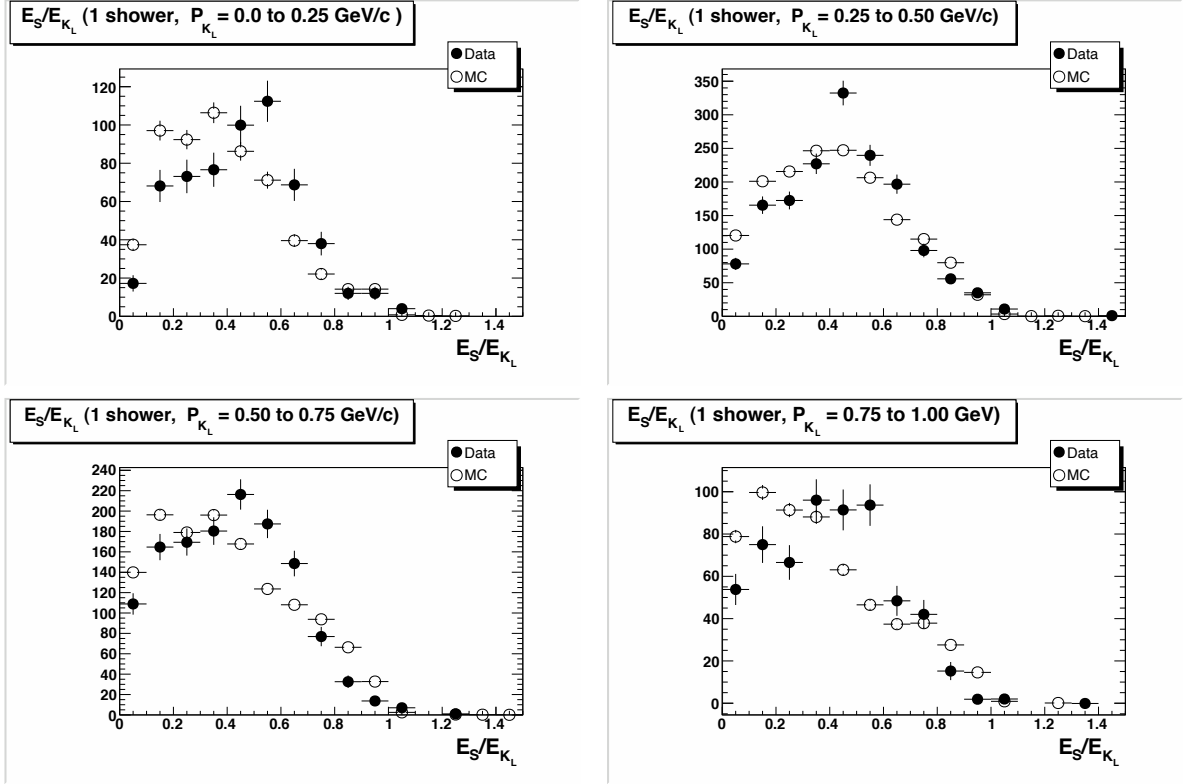
Figure 5.22: Ratio of shower energy to K_L energy in the situation where the K_L deposits only one splitoff-approved shower in the calorimeter. We show the momentum range 0.0 to 0.25 GeV/c (top left), 0.25 GeV/c to 0.50 GeV/c (top right), 0.50 GeV/c 0.75 GeV/c (bottom left), and 0.75 to 1.00 GeV/c (bottom right).

5.8   Tracking Corrections

All tracks in this analysis are required to be trkman-approved. A previous study [33] measured the trkman-approval efficiency using $\psi(2S) \to J/\psi\pi^+\pi^-$ and $J/\psi \to e^+e^-$ and found a Monte Carlo correction of 1.0004 ± 0.0009. We use this result to correct the Monte Carlo trkman-approval efficiency. To determine other tracking corrections we use the missing mass technique with the $D\bar{D}$ data at the $\Psi(3770)$. Using the decay $D^+ \to K^-\pi^+\pi^+$ we study the rate that kaons are either successfully identified or misidentified as pions. We find a charged D-tag, then generically reconstruct the other side D and require
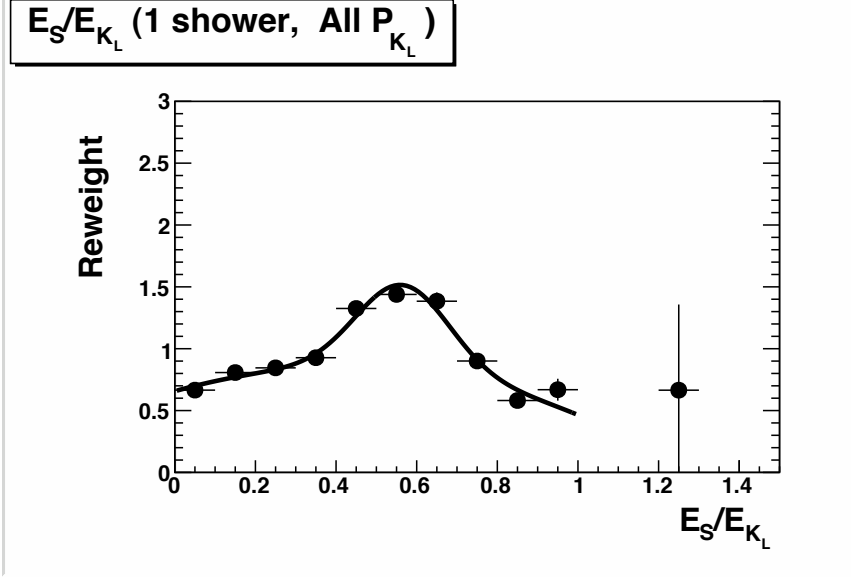
Figure 5.23: The reweight for the ratio between the shower energy and the parent K_L energy in the situation where the K_L deposits only one splitoff approved shower in the calorimeter.

that there are two pions with equal charge and an additional trkman-approved track (t_k) with the same charge as the D-tag. We use the conservation of energy and momentum and the beam energy to determine the expected mass of track t_k. Events where the expected mass of t_k is consistent with a kaon are considered true $D^+ \rightarrow K^-\pi^+\pi^+$ events.

The efficiency for identifying a trkman-approved kaon track as a kaon is determined by the number of events where the dE/dx and RICH information of t_k are consistent with a kaon. We find a kaon identification correction of 0.982 ± 0.015. We also want a correction for the rate that kaons are faking pions. There are two types of charged pion criteria in this analysis, the generic reconstruction criteria, and a "signal pion" criteria adopted from [33] used for charged pions in D-tags and semileptonic candidates. The correction for kaons faking generically reconstructed pions is 1.126 ± 0.036, and the correction for kaons faking signal pions is 1.17 ± 0.14. We also find a correction for true
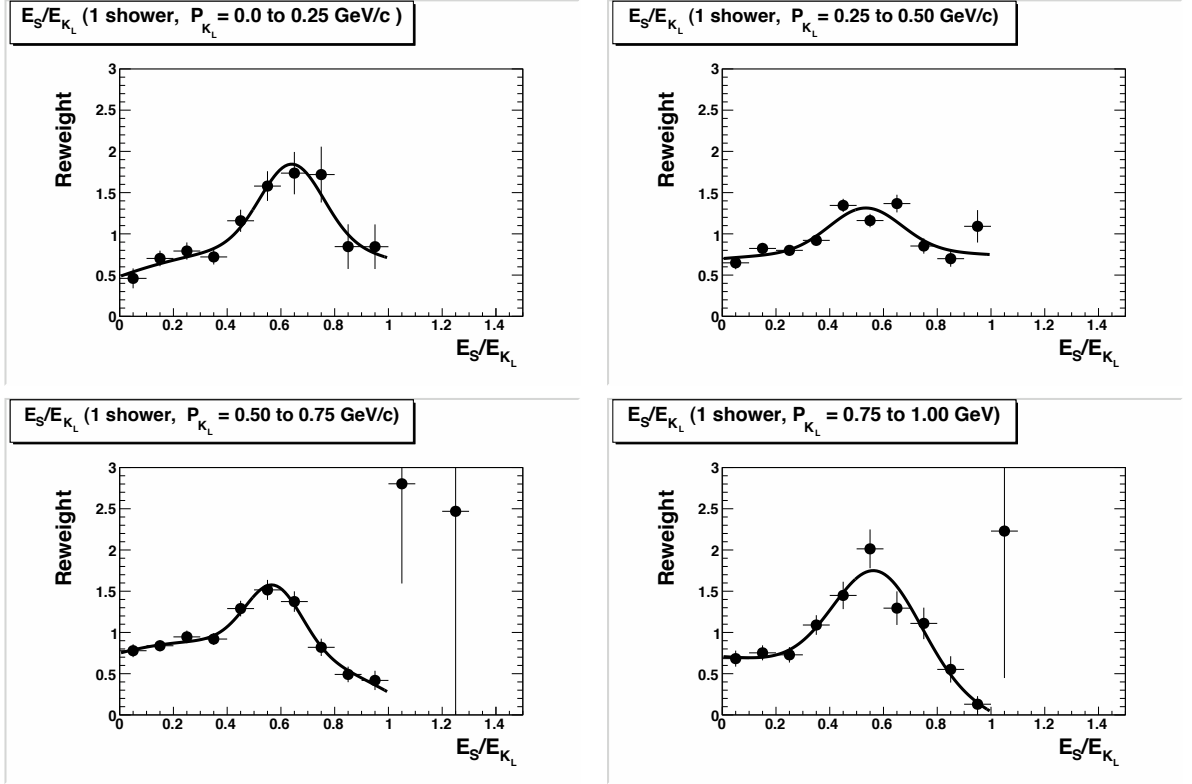
Figure 5.24: Correction factors for E_S/E_{K_L} in the situation where the K_L deposits only one splitoff-approved shower in the calorimeter. We show the momentum range 0.0 to 0.25 GeV/c (top left), 0.25 GeV/c to 0.50 GeV/c (top right), 0.50 GeV/c 0.75 GeV/c (bottom left), and 0.75 to 1.00 GeV/c (bottom right).

pions to fall into the signal pion category by looking at the the two charged pions in the generically reconstructed $K^-\pi^+\pi^+$ and find a pion correction of 0.998 ± 0.008.

5.9   Net Charge (Fake Track) Correction

In this analysis we make an event level requirement that the net charge of all trkman-approved tracks in the event is zero because a non-zero net charge indicates that we have either lost a track or have a fake track. We also make a candidate level requirement that all tracks in the other side D must either be part of a $K_S \rightarrow \pi^+\pi^-$ candidate or pass
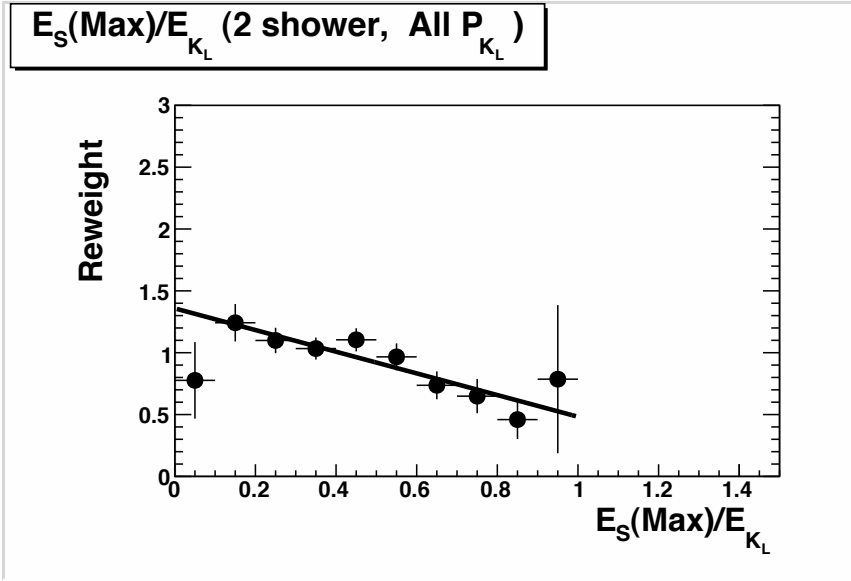
Figure 5.25: The reweight in the ratio between the shower energy and the parent K_L energy in the situation where the K_L deposits two splitoff approved shower in the calorimeter and we examine the highest energy shower.

strict vertex requirements. The vertex requirements remove bad candidates where a true $K_S \to \pi^+\pi^-$ is split between the two D candidates, but also helps to remove events with fake tracks that have managed to pass the net charge requirement. For example, events that have not detected a charged particle but reconstructed a track from random hits can pass the net charge requirement. In this situation, a track created from random hits is unlikely to pass the vertex requirements.

To determine if the efficiency for passing these requirements is correct in the Monte Carlo simulation, we study the rate that extra tracks cause the candidates to be rejected. We consider double tagged events where both D's can be described by D-tags with a beam constrained mass within 0.005GeV/c^2 of the D mass and $|\Delta E| < 0.025$ GeV. We require that all tracks in the D-tags are trkman-approved. The $\eta \to \gamma\gamma$ and $\pi^0 \to \gamma\gamma$ have $|\chi_m| < 3$ and are composed of splitoff-approved showers. Events are vetoed if there
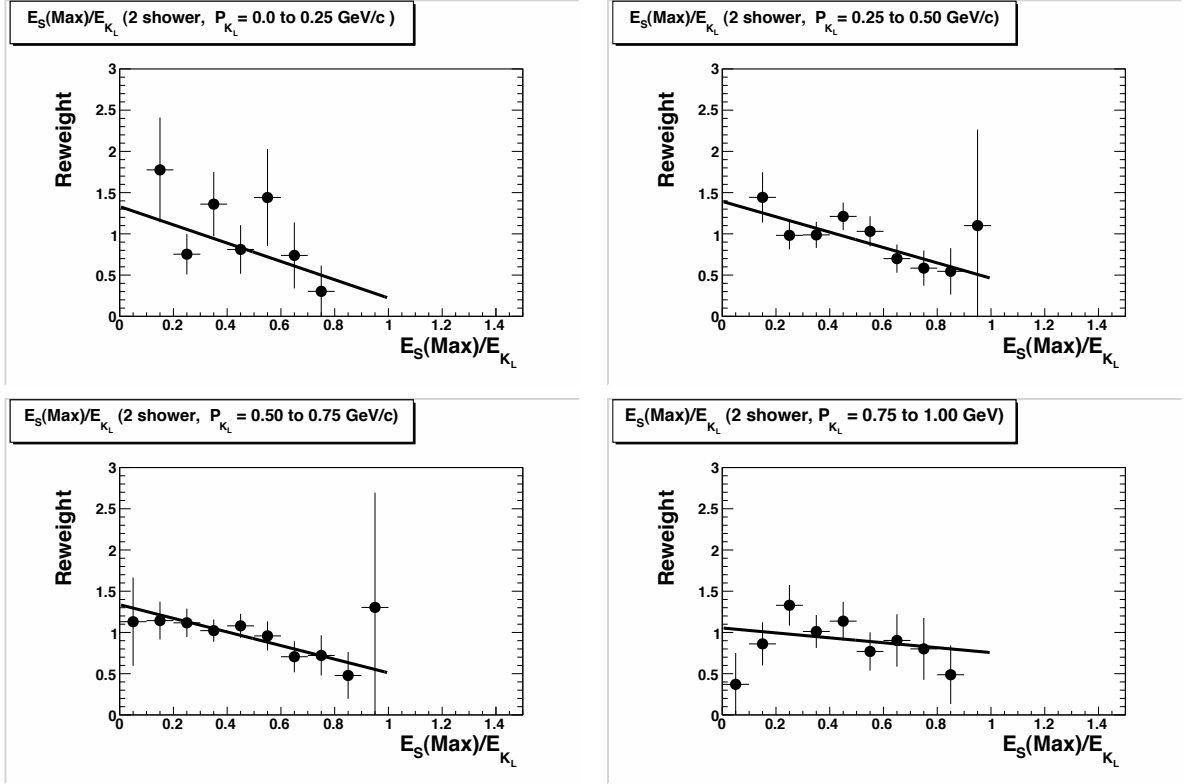
Figure 5.26: Correction factors for $E_S(\mathrm{Max})/E_{K_L}$ in the situation where the K_L deposits two splitoff-approved shower in the calorimeter. We show the momentum range 0.0 to 0.25 GeV/c (top left), 0.25 GeV/c to 0.50 GeV/c (top right), 0.50 GeV/c 0.75 GeV/c (bottom left), and 0.75 to 1.00 GeV/c (bottom right).

are splitoff approved showers greater than 250 MeV in energy that are not part of a η or π^0. Extra tracks are ignored in the double tagged events.

We study the rate that these double tagged events pass the generic reconstruction tracking requirements by using one D-tag for the signal side and generically reconstruct the other D tag. Events with extra tracks that passed the double tag requirement fail the generic reconstruction requirements. Previous neutrino reconstruction studies [33] found that the zero net charge efficiency varied with the number of low transverse momentum tracks in the event. We adopt the parametrization of [33] and determine the efficiency of our net charge and track vertex veto as a function of the number of low
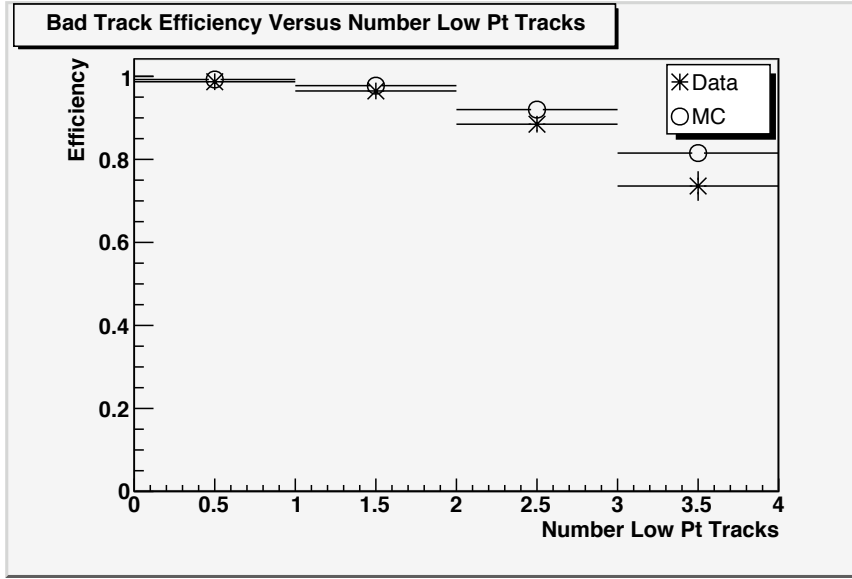
Figure 5.27: The efficiency in the data and in the Monte Carlo sample for passing
the net charge 0 and track vertex requirements.

transverse momentum tracks in the event (Figure 5.27). Table 5.11 shows the efficiency

corrections applied to the Monte Carlo sample.

Table 5.11: Corrections to the efficiency for passing the net charge 0 and track
vertex requirements as a function of the number of low transverse
momentum tracks ($P_t < 0.15 GeV/c$).

Number Low P_t Tracks	reweight
0	0.995 ± 0.006
1	0.987 ± 0.008
2	0.96 ± 0.02
3 or more	0.88 ± 0.04

5.10 Final State Radiation Correction

Our Monte Carlo sample was generated with final state radiation (FSR) implemented using the general purpose package PHOTOS [46]. Another program known as KLOR ([47]) is based on calculations of the FSR amplitudes for the semileptonic decays (specifically $K^+ \rightarrow \pi^0 e^+ \nu_e$) and takes into account interference terms that are not accounted for in PHOTOS. We modify the Monte Carlo sample to match the KLOR prediction for the number of events with no FSR photons, FSR photons with $E_\gamma < 1$ MeV, and FSR photons with $E_\gamma > 1$ MeV. To properly account for interference terms, we reweight the two dimensional E_γ versus $cos(\theta_{\gamma e^+})$ distribution to match KLOR.

CHAPTER 6

FITTING FOR SEMILEPTONIC YIELDS

This chapter describes the fitting procedure used to determine the efficiency corrected yields of the $D^{\pm} \to \eta' e^{\pm} \nu$, three q^2 ranges of $D^{\pm} \to \eta e^{\pm} \nu$ ($q^2 < 0.5 \text{ GeV}^2$, $0.5 \text{ GeV}^2 < q^2 < 1.0 \text{ GeV}^2$, $q^2 > 1.0 \text{ GeV}^2$), and the calibration mode $D^+ \to K^- \pi^+ \pi^+$. We determine the yields by a binned maximum likelihood fit to the M_{BC} distributions using our predicted contributions from the signal modes and the different backgrounds. This fit follows the method of Barlow and Beeston [36], which accounts for finite statistics in the Monte Carlo predictions. The contribution that each event makes to the M_{BC} distribution is scaled by the product of all corrections described in Chapter 5.

The $D^{\pm} \to \eta' e^{\pm} \nu$ and $D^{\pm} \to \eta e^{\pm} \nu$ decays are potentially backgrounds to one another as are the different q^2 regions of $D^{\pm} \to \eta e^{\pm} \nu$. To understand the cross feed, or how often one type of signal decay is incorrectly reconstructed as another type of signal, we separate the signal Monte Carlo samples by true decay ($\eta e^{\pm} \nu$, $\eta' e^{\pm} \nu$, $K^- \pi^+ \pi^+$) and for $\eta e^{\pm} \nu$ the true q^2. For each sample with a particular true decay and true q^2 we create a separate M_{BC} distribution for each reconstructed decay mode, reconstructed q^2 region, and quality bin. The number of events in each distribution gives us the efficiency for signal mode i to be reconstructed as signal mode j with a particular reconstructed q^2 region and quality classification. As the fit varies the signal yields of each true decay and true q^2 region, the background contributions from one mode into another scale accordingly.

For each reconstructed M_{BC} distribution for a semileptonic decay we consider contributions from the following sources: three q^2 regions of $D^{\pm} \to \eta e^{\pm} \nu$, $D^{\pm} \to \eta' e^{\pm} \nu$, generic $D\bar{D}$ decays (excluding $\eta e^{\pm} \nu$ and $\eta' e^{\pm} \nu$), continuum backgrounds, and events with fake leptons. For the calibration mode ($K^- \pi^+ \pi^+$) we consider contributions to the M_{BC} distributions from the following sources: $D^+ \to K^- \pi^+ \pi^+$, generic $D\bar{D}$ decays (excluding $D^+ \to K^- \pi^+ \pi^+$), and continuum backgrounds. Contributions from the contin-

uum and fake lepton sources are fixed and normalized to the expected contributions from the luminosity captured by the detector. The normalization of the $D\bar{D}$ backgrounds are allowed to float to match the apparent background levels in the M_{BC} distribution in each decay mode. We do not use a common $D\bar{D}$ background normalization for all signal modes because each one has contributions from different D decays.

There are a total of 15 free parameters in the fit. There are five yield parameters: $\eta'e^{\pm}\nu$, the three q^2 regions of $\eta e^{\pm}\nu$, and $K^-\pi^+\pi^+$. There are an additional ten normalization parameters for the generic $D\bar{D}$: six for the η' decay modes ($\gamma\gamma$, $\rho^0\gamma$, $\pi^+\pi^-\eta(\gamma\gamma)$, $\pi^+\pi^-\eta(\pi^+\pi^-\pi^0)$, $\pi^+\pi^-\eta(\pi^0\pi^0\pi^0)$, and $\pi^0\pi^0\eta(\gamma\gamma)$), three for the η decay modes ($\gamma\gamma$, $\pi^+\pi^-\pi^0$, and $\pi^0\pi^0\pi^0$), and one for $K^-\pi^+\pi^+$.

Each M_{BC} distribution used as input to the fitter is divided into 16 bins of equal width in the range 1.79 GeV/c^2 to 1.890 GeV/c^2. There are 18 M_{BC} distributions for $\eta'e^{\pm}\nu$ candidates from nine decay modes (including the 4 ρ^0 mass bins for $\eta' \to \rho^0\gamma$) and two quality bins ($9 \times 2 = 18$). There are 18 M_{BC} distributions for the $\eta e^{\pm}\nu$ candidates from three decay modes, three q^2 bins for each decay modes, and two quality bins ($3 \times 3 \times 2 = 18$). There are two M_{BC} distributions for the $K^-\pi^+\pi^+$ candidates from the quality bins. This results in a total of 608 bins ($16 \times (18 + 18 + 2) = 608$), and given the 15 free parameters in the fit we have in total 593 degrees of freedom.

The efficiency-corrected yields obtained from the fit are given in Table 6.1. Since the number of events in the $D^{\pm} \to \eta'e^{\pm}\nu$ study are so low, and scattered among different decay modes, it is instructive to see how the efficiency-corrected yields vary were we to only consider one of the η' decay modes at a time. Table 6.2 shows the yields for each of the η' decay modes, and also gives the change in $-2log\mathcal{L}$ between the best fit value and zero. We have obtained a statistically significant observation of the $D^{\pm} \to \eta'e^{\pm}\nu$ decay,

Table 6.1: The efficiency-corrected yields for $K\pi\pi$, $\eta'ev$ and 3 q^2 bins of ηev.

decay	q^2 range	Efficiency-Corrected Yield
$K\pi\pi$	NA	$(4.30 \pm 0.04) \times 10^5$
$\eta'ev$	ALL	1020 ± 250
ηev	$q^2 < 0.5\,\mathrm{GeV}^2$	2687 ± 295
ηev	$0.5\,\mathrm{GeV}^2 < q^2 < 1.0\,\mathrm{GeV}^2$	1877 ± 291
ηev	$q^2 > 1.0\,\mathrm{GeV}^2$	957 ± 223

Table 6.2: The $\eta'ev$ efficiency-corrected yield obtained by using only one η' decay mode. We also show the difference in $-2Log\mathcal{L}$ between the best fit yield and zero.

η' Decay	Yield	$-2\Delta Log\mathcal{L}$
All	1020 ± 250	31.9
$\gamma\gamma$	0 ± 593	0.0
$\rho^0\gamma$	1144 ± 434	15.3
$\pi\pi\gamma\gamma$	1881 ± 589	28.6
$\pi\pi\pi\pi\pi^0$	0 ± 383	0
$\pi^0\pi^0\gamma\gamma$	0 ± 396	0

where the reconstructed signal is primarily found in the $\eta' \rightarrow \rho^0\gamma$ and $\eta' \rightarrow \pi^+\pi^-\gamma\gamma$ decay modes.

The results for $D^\pm \rightarrow \eta e^\pm v$ are given in Figures 6.1, 6.2, and 6.3, which show the different q^2 bins, decay modes, and decay modes separated by quality bins respectively. In all cases there is good agreement between the data and the fit. For events with M_{BC} within 15 MeV/c^2 of the D mass the distributions of other variables that were not directly

129
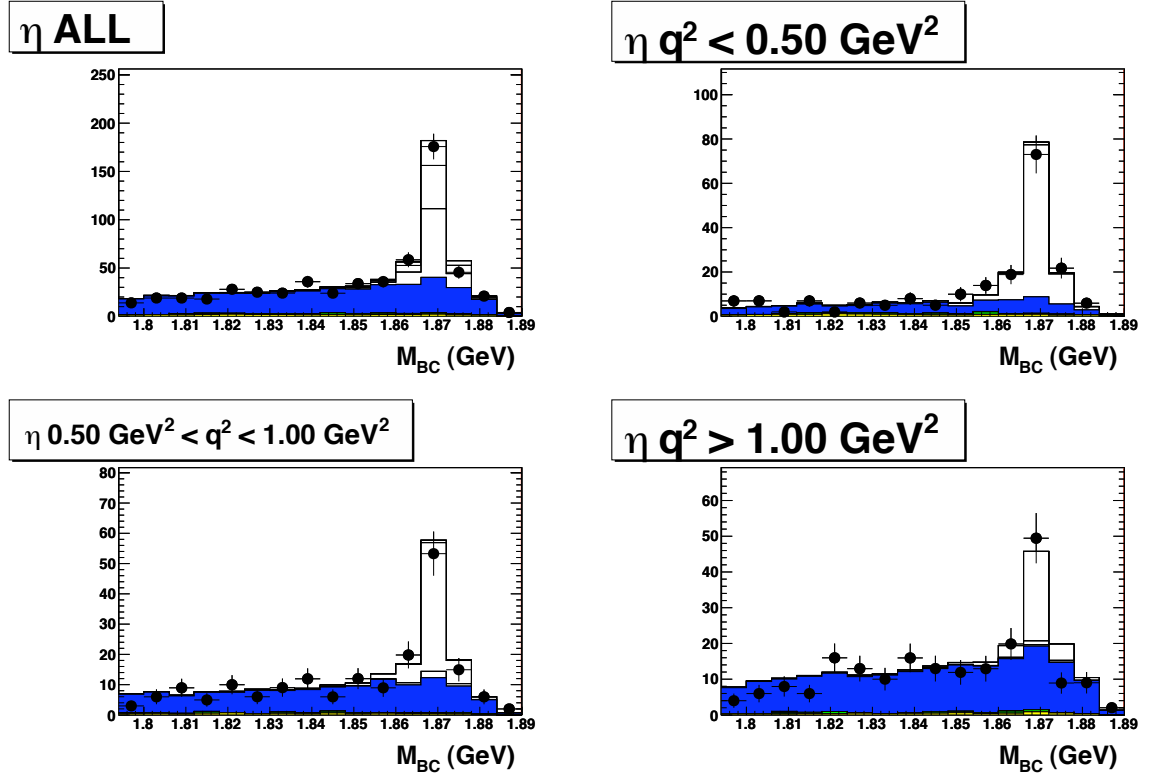
Figure 6.1: The beam constrained mass (M_{BC}) distribution for all η decay modes and all q^2 (top left), $q^2 < 0.5$ GeV^2 (top right), 0.5 GeV$^2 < q^2 <$ 1.0 GeV^2 (bottom left), $q^2 > 1.0$ GeV^2 (bottom right). The black dots are data, the clear histogram is the $D^{\pm} \rightarrow \eta e^{\pm} \nu$ contribution, the blue histogram is $D\bar{D}$ backgrounds, the continuum background is green, and fake leptons are yellow.

used in the fit are shown in Figure 6.4. These additional distributions include: ΔE, E_{Miss}, the electron momentum, the $cos(\theta_{We})$, as well as the inclusive momentum spectrum of $K_S \rightarrow \pi^+ \pi^-$ and π^+ of the other side D. The $cos(\theta_{We})$ is the cosine between the direction of the W boson and the electron in the W rest frame, and is expected to have a $1 - cos^2(\theta_{We})$ distribution. These distributions are also in good agreement with the

130
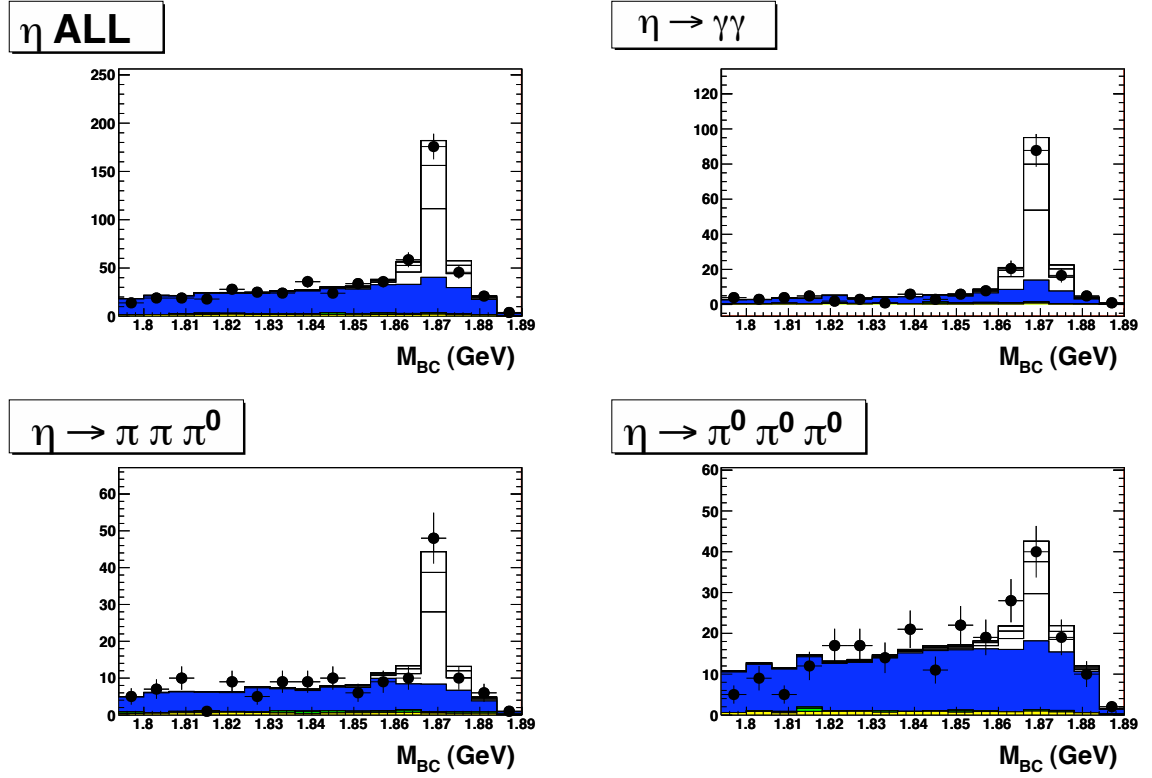
Figure 6.2: The beam constrained mass (M_{BC}) distribution for the full q^2 range of $\eta e^{\pm}\nu$ and all decay modes (top left), $\eta \rightarrow \gamma\gamma$ (top right), $\eta \rightarrow \pi\pi\pi^0$ (bottom left), $\eta \rightarrow \pi^0\pi^0\pi^0$ (bottom right). The black dots are data, the clear histogram is the $D^{\pm} \rightarrow \eta e^{\pm}\nu$ contribution, the blue histogram is $D\bar{D}$ backgrounds, the continuum background is green, and fake leptons are yellow.

data and show that the fit parameters not only describe the M_{BC} distributions but also all aspects of the decays.

The results for $D^{\pm} \rightarrow \eta' e^{\pm}\nu$ are given in Figures 6.5, and 6.3, which show the fit results for the different decay modes, and quality bins respectively. In all cases there is good agreement between the data and the fit. For events with M_{BC} within 15 MeV/c^2 of the D mass, the distributions of other variables that were not directly used in the fit are shown in Figure 6.7. These additional distributions include: ΔE, E_{Miss}, the electron momentum, and $cos(\theta_{We})$. These distributions are also in good agreement with the data
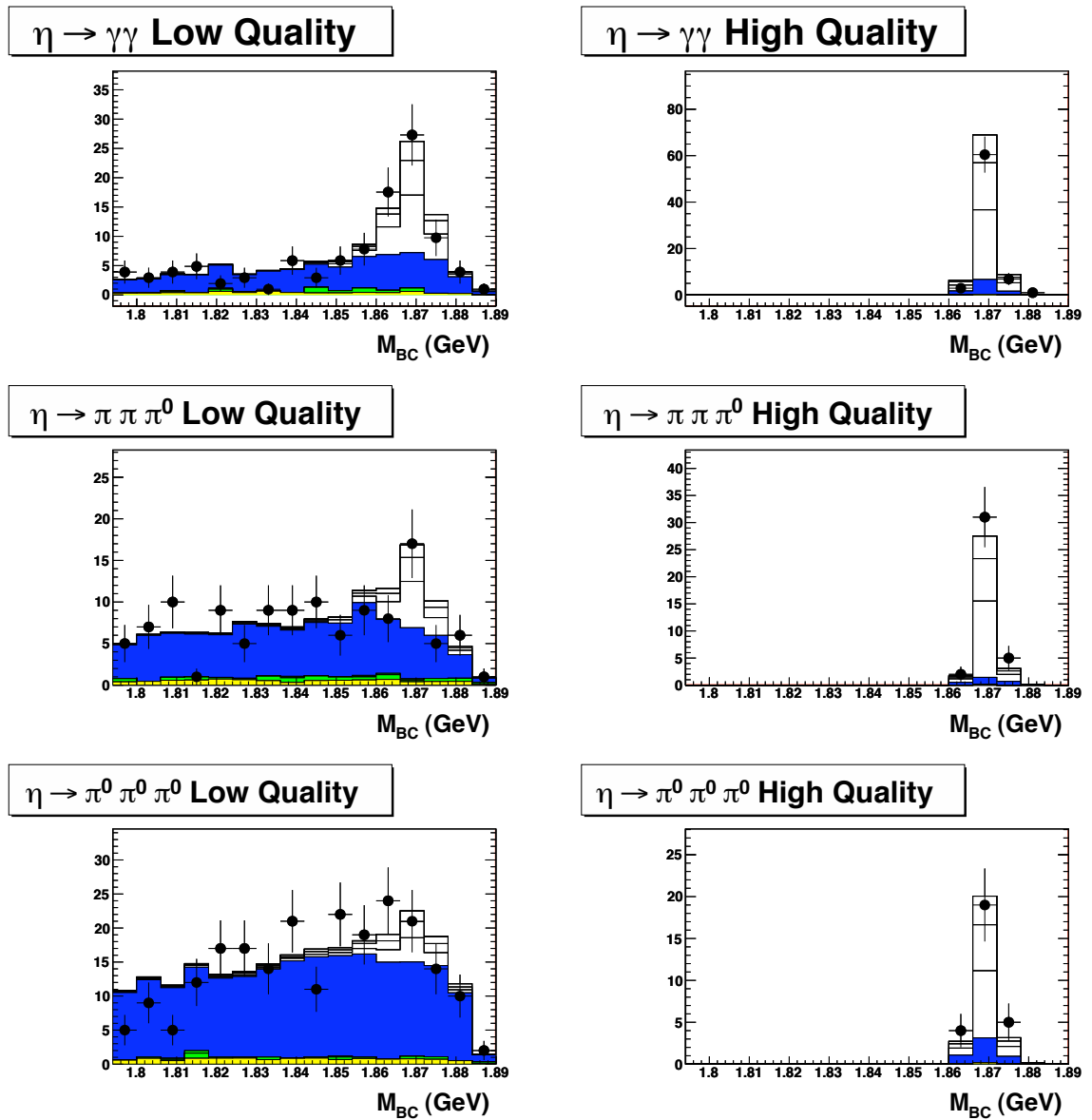
Figure 6.3: The beam constrained mass (M_{BC}) distribution for the full q^2 range of $\eta e\nu$ with low quality bins on the left side and high quality bins on the right side. The black dots are data, the clear histogram is the $D^{\pm} \to \eta e^{\pm}\nu$ contribution, the blue histogram is $D\bar{D}$ backgrounds, the continuum background is green, and fake leptons are yellow.
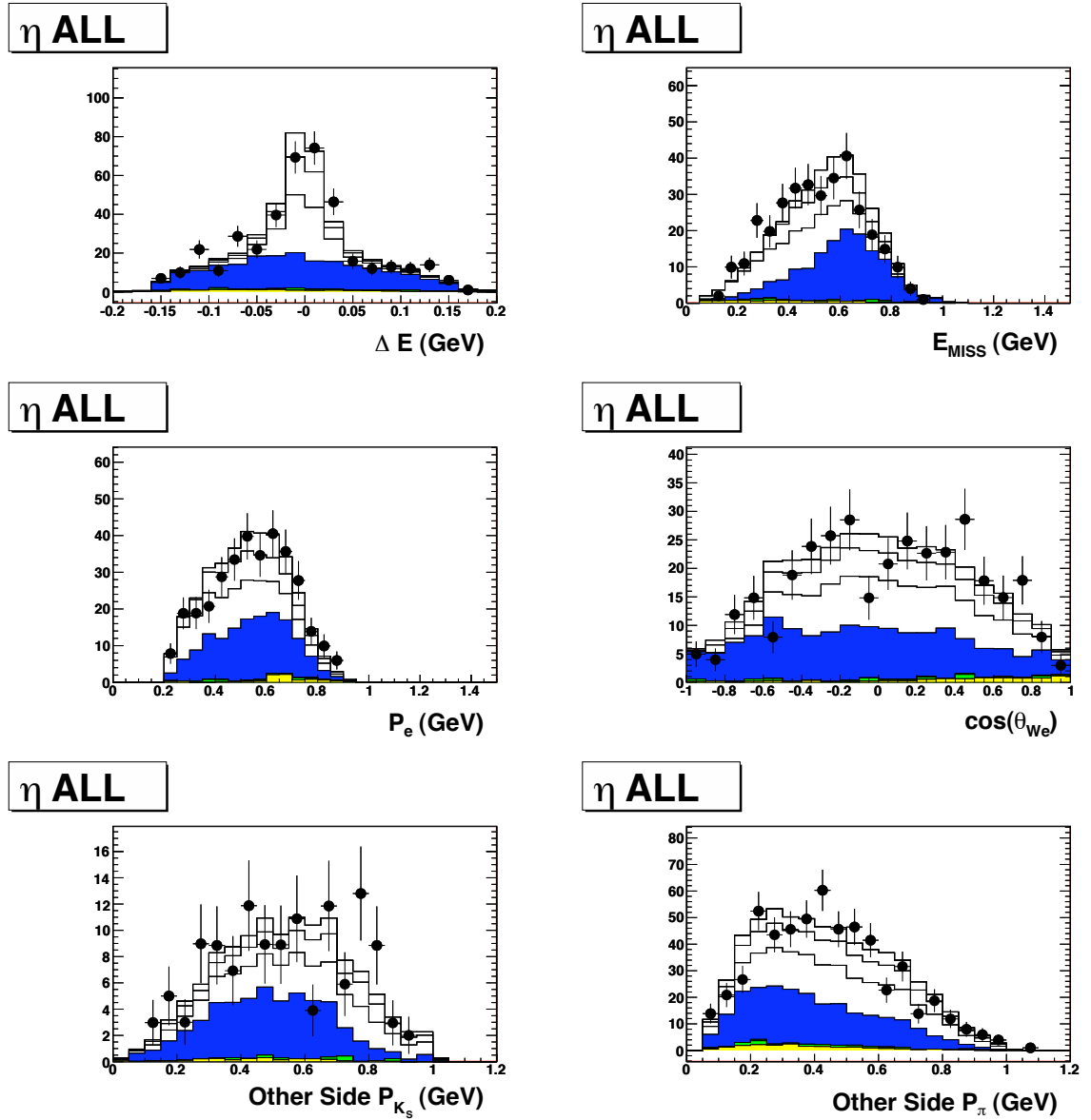
Figure 6.4: The distributions of $D^{\pm} \to \eta e^{\pm} \nu$ quantities not involved in the fit. Plots shown: ΔE (top left), missing energy (top right), electron momentum (middle left), $cos(\theta_{We})$ (middle right), other side K_S momentum distribution (bottom left), other side π momentum distribution (bottom right). The black dots are data, the clear histogram is the $D^{\pm} \to \eta e^{\pm} \nu$ contribution, the blue histogram is $D\bar{D}$ backgrounds, the continuum background is green, and fake leptons are yellow.

and show that the fit parameters not only describe the M_{BC} distributions but also all aspects of the decays.

The results for the $D^+ \rightarrow K^- \pi^+ \pi^+$ calibration mode are given in Figure 6.8, which shows the M_{BC} distribution for both quality bins separately and added together (log scale). The figure also shows the momentum spectrum of the other side D K_S, π^0, and $\eta \rightarrow \gamma\gamma$ for events with M_{BC} within 15 MeV/c^2 of the D mass. The fit is in sufficient agreement with data.
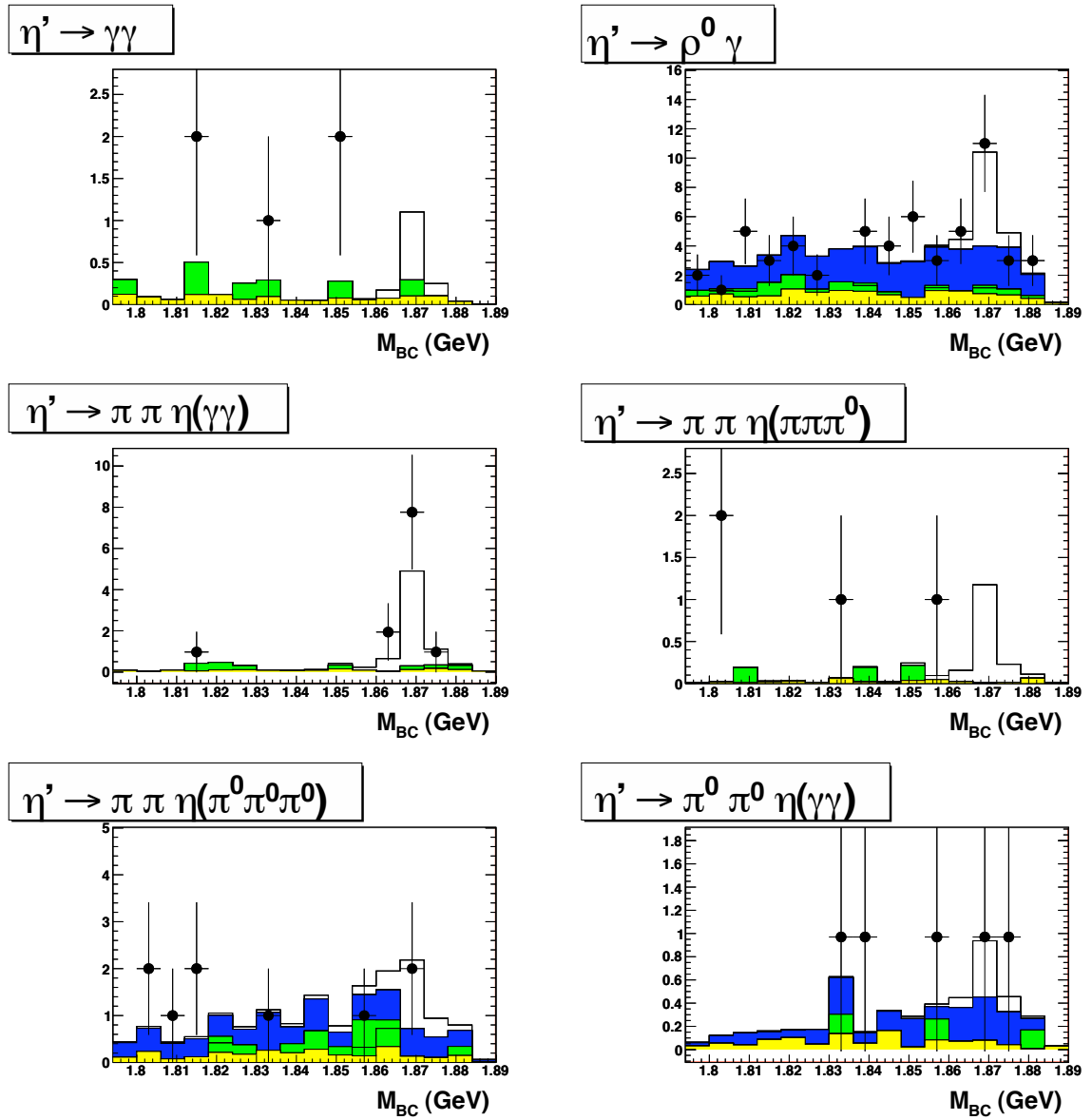
Figure 6.5: The beam constrained mass M_{BC} for each of the η' decay modes. The black dots are data, the clear histogram is the $D^{\pm} \rightarrow \eta' e^{\pm} \nu$ contribution, the blue histogram is $D\bar{D}$ backgrounds, the continuum background is green, and fake leptons are yellow.
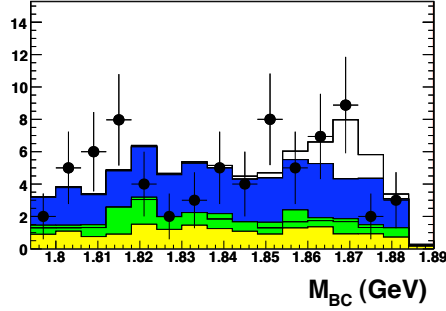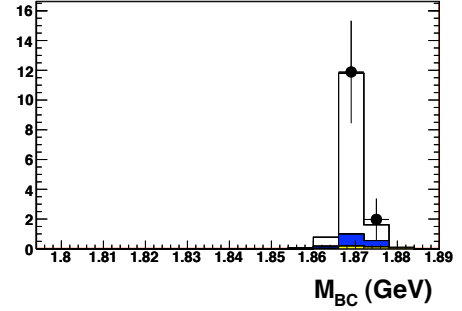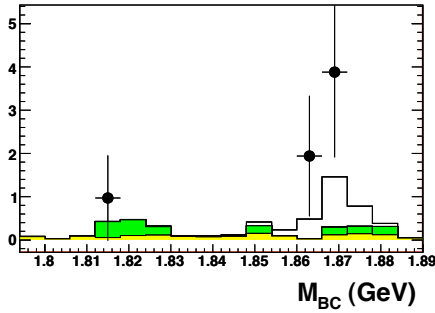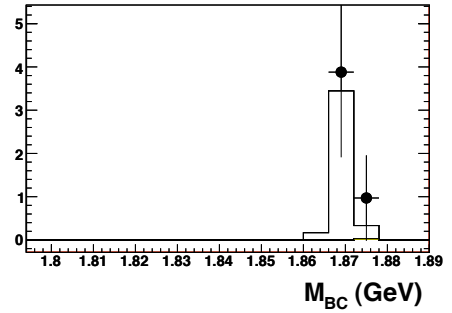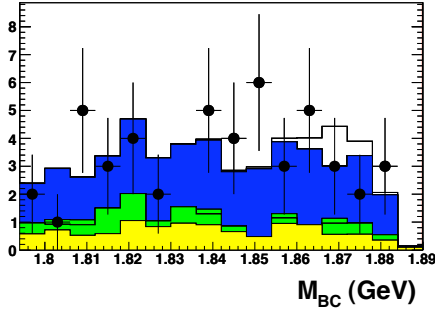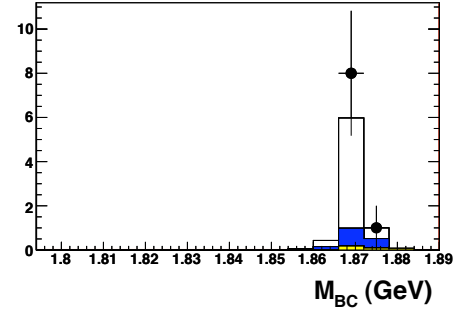
Figure 6.6: The beam constrained mass (M_{BC}) distribution for $\eta' e\nu$ with low quality bins on the left side and high quality bins on the right side for the two η' decay modes with the largest efficiency. The black dots are data, the clear histogram is the $D^{\pm} \rightarrow \eta' e^{\pm} \nu$ contribution, the blue histogram is $D\bar{D}$ backgrounds, the continuum background is green, and fake leptons are yellow.

136
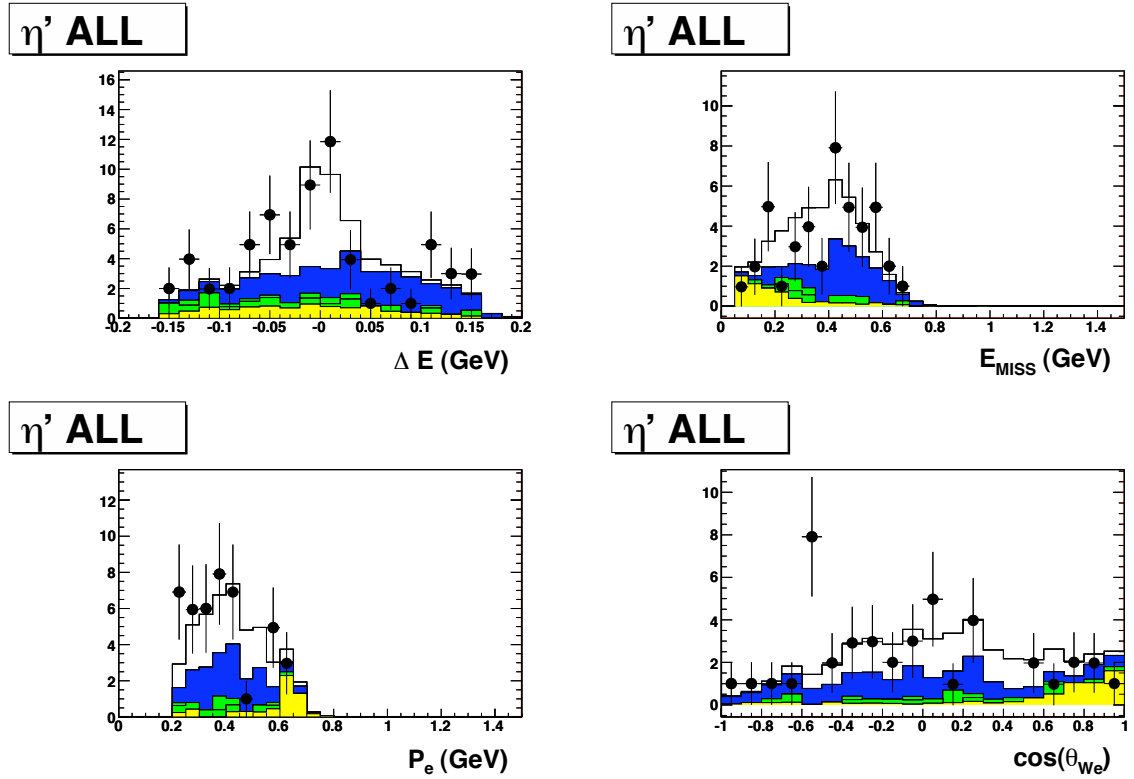
Figure 6.7: Distributions of $D^\pm \to \eta' e^\pm \nu$ variables not used in the fit. All candidates have a M_{BC} within 15 MeV/c^2 of the D mass. The black dots are data, the clear histogram is the $D^\pm \to \eta' e^\pm \nu$ contribution, the blue histogram is $D\bar{D}$ backgrounds, the continuum background is green, and fake leptons are yellow.
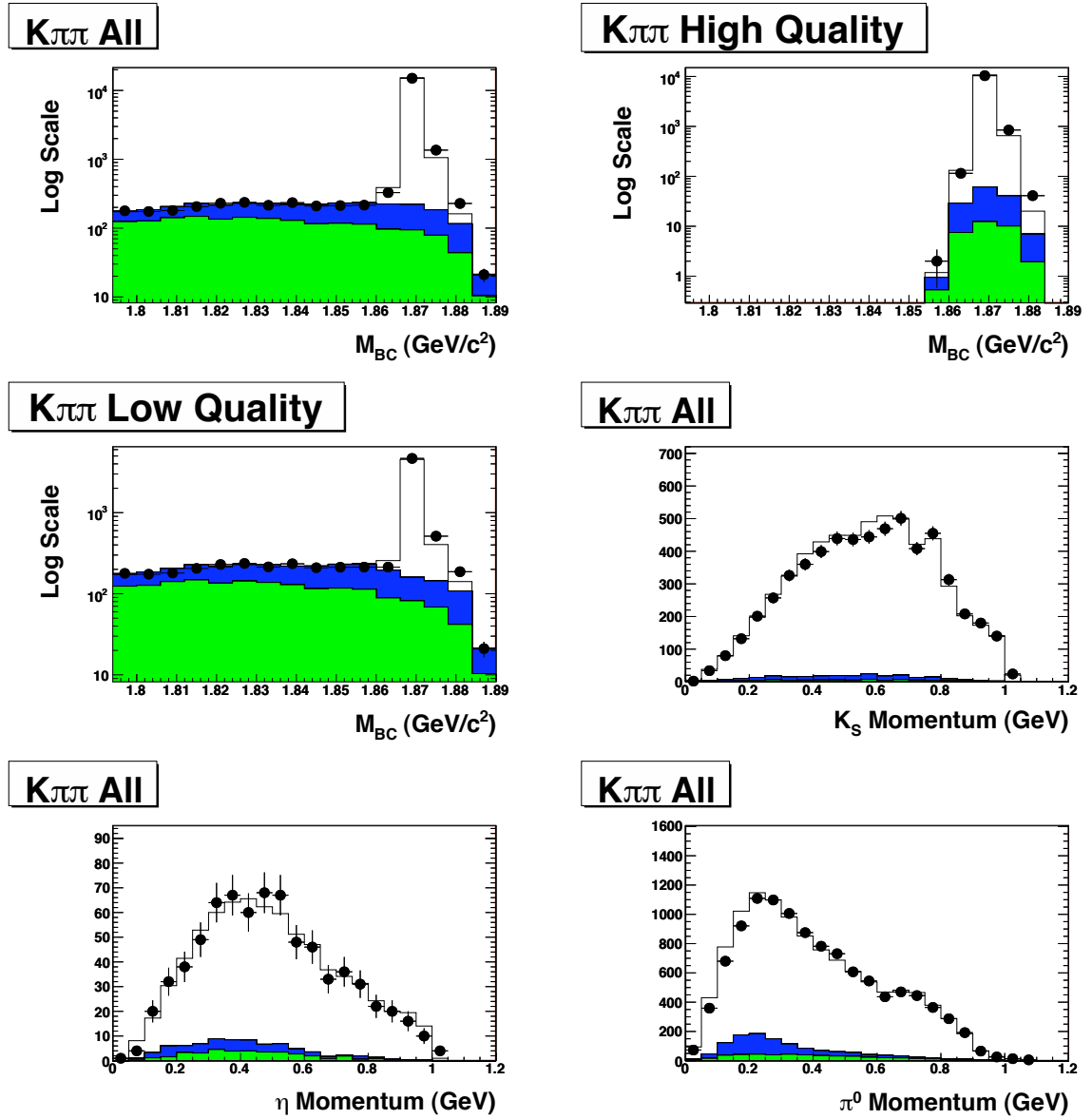
Figure 6.8: Results of the $K^-\pi^+\pi^+$ fit. We show M_{BC} (top left), M_{BC} for high quality (top right), M_{BC} for low quality (middle left), other side $K_S \rightarrow \pi^+\pi^-$ spectrum (middle right), other side $\eta \rightarrow \gamma\gamma$ spectrum (bottom left), and other side π^0 spectrum (bottom right). The black dots are data, the clear histogram is the $D^\pm \rightarrow \eta e^\pm \nu$ contribution, the blue histogram is $D\bar{D}$ backgrounds, the continuum background is green, and fake leptons are yellow.

SYSTEMATIC UNCERTAINTIES

This section describes the different systematic uncertainties that affect the hadronic branching fraction measurements and the efficiency-corrected yields of the $K\pi\pi$, $\eta e^{\pm}\nu$ and $\eta' e^{\pm}\nu$. Table 7.1 summarizes the systematic uncertainties of the efficiency-corrected yields (σ_y) given as a percentage of the nominal values ($100 \times \sigma_y/y$). A negative sign indicates when varying a process or efficiency moves yields in opposite directions. For each source of systematic uncertainty, the systematic error on the ratio of two yields (σ_r) is approximately given by,

$$\sigma_r/r \sim \sigma_{y_a}/y_a - \sigma_{y_b}/y_b, \tag{7.1}$$

where $r = y_a/y_b$. In most cases σ_r/r is smaller than σ_y/y.

We determine the D^+ (D^0) hadronic branching fractions relative to previously measured calibration modes $\mathcal{B}(D^+ \to K^-\pi^+\pi^+)$ ($\mathcal{B}(D^0 \to K^-\pi^+)$). Table 7.2 (7.3) summarizes the systematic errors of the ratio of the D^+ (D^0) hadronic branching fractions to the corresponding calibration mode.

Below we describe how the different contributions to the systematic uncertainties were calculated.

7.1 Other D Branching Fractions

For both the semileptonic and hadronic branching fraction measurements there are systematic uncertainties from how well all of the other D branching fractions are known. For the semileptonic yields these systematic uncertainties primarily affect the signal efficiencies, and for the hadronic branching fraction measurements this uncertainty affects the backgrounds. Below we describe the means of calculating this systematic uncertainty.

Table 7.1: The systematic uncertainties for the $\eta'ev$, ηev (3 q^2 bins and the total), and the $K^-\pi^+\pi^+$ yield. A minus sign has been applied to modes where the systematic uncertainty of one mode or bin pushes it in the opposite direction of all of the others. Below, OS stands for "other side D", and EDEP stands for "energy deposition".

Knob	$K^-\pi^+\pi^+$	$\eta'ev$	$\eta ev\ q_1^2$	$\eta ev\ q_2^2$	$\eta ev\ q_3^2$	ηev All
$\eta \to \gamma\gamma$ Eff (%)	0.09	1.38	2.32	2.51	2.96	2.49
K_L EDEP (%)	0.21	-0.68	0.21	0.83	1.58	0.66
K ID (%)	0.80	0.87	0.85	0.94	1.09	0.92
Fake Tracks (%)	0.78	1.46	0.76	0.74	0.86	0.77
$\pi^0 \to \gamma\gamma$ Eff (%)	0.64	0.69	1.11	1.00	0.82	1.02
Splitoff Escape (%)	0.29	-0.49	0.87	0.34	2.10	0.9
Pion ID (%)	1.58	1.48	0.43	0.37	0.34	0.40
Tracking Eff(%)	0.48	0.49	0.37	0.36	0.38	0.37
OS BF (%)	1.68	1.72	1.66	1.64	1.85	1.67
OS Spectrum (%)	-0.20	0.90	0.14	-0.50	0.01	-0.10
$K_S \to \pi\pi$ Eff (%)	0.31	0.26	0.36	0.19	0.19	0.27
K faking π (%)	0.00	0.00	-0.02	-0.01	-0.00	-0.01
EID (%)	0.00	0.50	0.30	0.30	0.30	0.30
FSR (%)	0.00	-0.50	-0.50	-0.76	-1.27	-0.72

Table 7.2: The breakdown of systematic uncertainties on the D^+ hadronic branching fractions given in percent of the nominal values. The table uses the following symbols and abbreviations: $\epsilon(\eta)$ is the $\eta \rightarrow \gamma\gamma$ efficiency; $\epsilon(\pi^0)$ is the $\pi^0 \rightarrow \gamma\gamma$ efficiency; SE is the modeling of splitoff escapes; E_{K_L} is the modeling of the K_L energy deposition; $\epsilon(\text{Trk})$ is trkman efficiency; $\epsilon_\pi(\text{K})$ is the rate for kaons to fake "signal pions"; $\epsilon_K(K)$ kaon identification; $\epsilon_\pi(\pi)$ is pion identification; $\epsilon(K_S)$ is $K_S \rightarrow \pi^+\pi^-$ identification; $Q = 0$ is the net charge and track quality requirements; "Spec." is the spectrum of daughter particles of both the signal and background; $\mathcal{B}(D)$ is from uncertainty in the branching fractions of backgrounds.

Mode	$\epsilon(\eta)$	$\epsilon(\pi^0)$	SE	E_{K_L}	$\epsilon(\text{Trk})$	$\epsilon_\pi(K)$	$\epsilon_K(K)$	$\epsilon_\pi(\pi)$	$\epsilon(K_S)$	$Q=0$	Spec.	$\mathcal{B}(D)$	Cont.
$\pi^+\pi^0$	0.46	-0.89	0.16	-0.02	0.63	0.46	2.04	0.46	0.46	0.52	0.15	1.66	3.05
$\pi^+\pi^-\pi^+$	0.52	0.54	0.8	0.02	0.52	0.52	2.1	0.52	0.54	0.52	0.5	2.32	1.1
$\bar{K}^0\pi^+$	0.16	0.15	0.47	0	0.16	0.16	1.71	0.16	-1.92	0.12	0.17	0.93	0.19
$K^+\pi^0$	-1.44	-2.9	-1.34	0	-1.28	-1.47	-1.53	-1.48	-1.49	-1.31	3.33	10.88	17.05
$\pi^+\pi^0\pi^0$	-0.1	-2.9	0.36	0.02	0.06	-0.11	1.52	-0.1	-0.04	-0.07	0.23	5.61	3.83
$\pi^+\pi^-\pi^+\pi^0$	0.14	-1.22	0.75	0.07	0.12	0.12	1.8	0.14	0.16	0.01	0.2	5.65	2.48
$\pi^+\eta(\gamma\gamma)$	-4.3	-1.08	0.06	-0.39	-0.92	-1.08	0.44	-1.08	-1.07	-1.03	1.37	0.6	0.26
$\pi^+\pi^-\pi^+\pi^-\pi^+$	0.37	0.51	0.95	0.11	0.17	0.35	2.08	0.38	0.4	-0.03	0.33	8.47	0.93
$K^+\bar{K}^0$	0.72	0.72	-0.32	0	0.72	0.73	0.73	0.72	-1.1	0.67	0.27	0.85	0.11
$\bar{K}^0\pi^+\pi^0$	0.46	-0.87	0.6	0	0.46	0.46	2.03	0.47	-0.61	0.24	1.52	1.5	0.24
$K^+\pi^0\pi^0$	-17.2	-27.1	4.3	3.3	-17.0	-17.9	-19.3	-17.8	-18.3	-15.0	23.0	204.3	37.8
$K^+K^-\pi^+$	0.7	0.7	-1.42	0	0.7	0.71	-0.82	0.7	0.71	0.7	4.51	0.96	0.09
$\pi^+\pi^0\pi^0\pi^0$	-0.09	-4.66	0.79	0.13	0.09	-0.14	1.64	-0.1	0.09	0	3.19	14.93	5.47
$\bar{K}^0\pi^+\pi^-\pi^+$	0.18	0.19	1.19	0.01	0.01	0.17	1.74	0.18	-0.23	-0.22	1.81	4.03	0.18
$K^-\pi^+\pi^+\pi^0$	0.14	-1.2	0.02	0.04	0.13	0.13	0.12	0.14	0.13	0.08	3.1	3.23	0.37
$\pi^+\pi^-\pi^+\pi^0\pi^0$	-0.57	-3.62	1.35	0.25	-0.61	-0.62	1.32	-0.56	-0.62	-0.82	0.62	18.57	5.05

Table 7.2 (Continued)

Mode	$\epsilon(\eta)$	$\epsilon(\pi^0)$	SE	E_{K_L}	$\epsilon(\text{Trk})$	$\epsilon_\pi(K)$	$\epsilon_K(K)$	$\epsilon_\pi(\pi)$	$\epsilon(K_S)$	$Q=0$	Spec.	$\mathcal{B}(D)$	Cont.
$\pi^+\pi^0\eta(\gamma\gamma)$	-3.26	-0.77	-0.01	-2.56	0.48	0.27	1.98	0.3	0.44	0.43	4.15	16.53	6.55
$K^-\pi^-\pi^+\pi^+$	-0.09	-0.03	-0.26	0.05	-0.27	-0.1	-0.12	-0.09	-0.1	-0.54	5.62	3.89	0.17
$\pi^+\pi^-\pi^+\pi^-\pi^+\pi^0$	-0.69	-2.05	2.15	0.56	-1.04	-0.79	1.44	-0.63	-0.8	-2.44	3.52	33.08	1.33
$\bar{K}^0K^0\pi^+$	-1.02	-1	1.58	0	-1.19	-1.02	0.52	-1.02	-3.2	-1.66	8.91	41.48	0.26
$\pi^+\pi^-\pi^+\eta(\gamma\gamma)$	-4.09	-0.69	0.45	-0.2	-0.75	-0.75	0.82	-0.75	-0.74	-1.05	0.02	3.47	0.54
$K^+\bar{K}^0\pi^0$	0.94	-0.41	-0.1	0.02	0.94	0.94	0.93	0.94	0.02	0.78	1.47	2.5	0.53
$K^+K^-K^+$	2.87	2.89	-4.26	0.03	2.87	2.86	-0.39	2.86	2.89	2.88	0.41	3.03	6.01
$\bar{K}^0\pi^+\pi^0\pi^0$	-0.06	-2.78	1.04	0.07	-0.07	-0.07	1.56	-0.06	-0.39	-0.32	0.37	13.17	0.78
$K, K^0, 2\times\pi,$	2.14	2.17	0.79	0.03	1.97	2.14	2.13	2.14	2.16	1.6	2.87	33.52	0.1
$K^+K^-\pi^+\pi^0$	0.63	-0.72	-2.52	0.06	0.62	0.61	-1.05	0.63	0.61	0.53	0.07	4.66	0.59
$\pi^+\pi^0\pi^0\pi^0\pi^0$	12.52	5.98	2.9	-0.49	12.77	12.46	14.63	12.55	12.69	12.82	6.6	42.83	8
$\bar{K}^0\pi^+\pi^-\pi^+\pi^0$	-0.16	-1.49	1.02	0.09	-0.35	-0.17	1.49	-0.16	-0.29	-1.07	1.85	22.55	0.56
$K^-\pi^+\pi^+\pi^0\pi^0$	2.31	-0.81	-0.86	0.39	2.25	2.24	2.11	2.31	2.24	2.1	2.3	22.74	1.26
$\bar{K}^0\pi^+\eta(\gamma\gamma)$	-4.03	-0.74	0.55	0	-0.76	-0.77	0.77	-0.76	-1.36	-0.97	0.77	5.89	0.32

Table 7.2 (Continued)

Mode	$\epsilon(\eta)$	$\epsilon(\pi^0)$	SE	E_{K_L}	ϵ(Trk)	$\epsilon_\pi(K)$	$\epsilon_K(K)$	$\epsilon_\pi(\pi)$	$\epsilon(K_S)$	$Q=0$	Spec.	$\mathcal{B}$(D)	Cont.
$\pi^+\pi^-\pi^+\pi^0\pi^0\pi^0$	-5.23	-13.53	2.61	1.4	-5.53	-5.6	-1.5	-5.14	-5.63	-6.16	4.64	111.63	10.12
$\pi^+\pi^0\pi^0\eta(\gamma\gamma)$	-2.3	-1.48	1.29	0.14	1.33	1.09	2.85	1.13	1.27	1.24	0.36	28.39	3.34
$K^-\pi^+\pi^-\pi^+\pi^0$	4.33	2.99	0.9	0.26	4.09	4.29	4.22	4.3	4.27	2.55	0.88	15.38	1.46
$K^+\bar{K}^0K^0$	1.68	1.68	1.03	0	1.52	1.68	1.68	1.68	1.6	0.98	2.31	12.91	0.17
$K^-\pi^+\pi^+\eta(\gamma\gamma)$	-2.69	1.02	-1.22	0.13	0.84	0.84	0.79	0.85	0.81	0.62	1.9	9.7	1.51
$\pi^+\pi^-\pi^+\pi^-\pi^+\pi^0\pi^0$	-4.1	-6.78	5.16	0.27	-4.38	-4.16	-2.31	-4.1	-4.16	-6.51	42.665	20.42	1.39
$\bar{K}^0K^0\pi^+\pi^0$	-8.97	-10.15	3.48	0.12	-9.17	-9	-7.34	-8.98	-9.04	-9.87	14.75	356.51	2.43
$\pi^+\pi^-\pi^+\pi^0\eta(\gamma\gamma)$	-2.62	-0.32	0.34	-0.07	0.88	0.88	2.66	0.92	0.85	-0.04	2.54	12.39	2.4
$K^+\bar{K}^0\pi^0\pi^0$	-6.57	-9.71	1.04	0.41	-6.62	-6.64	-6.72	-6.6	-6.65	-6.78	10.17	30.91	2.97
$\bar{K}^0\pi^+\pi^0\pi^0\pi^0$	-2.87	-6.87	2.19	0.28	-2.9	-2.91	-1.12	-2.85	-3.33	-3.1	4.12	59.42	0.78
$\bar{K}^0\pi^+\pi^-\pi^+\eta(\gamma\gamma)$	-1.45	2.02	2.08	0.05	1.82	1.99	3.61	2	2.21	-0.37	0.02	4.27	1.9
$\bar{K}^0\pi^+\pi^0\eta(\gamma\gamma)$	-5.17	-1.05	3.02	0.7	-0.56	-0.57	1.61	-0.46	-0.7	-0.87	11.55	61.87	4.36
$\pi^+\pi^0\pi^0\pi^0\eta(\gamma\gamma)$	-19.45	-19.45	5.38	0.36	-16.25	-16.47	-14.88	-16.43	-16.54	-16.25	22.61	43.4	4.01
$\pi^+\eta(\gamma\gamma)\eta(\gamma\gamma)$	-6.07	0.04	-1.96	-0.17	-0.03	0.28	0.28	-0.75	-0.04	-0.39	0.18	3.09	0.31

144

Table 7.3: The breakdown of systematic uncertainties on the D^0 hadronic branching fractions given in percent of the nominal values. The table uses the following symbols and abbreviations: $\epsilon(\eta)$ is the $\eta \rightarrow \gamma\gamma$ efficiency; $\epsilon(\pi^0)$ is the $\pi^0 \rightarrow \gamma\gamma$ efficiency; SE is the modeling of splitoff escapes; E_{K_L} is the modeling of the K_L energy deposition; $\epsilon(\text{Trk})$ is trkman efficiency; $\epsilon_\pi(K)$ is the rate for kaons to fake "signal pions"; $\epsilon_K(K)$ kaon identification; $\epsilon_\pi(\pi)$ is pion identification; $\epsilon(K_S)$ is $K_S \rightarrow \pi^+\pi^-$ identification; $Q = 0$ is the net charge and track quality requirements; "Spec." is the spectrum of daughter particles of both the signal and background; $\mathcal{B}(D)$ is from uncertainty in the branching fractions of backgrounds.

Mode	$\epsilon(\eta)$	$\epsilon(\pi^0)$	SE	E_{K_L}	$\epsilon(\text{Trk})$	$\epsilon_\pi(K)$	$\epsilon_K(K)$	$\epsilon_\pi(\pi)$	$\epsilon(K_S)$	$Q=0$	Spec.	$\mathcal{B}(D)$	Cont.
$\pi^+\pi^-$	-0.59	-0.59	1.32	0	-0.59	-0.59	0.93	-0.59	-0.59	-0.59	0.45	0.34	0.15
$\pi^0\pi^0$	0.72	-1.94	0.69	-0.06	0.89	0.76	2.27	0.73	0.72	0.72	0.79	0.51	1.01
$\pi^+\pi^-\pi^0$	0.29	-1.04	1.06	0	0.29	0.27	1.84	0.29	0.3	0.24	0.36	0.77	0.49
$\pi^+\pi^-\pi^+\pi^-$	0.13	0.13	1.47	0	-0.03	0.11	1.67	0.12	0.13	0.03	0.22	0.75	0.14
$\bar{K}^0\pi^0$	0.16	-1.17	1.22	0	0.16	0.18	1.7	0.16	-1.96	0.1	0.03	1.36	0.24
K^+K^-	0.76	0.76	-1.11	0	0.76	0.74	-0.75	0.76	0.76	0.76	0.59	0.15	0.02
$\pi^0\pi^0\pi^0$	3.6	-1.65	2.43	-0.51	3.86	3.49	5.28	3.5	5.57	3.67	1.33	71.69	17.52
$\bar{K}^0\pi^+\pi^-$	0.01	0.02	1.92	0	-0.14	0	1.55	0.01	-0.68	-0.2	0.48	1.66	0.22
$K^-\pi^+\pi^0$	0.04	-1.27	0.23	0	0.04	0.06	0.04	0.04	0.04	0	0.53	0.12	0.13
$\pi^+\pi^-\pi^0\pi^0$	0.34	-2.47	1.14	0	0.32	0.29	1.96	0.31	0.33	0.3	0.25	4.28	1.67
$\pi^0\eta(\gamma\gamma)$	-1.56	0.42	0.51	-1.21	1.91	1.71	3.3	1.74	1.77	1.75	1.06	3.46	1.7
$K^-\pi^+\pi^-\pi^+$	0.21	0.22	0.84	0	0.05	0.18	0.21	0.21	0.21	0.09	4.34	0.28	0.07
$\pi^+\pi^-\pi^+\pi^-\pi^0$	0.4	-1.07	1.67	0.05	0.19	0.34	2.12	0.36	0.38	0.05	3.88	8.02	0.92
$\bar{K}^0K^0$	-10.46	-10.43	-0.69	0.03	-10.61	-10.36	-9.08	-10.45	-24.89	-11.14	32.77	107.28	1.86

Table 7.3 (Continued)

Mode	$\epsilon(\eta)$	$\epsilon(\pi^0)$	SE	E_{K_L}	ϵ(Trk)	$\epsilon_\pi(K)$	$\epsilon_K(K)$	$\epsilon_\pi(\pi)$	$\epsilon(K_S)$	$Q=0$	Spec.	$\mathcal{B}$(D)	Cont.
$\pi^+\pi^-\eta(\gamma\gamma)$	-4.79	-1.48	-0.25	-0.88	-1.54	-1.51	-0.02	-1.54	-1.52	-1.57	2.22	2.73	1.93
$\bar{K}^0\pi^0\pi^0$	-0.1	-2.74	1	-0.01	-0.11	-0.12	1.43	-0.11	-0.87	-0.24	0.35	2.83	0.47
$\pi^+\pi^-\pi^+\pi^-\pi^+\pi^-$	-1.63	-1.62	4.62	0	-1.96	-1.66	-0.08	-1.63	-1.64	-2.99	0.02	6.58	0.42
$K, K^0, \pi,$	0.63	0.64	2.24	-0.01	0.46	0.61	0.62	0.62	-0.78	0.35	11.06	27.22	0.17
$K^+K^-\pi^0$	0.53	-0.79	-1.44	-0.01	0.52	0.49	-1	0.52	0.52	0.5	0.4	0.49	0.47
$\pi^0\pi^0\pi^0\pi^0$	-4.61	-9.86	2.03	-0.1	-4.51	-4.45	-3.26	-4.72	-4.38	-4.68	4.39	39.87	7.56
$\bar{K}^0\pi^+\pi^-\pi^0$	0.18	-1.14	1.77	0	0.01	0.15	1.72	0.17	-0.2	-0.12	1.37	2.86	0.36
$K^-\pi^+\pi^0\pi^0$	0.32	-2.27	-0.18	0	0.32	0.3	0.32	0.32	0.32	0.28	0.25	0.34	0.21
$\bar{K}^0\eta(\gamma\gamma)$	-3.8	-0.57	1.02	0	-0.58	-0.58	0.93	-0.58	-2.3	-0.66	0.41	1.36	0.43
$2\times K, 2\times\pi,$	-0.51	-0.5	-2.78	0	-0.68	-0.51	-2.03	-0.52	-0.51	-0.77	0.47	1.32	0.28
$\pi^+\pi^-\pi^0\pi^0\pi^0\pi^0$	-9.72	-16.67	10.25	12.32	-9.64	-10.01	-7.14	-9.96	-9.3	-9.37	11.43	67.7	15.9
$\bar{K}^0\pi^+\pi^-\pi^+\pi^-$	0.06	0.08	2.89	0	-0.26	0.05	1.62	0.06	0.23	-1.01	6.2	20.94	0.13
$K^-\pi^+\pi^-\pi^+\pi^0$	0.14	-1.16	0.29	0	-0.01	0.12	0.13	0.14	0.14	-0.26	0.17	1.88	0.17
$K^-\pi^+\eta(\gamma\gamma)$	-2.79	0.49	0.05	0	0.46	0.44	0.46	0.46	0.46	0.41	4.98	0.27	0.21

147

Table 7.3 (Continued)

Mode	$\epsilon(\eta)$	$\epsilon(\pi^0)$	SE	E_{K_L}	$\epsilon(\text{Trk})$	$\epsilon_\pi(K)$	$\epsilon_K(K)$	$\epsilon_\pi(\pi)$	$\epsilon(K_S)$	$Q=0$	Spec.	$\mathcal{B}(D)$	Cont.
$\pi^+\pi^-\pi^+\pi^-\pi^0\pi^0$	0.11	-2.59	1.88	0	-0.08	0.1	1.77	0.08	0.07	-0.72	0.38	7.43	1.23
$\bar{K}^0K^0\pi^0$	-7.03	-8.31	3.57	0.04	-7.19	-7.12	-5.56	-7.05	-12.59	-7.53	10.37	181.94	2.37
$\pi^+\pi^-\pi^0\eta(\gamma\gamma)$	-4.22	-2.21	0.76	-0.27	-0.94	-0.97	0.62	-0.95	-0.94	-1.08	0.86	9.64	0.96
$\eta(\gamma\gamma)\eta(\gamma\gamma)$	-6.04	0.32	0.29	0	0.5	0.28	1.87	0.34	0.34	0.34	0.85	0	0.3
$K^+K^-\bar{K}^0$	-0.14	-0.13	-2.39	0	-0.31	-0.17	-1.66	-0.15	-0.55	-0.43	13.99	5.39	0.16
$\bar{K}^0\pi^0\pi^0\pi^0$	1.02	-2.81	1.06	-0.06	1.01	0.99	2.57	1.01	0.43	0.87	1.08	44.16	0.5
$\bar{K}^0K^0\pi^+\pi^-$	1.29	1.29	3.11	-0.02	0.95	1.22	2.87	1.28	1.3	0.25	5.56	70.41	0.25
$\pi^+\pi^-\pi^+\pi^-\eta(\gamma\gamma)$	2.75	6.36	0.73	-0.19	6.06	6.18	7.92	6.24	6.29	5.18	8.82	34.98	3.85
$K, K^0, \pi, \pi^0,$	32.47	30.28	32.42	-0.48	32.09	32.77	32.33	32.3	32.81	33.9	118.85	1045.45	8.65
$K^+K^-\pi^0\pi^0$	1.48	-1.48	-2.79	0	1.47	1.58	-0.23	1.47	1.47	1.48	0.67	10.74	1.75
$\bar{K}^0\pi^+\pi^-\pi^0\pi^0$	-0.89	-3.49	2.35	0	-1.07	-0.89	0.66	-0.91	-1	-1.62	0.7	134.44	0.7
$K^-\pi^+\pi^0\pi^0\pi^0$	2.44	-1.28	0.7	0	2.44	2.47	2.43	2.44	2.43	2.38	8.19	24.76	0.59
$\bar{K}^0\pi^0\eta(\gamma\gamma)$	-1.3	0.7	0.67	-0.13	1.99	1.97	3.56	1.99	1.31	1.85	1.41	4.62	0.19
$2\times K, 2\times\pi, \pi^0,$	1.8	0.46	-1.58	-0.04	1.62	1.77	0.19	1.78	1.78	0.91	2.9	5.48	0

Table 7.3 (Continued)

Mode	$\epsilon(\eta)$	$\epsilon(\pi^0)$	SE	E_{K_L}	ϵ(Trk)	$\epsilon_\pi(K)$	$\epsilon_K(K)$	$\epsilon_\pi(\pi)$	$\epsilon(K_S)$	$Q=0$	Spec.	$\mathcal{B}(D)$	Cont.
$\pi^+\pi^-\pi^0\pi^0\pi^0$	-2.25	-6.83	3.33	-0.57	-2.25	-2.4	-0.67	-2.29	-2.26	-2.4	3.81	15.73	3.89
$K^+K^-\eta(\gamma\gamma)$	-6.43	-3.21	-5.42	1.11	-3.29	-3.41	-4.75	-3.3	-3.28	-3.43	2.34	36	0
$\bar{K}^0\pi^+\pi^-\pi^+\pi^-\pi^0$	4.98	3.58	4.13	0.02	4.6	5.01	6.65	4.97	4.27	2.13	6.1	8.01	0
$\bar{K}^0K^0\bar{K}^0$	0.34	0.35	2.95	0	0	0.32	1.92	0.33	0.01	-0.97	3.71	53.12	0.44
$\pi^0\pi^0\pi^0\eta(\gamma\gamma)$	-3.85	-4.47	-0.47	-0.43	-0.65	-1.03	0.74	-0.9	-0.65	-0.77	0.6	28.9	1.11
$\bar{K}^0\pi^+\pi^-\eta(\gamma\gamma)$	-2.66	0.65	1.01	0	0.45	0.58	2.17	0.61	0.08	-0.2	1.44	6.31	0.35
$\pi^+\pi^-\pi^+\pi^-\pi^0\pi^0\pi^0$	-4.27	-7.39	1.52	-0.1	-4.45	-4.45	-2.69	-4.31	-4.27	-5.46	7.96	40.76	2.92
$\bar{K}^0K^0\pi^0\pi^0$	3.17	0.45	1.37	-0.05	3.02	3.28	4.75	3.18	3.29	2.71	1.97	302.77	1.12
$\pi^+\pi^-\pi^0\pi^0\eta(\gamma\gamma)$	-15.47	-14.79	1.39	-0.56	-12.48	-12.6	-10.99	-12.58	-12.42	-12.58	7.52	135.68	4.12
$K^-\pi^+\pi^-\pi^+\pi^-\pi^0$	2.07	0.77	1.26	0	1.73	1.95	2.07	2.06	2.06	-1.34	2.04	1.2	0
$K^-\pi^+\pi^+\eta(\gamma\gamma)$	-3.65	-0.39	0.25	0	-0.57	-0.47	-0.41	-0.41	-0.41	-2.1	0.4	0.44	0
$\bar{K}^0\pi^0\pi^0\pi^0\pi^0$	2.4	-2.2	2.29	-0.87	2.39	2.43	3.97	2.39	1.95	2.25	3.33	12.15	0.92
$\pi^+\pi^-\pi^+\pi^-\pi^0\eta(\gamma\gamma)$	-2.98	-0.78	2.59	-0.61	0.15	0.23	1.96	0.31	0.31	-1.95	0.28	57.67	0
$\pi^+\pi^-\eta(\gamma\gamma)\eta(\gamma\gamma)$	-5.09	1.4	0.75	-0.08	1.37	1.39	2.95	1.37	1.37	0.57	0.19	3.83	0

Table 7.3 (Continued)

Mode	$\epsilon(\eta)$	$\epsilon(\pi^0)$	SE	E_{K_L}	$\epsilon(\text{Trk})$	$\epsilon_\pi(K)$	$\epsilon_K(K)$	$\epsilon_\pi(\pi)$	$\epsilon(K_S)$	$Q=0$	Spec.	$\mathcal{B}(D)$	Cont.
$\bar{K}^0\pi^+\pi^-\pi^0\pi^0$	5.48	1.55	5.78	0.29	5.27	5.48	7.2	5.45	5.29	4.26	4.06	12.85	2.21
$\bar{K}^0\pi^0\pi^0\eta(\gamma\gamma)$	-5.76	-4.72	1.5	0	-2.61	-2.64	-1.1	-2.61	-2.73	-2.78	4.32	18.17	0.73
$\bar{K}^0\pi^+\pi^-\pi^0\eta(\gamma\gamma)$	12.81	15.31	-1.87	0.02	16.5	16.52	18.52	16.68	17.55	14.79	14.21	30.73	1.23
$K^-\pi^+\pi^0\pi^0\eta(\gamma\gamma)$	-4.97	-3.94	0.72	0	-1.78	-1.81	-1.78	-1.78	-1.78	-1.99	0.27	51.84	0
$K^-\pi^+\pi^0\eta(\gamma\gamma)$	-2.28	-0.72	-1.19	0	0.63	0.95	-0.56	0.15	0.95	0.22	2.01	16.84	0.62

7.1.1 Semileptonic Yields

We define our exclusive semileptonic efficiency as the number of $D^+ \to Xe^+\nu$ reconstructed divided by the total number produced by e^+e^- collisions. Since the final state of the other side D affects our ability to reconstruct the neutrino, our efficiency-corrected yields are sensitive to all of the branching fractions of the other side D. We correct our efficiency prediction by measuring as many of the D hadronic decays as possible and using them in our Monte Carlo simulation. The uncertainty of each branching fraction measurement, both previously measured D decays and decays first measured by this analysis, contribute to the systematic uncertainty on the overall efficiency. We minimize these uncertainties in the absolute branching fractions by using $K\pi\pi$ yields and previous measurements of $\mathcal{B}(D^+ \to K^-\pi^+\pi^+)$ to normalize the $\mathcal{B}(D^\pm \to \eta^{(\prime)}e^\pm\nu)$ measurements. However, the cancelation of errors in the final branching fractions is dependent on whether or not the ratio of $\eta^\pm e^\pm \nu$ to $K\pi\pi$ efficiency-corrected yields remain constant with variations in the generic D branching fractions. Therefore, we calculate the systematic uncertainties on the efficiency-corrected yields from our knowledge of the D branching fractions, and explicitly show that normalizing to $K\pi\pi$ removes this class of uncertainties.

We calculate the systematic uncertainty in the efficiency-corrected yields by individually varying each branching fraction measurement by one standard deviation, and then adding the corresponding changes to the efficiency-corrected yields in quadrature to obtain an error on the yield. However, with each variation we must maintain the physical requirement that $\sum_j^N \mathcal{B}_j = 1$. So, with each variation we repeat the N-1 parameter fit to the N branching fraction measurements described in Section 5.2.

In addition to varying the measurements of all known decays, we consider the possibility that there is a class of decays that we know nothing about with an inclusive branching fraction of $\mathcal{B}_U$. For our nominal corrections we assume $\mathcal{B}_U = 0$. However,

the sum of the inclusive semileptonic and hadronic branching fractions is 97.2% ± 2%, which allows for $\mathcal{B}_U$ to be as large as 4.8%. If $\mathcal{B}_U$ is non-zero there are two reasons why the decays have not been discovered: they either have very low efficiency for being fully reconstructed, or they are a large number of decays that are individually too small to produce a statistically significant signal in the data. Inefficient final states will not contribute to our overall efficiency, but a diverse collection of efficient final states will. A systematic uncertainty from $\mathcal{B}_U$ = 4.8% of inefficient final states is probably overly conservative, so for the systematic error associated with $\mathcal{B}_U$ we take the difference between $\mathcal{B}_U$ = 0 and $\mathcal{B}_U$ = 2.8% where the efficiency for the unknown decays is assumed to be zero.

Table 7.4 lists the systematic uncertainty associated with the non-signal D branching fractions for the following 4 classes of decays:

1. Efficiency systematic uncertainty from Inclusive semileptonic branching fraction.

2. Efficiency systematic uncertainty from hadronic branching fractions containing K^0

3. Efficiency systematic uncertainty from hadronic branching fractions not containing K^0

4. Efficiency systematic uncertainty for size of $\mathcal{B}_U$.

Each class of decays described above have unique contributions to the total systematic uncertainty. The other side D semileptonic decays should have essentially zero efficiency for contributing to our signal, but in the $\sum_j^N \mathcal{B}_j$ = 1 fit the value still affects the absolute scale of other side decays that do contribute to the efficiency. The hadronic decays that have K^0 should have lower efficiencies than decays without K^0 because 50% of the time $K^0 \rightarrow K_L$. The systematic uncertainty from whether or not to include $\mathcal{B}_U$ is not directly derived from a measurement, and so belongs in a class of its own.

Table 7.4: The systematic uncertainties of the efficiency-corrected yields associated with the different types of other side D branching fractions. We show the percent change in the efficiencies in the $\eta'ev$, ηev (3 q^2 bins and the total), and the $K^-\pi^+\pi^+$. We choose to use the $\mathcal{B}_U = 2.8\%$ estimate as the systematic uncertainty in this analysis.

Decay	$\mathcal{B}(D^+ \to X^0\ell^+\nu)$	$\mathcal{B}(D^+ \to XK^0)$	$\mathcal{B}(D^+ \to X[\text{no } K^0])$	$\mathcal{B}_U = 2.8\%/4.8\%$
$K^-\pi^+\pi^+$	0.41%	0.44%	0.61%	1.45% / 2.45%
$\eta'ev$	0.42%	0.46%	0.63%	1.48% / 2.25%
ηev	0.41%	0.44%	0.60%	1.44% / 2.52%
$\eta ev\ q_1^2$	0.41%	0.46%	0.60%	1.42% / 2.50%
$\eta ev\ q_2^2$	0.40%	0.41%	0.60%	1.41% / 2.41%
$\eta ev\ q_3^2$	0.45%	0.54%	0.63%	1.59% / 2.79%

The total systematic uncertainty on all of the efficiency-corrected yields is approximately 1.6% of the central values. Since the uncertainties are essentially the same for both the signal ($D^\pm \to \eta^{(')}e^\pm\nu$) and normalization ($D^+ \to K^-\pi^+\pi^+$) decays, the error in the final branching fractions, which is derived from a ratio of the two yields, is be negligible.

7.1.2 Hadronic Branching Fractions

We determine the hadronic branching fractions using double tagged events and so our signal efficiencies are not sensitive to other D branching fractions, but our background levels are. We determine the branching fractions by inverting the cross-feed matrix and multiplying it by the vector of observed events. The total $D\bar{D}$ background in decay i is given by:

$$\sum_{j,\ j\neq i} \frac{N_{\text{TAG}}(\text{DATA})}{N_{\text{TAG}}(\text{MC})} A_{ij} W_j, \tag{7.2}$$

The statistical uncertainties on the W_j for all j decays with a non-zero A_{ij} contributes to the uncertainty in the decay i backgrounds. We individually vary the W_j by 1 standard deviation and add the corresponding changes to the signal in quadrature to obtain a systematic uncertainty.

7.2 Continuum

In the semileptonic measurements we constrain the overall background level using the signal-free region of the M_{BC} distribution. In the scheme used to measure the hadronic branching fractions there is no means by which to constrain the continuum backgrounds. Therefore, for the hadronic branching fractions, we separately vary the continuum background for each decay mode by 20% and assign the corresponding change in the number of signal events as the systematic uncertainty.

7.3 Hadronic Daughter Spectra

We assign a systematic uncertainty for the effect of the spectrum of daughter particles of hadronic D decays on the efficiency-corrected yields of $D^{\pm} \rightarrow \eta e^{\pm} \nu$, $D^{\pm} \rightarrow \eta' e^{\pm} \nu$, and $D^{+} \rightarrow K^{-} \pi^{+} \pi^{+}$ by taking the difference between the yields with and without the spectrum corrections.

Both the efficiency and the backgrounds of hadronic decays are affected by the spectra of daughter particles. The affect on the backgrounds is found by taking the difference between the results with and without the spectrum corrections. The systematic uncertainty from how the spectra affects the efficiency of the final state is determined by radically altering the spectra generated by the Monte Carlo simulation (prior to reconstruction) and calculating the subsequent change. For each generated momentum distribution we find the average momentum, which divides the area of the spectrum in

154

half, and weight events with momentum below the average by 1.5 and events above the average by 0.5. This reweighting conserves the total number of generated events but increases the fraction of particles with low momentum, and low efficiency, by 50%. If after this change a comparison of the reconstructed spectra of the data and Monte Carlo (both normalized to the same area) have a $\chi^2/(d.o.f) > 1$, then we divide the change in efficiency by $\sqrt{\chi^2/(d.o.f)}$ to account for the disagreement with observation. We repeat this procedure weighting the spectra high rather than low, and whichever reweighting produces the largest change in the efficiency is assigned to be the systematic uncertainty. The systematic uncertainty for each type of daughter particle is added in quadrature to obtain the total systematic uncertainty on the efficiency from our knowledge of the spectra.

7.4 Electron ID Systematic Uncertainty

The electron identification efficiency was studied in [37], and [38]. The expected systematic uncertainty on the total $\eta e^{\pm}\nu$ efficiency given the electron spectrum is 0.3% of itself, and for $\eta' e\nu$ it is 0.5% of itself.

7.5 Other Uncertainties

For the following sources of systematic uncertainty, we determine the error by taking the difference between our results with the corresponding corrections described in Chapter 5 and without them:

1. The simulation of splitoff escapes.

2. The simulation of how a K_L deposits energy in the crystal calorimeter.

3. The FSR (final state radiation) in $D^{\pm} \rightarrow \eta^{(\prime)}e^{\pm}\nu$.

For the following sources of systematic uncertainty, we determine the error by changing the corresponding corrections described in Chapter 5 by 1 standard deviation, and calculating the change in the yields.

1. $\eta \rightarrow \gamma\gamma$ reconstruction efficiency.

2. $\pi^0 \rightarrow \gamma\gamma$ reconstruction efficiency.

3. Efficiency for a track to be trkman-approved.

4. Kaon identification efficiency.

5. The rate for K to fake "signal pions".

6. The efficiency to identify π as "signal pion".

7. Net charge and track quality efficiency as a function of number of low p_T tracks.

This section describes the results of this study, including systematic uncertainties. We begin with discussing the hadronic branching fraction measurements, as these measurements feed into the semileptonic yields and branching fractions as systematic uncertainties.

8.1 Hadronic Branching Fractions

We use the Generic Reconstruction algorithm with a D-Tag to reconstruct the number of $\pi^{\pm}$, $K^{\pm}$, $K_S \rightarrow \pi^+\pi^-$, $\pi^0 \rightarrow \gamma\gamma$, and $\eta \rightarrow \gamma\gamma$ in the final state the other side D. We use the Monte Carlo simulation to predict the efficiency of reconstructing each final state, as well as the rate that one final state is incorrectly reconstructed as another. Given the efficiencies and the number of observed events in each final state we solve for the relative branching fraction of each D^+ and each D^0 decay. We calibrate the D^+ branching fractions using a previous CLEO-c measurement $\mathcal{B}(D^+ \rightarrow K^-\pi^+\pi^+) = (9.14 \pm 0.10 \pm 0.16 \pm 0.07)\%$, and calibrate D^0 branching fractions using another previous CLEO-c measurement $\mathcal{B}(D^0 \rightarrow K^-\pi^+) = (3.891 \pm 0.035 \pm 0.059 \pm 0.035)\%$. All hadronic decays presented are 100% correlated with the corresponding calibration mode and the systematic uncertainties contain the total uncertainty of the calibration decay (statistical and systematic uncertainties added in quadrature).

The branching fractions are determined in terms of the number of $\pi^{\pm}$, $K^{\pm}$, K^0, π^0, $\eta \rightarrow \gamma\gamma$ in the final state, so decays such as $D^+ \rightarrow \pi^+\eta$ contribute to multiple final states including: $D^+ \rightarrow \pi^+\pi^+\pi^-\pi^0$, $D^+ \rightarrow \pi^+\pi^0\pi^0\pi^0$, and $D^+ \rightarrow \pi^+\eta(\gamma\gamma)$. Final states may have multiple contributions from previously measured decays such as $D^+ \rightarrow \pi^+\pi^+\pi^-\pi^0$ that has contributions from $D^+ \rightarrow \pi^+\eta$ and $D^+ \rightarrow \pi^+\omega$.

For each final state we calculate the statistical significance in terms of the number of standard deviations the background prediction would have to fluctuate in order to equal the number of observed events ($N(\sigma_B)$). Final states with statistical significance greater than 3 σ_B constitute evidence-for the decay, and states greater than 5 σ_B constitute observations.

For the D^+ we attempt to measure the branching fraction of 44 final states seen in data. Of those 44 final states, 28 have $N(\sigma_B) > 5$, and 6 have $5 > N(\sigma_B) > 3$. Of the final states with $N(\sigma_B) > 5$, 13 are not listed in PDG 2008. The D^+ final states with PDG values are listed in Table 8.1, and those that are not listed in the PDG are given in Table 8.2. A 90% upper limit is calculated for every final state that is not listed in the PDG.

For the D^0 we attempt to measure the branching fraction of 62 final states seen in data. Of those 62 final states, 39 have $N(\sigma_B) > 5$ and 4 have $5 > N(\sigma_B) > 3$. Of the final states with $N(\sigma_B) > 5$, 19 are not listed in PDG 2008. The D^0 final states with PDG values are listed in Table 8.3, and those that are not listed in the PDG are given in Table 8.4. A 90% upper limit is calculated for every final state that is not listed in the PDG.

Of all of the final states that have been measured, we observe two final states that have no contributions from any of the decays programmed into the CLEO-c Monte Carlo simulation: $D^+ \to \pi^+\eta(\gamma\gamma)\eta(\gamma\gamma)$ and $D^0 \to K^-\pi^+\pi^0\eta(\gamma\gamma)$. The decay $D^+ \to \pi^+\eta\eta$ is particularly interesting because the branching fraction is roughly the same size as $\mathcal{B}(D^+ \to \pi^+\pi^0\pi^0)$. With all else being equal, one would naively expect the ratio $\mathcal{B}(D^+ \to \pi^+\eta\eta)/\mathcal{B}(D^+ \to \pi^+\pi^0\pi^0) \sim 0.08$ due to additional phase space constraints in $\pi\eta\eta$. We find $\mathcal{B}(D^+ \to \pi^+\eta(\gamma\gamma)\eta(\gamma\gamma)) = (0.052 \pm 0.008 \pm 0.005)\%$ that corresponds to $\mathcal{B}(D^+ \to \pi^+\eta\eta) = (0.337 \pm 0.057 \pm 0.032)\%$. The ratio $\mathcal{B}(D^+ \to \pi^+\eta\eta)/\mathcal{B}(D^+ \to \pi^+\pi^0\pi^0) = 0.73 \pm 0.16$, which is nearly a factor of 10 larger than naive expectations. The comparatively large size of the $D^+ \to \pi^+\eta\eta$ branching fraction indicates contributions
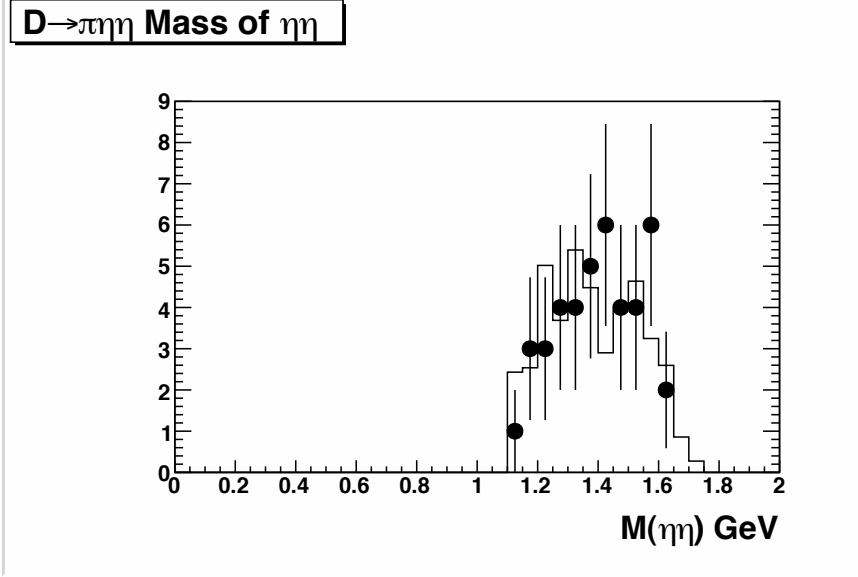
Figure 8.1: The invariant mass of the two η in the decay $D^+ \to \pi^+\eta\eta$. The dots are data, the histogram is Monte Carlo simulation using 3 body phase space.

from either an $\eta\eta$ or $\pi\eta$ resonance. Figure 8.1 shows the invariant mass of the two η compared to Monte Carlo expectations from three-body phase space predictions. The Monte Carlo $M(\eta\eta)$ prediction is consistent with data. Figure 8.2 is the mass of $\pi\eta_1$ versus the mass of $\pi\eta_2$, and the data appears to be restricted to a smaller region of phase space than the 3-body phase space prediction, possibly indicating a $\pi\eta$ resonance.

8.2 $D^\pm \to \eta e^\pm \nu$ and $D^\pm \to \eta' e^\pm \nu$

The ratio of the efficiency-corrected yields of the $D^+ \to \eta e^+ \nu$ ($D^+ \to \eta' e^+ \nu$) and the $D^+ \to K^-\pi^+\pi^+$ is equal to the ratio of the corresponding branching fractions. We find

$$\frac{\mathcal{B}(D^+ \to \eta' e^+ \nu)}{\mathcal{B}(D^+ \to K^-\pi^+\pi^+)} = (23.7 \pm 5.8 \pm 0.5) \times 10^{-4}, \tag{8.1}$$

and

$$\frac{\mathcal{B}(D^+ \to \eta e^+ \nu)}{\mathcal{B}(D^+ \to K^-\pi^+\pi^+)} = (128.4 \pm 11.0 \pm 3.7) \times 10^{-4}. \tag{8.2}$$

159

Table 8.1: The D^+ Hadronic branching fractions found in this analysis that have a listing in the PDG 2008

Mode	Bran. Frac. (%)	MC BF	PDG (08)	$\Delta\mathcal{B}/\sigma$
$\pi^+\pi^0$	$0.098 \pm 0.008 \pm 0.005$	0.129	0.128 ± 0.008	-2.49
$\pi^+\pi^-\pi^+$	$0.32 \pm 0.01 \pm 0.01$	0.34	0.33 ± 0.02	-0.35
$\bar{K}^0\pi^+$	$2.965 \pm 0.100 \pm 0.108$	2.925	2.940 ± 0.120	0.13
$K^+\pi^0$	$0.011 \pm 0.004 \pm 0.002$	0.024	0.024 ± 0.003	-2.60
$\pi^+\pi^0\pi^0$	$0.43 \pm 0.03 \pm 0.04$	0.48	0.48 ± 0.04	-0.78
$\pi^+\pi^-\pi^+\pi^0$	$1.213 \pm 0.044 \pm 0.086$	1.179	1.180 ± 0.090	0.25
$\pi^+\eta(\gamma\gamma)$	$0.145 \pm 0.009 \pm 0.009$	0.137	0.138 ± 0.013	0.40
$\pi^+\pi^-\pi^+\pi^-\pi^+$	$0.15 \pm 0.01 \pm 0.01$	0.18	0.17 ± 0.02	-0.71
$K^+\bar{K}^0$	$0.64 \pm 0.03 \pm 0.02$	0.59	0.59 ± 0.04	0.88
$\bar{K}^0\pi^+\pi^0$	$14.39 \pm 0.36 \pm 0.64$	13.98	14.00 ± 1.00	0.31
$K^+K^-\pi^+$	$0.94 \pm 0.03 \pm 0.06$	1.00	1.00 ± 0.04	-0.74
$\bar{K}^0\pi^+\pi^-\pi^+$	$5.95 \pm 0.15 \pm 0.32$	6.21	6.20 ± 0.44	-0.44
$K^-\pi^+\pi^+\pi^0$	$5.79 \pm 0.16 \pm 0.32$	5.98	6.00 ± 0.28	-0.46
$K^-\pi^+\pi^-\pi^+\pi^+$	$0.57 \pm 0.03 \pm 0.05$	0.62	0.58 ± 0.06	-0.12
$\bar{K}^0 K^0\pi^+$	$1.45 \pm 0.15 \pm 0.62$	2.70	2.12 ± 0.92	-0.60
$K^+K^-K^+$	$0.008 \pm 0.004 \pm 0.001$	0.009	0.009 ± 0.002	-0.22
$K, K^0, 2\times\pi,$	$0.77 \pm 0.06 \pm 0.27$	0.82	0.48 ± 0.06	1.05
$K^+\bar{K}^0 K^0$	$0.96 \pm 0.10 \pm 0.16$	1.01	1.84 ± 0.87	-0.99

Table 8.2: The D^+ hadronic branching fractions not listed in PDG.

Mode	Bran. Frac. (%)	MC BF	N Observed	Background	Stat. Significance (σ)	90% U.L.(%)
$K^+\bar{K}^0\pi^0$	$1.043 \pm 0.074 \pm 0.086$	1.401	237	16.1 ± 6.1	36.0	< 1.254
$\pi^+\eta(\gamma\gamma)\eta(\gamma\gamma)$	$0.052 \pm 0.008 \pm 0.005$	NA	42	0.8 ± 1.2	32.0	< 0.070
$\pi^+\pi^-\pi^+\eta(\gamma\gamma)$	$0.18 \pm 0.01 \pm 0.01$	0.20	203	19 ± 6.5	28.0	< 0.21
$K^+K^-\pi^+\pi^0$	$0.52 \pm 0.05 \pm 0.08$	0.42	165	16.2 ± 7.4	19.8	< 0.71
$\bar{K}^0\pi^+\eta(\gamma\gamma)$	$0.98 \pm 0.05 \pm 0.08$	0.94	405	29 ± 22.1	17.0	< 1.16
$\bar{K}^0\pi^+\pi^-\pi^+\eta(\gamma\gamma)$	$0.041 \pm 0.017 \pm 0.004$	0.086	7	0.6 ± 0.4	14.3	< 0.077
$K^-\pi^+\pi^+\eta(\gamma\gamma)$	$0.042 \pm 0.009 \pm 0.007$	0.240	36	6.7 ± 3	9.6	< 0.059
$\pi^+\pi^-\pi^+\pi^0\eta(\gamma\gamma)$	$0.12 \pm 0.02 \pm 0.02$	0.03	57	14.2 ± 5.3	8.0	< 0.18
$\bar{K}^0\pi^+\pi^0\pi^0$	$5.65 \pm 0.26 \pm 0.80$	6.90	761	124.7 ± 83.9	7.5	< 7.20
$\pi^+\pi^0\pi^0\pi^0$	$0.40 \pm 0.05 \pm 0.07$	0.52	165	68.7 ± 15.4	6.2	< 0.57
$\pi^+\pi^0\eta(\gamma\gamma)$	$0.047 \pm 0.010 \pm 0.010$	0.055	72	30.2 ± 7.5	5.5	< 0.069
$\pi^+\pi^-\pi^+\pi^0\pi^0$	$0.85 \pm 0.07 \pm 0.17$	1.31	393	157.7 ± 45.6	5.1	< 1.18
$K^-\pi^+\pi^-\pi^+\pi^+\pi^0$	$0.07 \pm 0.02 \pm 0.02$	0.26	16	3.7 ± 2.4	5.1	< 0.12
$\pi^+\pi^-\pi^+\pi^-\pi^+\pi^0\pi^0$	$0.13 \pm 0.05 \pm 0.07$	0.02	11	3.1 ± 1.6	4.7	< 0.36
$\bar{K}^0\pi^+\pi^-\pi^+\pi^0$	$2.89 \pm 0.17 \pm 0.67$	2.38	485	92.3 ± 88.5	4.4	< 4.19
$K^-\pi^+\pi^+\pi^0\pi^0$	$0.60 \pm 0.08 \pm 0.15$	0.84	140	45.4 ± 21.5	4.3	< 0.91

Table 8.2 (Continued)

Mode	Bran. Frac. (%)	MC BF	N Observed	Background	Stat. Significance (σ)	90% U.L.(%)
$\pi^+\pi^0\pi^0\eta(\gamma\gamma)$	$0.14 \pm 0.03 \pm 0.04$	0.18	63	25.6 ± 10.6	3.5	< 0.23
$K^+\bar{K}^0\pi^0\pi^0$	$0.13 \pm 0.06 \pm 0.05$	0.12	15	5.7 ± 2.9	3.1	< 0.28
$\pi^+\pi^-\pi^+\pi^-\pi^+\pi^0$	$0.21 \pm 0.03 \pm 0.07$	0.25	112	47.2 ± 21.6	2.9	< 0.34
$\pi^+\pi^0\pi^0\pi^0\eta(\gamma\gamma)$	$0.12 \pm 0.07 \pm 0.09$	0.01	11	5.1 ± 2.5	2.3	< 0.43
$\pi^+\pi^0\pi^0\pi^0\pi^0$	$0.13 \pm 0.07 \pm 0.08$	0.05	18	9.7 ± 4	2	< 0.34
$\bar{K}^0\pi^+\pi^0\pi^0\pi^0$	$1.22 \pm 0.24 \pm 0.74$	0.99	48	13.1 ± 20.7	1.6	< 2.58
$\bar{K}^0\pi^+\pi^0\eta(\gamma\gamma)$	$0.05 \pm 0.03 \pm 0.03$	0.12	22	13.5 ± 5.2	1.6	< 0.13
$\pi^+\pi^-\pi^+\pi^0\pi^0\pi^0$	$0.16 \pm 0.09 \pm 0.18$	0.27	42	30.6 ± 12.9	0.8	< 0.45
$K^+\pi^0\pi^0$	$0.005 \pm 0.007 \pm 0.012$	0.003	30	25.6 ± 9.4	0.4	< 0.033
$\bar{K}^0K^0\pi^+\pi^0$	$0.3 \pm 0.2 \pm 1.2$	0.8	84	69 ± 53.3	0.2	< 2.2
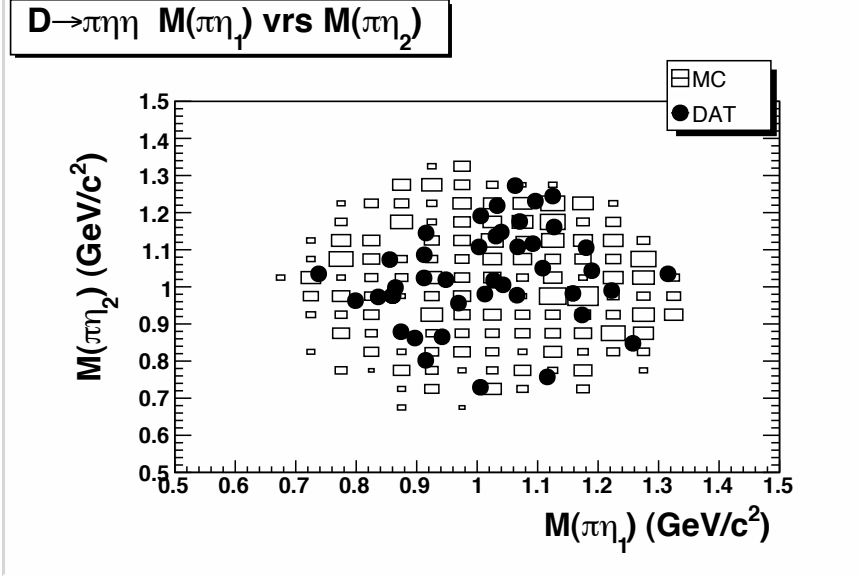
Figure 8.2: The invariant mass of $\pi\eta_1$ versus the invariant mass of $\pi\eta_2$ in the decay $D^+ \rightarrow \pi^+\eta\eta$. The black dots are data, the squares are from a Monte Carlo simulation using 3 body phase space.

We convert these branching fraction ratios to branching fractions using the CLEO-c measurement from the most recent double tag fit: $\mathcal{B}(D^+ \rightarrow K^-\pi^+\pi^+) = (9.14 \pm 0.10 \pm 0.16 \pm 0.07)\%$ [39]. We find the branching fractions:

$$\mathcal{B}(D^+ \rightarrow \eta' e^+ \nu) = (2.16 \pm 0.53_{stat} \pm 0.05_{syst} \pm 0.05_{K\pi\pi}) \times 10^{-4}, \qquad (8.3)$$

and

$$\mathcal{B}(D^+ \rightarrow \eta e^+ \nu) = (11.70 \pm 0.98_{stat} \pm 0.34_{syst} \pm 0.26_{K\pi\pi}) \times 10^{-4}. \qquad (8.4)$$

Table 8.5 summarizes the branching fraction ratios and branching fractions for the above as well as the three q^2 regions of $D^+ \rightarrow \eta e^+ \nu$.

8.3 $D^\pm \rightarrow \eta e^\pm \nu$ Form Factor Expansion Fit

We expect the q^2 distribution of $D^+ \rightarrow \eta e^+ \nu$ to be dominated by the phase space dependence. However, with the three q^2 bins we fit for the form factor with the series

Table 8.3: The D^0 Hadronic branching fractions found in this analysis that have a listing in the PDG 2008

Mode	Bran. Frac. (%)	MC BF	PDG (08)	$\Delta\mathcal{B}/\sigma$
$\pi^+\pi^-$	$0.151 \pm 0.007 \pm 0.005$	0.138	0.137 ± 0.003	1.48
$\pi^0\pi^0$	$0.093 \pm 0.008 \pm 0.004$	0.081	0.079 ± 0.008	1.16
$\pi^+\pi^-\pi^0$	$1.567 \pm 0.039 \pm 0.055$	1.407	1.410 ± 0.080	1.50
$\pi^+\pi^-\pi^+\pi^-$	$0.75 \pm 0.02 \pm 0.02$	0.73	0.73 ± 0.03	0.47
$\bar{K}^0\pi^0$	$2.057 \pm 0.083 \pm 0.081$	2.258	2.260 ± 0.240	-0.76
K^+K^-	$0.47 \pm 0.02 \pm 0.01$	0.39	0.39 ± 0.01	3.58
$\bar{K}^0\pi^+\pi^-$	$6.15 \pm 0.13 \pm 0.22$	5.83	5.76 ± 0.38	0.85
$K^-\pi^+\pi^0$	$15.13 \pm 0.26 \pm 0.37$	13.61	13.50 ± 0.60	2.17
$\pi^+\pi^-\pi^0\pi^0$	$0.97 \pm 0.04 \pm 0.06$	0.99	0.98 ± 0.09	-0.09
$K^-\pi^+\pi^-\pi^+$	$8.08 \pm 0.14 \pm 0.39$	7.81	7.70 ± 0.25	0.79
$\pi^+\pi^-\pi^+\pi^-\pi^0$	$0.37 \pm 0.03 \pm 0.04$	0.42	0.41 ± 0.05	-0.57
$\bar{K}^0 K^0$	$0.05 \pm 0.02 \pm 0.06$	0.03	0.14 ± 0.03	-1.34
$\pi^+\pi^-\pi^+\pi^-\pi^+\pi^-$	$0.066 \pm 0.009 \pm 0.007$	0.040	0.040 ± 0.011	1.67
$K, K^0, \pi,$	$0.90 \pm 0.07 \pm 0.27$	1.22	0.68 ± 0.10	0.74

expansion given by

$$F_+(q^2) = \frac{1}{P(q^2)\phi(q^2,t_0)} \sum_{k=0}^{k_{max}} a_k(t_0)[z(q^2,t_0)]^k, \tag{8.5}$$

where the variables and functions are described in Chapter 1.2, [40]. Since we only have three data points, and an overall normalization, we only consider form factor contributions to order $k = 1$. We use the arbitrary value of $t_0 = 0$.

Let the form factor be described by:

$$F_+(q^2) = a_0 F(q^2, 0) + a_1 F(q^2, 1), \tag{8.6}$$

Table 8.3 (Continued)

Mode	Bran. Frac. (%)	MC BF	PDG (08)	$\Delta\mathcal{B}/\sigma$
$K^+K^-\pi^0$	$0.36 \pm 0.02 \pm 0.02$	0.33	0.32 ± 0.02	1.11
$\bar{K}^0\pi^+\pi^-\pi^0$	$10.36 \pm 0.24 \pm 0.49$	10.72	10.60 ± 1.20	-0.18
$\bar{K}^0\eta(\gamma\gamma)$	$0.34 \pm 0.02 \pm 0.02$	0.30	0.30 ± 0.05	0.69
$2 \times K, 2 \times \pi,$	$0.23 \pm 0.02 \pm 0.02$	0.25	0.23 ± 0.01	0.00
$\bar{K}^0\pi^+\pi^-\pi^+\pi^-$	$0.74 \pm 0.05 \pm 0.16$	0.57	0.55 ± 0.06	1.05
$K^-\pi^+\pi^-\pi^+\pi^0$	$5.06 \pm 0.13 \pm 0.17$	3.53	4.10 ± 0.40	2.12
$K^+K^-\bar{K}^0$	$1.062 \pm 0.069 \pm 0.191$	0.920	0.910 ± 0.068	0.71
$\bar{K}^0K^0\pi^+\pi^-$	$0.57 \pm 0.09 \pm 0.40$	0.52	0.12 ± 0.02	1.10
$\bar{K}^0\pi^0\eta(\gamma\gamma)$	$0.90 \pm 0.06 \pm 0.09$	0.42	0.41 ± 0.09	3.45
$2 \times K, 2 \times \pi, \pi^0,$	$0.028 \pm 0.014 \pm 0.003$	0.316	0.310 ± 0.200	-1.41
$\bar{K}^0K^0\bar{K}^0$	$0.40 \pm 0.09 \pm 0.21$	0.50	0.74 ± 0.10	-1.36

where

$$F(q^2, k) = \frac{1}{P(q^2)\phi(q^2, 0)}[z(q^2, 0)]^k. \tag{8.7}$$

Let $\mathcal{F}_j(k_1, k_2)$ be defined by:

$$\mathcal{F}_j(k_1, k_2) = \int_j \left(F(q^2, k_1)F(q^2, k_2) \right) \Omega(q^2)\partial q^2, \tag{8.8}$$

where j represents a particular q^2 region, and $\Omega(q^2)$ is a phase space factor. The branching fraction for q^2 region j ($\mathcal{B}_j$) is given by:

$$\mathcal{B}_j = C \times \left(\mathcal{F}_j(0, 0) + 2\frac{a_1}{a_0}\mathcal{F}_j(0, 1) + \left(\frac{a_1}{a_0}\right)^2 \mathcal{F}_j(1, 1) \right), \tag{8.9}$$

where C is a normalization constant. The values of $\mathcal{F}_j(0, 0)$, $\mathcal{F}_j(0, 1)$, and $\mathcal{F}_j(1, 1)$ are numerically calculated and are given in arbitrary units in Table 8.6.

We fit the measurements of the branching fractions in the q^2 bins with C and a_1/a_0 as free parameters (Figure 8.3). To determine the systematic uncertainties, we repeat the fit

Table 8.4: The D^0 hadronic branching fractions not listed in PDG.

Mode	Bran. Frac. (%)	MC BF	N Observed	Background	Stat. Significance (σ)	90% U.L.(%)
$\eta(\gamma\gamma)\eta(\gamma\gamma)$	$0.028 \pm 0.004 \pm 0.002$	0.027	41	0.2 ± 0.1	336.6	< 0.037
$K^-\pi^+\eta(\gamma\gamma)$	$0.75 \pm 0.03 \pm 0.06$	0.70	1034	21.6 ± 3.8	254.3	< 0.88
$K^-\pi^+\pi^0$	$8.58 \pm 0.19 \pm 0.28$	7.60	3609	63.9 ± 14	252.2	NA
$K^-\pi^+\pi^-\pi^+\eta(\gamma\gamma)$	$0.09 \pm 0.01 \pm 0.01$	0.13	41	0.2 ± 0.2	118.9	< 0.13
$K^-\pi^+\pi^-\pi^+\pi^-\pi^+\pi^0$	$0.072 \pm 0.026 \pm 0.007$	0.077	8	0 ± 0	72.5	< 0.129
$\bar{K}^0\pi^0\pi^0$	$2.50 \pm 0.11 \pm 0.14$	2.85	655	45.5 ± 18.1	33.4	< 2.83
$\pi^+\pi^-\eta(\gamma\gamma)$	$0.048 \pm 0.006 \pm 0.004$	0.047	89	12.3 ± 2.5	28.7	< 0.060
$\pi^0\eta(\gamma\gamma)$	$0.025 \pm 0.004 \pm 0.002$	0.024	40	3.8 ± 1.3	23.9	< 0.033
$\pi^+\pi^-\eta(\gamma\gamma)\eta(\gamma\gamma)$	$0.010 \pm 0.004 \pm 0.001$	0.009	7	0.2 ± 0.2	19.4	< 0.018
$\bar{K}^0\pi^+\pi^-\eta(\gamma\gamma)$	$0.50 \pm 0.04 \pm 0.04$	0.43	158	7.8 ± 9.4	15.6	< 0.62
$\pi^+\pi^-\pi^+\pi^-\pi^0\pi^0$	$0.43 \pm 0.05 \pm 0.04$	2.72	100	17.8 ± 6.1	13.2	< 0.53
$\pi^+\pi^-\pi^0\eta(\gamma\gamma)$	$0.24 \pm 0.02 \pm 0.03$	0.20	197	27.8 ± 16.3	10.2	< 0.31
$\bar{K}^0\pi^+\pi^-\pi^+\pi^-\pi^0$	$0.27 \pm 0.06 \pm 0.05$	0.24	27	2.4 ± 2.4	9.6	< 0.41
$K^+K^-\pi^0\pi^0$	$0.07 \pm 0.02 \pm 0.01$	0.30	17	3 ± 1.5	9	< 0.11

Table 8.4 (Continued)

Mode	Bran. Frac. (%)	MC BF	N Observed	Background	Stat. Significance (σ)	90% U.L.(%)
$\bar{K}^0\pi^0\pi^0\pi^0\pi^0$	$1.30 \pm 0.32 \pm 0.26$	0.34	21	2.1 ± 2.5	7.2	< 2.18
$\bar{K}^0\pi^+\pi^-\pi^0\pi^0\pi^0$	$0.6 \pm 0.2 \pm 0.1$	2.2	16	3.6 ± 2	6.1	< 1.0
$\pi^+\pi^-\pi^0\pi^0\pi^0\pi^0$	$0.20 \pm 0.08 \pm 0.05$	0.17	13	3.3 ± 1.5	5.8	< 0.38
$K^-\pi^+\pi^0\eta(\gamma\gamma)$	$0.14 \pm 0.02 \pm 0.03$	NA	86	16.4 ± 11.9	5.8	< 0.21
$\bar{K}^0\pi^0\pi^0\eta(\gamma\gamma)$	$0.24 \pm 0.06 \pm 0.05$	1.14	20	3.1 ± 3	5.4	< 0.37
$K^-\pi^+\pi^0\pi^0\pi^0$	$1.136 \pm 0.100 \pm 0.316$	0.730	146	6.8 ± 34.4	4	< 1.787
$\pi^0\pi^0\pi^0\eta(\gamma\gamma)$	$0.05 \pm 0.02 \pm 0.02$	0.05	16	5 ± 3.2	3.2	< 0.10
$\pi^+\pi^-\pi^+\pi^-\eta(\gamma\gamma)$	$0.013 \pm 0.005 \pm 0.006$	0.008	12	3 ± 3.1	2.8	< 0.029
$K^+K^-\eta(\gamma\gamma)$	$0.012 \pm 0.005 \pm 0.005$	0.003	6	0.5 ± 2	2.5	< 0.033
$\pi^0\pi^0\pi^0\pi^0$	$0.04 \pm 0.02 \pm 0.02$	0.06	13	5.8 ± 2.9	2.4	< 0.09
$\bar{K}^0\pi^0\pi^0\pi^0$	$1.95 \pm 0.18 \pm 0.87$	1.62	134	7.2 ± 55.9	2.2	< 3.67
$\pi^+\pi^-\pi^+\pi^-\pi^0\pi^0\pi^0$	$0.11 \pm 0.05 \pm 0.06$	0.01	8	1.7 ± 2.5	2.3	< 0.36
$K^-\pi^+\pi^0\pi^0\eta(\gamma\gamma)$	$0.05 \pm 0.02 \pm 0.03$	0.06	7	0.3 ± 3.4	1.9	< 0.13
$\pi^0\pi^0\pi^0$	$0.015 \pm 0.008 \pm 0.011$	0.018	27	17.4 ± 7.1	1.3	< 0.040
$\pi^+\pi^-\pi^0\pi^0\pi^0$	$0.07 \pm 0.05 \pm 0.06$	0.46	51	39.8 ± 8.5	1.2	< 0.19

Table 8.4 (Continued)

Mode	Bran. Frac. (%)	MC BF	N Observed	Background	Stat. Significance (σ)	90% U.L.(%)
$\bar{K}^0\pi^+\pi^-\pi^0\pi^0$	$3.12 \pm 0.22 \pm 4.20$	3.67	291	46.1 ± 329.2	0.7	< 10.96
$\pi^+\pi^-\pi^0\pi^0\eta(\gamma\gamma)$	$0.03 \pm 0.01 \pm 0.05$	0.00	18	8.7 ± 12.5	0.7	< 0.15
$\bar{K}^0K^0\pi^0$	$0.8 \pm 0.3 \pm 1.4$	0.1	214	179.4 ± 62.8	0.5	< 3.9
$\bar{K}^0K^0\pi^0\pi^0$	$0.3 \pm 0.2 \pm 0.9$	0.2	30	19.8 ± 30.6	0.3	< 2.0
$\pi^+\pi^-\pi^+\pi^-\pi^0\eta(\gamma\gamma)$	$0.02 \pm 0.01 \pm 0.01$	0.01	6	0.7 ± 3	1.7	< 0.06
$K,K^0,\pi,\pi^0,$	$0.06 \pm 0.12 \pm 0.67$	1.01	448	436.5 ± 121.1	0	< 1.21

170

Table 8.5: The ratio of the semileptonic branching fractions with $\mathcal{B}(K\pi\pi)$ and the semileptonic branching fractions determined using $\mathcal{B}(D^+ \to K^-\pi^+\pi^+) = (9.14 \pm 0.10 \pm 0.16 \pm 0.07)\%$ [39].

Decay	q^2 Range (GeV^2)	$\mathcal{B}/\mathcal{B}(K^-\pi^+\pi^+) \times 10^4$	$\mathcal{B} \times 10^4$
$\eta' ev$	ALL	$23.7 \pm 5.8 \pm 0.5$	$2.16 \pm 0.53_{stat} \pm 0.05_{syst} \pm 0.05_{K\pi\pi}$
ηev	0.0 to 0.5	$62.5 \pm 6.9 \pm 1.8$	$5.71 \pm 0.63_{stat} \pm 0.16_{syst} \pm 0.12_{K\pi\pi}$
ηev	0.0 to 1.0	$43.7 \pm 6.8 \pm 1.3$	$3.99 \pm 0.62_{stat} \pm 0.12_{syst} \pm 0.09_{K\pi\pi}$
ηev	> 1.0	$22.3 \pm 5.2 \pm 1$	$2.03 \pm 0.47_{stat} \pm 0.08_{syst} \pm 0.04_{K\pi\pi}$
ηev	ALL	$128.4 \pm 11.0 \pm 3.7$	$11.70 \pm 0.98_{stat} \pm 0.34_{syst} \pm 0.26_{K\pi\pi}$

Table 8.6: The integrals ($\mathcal{F}_j(k_1, k_2)$) used in the $D^+ \to \eta e^+ v$ form factor fit. The integrals are given in arbitrary units, and are integrated over the phase space in the $\eta e^+ v\ q^2$ bins.

q^2 Region	$\mathcal{F}(0,0)$	$\mathcal{F}(0,1)$	$\mathcal{F}(1,1)$
0.0 GeV$^2 < q^2 <$ 0.5 GeV^2	1419520.0	-14502.5	206.2
0.5 GeV$^2 < q^2 <$ 1.0 GeV^2	833084.0	-27565.4	952.3
$q^2 >$ 1.0 GeV^2	355826.0	-20863.9	1251.05

for each systematic uncertainty described in Chapter 7, and take the change in the values as the systematic errors on the paramters. We obtain $(a_1/a_0)_{\eta e^\pm v} = -4.2 \pm 3.2_{stat} \pm 0.25_{syst}$. We expect the $D^+ \to \eta e^+ v$ form factors to be essentially the same as $D^+ \to \pi^0 e^+ v$. In [33] a similar fit was performed on $D^+ \to \pi^0 e^+ v$ where it was found that $(a_1/a_0)_{\pi^0 e^\pm v} = -2.6 \pm 0.7$, which is consistent with the $\eta e^\pm v$ result.
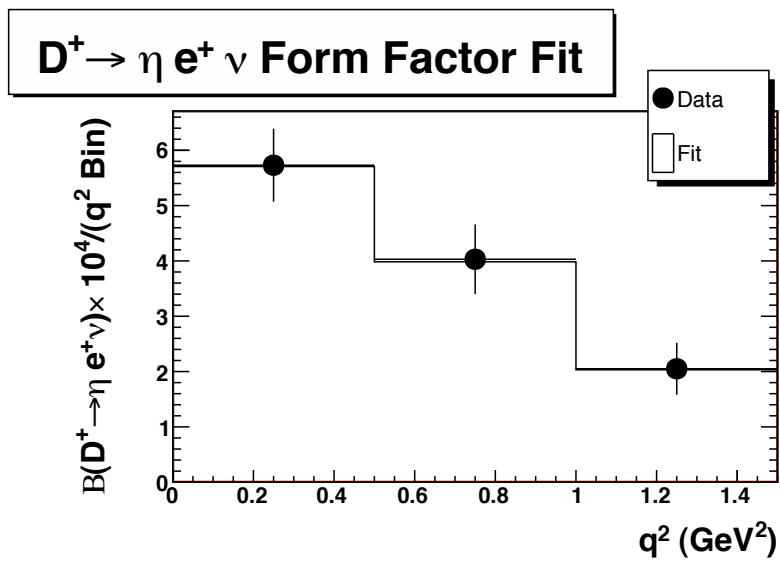
Figure 8.3: The $D^+ \rightarrow \eta e^+\nu$ form factor fit to the branching fractions found for the three q^2 regions.

CHAPTER 9

CONCLUSIONS

We have studied the semileptonic decays $D^+ \rightarrow \eta' e^+ \nu$ and $D^+ \rightarrow \eta e^+ \nu$ with a technique involving missing energy reconstruction via a generic reconstruction of the non-leptonically decaying D. The generic reconstruction allows us to place strict requirements on tracks in the events, as well as to remove extra showers from our missing energy calculations. We obtain the first observation of $D^+ \rightarrow \eta e^+ \nu$ and the most precise measurement of $D^+ \rightarrow \eta e^+ \nu$ in three different q^2 regions. For the measurement of the $D^+ \rightarrow \eta e^+ nu$ we do a series expansion form factor fit up to order 1 in $z(q^2, t_0)$. We find a value of $a_1/a_0 = -4.2 \pm 3.2_{stat} \pm 0.25_{syst}$, which is consistent with previous fits to $D^+ \rightarrow \pi^0 e^+ \nu$. Though the uncertainty is large, this is the first measurement of the $D^+ \rightarrow \eta e^+ \nu$ form factor.

One reason for performing this study was to see if there were evidence for extra gluon couplings enhancing the $D^\pm \rightarrow \eta' e^\pm \nu$ branching fraction. The form factors for the D to the SU(3) octet component of the η' should be nearly the same as $D \rightarrow \pi$ form factors multiplied by FKS constants. If this approximation is valid, and if there were no extra gluon coupling, then we would expect approximately 1.6×10^{-4} for the branching fraction of $D^\pm \rightarrow \eta' e^\pm \nu$. In our study we find this branching fraction to be $(2.16 \pm 0.53 \pm 0.05 \pm 0.05) \times 10^{-4}$. This branching fraction is 1σ above the no-two-gluon prediction. Though this measurement is 35% larger than the FKS minimum value, the uncertainty is large enough such that it could still be consistent with no enhancement. However, if there were no two gluon coupling the central value could have easily been one or two standard deviations below the FKS minimum rather than above it, and that would have been strong evidence against two gluon enhancement. Therefore, even though we have not conclusively shown whether or not there is a two gluon coupling in this decay, the fact that it has not been ruled out is still a very important piece of information.

By using a D-tag instead of a semileptonic decay, the same generic reconstruction algorithm was used to measure the D^+ and D^0 hadronic branching fractions in terms of final states involving: $\pi^\pm$, $K^\pm$, K^0, π^0, $\eta \to \gamma\gamma$. We observed 28 D^+ hadronic decays (13 of which are not reported in PDG 2008), found evidence for 6, and set 90% upper limits on 10. We observed 39 D^0 hadronic decays (19 of which are not reported in PDG 2008), found evidence for 4, and set 90% upper limits on 19. One of the newly discovered D^+ hadronic decays is $D^+ \to \pi^+\eta\eta$ which has a branching fraction similar in size to $D^+ \to \pi^+\pi^0\pi^0$ despite the phase space restrictions.

APPENDIX A

HADRONIC SPECTRA FIGURES

The following figures show the spectra of the different daughter particles in the D hadronic decays that required reweighting. Distributions were only reweighted if the χ^2 per degree of freedom for the distribution was greater than 4.

In order to help keep track of the different types of decays, each final state is assigned a descriptive code given by:

$$3000 + 2^{n_\pi} \times 3^{n_{\pi^0}} \times 5^{n_K} \times 7^{n_{K^0}} \times 13^{n_{\eta \to \gamma\gamma}}, \tag{A.1}$$

where n_π is the number of charged pions in the decay, n_{π^0} is the number of π^0, n_K the number of K, n_{K^0} the number of K^0, and $n_{\eta \to \gamma\gamma}$ the number of $\eta \to \gamma\gamma$. For example, the decay $D^+ \to K^-\pi^+\pi^+$ is represented by 3020 where 3020 is $3000 + 5 \times 2^2$.
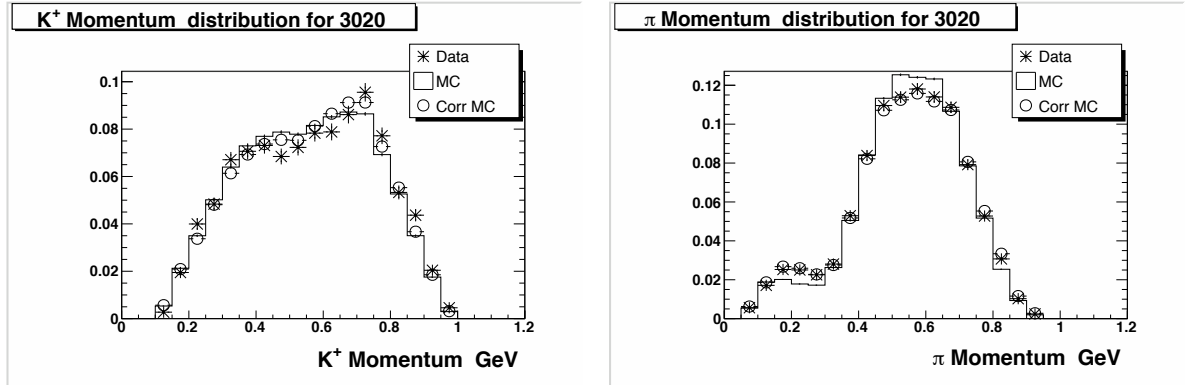
Figure A.1: The daughter spectra of the decays $D^+ \to K^- \pi^+ \pi^+$.
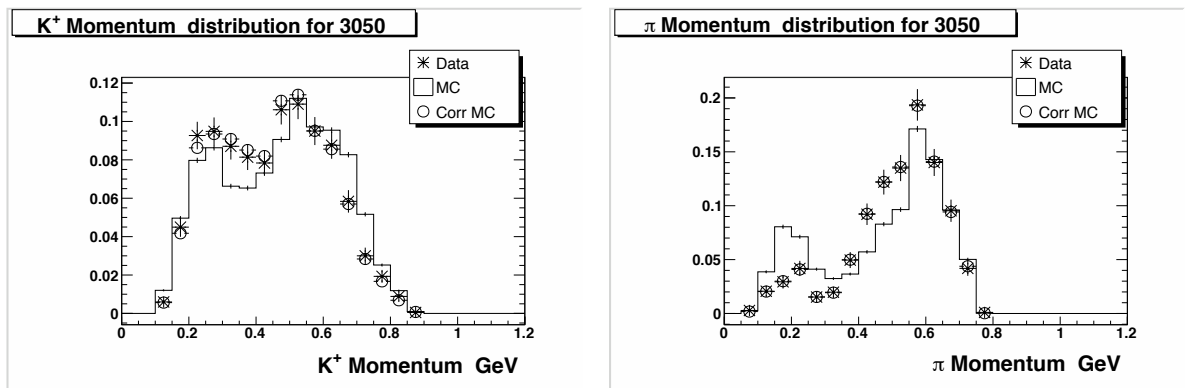
Figure A.2: The daughter spectra of the decays $D^+ \to K^- K^+ \pi^+$.

176
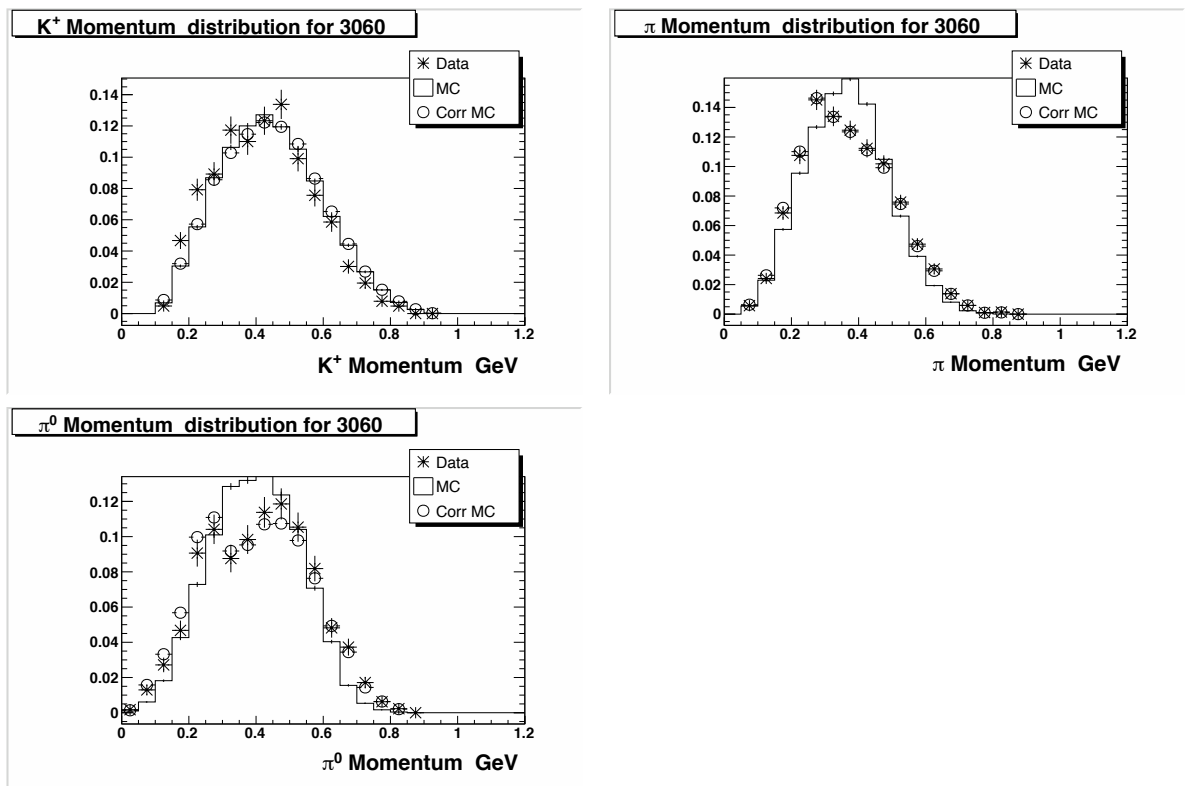
Figure A.3: The daughter spectra of the decays $D^+ \rightarrow K^- \pi^+ \pi^+ \pi^0$.

177
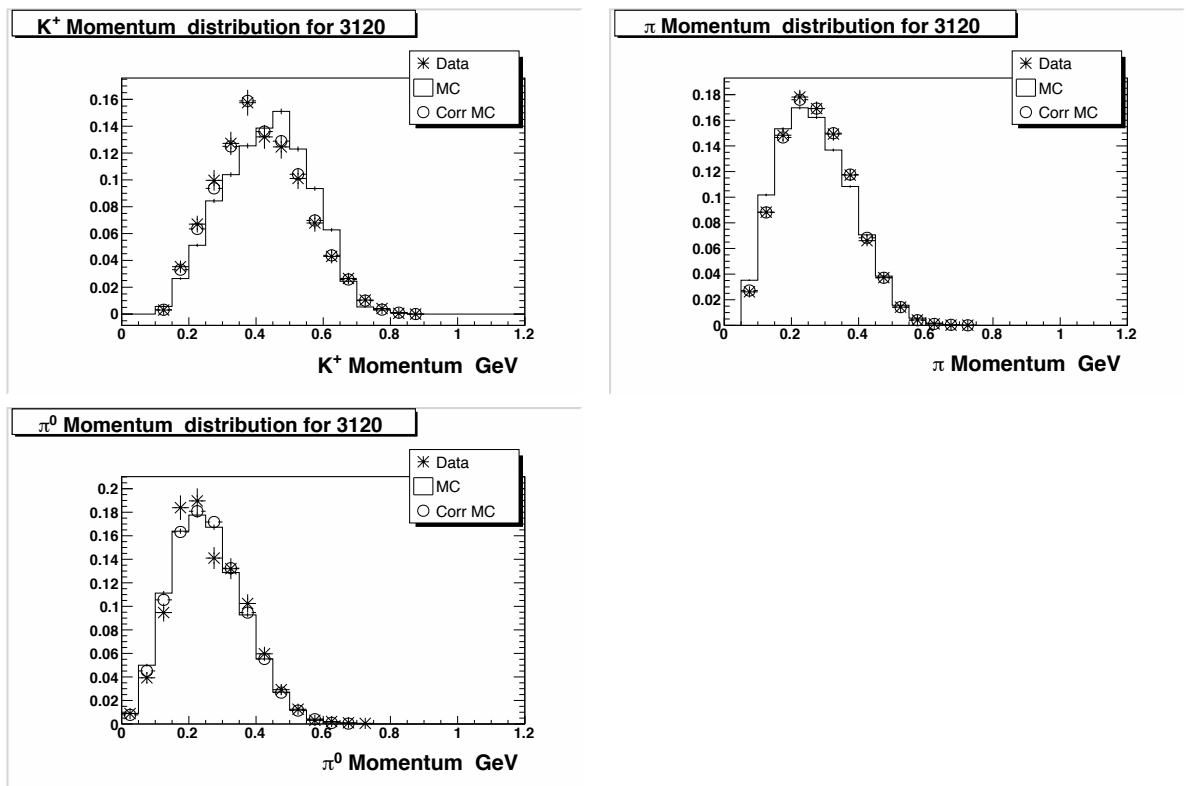
Figure A.4: The daughter spectra of the decays $D^0 \rightarrow K^- \pi^+ \pi^+ \pi^- \pi^0$.
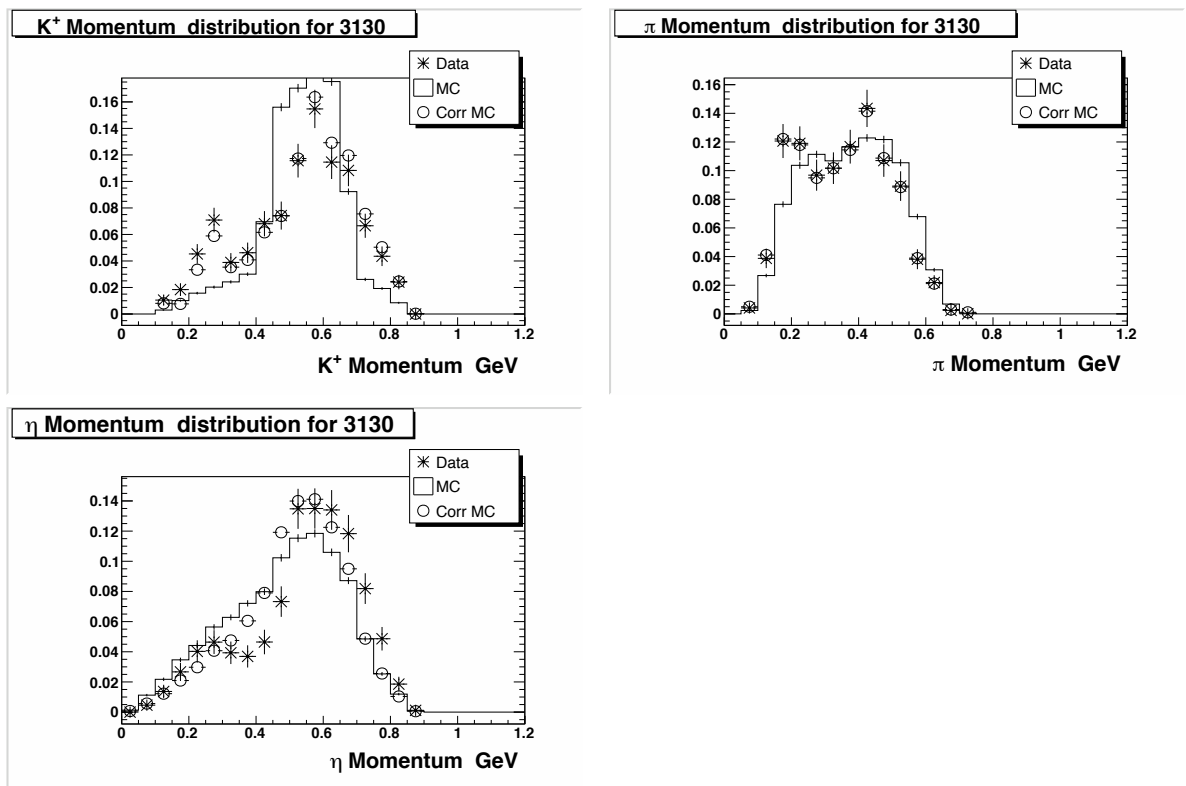
Figure A.5: The daughter spectra of the decays $D^0 \rightarrow K^- \pi^+ \eta$.
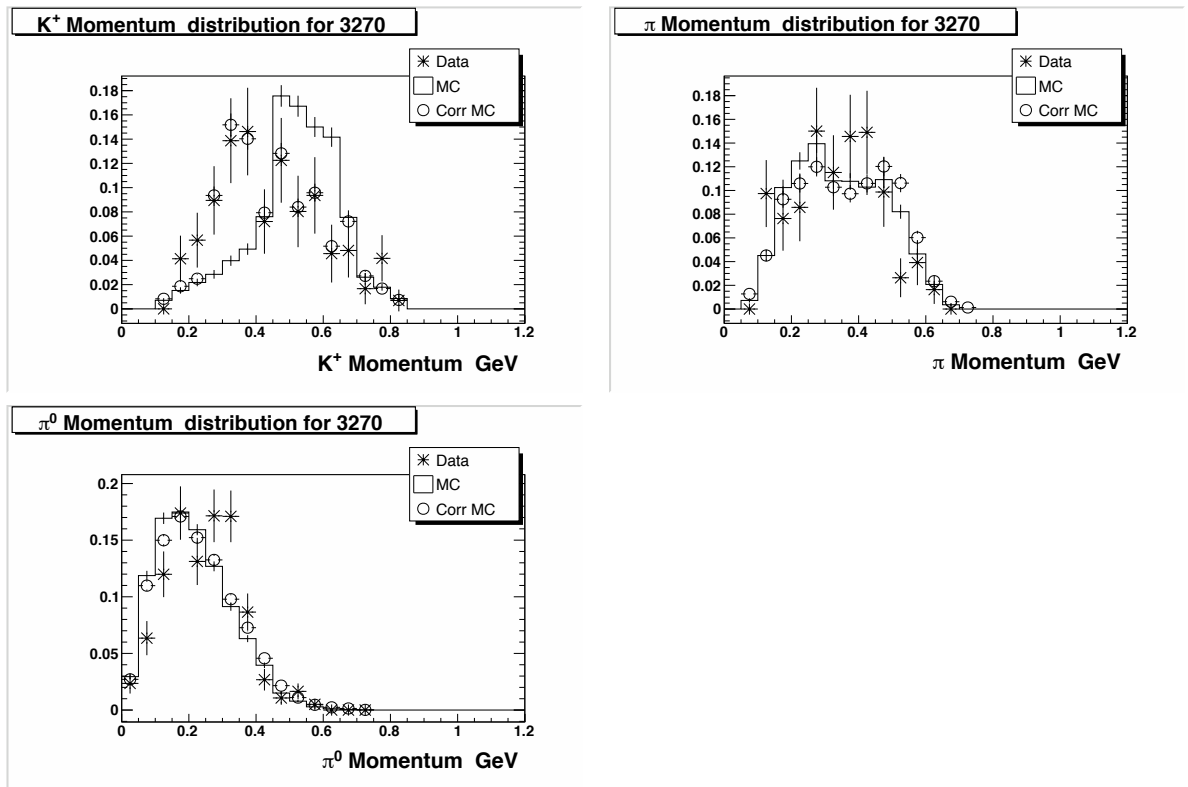
Figure A.6: The daughter spectra of the decays $D^0 \to K^- \pi^+ \pi^0 \pi^0 \pi^0$.
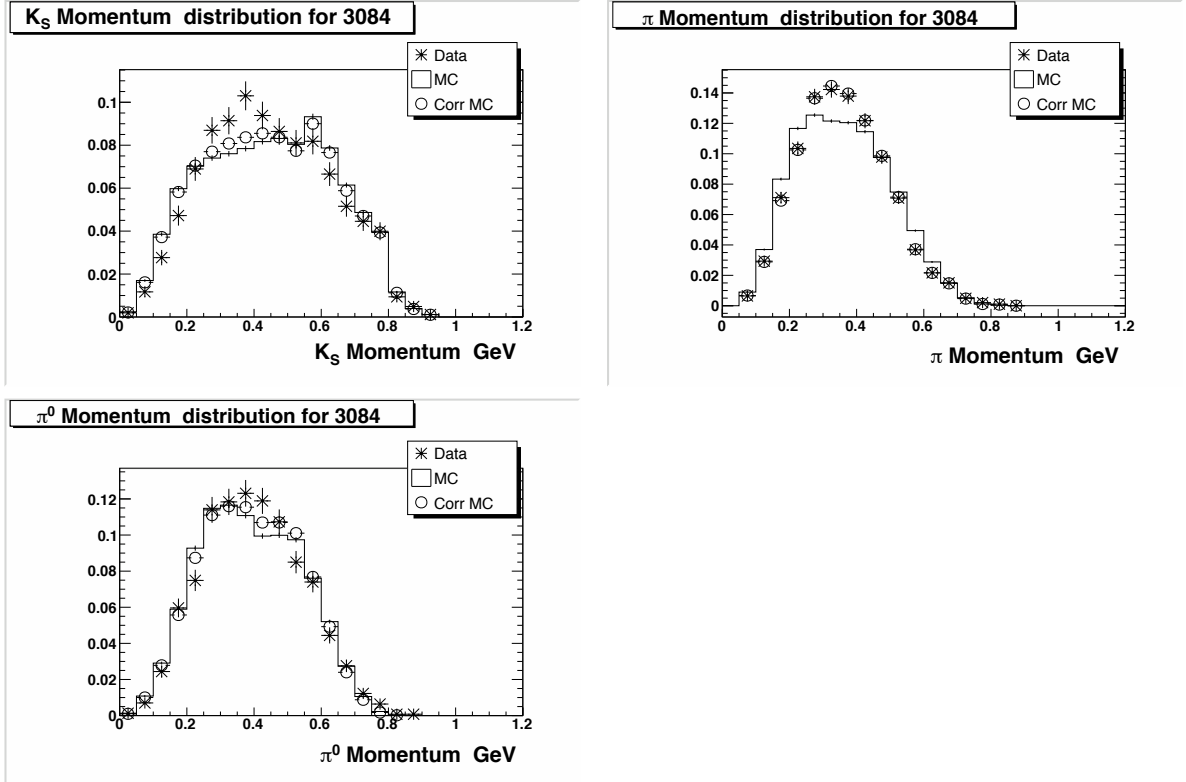
Figure A.7: The daughter spectra of the decays $D^0 \rightarrow K^0\pi^+\pi^-\pi^0$.
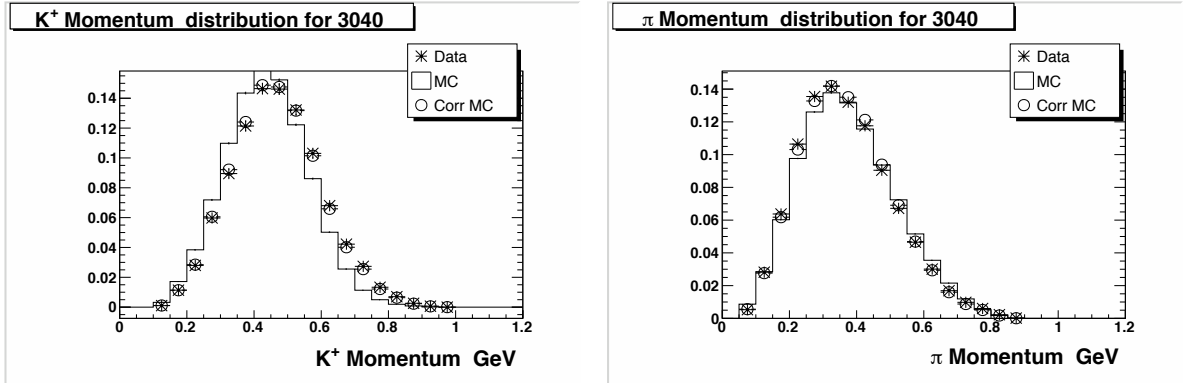
Figure A.8: The daughter spectra of the decays $D^0 \rightarrow K^-\pi^+\pi^+\pi^-$.
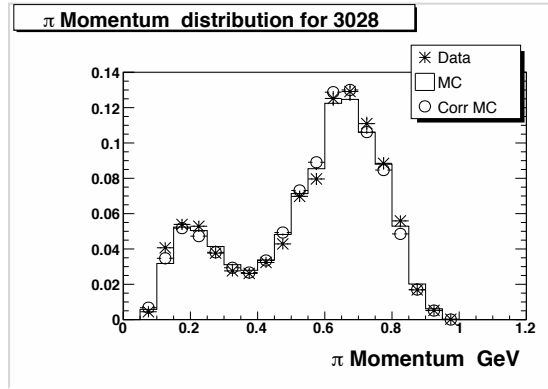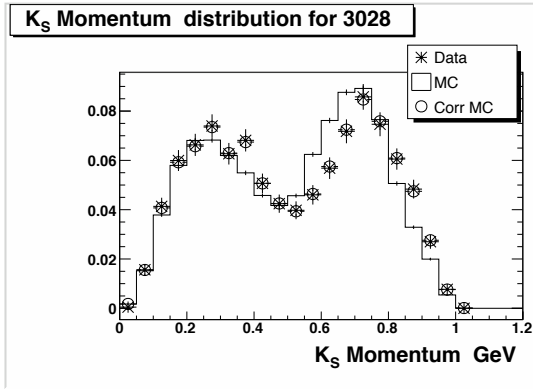
Figure A.9: The daughter spectra of the decays $D^0 \to K^0\pi^+\pi^+$.
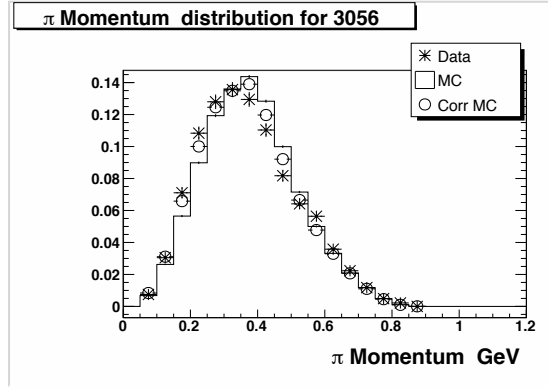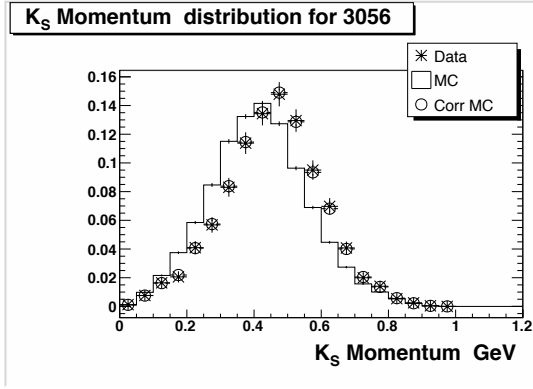
Figure A.10: The daughter spectra of the decays $D^+ \to K^0\pi^+\pi^+\pi^-$.
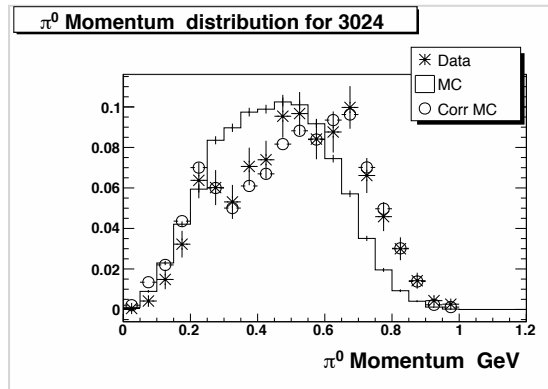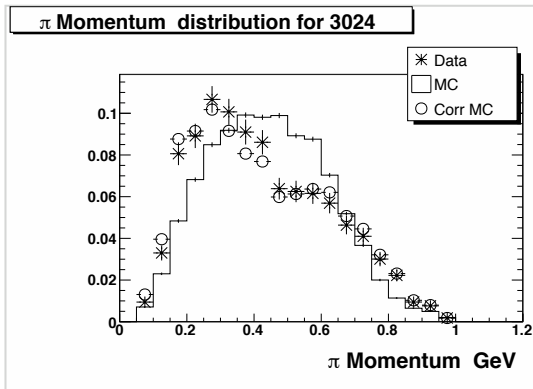
Figure A.11: The daughter spectra of the decays $D^+ \to \pi^+\pi^+\pi^-\pi^0$.
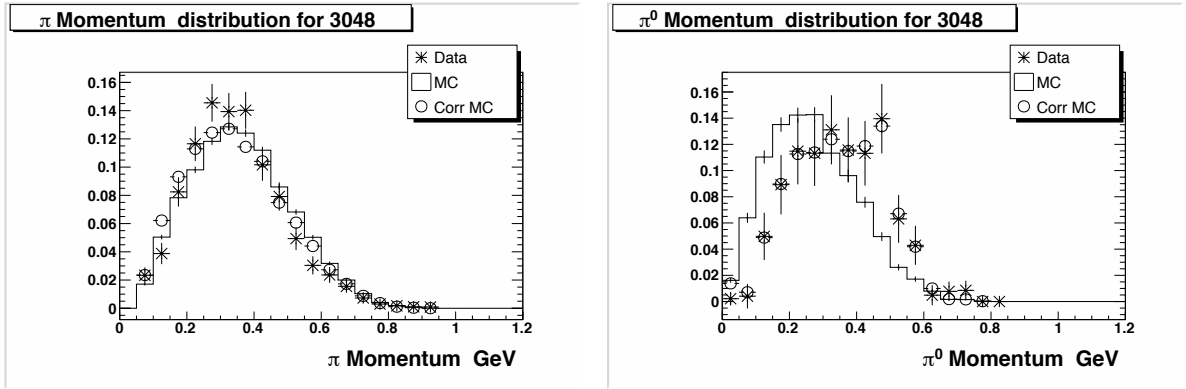
Figure A.12: The daughter spectra of the decays $D^0 \to \pi^+\pi^+\pi^-\pi^-\pi^0$.
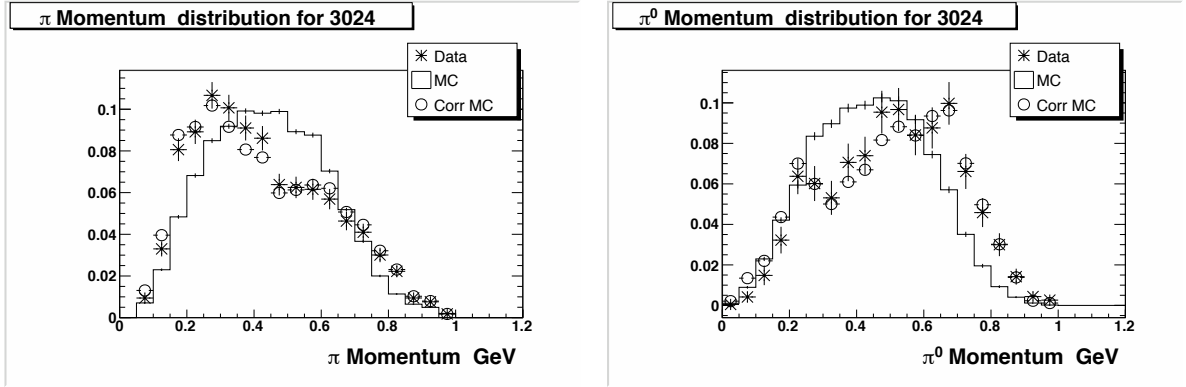
Figure A.13: The daughter spectra of the decays $D^+ \to \pi^+\pi^+\pi^-\pi^0$.
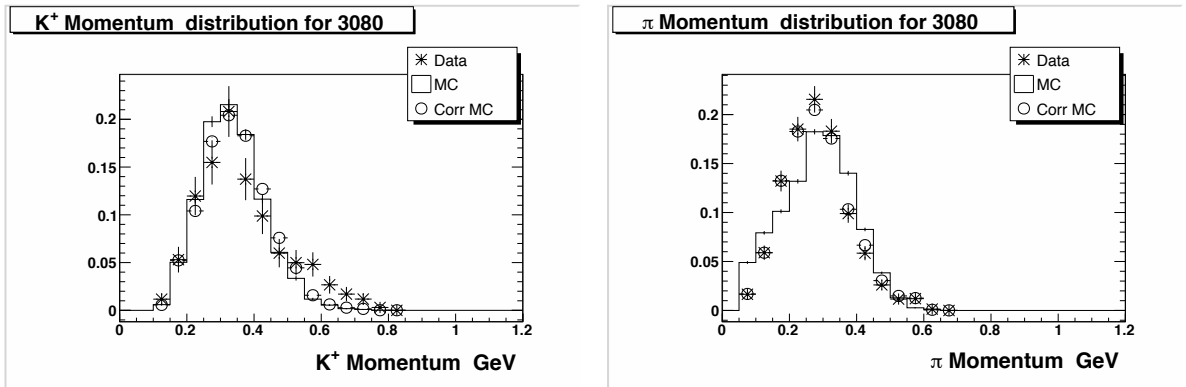
Figure A.14: The daughter spectra of the decays $D^+ \to K^-\pi^+\pi^+\pi^+\pi^-$.
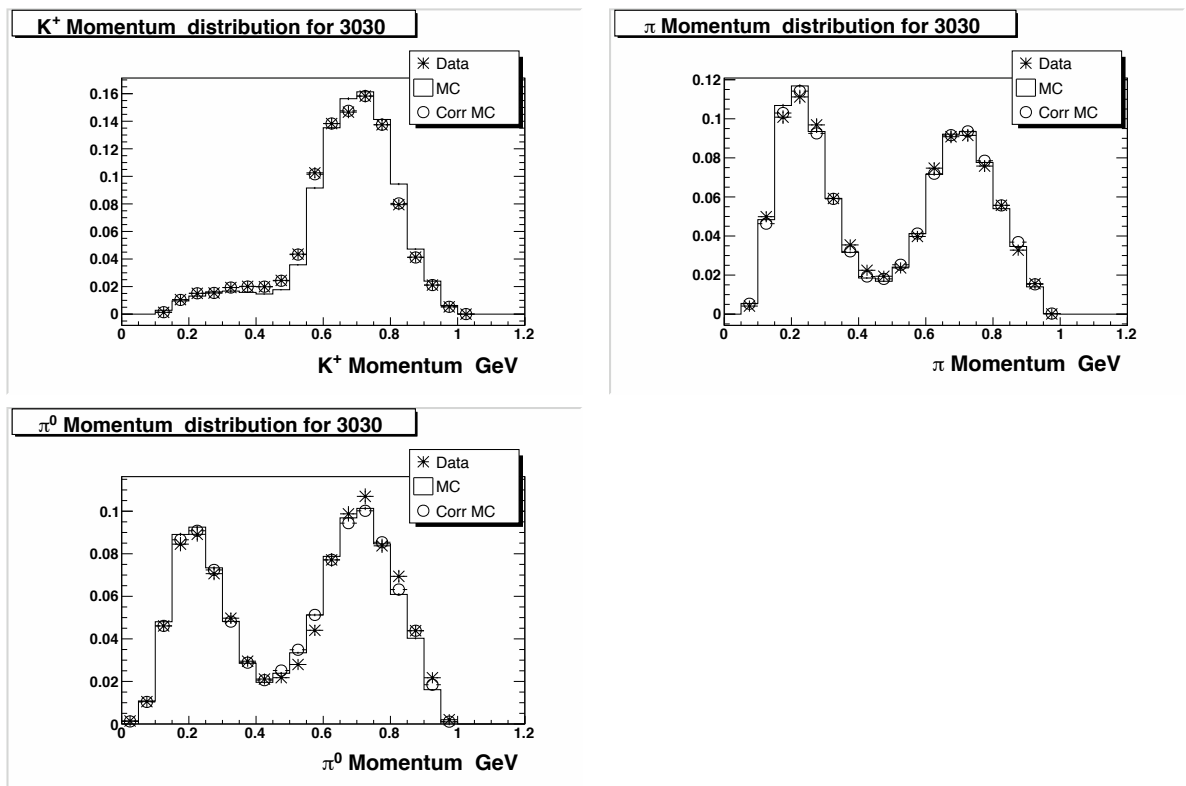
Figure A.15: The daughter spectra of the decays $D^0 \rightarrow K^- \pi^+ \pi^0$.
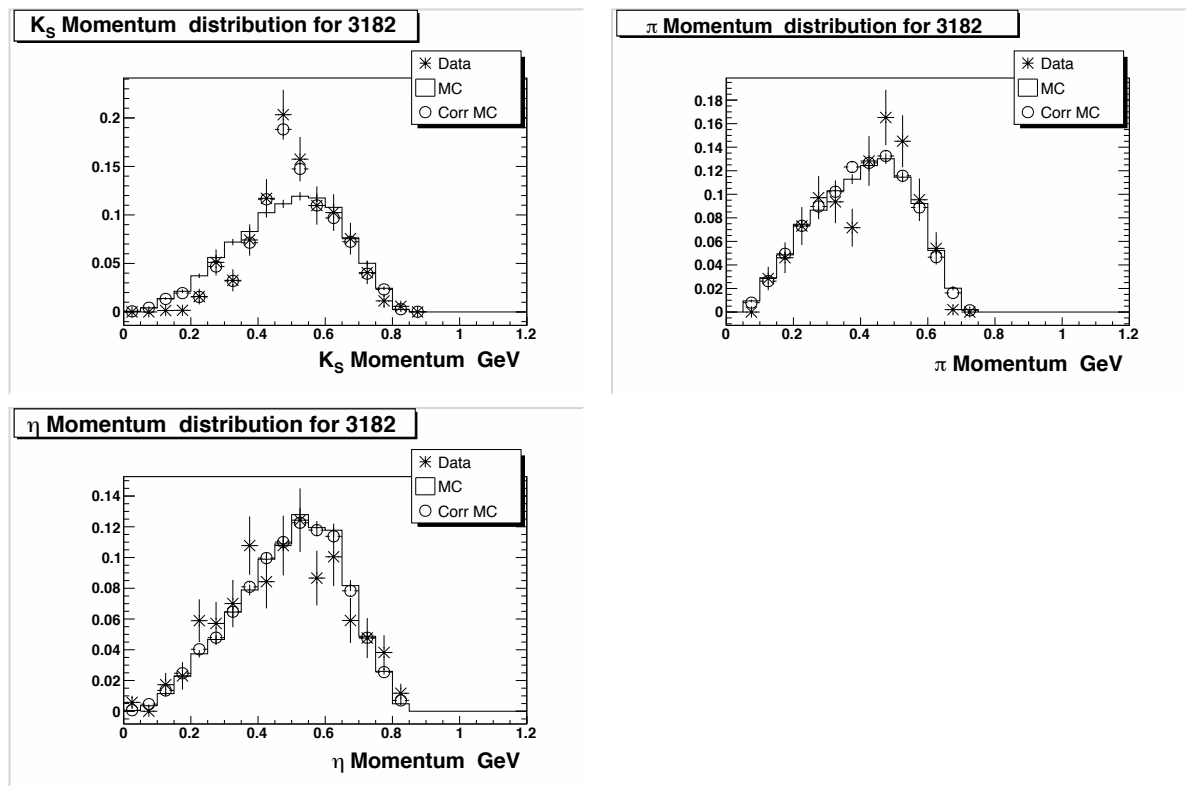
Figure A.16: The daughter spectra of the decays $D^0 \rightarrow K^0 \pi^+ \eta$.
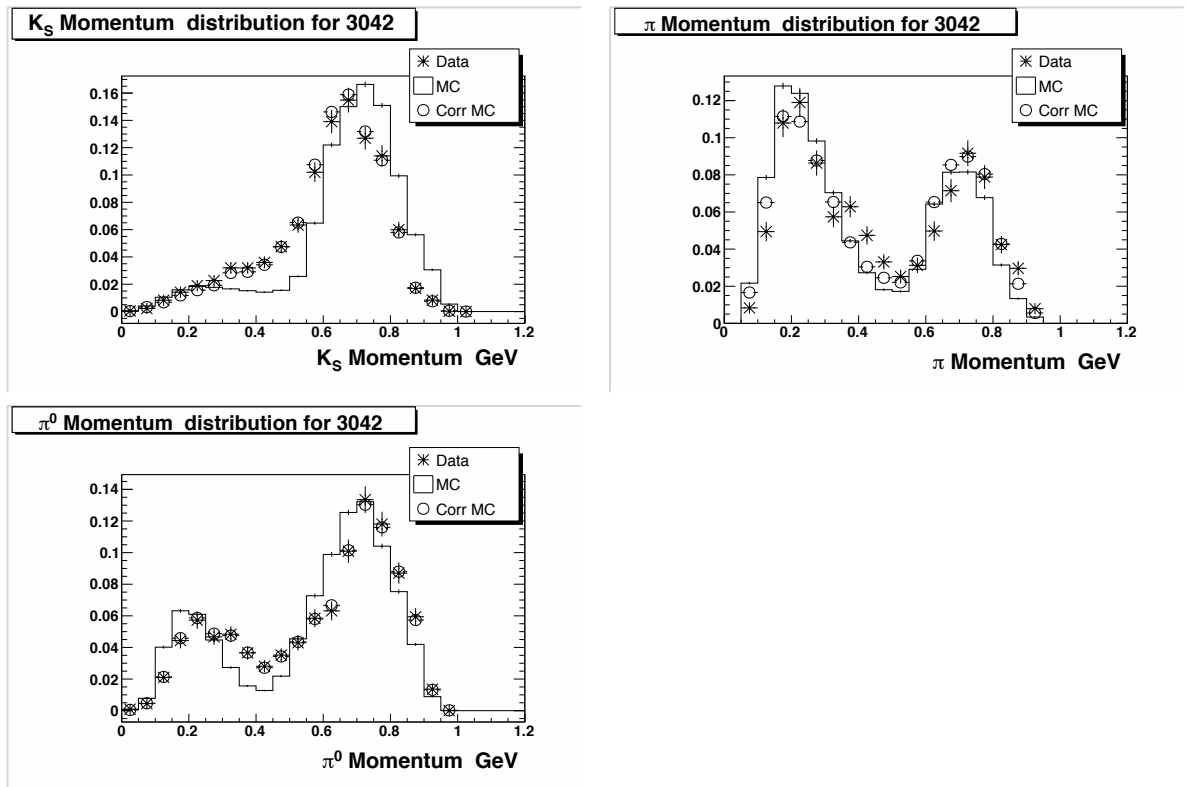
Figure A.17: The daughter spectra of the decays $D^+ \rightarrow K_S \pi^+ \pi^0$.

BIBLIOGRAPHY

[1] "B Decays to Two Charmless Pseudoscalar Mesons at CLEO", Frank Wurthwein, Jun 11, 1997 hep-ex/9706010

[2] "Why is the $B \to \eta' X$ Decay Width So Large?" Igor Halperin, Ariel Zhitnitsky, May 1997, Physical Review Letters Volume 80, Number 3

[3] "Study of Exclusive Charmless Semileptonic B Decays and $|Vub|$" Phys. Rev. Lett. 99, 041802 (2007)

[4] "Measurements of $B \to \{\pi, \eta, \eta'\}\ell\nu$ Branching Fractions and Determination of $|V_{ub}|$", May 2008, hep-ex/arXiv:0805.2408v1

[5] "Weak Decays Beyond the Leading Logarithms" Gerhard Buchalla, Andrzej J. Buras, Markus E. Lautenbacher, Dec 15 1995, hep-ph/9512380

[6] "An Introduction to Quantum Field Theory", Michael E. Peskin, Daniel V. Schroeder. 1995 Perseus Books Publishing, Cambridge Massachusetts.

[7] "Gauge Theory of Elementary Particle Physics: Problems and Solutions", Pg 97-99, Ta-Pei Cheng and Ling-Fong Li, Oxford University Press 2000.

[8] "On the Short Distance Part of the QCD Anomaly Contribution to the $b \to s\eta'$ Amplitude" Jan O. Eeg, Kresimir Kumericki, Ivica Picek, Apr 29 2003, hep-ph/0304274

[12] "Contribution of $b \to sgg$ through the QCD Anomaly in Exclusive Decays $B^{\pm} \to (\eta', \eta)(K^{\pm}, K^{*\pm})$ and $B^0 \to (\eta', \eta)(K^0, K^{*0})$" A. Ali, J. Chay, C. Greub, P. Ko, Physics Letters B, April 2 19998, 424 (1998) 161-174

[10] "Mixing and Decay Constants of Pseudoscalar Mesons", Th. Feldmann, P. Kroll, B.Stech, October 1998, Physical Review D, Volume 58. 114066

[11] "Introduction to Elementary Particles" David Griffiths 1987 John Wiley and Sons Inc.

[12] "Contribution of $b \to sgg$ through the QCD Anomaly in Exclusive Decays $B^\pm \to (\eta', \eta)(K^\pm, K^{*\pm})$ and $B^0 \to (\eta', \eta)(K^0, K^{*0})$" A. Ali, J. Chay, C. Greub, P. Ko, Physics Letters B, April 2 19998, 424 (1998) 161-174

[13] "A New Mechanism for $B^\pm \to \eta' K^\pm$ in Perturbative QCD", Dongsheng Du, C.S. Kim, Yadong Yang. Physics Letters B. 426 (1998) 133-138

[14] "Flavor-Singlet B-decay Amplitudes in QCD Factorization" Martin Beneke, Matthias Neubert, Nuclear Physics B 651 (2003) 225-248

[15] "Study of the q^2-dependence of $B \to \pi l\nu$ and $B \to \rho(\omega)l\nu$ Decay and Extraction of $|V_{ub}|$", CLEO Collaboration, April 2003, hep-ex/0304019

[16] "Measurement of the CKM Matrix Element $|V_{ub}|$ and Exculsive $B \to \pi l\nu$ and $B \to \rho l\nu$ Decays" Lawrence K. Gibbons, Annu. Rev. Nucl. Part. Sci. 1998 48:121-74

[17] "$B \to \eta' l\nu$ Decays and the Flavor-Singlet Form Factors" C. S. Kim, Sechul Oh, and Chaehyun Yu. Jul 2004, hep-ph/0305032

[18] "CLEO-c/CESR-c Taskforces & CLEO-c Collaboration", Cornell LEPP preprint, CLNS 01/1742 (2001) (unpublished)

[19] "The CLEO III Drift Chamber", Peterson, D. and others, Nucl. Instrum. Meth. A, 2002, 478, 142-146

[20] "Application of Kalman Filtering to Track and Vertex Fitting", Fruhwirth, R., Nucl. Instrum. Meth. A., 1987, 262, 444-450.

[21] "The CLEO RICH Detector", Artuso, M. and others, Nucl. Instrum. Meth. A, 2005, 554, 147-194

[22] "The CLEO-II detector", Kubota, Y. and others, Nucl. Instrum. Meth. A., 1992, 320, 66-113

[23] "$B \rightarrow \eta^{(\prime)}(\ell v, \ell\ell, K, K^*)$ Decays in the Quark Flavor Mixing Scheme". A.G. Akeroyd et.al. hep-ph/0701012

[24] "Study of exclusive charmless semileptonic B decays and extraction of $|Vub|$ at CLEO" Phys. Rev. D 76, 012007 (2007) (22 pages)

[25] B. Xin, V. Pavlunin, I. Shipsey CBX06-15

[26] S. Fa jfer and J. Kemenik, Phys. Rev. D 71, 014020 2005

[27] J. Adler et al. [Mark III Collaboration], Phys. Rev. Lett. 62, 1821 (1989).

[28] Q. He et al. [CLEO Collaboration], Phys. Rev. Lett. 95, 121801 (2005).

[29] T. Meyer, https://www.lns.cornell.edu/ cleo3/development/src/SplitoffProd/Doc.

[30] L. Fields, "Trkman-C", CBX 04-37 (2004)

[31] C. S. Park, Personal communication.

[32] "Observation of the Decay $D \rightarrow \eta ev$", CBX 06-15

[33] "A Study of Exclusive Semileptonic D Decays to Pseudoscalar Pion and Kaon Final States with the CLEO-c Detector", N. E. Adam, Cornell University Thesis.

[34] N. Adam, L. Gibbons, CBX05-59(2005)

[35] W. ParkandE. Thorndike, CBX03-25(2003).

[36] R. Barlow and C. Beeston, Comput. Phys. Commun. 77, 219 (1993)

[37] "A Study of $D \rightarrow e^+X$ Decays" C-S. Park, E. Thorndike. CBX 05-73.

[38] C. S. Park, https://hypernews.lepp.cornell.edu/HyperNews/get/PIDPerf/2.html

[39] "Measurement of Absolute Hadronic Branching Fractions of D Mesons and $e^+e^- \rightarrow D\bar{D}$ Cross Sections at the $\psi(3770)$" hep-ex/arXiv:0709.3783v2

[40] T. Becher and R. J. Hill, Phys. Lett. B 633, 61 (2006), hep-ph/0509090.

[41] "Study of $b \rightarrow u\ell\nu$ Decays on the Recoil of Fully Reconstructed B Mesons and Determination of $|V_{ub}|$", The BABAR Collaboration, hep-ex/0408068

[42] "Measurement of the $B \rightarrow \eta\ell\nu$ and $B \rightarrow \eta'\ell\nu$ Branching Fractions using $\Upsilon(4S) \rightarrow B\bar{B}$ Events Tagged by a Fully Reconstructed B Meson", The BABAR Collaboration, hep-ex/0607066

[43] B. Aubert et al. [BaBar Collaboration], Phys. Rev. D 73, 012006 (2006). [arXiv:hep-ex/0509040]

[44] C. T. H. Davies et al [HPQCD Collaboration], Phys. Rev. Lett. 92, 022001 (2004) [airXiv:hep-lat/0304004].

[45] EID web page: http:www.lns.cornell.edurestrictedCLEOCLEO3softhintsEID.html

[46] E. Barberio, B. van Eijk and Z. Was, Comp. Phys. Comm. 79 (1994) 291

[47] T. C. Andre, Annals Phys. 322 (2007) 2518; T. Alexopoulos et al., Phys. Rev. D 71, 012001 (2005).